Emission Line Stars In and Beyond the Perseus Arm

Roberto Raddi

Submitted to the University of Hertfordshire in partial fulfilment of the requirements of the degree of Doctor of Philosophy in Astronomy

October 2012

Alla Mia Famiglia

Abstract

I present low-resolution ($\Delta\lambda \approx 6$ Å) follow-up spectroscopy of 370 Hα emitters ($12 \lesssim r \lesssim 17$) identified with IPHAS, in a 100 deg^2 wide section of the Galactic plane that is located between $\ell = (120°, 140°)$ and $b = (-1°, +4°)$. Classical Be stars are found to be the most numerous group of the observed targets ($\sim 60\%$). Sixty-eight classical Be stars have also been observed at higher spectral resolution ($\Delta\lambda \approx 2-4$ Å) and S/N ratio, which allows spectral typing to an estimated precision of ± 1 sub-type. Colour excesses were measured via spectral energy distribution fitting of flux-calibrated data. I took care to remove the circumstellar contribution to the measured colour excess, using an established scaling to the Hα equivalent widths. In doing so, this method of correction was re-evaluated and modified to better suit the data at hand. Spectroscopic parallaxes were measured constraining the luminosity class via estimates of distances to main sequence A/F stars, which are found within a few arcminutes of each classical Be star on the sky.

In order to probe the structure of the outer Galactic disc, I studied the spatial distribution of 63 out of 248 classical Be stars identified. Their cumulative distribution function with respect to the distance is statistically compatible both with a smooth exponential density profile and with a simple spiral arms representation. The distribution of reddenings of classical Be stars is compared with estimates of the total Galactic reddening along their sightlines. It is expected that the measured reddenings match the integrated Galactic values, for distant stars located outside the Galactic dust layer, or they are smaller than the asymptotic values if the stars are less distant. The outcome meets expectations, and lends support to the conclusion that the measured reddenings are determined to a precision of 10%.

The sample of 248 objects doubles the number of known classical Be stars in this part of the Galactic plane. Unlike the pre-existing bright sample, the new objects are seen at large distances, between 2 – 8 kpc with typical $E(B-V) \sim 0.9$. Only four stars are members of known clusters. Ten classical Be stars are proposed to be well beyond the putative Outer Arm, at distances larger than 8 kpc. The large sample of stars, which has been identified here, is the result of a successful selection and analysis of classical Be stars that is offered for more exploitation in future. The proposition is that GAIA observations will use the present sample of classical Be stars as a new tracer of the Galactic disc.

Contents

Abstract iii

Table of Contents iv

List of Tables ix

List of Figures xi

Introduction xv

1 Literature review 1

1.1 The Milky Way . . . 1

1.1.1 The current picture . . . 2

1.1.1.1 The position of the Sun within the Milky Way . . . 3

1.1.1.2 The size of the Milky Way disc . . . 4

1.1.1.3 Properties of the Galactic disc . . . 5

1.1.1.4 Spiral structure . . . 5

1.1.1.5 Dust and extinction . . . 8

1.2 The Galactic Plane between $120^\circ \leq \ell \leq 140^\circ$ and $-1^\circ \leq b \leq +4^\circ$ . . . 9

1.2.1 The Perseus Arm . . . 10

1.2.1.1 W4, the Heart Nebula . . . 11

1.2.1.2 IC 1805 . . . 11

1.2.1.3 W5, the Soul Nebula . . . 13

1.2.1.4 CAS OB7 . . . 15

1.2.2 The Outer Arm . . . 15

1.3 Emission line stars . . . 16

1.3.1 Classical Be stars . . . 20

1.3.1.1 Parameters of CBe stars . . . 22

1.3.1.2 Where CBe stars are found . . . 26

1.3.1.3 More on the evolutionary status of CBe stars . . . 27

1.3.1.4 Known CBe stars . . . 27

1.3.2 Young stars . . . 28

1.3.3 Evolved stars . . . 31

2 Initial spectroscopic follow-up: lowest-resolution observations 33
2.1 Introduction 33
2.2 Sample selection 35
2.3 Observations and data reduction 39
2.4 Sample properties 40
2.4.1 Initial spectral grouping 40
2.4.2 Hα equivalent widths 42
2.4.3 Near-IR colour excess 47
2.4.4 Spatial distribution 50
2.5 Classical Be and Herbig Be stars 50
2.5.1 Spectral typing 53
2.5.1.1 The equivalent width ratio method 53
2.5.1.2 Fitting the range 3600 –5000 Å 57
2.5.2 Diffuse interstellar bands 60
2.6 Late-type stars 60
2.7 Summary 61

3 Second stage spectroscopic follow-up: intermediate-resolution spectra 95
3.1 Introduction 95
3.2 Sample selection 95
3.3 Observations and data reduction 97
3.3.1 Flux calibration 99
3.4 Spectral classification 102
3.4.1 CBe stars 103
3.4.2 Non CBe stars 108
3.5 Summary 110

4 Measuring reddenings of the classical Be stars 115
4.1 Introduction 115
4.2 Reddening estimation: spectroscopic method 116
4.3 Reddening estimation: photometric method 118
4.3.1 The UVEX view on reddenings 121
4.4 Summary 121

5 Correcting classical Be star reddenings for circumstellar disc emission 125
5.1 Introduction 125
5.2 Modelling the circumstellar emission of classical Be stars 126
5.3 Estimating the circumstellar colour excess 127
5.3.1 Accounting for the circumstellar colour excess with $EW(\mathrm{H}\alpha)$ measures 129
5.3.2 Comparison with the observations 130
5.3.2.1 The corrected reddenings and r-magnitudes 133

5.4 Disentangling the interstellar reddening from the circumstellar colour excess: the 4000 – 7000 Å range 133
5.5 Summary 137

6 Distance determinations of the La Palma spectroscopic sample of classical Be stars 151
6.1 Introduction 151
6.2 Distances from spectroscopic parallax 152
6.3 Constraining the luminosity class 152
6.4 Testing the spectral typing and luminosity classification with the BCD method 155
6.5 Spatial distribution of the CBe sample 156
6.6 Measuring extinction distances: an H-MEAD test 159
6.6.1 Spatial distribution for the CBe stars with bounded extinction distances 161
6.6.2 Lower limiting extinction distances 163
6.7 Discussion 165
6.7.1 Possible measurement biases 165
6.7.1.1 The absolute magnitude scale and luminosity classification 165
6.7.1.2 Disc fraction estimates 166
6.7.1.3 Choice of reddening law 166
6.7.1.4 Unresolved binaries 167
6.7.1.5 Gravitational darkening effects 167
6.7.2 The cumulative distribution of CBe-star distances 168
6.7.2.1 What would be needed to improve the present results . 172
6.8 Summary 173

7 Measures of radial velocities 179
7.1 Introduction 179
7.2 Kinematic distances of the CBe stars 180
7.3 Summary 186

8 Exploring the properties of the interstellar medium with the classical Be stars 187
8.1 Introduction 187
8.2 Measures of diffuse interstellar bands equivalent widths 188
8.3 Comparison between colour excesses of CBe stars and total Galactic reddenings 192
8.3.1 Classical Be stars with La Palma observations 192
8.3.1.1 Star # 59, a special case 195
8.3.2 Classical Be stars with FLWO/FAST observations 195

9 Discussion and conclusions **205**
9.1 Constraints on widening the CBe sample for mapping the space distance . 205
9.2 Comparison with previously known CBe stars 206
9.3 Association with known clusters 208
9.4 Most distant CBe stars in the Milky Way 210
9.5 Final remarks 211

Acknowledgements **219**

Bibliography **221**

List of Tables

1.1 Tabulated determinations of R_0 3

2.1 IPHAS photometry of the FLWO/FAST sample 62
2.2 Spectral classification and measures of equivalent widths from the FLWO/FAST spectra 76

3.1 La Palma observations 97
3.2 Photometry, $EW(\mathrm{H}\alpha)$ and spectral types of the stars with intermediate-resolution spectra 111

4.1 Colour excesses and spectral types of the CBe stars with intermediate-resolution spectra 123

5.1 Tabulation of circumstellar colour excess in the $\lambda\lambda3800-5000$ Å range . 138
5.2 Tabulation of red-optical circumstellar colour excess 138
5.3 Tabulation of r-band brightening 139
5.4 Spectroscopic reddenings corrected for circumstellar colour excess, for the CBe stars with intermediate-resolution spectra 140
5.5 Photometric reddenings corrected for circumstellar colour excess, for 181 candidate CBe stars with FLWO/FAST spectra 142

6.1 BCD parameters of the intermediate-resolution spectra 157
6.2 Spectroscopic parallaxes of the CBe stars with La Palma spectra 175

7.1 Kinematic distances of CBe stars 182

8.1 Measures of DIBs equivalent widths (La Palma sample) 198
8.2 Measures of DIBs equivalent widths (FLWO/FAST sample) 200

9.1 Known CBe stars and candidate CBe stars within the surveyed area 207
9.2 Open clusters within the surveyed area with at least one CBe star found inside the cluster radius 209
9.3 Properties of the 10 CBe stars more distant than 8 kpc 211

9.4 Spectroscopic parallaxes of the 4 CBe stars with NOT/ALFOSC spectra, for which the correction for circumstellar emission was computed via the $EW(\mathrm{H}\alpha)_{\mathrm{P}}$ . . . 215
9.5 Spectroscopic parallaxes of the CBe stars with FLWO/FAST spectra . . . 215

List of Figures

1.1 The grand design spiral galaxy M 101 2
1.2 Fig. 8 from Sale et al. (2010) 4
1.3 Fig. 2 from Drimmel (2000) 7
1.4 Spatial distribution of open clusters around $\ell \sim 130^{\circ}$ and $b \sim +1.5^{\circ}$ . . . 10
1.5 Mosaic of Hα frames of the W4 H II region. 12
1.6 Mosaic of IPHAS Hα frames in W5. 14
1.7 Fig. 1a from Kimeswenger & Weinberger (1989), Fig. 7 from Negueruela & Marco (2003) and Fig. 5 from Russeil et al. (2007) 17
1.8 Fig. 1 and Fig. 2 from Corradi et al. (2008) 19
1.9 Emission line stars towards the Perseus Arm 20
1.10 Fig. 10 from Kaiser (1989) and Fig. 11 from Dachs et al. (1988) 21
1.11 Temperature calibrations of luminosity class V and III stars 24
1.12 $(r-i)_o$ vs. spectral type relationship for luminosity class V stars 25
1.13 Absolute magnitude calibrations for luminosity class V and III stars . . . 25
1.14 Fig. 1 and 2 from Fabregat & Gutierrez-Soto (2005). 26
1.15 Magnitude distribution of CBe stars from the BeSS catalogue 28
1.16 Fig. 1 from Gullbring et al. (1998) and Fig. 1 from Hernandez (2004) . . 30

2.1 Fig. 1 from Witham et al. (2008) explaining the extraction of Hα emitters from IPHAS photometry 34
2.2 All-sky distribution of Witham et al. (2008) emission line candidates . . . 35
2.3 Spatial distribution of Witham et al. (2008) candidate emission line stars . 36
2.4 IPHAS colour-colour diagram of the Witham et al. (2008) candidate emission line stars 37
2.5 r magnitude distribution of the FLWO/FAST sample 38
2.6 IPHAS colour-colour diagram of the observed candidate emission line stars 39
2.7 FLWO/FAST observations schedule 40
2.8 IPHAS colour-colour diagram of the observed candidate emitters (with classification scheme) 42
2.9 Examples of Be FLWO/FAST spectra 43
2.10 Example of late-type FLWO/FAST spectra 44
2.11 Examples of Be FLWO/FAST spectra 45
2.12 Examples of three peculiar FLWO/FAST spectra 46

2.13 Comparison between $EW(\mathrm{H}\alpha)_\mathrm{S}$ and $EW(\mathrm{H}\alpha)_\mathrm{P}$ 48
2.14 Comparison between measures of $EW(\mathrm{H}\alpha)_\mathrm{S}$ at different epochs 48
2.15 Distribution of measured $EW(\mathrm{H}\alpha)_\mathrm{S}$. 48
2.16 Near-IR colour-colour diagram of the FLWO/FAST sample 49
2.17 Spatial distribution and longitude-counts the FLWO/FAST targets 51
2.18 Theoretical He I/Mg II vs spectral type curves 54
2.19 Spectral lines fitting 55
2.20 Initial spectral type assignment via measures of $\log W_{\lambda 4471}/W_{\lambda 4481}$ 56
2.21 Distribution of the S/N ratios measured at λ4500 Å , for the Be stars in the FLWO/FAST sample 57
2.22 Distribution of the spectral types as determined from the measure of the He I(4471 Å)/Mg II(4481 Å) line ratio 58
2.23 Examples of spectral type determination, via the spectrum fitting over the blue spectral range 59
2.24 Spectral typing comparison between the He I(4471 Å)/Mg II(4481 Å) line ratio and the line fit methods 60

3.1 2MASS colour-colour diagram of the La Palma targets 96
3.2 Spatial distribution of the La Palma targets 98
3.3 IPHAS colour-colour diagram of the La Palma targets 98
3.4 Sensitivity functions of the NOT/ALFOSC observations 100
3.5 Sensitivity functions of the INT/IDS observations 101
3.6 The S/N ratio plotted against r-magnitudes for the CBe stars 103
3.7 Spectral types determination of intermediate-resolution spectra (CBe stars) 104
3.8 Examples of spectral type assignments (NOT/ALFOSC) 105
3.9 Examples of spectral type assignments (INT/IDS) 106
3.10 Comparison between spectral types of CBe stars, assigned both from FLWO/FAST and La Palma spectra 107
3.11 Examples of non CBe star spectra 109
3.12 Comparison between different epoch Hα observations 110

4.1 Comparison between reddening laws 117
4.2 INT/WFC filters throughput 117
4.3 Examples of measures of spectroscopic reddenings 119
4.4 Difference between spectroscopic and photometric reddenings (IPHAS) . 122
4.5 Difference between IPHAS and UVEX reddening estimates 122

5.1 Nebular recombination continua 127
5.2 Circumstellar colour excess and r magnitude brightening vs f_D 128
5.3 The distribution of spectroscopic Hα equivalent widths, for the intermediate-resolution spectra of CBe stars 130
5.4 The distribution of photometric Hα equivalent widths, for the FLWO/FAST spectra of CBe stars 130
5.5 Comparison between corrected spectroscopic and photometric reddenings 131

5.6 Difference between red and blue measures of colour excess vs $EW(\mathrm{H}\alpha)$, for the intermediate-resolution spectra 132
5.7 Histogram distribution of reddenings corrected for circumstellar colour excess and r-magnitudes corrected for excess band emission, for the CBe stars identified in this work 134
5.8 Simulations of SED fitting procedure 135
5.9 Monte Carlo simulations of simultaneous $E^{is}(B-V)$ and f_D measures from model atmospheres 136

6.1 Examples of luminosity class assignment based on IPHAS photometry of MS stars nearby the CBe star 154
6.2 Example of measure of BCD parameters (Zorec et al. 2009) 156
6.3 Example of Balmer discontinuity in Be star (Kaiser 89) 156
6.4 Spatial distribution of the CBe stars with intermediate-resolution spectra . 158
6.5 Examples of distance estimates via use of H-MEAD extinction-distance curves 160
6.6 Spatial distribution of the CBe stars with intermediate-resolution spectra with bounded extinction distances 162
6.7 Histogram of the difference between extinction distances and spectroscopic parallaxes 162
6.8 Example of ill-behaving H-MEAD extinction curve 164
6.9 Histogram distribution of distances of the 63 CBe stars with La Palma spectra 168
6.10 Spiral arms representation used in the MC simulations and distance errors distribution with respect to the measured spectroscopic parallaxes 170
6.11 Histogram distribution and cumulative distribution of the distances of the 63 CBe stars with La Palma spectra 171
6.12 Cumulative distribution of the distances of the 63 CBe stars with La Palma spectra 173
6.13 Simulated spiral arms' CDCs and disc A-star CDC 174

7.1 Examples of line fitting to determine Doppler shifts 181
7.2 Radial velocity field of the Galaxy between $120^\circ \leq \ell \leq 140^\circ$ 183
7.3 Comparison between spectroscopic parallaxes and kinematic distances . . 184

8.1 Comparison between equivalent widths of DIBs at $\lambda 4428$ Å and interstellar colour excess 189
8.2 Comparison between equivalent widths of DIBs at $\lambda 5780.5$ Å and interstellar colour excess 190
8.3 Comparison between equivalent widths of DIBs at $\lambda 5797$ Å and interstellar colour excess 191
8.4 Comparison between measured interstellar colour excess, for the CBe stars with La Palma spectra, with independent estimates of the total colour excess along the line-of-sight 193

8.5 Comparison between measured interstellar colour excess, for the CBe stars with FLWO/FAST spectra, with independent estimates of the total colour excess along the line-of-sight . . . 196
8.6 IPHAS colour-colour diagram of stars nearby the CBe star F281 . . . 197

9.1 *J*-magnitudes and red magnitudes distributions of CBe stars within the surveyed area . . . 206
9.2 IPHAS and 2MASS colour-colour diagrams of the CBe stars in the studied area . . . 213
9.3 $EW(\mathrm{H}\alpha)$ distribution plotted against spectral types for the 248 CBe stars in the sample . . . 214

Introduction

The single harmony produced by all the heavenly bodies singing and dancing together springs from one source and ends by achieving one purpose, and has rightly bestowed the name not of disordered but of ordered universe.
(Aristotle, *On the Heavens*, 384 BC – 322 BC)

One of the most stunning sights in nature, which, no doubt fascinated the first humans is the endless dance of celestial bodies in the night sky. Night and day, they wander with regular and constant pace, as if to keep time of human lives. Some are colourful and swiftly changeable, others are steady, almost still, belonging to the "Heaven of the fixed stars" (Dante Alighieri, Divina Commedia, Paradiso, 1300 circa). Various descriptions of nature that surrounds us have spanned the centuries, as a way of describing what human minds could not grasp yet. The galaxy in which we live is not exempt from fanciful stories of this kind. The names that we still use for it, the Galaxy or Milky Way, have origins dating back many centuries. One of the myths of creation links the Milky Way to the story of Heracles. The myth says that Heracles, as a child, was abandoned by his mother Alcmena and later found by Hera, the jealous wife of Zeus. Hera decided to keep Heracles with her and tried to breast-feed him. Already smart as a baby, the young hero, foreseeing a future of hatred from Hera, bit her breast causing her milk to spread over the sky, forming the Milky Way (Fig. 1). Although stories like this look very naive, we should not judge them too harshly and we should remember the serious limitations of naked eye observations. Thankfully, these limits have long been overcome, but at the same time we are left with a great cultural heritage surrounding the myth of the creation of the Milky Way.

In parallel with the myths and legends created by men, natural philosophers were trying to explain the essence of things. Astronomy was a central science, playing a very important role in ancient societies, from the organisation of calendars to the choice of the time for harvesting. Despite the great advances in explaining the motion of planets, from Ptolemy (II century AD) to Copernicus (XVI century AD), no real advance was made. It is only in the early modern era that, with the development of optical instruments, celestial bodies started to have a shape and stopped being thought of as merely bright points in the sky.

Figure 1: "The Origin of the Milky Way", circa 1575, Jacopo Tintoretto - The National Gallery, London.

The first observations of the Milky Way, by Galileo Galilei in circa 1600, showed that it was made of a very large number of stars, so closely spaced that they could not be resolved with the naked eye. But it was not until the 18th century that the idea of Galaxy started to take shape. Philosophical speculations on the nature of stellar systems, or *Island Universes* as they were called by Kant in 1755, were confirmed to be true when Herschel managed to resolve the brighter stars in M31 and other galaxies, until then known generically as nebulae. Since then, many attempts have been made to understand our place in the Milky Way and its extent. This started with the rough estimates, made by Herschel, that placed the Sun in a central position and assigned to the Milky Way a diameter of ~ 3 kpc. This was late revised to a more peripheral position by Shapley in the 1920s (Shapley, 1921) using the distribution of globular clusters. More recently the stellar Galactic radius is settling to $R_{\mathrm{G}} \sim 25$ kpc, (Momany et al., 2006) up to eight times more than Herschel estimate. These distances look unimaginably large as compared to the ancients guesses about the size of the universe.

Much remains unknown about the Galaxy. The definitive spiral structure of the Milky Way is one of these. The spiral structure aspect is linked to young objects, such as H II regions and OB Associations, and to molecular or atomic gas (CO and H I), and indeed dust. The spiral arms are thought to originate from a density-wave perturbation of the Galactic potential (Lin & Shu, 1964; Roberts, 1972). According to the classical theory of spiral arms the molecular gas gathers within the spiral potential, which is quasi-stationary in a rotating frame with a fixed velocity or pattern speed, and the star formation happens within the spiral arms as induced by shocks in the interstellar medium or compression of the gas (e.g. Roberts, 1969; Lubow, Cowie & Balbus, 1986). This simplified model has been generally invoked to explain the observed spatial separation between gas and star formation tracers (Elmegreen, 2007), although observations might require a more complex picture with not just one pattern speed involved (Foyle et al., 2011). The general consensus seem to favour a four-arms model for the Milky Way, although spiral arms outside the solar circle fit into models only with more effort (cf. Georgelin & Georgelin, 1976; Russeil, 2003; Levine, Blitz & Heiles, 2006). It has been found that the use of different structure tracers does not always produce results in agreement with others (Drimmel & Spergel, 2001; Vallée, 2008). There are several reasons for the observed discrepancies. First of all, there are fewer tracers at large Galactocentric distances, as compared to those available in the inner disc (e.g. see Fig. 5, Russeil, 2003). A major issue is the lack of secure distance estimates for the majority of them. In fact, most of them are of kinematic origin and sometimes need revision (Russeil, Adami & Georgelin, 2007). Finally, our Galaxy appears to be a late-type spiral galaxy, with *grand design* spiral arms, and smaller-scale structures (Russeil, 2003; Lépine et al., 2011). In this context, it is useful to consider object classes that are well populated, which may help us in tracing the Milky Way's structure.

In this thesis, I present a large programme of follow-up spectroscopic observations, targeting the population of Hα emitters in a part of the outer Galactic plane. In recent times, classical Be stars have been discovered to be very easily picked in Hα digital surveys that can select them via their strong line emission (Witham et al., 2008). Studies have shown that their relative numbers are in excess of 60% of the total number of Hα emitters, in the range of magnitudes $r \approx 13 - 17$ (Corradi et al., 2008). These stars are well-known as being intrinsically luminous objects that are often observed in large numbers within open clusters with typical ages of ~ 20 Myr (Fabregat & Torrejón, 2000). All these properties could turn them into a useful tool for studying the Milky Way structure up to the limits of the stellar disc.

Therefore, I investigate the opportunity, which has not been examined before, of using the classical Be stars as Galactic structure tracers. A pool of candidate classical Be stars, chosen from the total sample of emission line stars, has been studied thoroughly, adapting established methods of analysis, with the final aim of analysing their spatial distribution as a probe of the disc structure in the outer Galaxy. Although I will find their distribution to be statistically compatible both with a smooth exponential density profile and with a simple spiral arms representation, this study lays the ground work for extending the method of selection and analysis to a larger number of classical Be stars. Finally, it constitutes a worked-example for the attempt of building a volume limited sample, that future GAIA observations will transform into a new tracer of the Galactic disc. The structure of the thesis is summarised below:

- **Chapter 1; Literature review:** In the first chapter I collect from the literature the relevant information regarding the topic under investigation in this work. The discussion focuses on the morphology of the Galaxy, with more attention on the second quadrant and in particular a 100 deg^2 wide section of it, towards the Perseus Arm. I also describe several types of emission line objects that are found in the analysis of the data, with particular attention to the literature on classical Be stars.

- **Chapter 2; Initial spectroscopic follow-up: lowest-resolution observations:** Here the first follow-up of candidate emission line stars is presented. A qualitative spectral typing is made and a more quantitative analysis is done for the early-type emitters that were observed, dividing them in candidate Herbig Ae/Be and classical Be stars.

- **Chapter 3; Second stage spectroscopic follow-up: intermediate-resolution spectra:** The second spectroscopic follow-up at improved spectral resolution is introduced. Data reduction and spectral typing are described. The data on classical Be stars, presented in this section, are the core of the thesis.

- **Chapter 4; Measuring reddenings of the classical Be stars:** Estimating the interstellar reddening of classical Be stars has to take account of circumstellar discs. I supply different measures of the circumstellar disc contribution to the spectral energy distribution in different wavelength ranges, and show how this can lead to contrasting results. This sets the discussion for the following chapter.

- **Chapter 5; Correcting classical Be star reddenings for circumstellar disc emission:** I present a model for the circumstellar continuum emission that updates previous approaches to the problem. The model is tested with simulated observations and against real data. The contribution of circumstellar colour excess is removed from the measured reddenings.

- **Chapter 6; Distance determinations of the La Palma spectroscopic sample of classical Be stars:** Distances are determined via spectroscopic parallax. Here, I present a method to assess the luminosity class of the stars with help of neighbouring main sequence stars (in the plane of the sky) and compare results with two alternative methods. Analysis of the spatial distribution and the possible biases affecting the measure of distances is provided. The cumulative distribution of the distances is presented.

- **Chapter 7; Measures of radial velocities:** Kinematic distances are estimated for a sub-sample of classical Be stars, leading to a limited comparison with the distances measured in the previous chapter.

- **Chapter 8; Exploring the properties of the interstellar medium with the classical Be stars:** This chapter focuses on the distribution of interstellar dust in this part of the Galactic disc. The correlation with equivalent widths of diffuse interstellar bands is re-opened and the classical Be stars are used to map the column of dust along the corresponding sightlines.

- **Chapter 9; Discussion and conclusions:** A final assessment on the properties of the whole sample of 248 classical Be stars identified is undertaken. These stars are compared with the population of previously known classical Be stars in the area. Possible members of known open clusters are searched for, among the studied sample. The most distant classical Be stars in this work are discussed also. Finally, the conclusions of this project are highlighted and some future developments are analysed.

Chapter 1

Literature review

In this first chapter I will go through the most relevant literature for this project. Starting from a very general overview of the Milky Way, with major emphasis on the disc properties and in particular the spiral structure, I will move the discussion onto the second quadrant of the Galactic plane. The project focuses on a 100 deg^2 section of the plane in the outer Galaxy direction, within the limits $\ell = (120°, 140°)$ and $b = (-1°, +4°)$. In this part of the Milky Way, stretches of the Perseus Arm and perhaps of the more distant Outer Arm are identified. Since the goal of the project is the study of young Hα emitting stars in the Milky Way, I will go through the most common types that are encountered across this thesis work.

1.1 The Milky Way

The position of the Sun in the Milky Way's disc has made it difficult to achieve a good understanding of its structure. It has often happened, that observations of other galaxies have paved the way for discoveries in our own. Emblematic examples are: (i) the early observations of dust lanes in edge-on spirals, presented by Curtis in the *great debate* of 1921 (Curtis, 1921), which anticipate the study of interstellar dust in the Milky Way; (ii) the identification of the Galactic bar, from streaming motion of H I (de Vaucouleurs, 1964); (iii) the observation of truncated light profiles in discs of edge-on external galaxies (van der Kruit, 1979), which anticipated the discovery of the truncation in the radial density profile of stars in the Galactic disc (Robin, Creze & Mohan, 1992; Ruphy et al., 1996; Sale et al., 2010). Early studies on the kinematic of stars in the solar neighbourhood, carried on by Lindblad (1927) and Oort (1927), proved that the Sun is rotating about the Galactic centre. Later on, Plaskett & Pearce (1930) found that the interstellar medium (ISM) was following the same rotation direction as the stars. It was with Oort, Kerr & Westerhout (1958) that the gaseous spiral structure of the Milky Way was firstly imaged in H I. These observations followed the optical identification of the Perseus Arm, made by Morgan, Whitford & Code (1953), with observation of O and B stars.

Figure 1.1: An example of a *grand design* spiral galaxy, the Pinwheel galaxy or M 101. Its Hubble type is intermediate, between normal spirals and barred spirals (SABcd), quite closely resembling to what the Milky Way would look like as seen far from the Galactic plane. The filters used for the image are the Baader LRGB (luminance, red, green and blue). It was taken at the Bayfordbury University of Hertfordshire Observatory (credits, David Campbell).

1.1.1 The current picture

The Milky Way is a barred late type spiral galaxy, with at least two major spiral arms but more probably four (Russeil, 2003), quite often referred to as a SABbc type (de Vaucouleurs & Pence, 1978), very likely resembling the face-on galaxy, M 101, in Fig 1.1. The basic building blocks of the Milky Way are its stars, gas, and dust. Very simply, these are organised similarly to other galaxies: (i) a bulge is found at the Galaxy centre, where a supermassive black hole ($M = 2-3\times10^6 M_\odot$) is located (Lacy et al., 1980; Ghez et al., 1998). the Galactic bar crosses the bulge with an inclination of $\sim 30^\circ$ with respect to the Sun-centre direction (de Vaucouleurs, 1964; Vallée, 2008); (iii) a disc, in which a thin and a thick components are identified (Gilmore & Reid, 1983); (iv) a stellar halo. Interstellar gas and dust are found mainly in the Galactic plane (Levine, Blitz & Heiles, 2006; Drimmel & Spergel, 2001) . In addition to visible matter, the Galaxy has an halo of dark matter extending up to several tens of kpc, whose presence dominates the mass distribution outside the solar circle (Klypin, Zhao & Somerville, 2002; Battaglia et al., 2005).

Table 1.1: More recent determinations of R_0 are listed along with the advised IAU values in 1964 and 1985. Kerr & Lynden-Bell (1986) and Reid (1993) are averaged values from compilations of different sources. The Galactocentric distance by Reid (1993) is estimated via fitting a kinematic model of the Galaxy to the parallaxes proper motions of masers in SFRs. The other sources are described in the text.

Source	R_0 (kpc)
IAU 1964	10
IAU 1985	8.5
Kerr & Lynden-Bell (1986)	8.5 ± 1.1
Reid (1993)	8.0 ± 0.5
Reid et al. (2009a)	8.4 ± 0.6
Reid et al. (2009b)	7.9 ± 0.7
Ghez et al. (2008)	8.4 ± 0.4
Trippe et al. (2008)	8.1 ± 0.3

In the following paragraphs, I will go through the properties of the Milky Way that are more relevant for this work. The focus will be prevalently on the characteristics of the Galactic disc, and specifically on the spiral structure of the Galaxy.

1.1.1.1 The position of the Sun within the Milky Way

Of primary importance for the astronomers is to establish the exact position of the Sun, since the exact knowledge of it has both effects on the study of the Galaxy itself and on the extragalactic scale distance (Reid et al., 2009a).

One of the most recent estimate for the Sun's height from the Galactic plane is $Z_0 = 25 \pm 5$ pc (Jurić et al., 2008, from studies of stellar densities).

Historically, several methods have been proposed to obtain a measure of the distance of the Sun from the Galactic centre (R_0), like the study of the observed distribution of globular clusters or RR Lyrae stars (Kerr & Lynden-Bell, 1986; Reid, 1993), being more or less in agreement with the IAU suggested value of $R_0 = 8.5$ kpc. Other indirect measures, which are often applied, come from the fit to the spiral structure of the Galaxy, in a way that by fiddling with R_0 as a free parameter, the best agreement between spiral arms and galaxy structure tracers is found (see e.g. Vallée, 2008; Reid et al., 2009a, for a few examples).

More direct methods, involve either the estimate of the distance to the central black hole, Sagitarius A*, (Reid et al., 2009b, quote $7.9^{+0.8}_{-0.7}$ kpc, obtained with measures of trigonometric parallaxes of H_2O masers nearby the central black hole) or the measure of proper motions of stars orbiting Sagitarius A* (Ghez et al., 2008). Similarly, Trippe et al. (2008) measured a distance of $R_0 = 8.07 \pm 0.32_{\rm stat} \pm 0.13_{\rm sys}$, derived from statistic parallaxes to the Galactic centre cluster stars. Some values of R_0, taken from the literature, are given in Table 1.1.

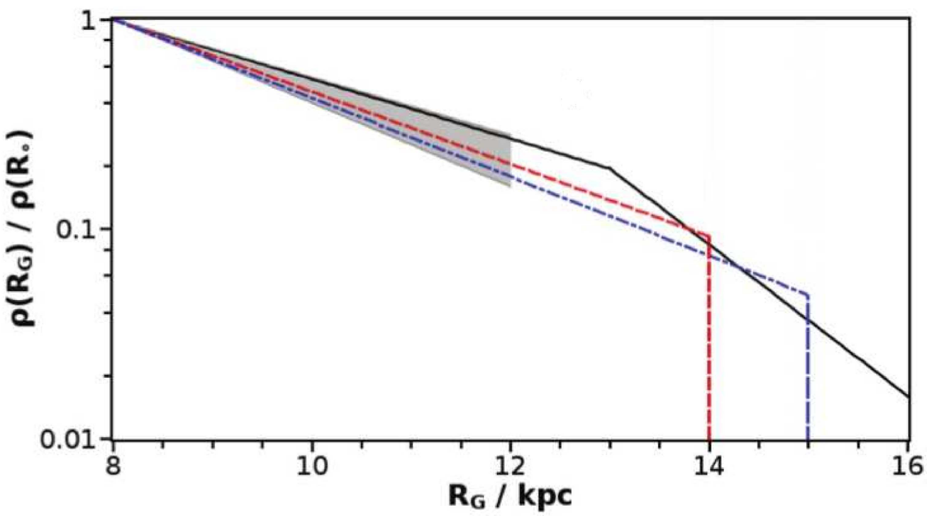

Figure 1.2: Fig. 8 from Sale et al. (2010), showing the best fitting radial density profile of the Galactic disc in black. For comparison the profiles from Robin, Creze & Mohan (1992) (red) and Ruphy et al. (1996) (blue) are also plotted. In grey is the inner scale length of (Jurić et al., 2008).

1.1.1.2 The size of the Milky Way disc

The Milky way, similarly to other galaxies, has been noticed to possess a truncation radius R_T, where the radial stellar density profile steepens appreciably (Kregel, van der Kruit & de Grijs, 2002; van der Kruit, 2007). This has been found to be in the range of 5 to 6 kpc away from the Sun in the anticentre direction (Robin, Creze & Mohan, 1992; Ruphy et al., 1996; Sale et al., 2010; Minniti et al., 2011). A practical description of the sudden steepening, observed at large Galactocentric radii, is provided by fits of two exponentials with different scale lengths to the stellar density profile. This change of scale lengths is expected to take place at what is called truncation radius: $R_T = 13$ (Sale et al., 2010, and Fig. 1.2). The scale length of the radial profile in the Solar neighbourhood is in the range of 2.5 – 3 kpc (Jurić et al., 2008; Sale et al., 2010). However, recent observations show that the Galactic stellar disc could extend up to $R \sim 23$ kpc (Momany et al., 2006). Possible origins for the truncation are discussed in van der Kruit (2007) and include: (i) the gas density drops below critical values for the star formation to happen (van der Kruit & Searle, 1981); (ii) shear forces arising from the differential rotation can become too large and halt the collapse of molecular clouds (Fall & Efstathiou, 1980); (iii) the truncation is the visible effect of a maximum allowed angular momentum, for a galactic disc, during the phase of formation of the protogalaxy (van der Kruit, 1987). The last option is proposed as the most plausible one by van der Kruit (2007), given the evidence of a steep drop of the H I surface density occurring at the truncation radius of edge-on galaxies. However, other studies, in external galaxies, show that also thin spiral arms traced both by H II regions and H I gas are seen at very large distances from the centre (Ferguson et al., 1998).

The first observations of the Milky Way in H I showed a much larger extension of the

Galactic Plane, which also appeared to be warped (Oort, Kerr & Westerhout, 1958). This feature is frequent in many other galaxies that have been found to display warping of the H I disc in opposition to a truncated stellar disc (van der Kruit, 2007). The Milky Way H I disc extends to very large distances, as compared to its stellar component, up to $R \approx 35$ kpc (Kalberla & Kerp, 2009). CO clouds, instead, have been observed up to 20 kpc (Digel, de Geus & Thaddeus, 1994), along with a warped mid-plane (Heyer et al., 1998), but they appear sparser in comparison to the H I. Very few molecular clouds in the extreme parts of the outer Galaxy are known to form stars (Digel, de Geus & Thaddeus, 1994; Snell, Carpenter & Heyer, 2002; Honma et al., 2011). The warp of the plane is observed also in the dusty disc (Freudenreich et al., 1994; Drimmel & Spergel, 2001) and in the stellar disc (Drimmel & Spergel, 2001; Momany et al., 2006; Witham et al., 2008). Whether the warp is caused by internal factors (e.g. the Galactic bar) or external factors (satellite galaxies) is still unclear (Momany et al., 2006).

1.1.1.3 Properties of the Galactic disc

In addition to the macroscopic properties of the Galaxy, local features of the disc are quite complex. The thin and thick disc components of the Milky Way's disc (Gilmore & Reid, 1983) appear to possess very distinct scale heights (recent measures are given in Jurić et al., 2008), kinematics, ages and metallicities (Bensby et al., 2005), although recent SEGUE observations suggest the contrary to be true (Bovy, Rix & Hogg, 2012). The thin disc is actively forming stars, while the thick disc, in average, has a much older population (Bensby et al., 2005) . Formation scenarios describe the thick disc as being formed from the merger of the Milky Way with one or more satellite galaxies (Abadi et al., 2003; Bensby et al., 2005) or as a progressive heating of the disc due to internal mechanisms as radial mixing (Sellwood & Binney, 2002). This last phenomenon is also invoked to explain observational properties such as the observed spread in thin disc metallicities (Lee et al., 2011). The disc is also observed to possess radially decreasing abundance gradients for the light elements (Gummersbach et al., 1998; Rolleston et al., 2000), which in turn are explained as the effect of "inside-out" formation of the disc (Hou, Prantzos & Boissier, 2000; Chiappini, Matteucci & Romano, 2001). The inside-out mechanism would be also responsible for a flattening of the gradients (Hou, Prantzos & Boissier, 2000), as it is measured from open clusters in the outer Galactic disc (Carraro et al., 2007; Chen, Hou & Wang, 2003).

1.1.1.4 Spiral structure

Along with the above mentioned characteristics, disc galaxies like the Milky Way fascinate observers with their spiral arms structure. Observations of spiral galaxies show that most of the newly formed stars are associated with spiral arms (Hodge, 1979; Elmegreen, 2007), although high resolution imaging shows that star formation also happens in filaments of molecular gas being torn apart from giant molecular clouds (GMCs) as the gas flows away from the spiral arms (Elmegreen, 2007). The basic idea on the formation of spiral structure dates back to the work of Lin & Shu (1964), on the existence of quasi-stationary density waves in the radial potential of spiral galaxies, which rotates with a constant phase velocity, also known as pattern speed. Interstellar gas is thought to gather within the potential well of a spiral density wave (Roberts, 1969), where it is accelerated triggering shock fronts. Here the elapsed time between the start of the collapse of a self-gravitating cloud and the first appearance of a star cluster is short, happening on dynamical time-scales of the order of few Myrs ($t_{\rm dyn} = (G\rho)^{-1/2}$ in Shu, Adams & Lizano, 1987; Elmegreen, 2007). Such a short time-scale fits in with observations, where young open clusters ($\lesssim 5$ Myr old) are seen embedded in the dusty gas-rich leading edges of spiral arms (Elmegreen, 2007). The collapse of GMC is generally fast, due to the quick dissipation of the supersonic turbulence within the cloud (McKee & Ostriker, 2007), while the mechanism of GMC formation, instead, is slower lasting up to a few tens Myrs (Elmegreen, 2007).

First identifications of the spiral structure in galaxies were of course in the visible light, which originates from the luminous young stellar population. It is a fact that the appearance of the spiral structure depends on the chosen pass-band (Elmegreen, Seiden & Elmegreen, 1989). One of the successes of the theory of density waves is obtained with the discovery of spiral structures also with infrared (IR) observations (Binney & Merrifield, 1998). Observations in the K-band and 240 μm prefer a 2-arms and a 4-arms spiral models respectively (see e.g. Fig 1.3 and Drimmel, 2000). This difference is due to the fact that the diffuse stellar emission, detected in the K-band, is associated to the non-axisymmetric Galactic potential and thereby traces the mass distribution in the Milky Way disc, which is observed as two broad widely open spiral arms (Rix & Zaritsky, 1995; Drimmel, 2000). On the other hand, the 240 μm, which does not coincide with the 2-arms pattern seen in the K-band, traces the short lived star formation events and it more closely resembles the optical spiral arms (Drimmel, 2000). Offsets of this kind are observed in external galaxies (Rand & Kulkarni, 1990) and also in the Milky Way (Heyer & Terebey, 1998).

The 4-arms model of the Milky Way, based on observations of H II regions by Georgelin & Georgelin (1976), has been referred to as the *standard model* (Reid et al., 2009a). As said in the previous section, ideal spiral tracers are young massive stars, open clusters, star forming regions (SFRs), which are seen mainly at the inner rim of the spiral arm. Vallée (2002), undertook a meta-study of the spiral structure of the Milky Way, concluding that our galaxy is more likely to have 4 spiral arms. This result has been confirmed in many recent papers that use a wide range of young tracers such as H II regions and young clusters (Russeil, 2003; Vázquez et al., 2008), CS emission from compact H II regions (Lépine et al., 2011), H I emission (Levine, Blitz & Heiles, 2006), CO emission (Dame, Hartmann & Thaddeus, 2001; Dame & Thaddeus, 2011), ISM in emission (Steiman-Cameron, Wolfire & Hollenbach, 2010), and the distribution of interstellar dust (Drimmel & Spergel, 2001).

The most commonly used method for assigning distances to spiral tracers is via use of a Galactic rotation curve, when measures of stellar parallaxes are not available (Russeil, 2003). The use of kinematic distances for positioning spiral arms is known to encounter the longstanding problem of the existence of peculiar motions, departing from the mean rotation law (Brand & Blitz, 1993). These are believed to originate as the effect of streaming

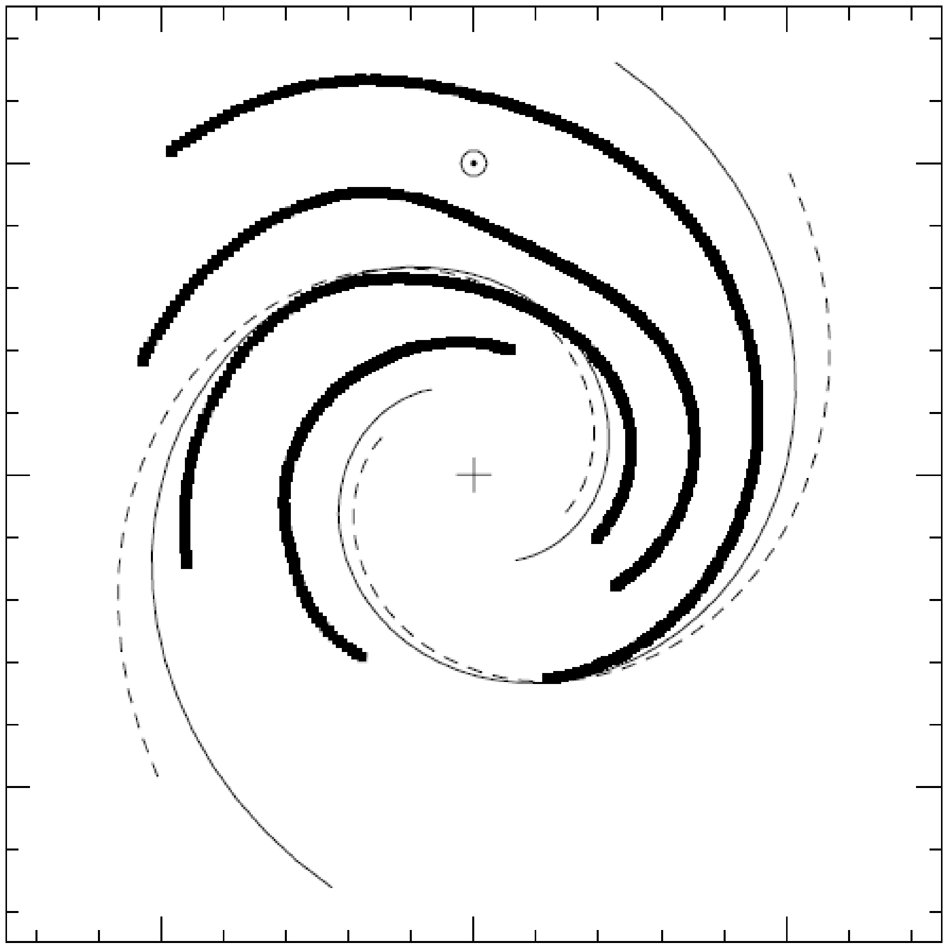

Figure 1.3: The picture is Fig. 2 taken from Drimmel (2000). It shows the 2-arm fit to the K-band Galactic profiles (thin solid and dashed lines) for two different pitch angles (15.5° and 19°), compared to the 4-arm model by Georgelin & Georgelin (1976). The Sun position is marked by the $\odot$ symbol.

motions along the spiral arms (Humphreys, 1976; Brand & Blitz, 1993; Heyer & Terebey, 1998; Russeil, 2003; Vallée, 2008). These results are particularly important in the second Galactic quadrant, where a degeneracy between radial velocities of the Perseus Arm and the Outer Arm is proposed (Vallée, 2008) When possible, the best fix to the problem is to find another more reliable way to measure distances (Russeil, Adami & Georgelin, 2007).

A solution to the problem of placing anchor points for the spiral arms, which has gained increasing success in the last few years, is the measure of very accurate trigonometric parallaxes of maser sources within SFRs (Reid et al., 2009a). From this series of observations, Brunthaler et al. (2011) proposed a new estimate of $\Theta_0 = 239 \pm 7$ km s^{-1} for the rotation speed of the Sun, which is higher than the IAU suggested value of ~ 220 km s^{-1}.

Outside the Solar Circle, within the range of Galactic Longitudes covered by the second Galactic quadrant ($90^\circ \leq \ell \leq 180^\circ$), the Perseus Arm is the first spiral arm crossed by Galactic plane sight-lines, with heliocentric distances ranging between 1 – 3 kpc. More distant is the Outer Arm, sometimes also known as Cygnus Arm, and ranges between 4 – 7.5 kpc (Fig 5 in Russeil, Adami & Georgelin, 2007). Within the second quadrant is the part of of the Galactic plane, rich in stellar and gaseous tracers of the spiral arms, which I am going to focus on for the rest of the discussion in Section 1.2.

1.1.1.5 Dust and extinction

Finally, to complete the picture of the Milky Way, it is important to have a look at distribution of interstellar dust. The realisation that dust has a dual effect of dimming the light emitted from a star and reddening it, was brought up at beginning of the century for estimating our location within the Milky Way (Trumpler, 1930; Binney & Merrifield, 1998).

One of the most cited papers, measuring the total column density of dust along galactic sightlines is the one by (Schlegel, Finkbeiner & Davis, 1998, hereafter SFD98). The authors utilised far-IR observations (combining IRAS and COBE/DIRBE data), in order to map the dust emissivity and temperature across the plane and transform it into a column density. The visual extinction is related to the dust column density via the equation $A_\mathrm{v} = 1.086\Delta\tau_\mathrm{v} = 1.086 N_d < Q_e \sigma >$ (Spitzer, 1978), where $\Delta\tau_\mathrm{v}$ is the optical depth of the dust, N_d is the column density, Q_e is the efficiency of the dust, σ is the dust cross section. Due to the coarse binning of their maps, SFD98 advice not to trust blindly the maps for $|b| < 5^\circ$, due to the fact that in areas of higher extinction the physical and temperature structure of clouds might not be resolved.

Some more sophisticated algorithms, using 2MASS photometry, have been introduced (the NICE series, Lada et al., 1996), to map smaller star forming clouds. Similarly, Rowles & Froebrich (2009, hereafter RF09), used 2MASS photometry to map the entire galactic plane, with a 49th nearest neighbour technique. The spatial resolution of their maps ranges between 1 to 10 arcmin, varying from the Galactic plane to the poles respectively. Examining sightlines toward nearby SFRs ($\lesssim 2$ kpc) of the galactic plane ($|b| \leq 5^\circ$), RF09 deduced systematic overestimate of the sightline extinctions given by SFD98, up to 1.5 – 2 mags of A_V.

The values measured by SFD98 have been also critiqued by Cambrésy, Jarrett & Beichman (2005). Using a sample of $\sim 10^5$ galaxies, they estimated asymptotic visual extinction for galactic sightlines covering about half of the sky, via a 5th nearest neighbours technique. Their result suggest that SFD98 in average overestimate the asymptotic A_V of 1 mag along the considered sightlines, proposing the discrepancy to be caused by an enhanced emissivity of the dust in the far-IR due to the presence of composite grains in the ISM.

Deep optical surveys have been shown to offer a new tool, allowing creation of extinction-distance curves (Sale et al., 2009). These have been tested on sightlines to some known clusters, supplying results comparable to those obtained by other methods. The knowledge of the amount of extinction, increasing with the Heliocentric distance, supplies an alternative method for the determination of distances that otherwise may be difficult to measure (Giammanco et al., 2011).

The knowledge of the wavelength dependence of the extinction law, is of fundamental importance in order to link the extinction to the reddening as determined by colour excess. Measures of $R_V = A_V/E(B-V)$ values, across the Galactic plane, show that the reddening law is not everywhere identical, although the shape is largely maintained (Fitzpatrick & Massa, 2007). Values of R_V for open clusters seem to be sometime different than the standard $R_V = 3.1$, suggesting particular care when one value is preferred to another, specially when very long sightlines are explored (cf. Pandey et al., 2003). It is known that R_V is generally greater for sightlines passing through molecular gas (see e.g. Cardelli, Clayton & Mathis, 1989).

1.2 The Galactic Plane between $120^\circ \leq \ell \leq 140^\circ$ and $-1^\circ \leq b \leq +4^\circ$

The area of the Galactic plane that has been chosen to be studied in this project, is not symmetrical with respect to $b = 0^\circ$. The choice of a slight offset toward positive latitudes, was made in order to capture the warping of the midplane towards positive latitudes in this part of the Galactic disc. Witham et al. (2008), indeed, showed that the median latitude of IPHAS Hα emitters is found at around $b \approx +1.5^\circ$, in the range $\ell = (120^\circ, 140^\circ)$.

In this part of the Galactic plane, measures of trigonometric parallaxes of masers in SFRs place the actively star-forming face of the Perseus Arm at 1.95 ± 0.04 kpc (W3OH, $\ell \approx 134^\circ$, Xu et al., 2006) and the Outer Arm is sampled at 6.0 ± 0.2 kpc (WB89-437, $\ell \approx 135^\circ$, Hachisuka et al., 2009). From the list of open clusters in Dias et al. (2002), it can be seen that 67 fall within the area. The median of the distribution of cluster distances is 2.4 kpc (the third quartile is found at 3.4 kpc), which is typical of Perseus Arm objects. These clusters are on average ~ 100 Myr old and quite scattered across the area. The spatial distribution of the open clusters and the masers is shown in Fig. 1.4, plotted over an extinction map of the area by SFD98. IR and sub-mm studies have revealed numerous aggregations of newly formed embedded clusters ($\lesssim 1$ Myr) in the Perseus Arm (Carpenter, 2001) and far beyond (Snell, Carpenter & Heyer, 2002). The embedded young clusters (not plotted in Fig. 1.4), are mainly distributed in the CAS OB6 area and are associated with knots of high total extinction. The complex of active SFRs, W3/W4/W5, in the Perseus Arm, is particularly well-known and studied (cf. Megeath et al., 2008, and references therein).

In a recent census of open clusters, de la Fuente Marcos & de la Fuente Marcos (2008) identified what looks to be a family of open clusters, spanning several degrees including the Cas OB6 Association within the area of interest. Members of this family share similar radial velocities and a sequence of ages that allows speculations on their common origin, as a result of interaction of GMCs and spiral density waves (de La Fuente Marcos & de La Fuente Marcos, 2009). In de la Fuente Marcos & de la Fuente Marcos (2008), the authors estimated the age of 10 –20 Myr as typical for cluster to dissolve in the Galactic field.

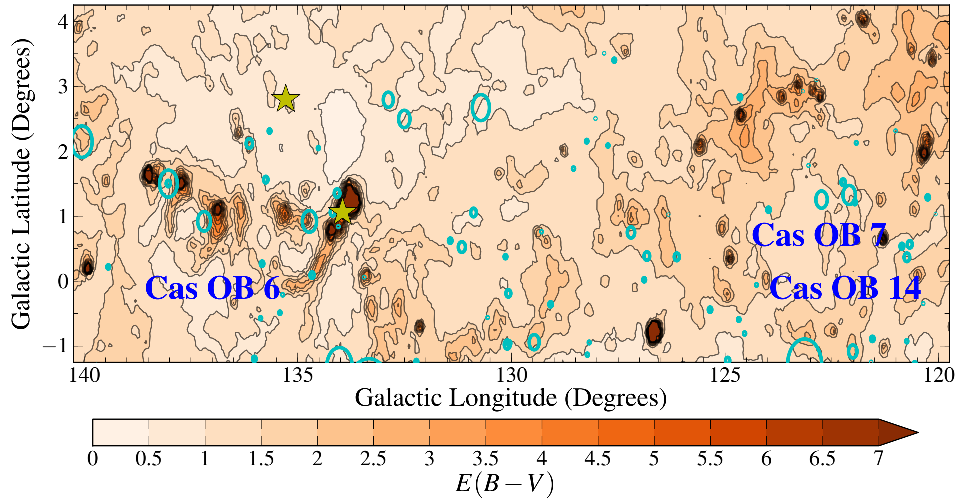

Figure 1.4: Spatial distribution of open clusters from Dias et al. (2002) plotted onto the integrated extinction map of the surveyed area (data from SFD98). Cyan circles mark the clusters' areas as defined in the catalogue. Yellow stars are the location of the masers with trigonometric parallaxes measured by Reid et al. (2009a). The location of three large OB Associations in the area are also shown. Colour levels are in magnitudes of extinction and the scale is shown in the colour bar.

Therefore, the observed spread in distances of old open clusters ($\geq$ 30 Myr) is consistent with the lack of structured appearance.

In the next few sections, I will give an overview of the young structures in the area, from which a very complex but interesting history of star formation events appears.

1.2.1 The Perseus Arm

The extensive complex of continuum radio-sources, detected by Westerhout (1958) surveying the Galactic Plane at 1390 Mhz, that is known as W3/W4/W5, is thought to be located in the closer part of the Perseus Arm (see also Georgelin & Georgelin, 1976; Dame, Hartmann & Thaddeus, 2001). Different determinations of the distance to the Perseus Arm exist in the literature - for instance, the most quoted one for W4 comes from spectroscopic parallax measures of the IC 1805 stars (Massey, Johnson & Degioia-Eastwood, 1995), which places the cluster at about 2.35 kpc from the Sun. The most accurate is the measure of trigonometric parallaxes for methanol masers in W3(OH), from Xu et al. (2006), finding a distance of 1.95 $\pm$ 0.04 kpc. This last result agrees, within the errors, with another estimate made by using, as source, H_2O masers in the same area (Hachisuka et al., 2006) that produced a distance of 2.04 $\pm$ 0.07 kpc. An average distance of about 2 kpc could, therefore, be assumed for W4 as well, considering the evidence of interaction, which I will examine later on, and the still open problem of the absolute magnitudes calibration for O stars[1].

Digel et al. (1996) and in particular Heyer & Terebey (1998) concluded that the molecular clouds in the Perseus Arm and especially the W3/W4/W5 complex, indeed, stand out as well-defined CO structures, for which it is reasonable to assume a common distance. Digel et al. (1996) rejected the possible kinematic estimate of distance (giving d $\approx$ 4 kpc) in favour of the nearer stellar distance from Massey, Johnson & Degioia-Eastwood (1995). Reid et al. (2009a), are providing further evidence of these systematic differences between star-forming regions and general rotation, with the help of parallactic measures of distance to high-mass SFRs using VLBA.

1.2.1.1 W4, the Heart Nebula

W4 is a large H II region, spanning over 2 deg^2 and roughly centred at Galactic coordinates (135°, +1°). It includes a number of dark clouds and the star cluster IC 1805. W4 is also called the Heart Nebula, because of the shape picked out in bright Hα emission. The current picture describes W4 as part of an originally extensive complex of molecular clouds, including W3 and probably W5. Normandeau, Taylor & Dewdney (1996) and Taylor et al. (1999) proposed the presence of a Galactic chimney candidate in association with W4. A 'chimney' is a elongated shell-like structure of ionised gas through which energetic photons can travel and heat up the Galactic corona. In Hα imaging, it mainly shows itself as a large bubble almost cleared of molecular gas, dominated by the IC 1805 cluster in its centre. It is hemmed in by the highly obscured W3 molecular cloud on its west border (Fig. 1.5). Evidence of what is generally seen as a physical boundary, between W4 and W3, was uncovered first by Lada et al. (1978), in a survey of CO emission, seen as the presence of compact condensations along the ionisation front bounding W4. Lada et al. (1978) even stressed how intense stellar winds, originating from the OB stars in the IC 1805 cluster, could have produced the High Density Layer (HDL, Lada et al., 1978) and triggered star formation inside W3; recent observations, by Oey et al. (2005) and Moore et al. (2007), seem to confirm this idea.

1.2.1.2 IC 1805

The cluster belongs to the Cas OB6 Association (de La Fuente Marcos & de La Fuente Marcos, 2009). Distance moduli and reddenings measured by Massey, Johnson & Degioia-Eastwood (1995) for individual stars, place the cluster at 2.35 $\pm$ 0.09 kpc with $\overline{E(B-V)}$ = 0.87 $\pm$ 0.02 (adopting a total-to-selective absorption ratio, R_V = 3.1). They inferred an age of 1-3 Myr from the isochrone positions in the Hertzsprung-Russel (HR) diagram. Pandey et al. (2003) analysed the ratio $E(\lambda - V)/E(V-B)$ for the cluster in several broad band filters, arguing in favour of a larger value of $R_{\text{cluster}} \sim 3.53 \pm 0.25$ (for $\lambda \leq \lambda_J$) with respect to normal extinction observed toward foreground stars. It is still unclear whether the

[1] Martins et al. (2005) point out as more detailed stellar models, including the effect of line-blanketing and winds on non-LTE atmospheres, reduce O stars' luminosities by $\sim$ 0.25 dex. Such a re-calibration makes the observed stars to be closer than previously computed; for the cluster IC 1805, it would be translated into a distance of about 2.0 kpc.

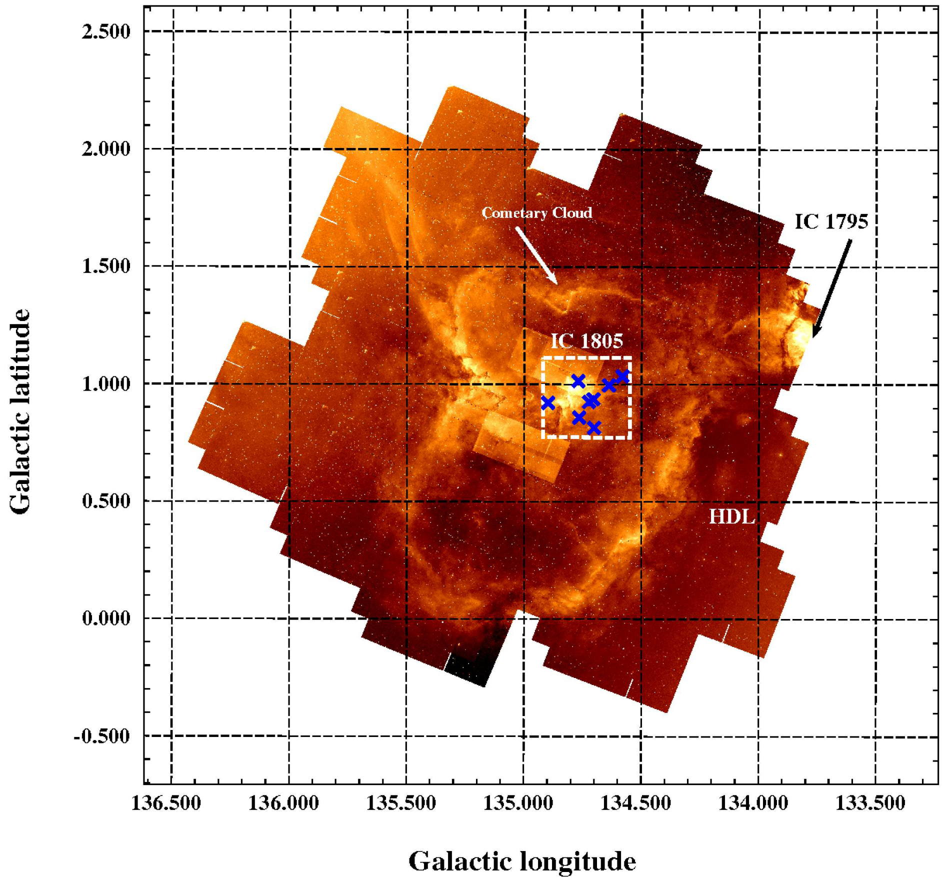

Figure 1.5: Mosaic of Hα frames of the W4 H II region, from the IPHAS Survey (Drew et al., 2005). Positions of the nine O stars in IC 1805 are shown (Massey, Johnson & Degioia-Eastwood, 1995); Hα emission distinctly traces the shape of the H II bubble, being emitted in the layer between the ionisation front and the shock front of it. The HDL is located westward of IC 1805, its presence is displayed by the Hα emission. The cluster IC 1795, site of current star formation (Oey et al., 2005), is located in W3 inside the HDL.

presence of a previous generation of massive stars triggered the formation of the currently observed OB stars; traces of an older population of stars could be linked to the dynamical evolution of the W4 H II region. In a study of the stellar content of IC 1795, Oey et al. (2005) suggested evidence of multiple events of hierarchical triggered star formation in W3/W4. They argue for three distinct phases of sequential star formation: (i) the W4 H II region (6-10 Myr old, following Dennison, Topasna & Simonetti, 1997); (ii) IC 1795 (3-5 Myr old) (Fig. 1.5), triggered by the W4 shell compressing the surrounding ISM; (iii) embedded young clusters (10^4-10^5 yr old) along the border of W3 (see references in Oey et al., 2005), triggered by the expanding W3 superbubble. This would place IC 1805 in the second generation of triggered star formation, due to the expansion of W4. They also comment that this cluster may not be in the centre of the bubble, but may just be projected onto it.

Massey, Johnson & Degioia-Eastwood (1995) also discussed evidence of an earlier population visible on the HR diagram, as evolved 15 $M_\odot$ stars may be present - the main sequence (MS) life, for such stars, can be as long as 6-8 Myr, based on the tracks of Schaller et al. (1992). Interestingly they also found stars compatible with masses between 5 - 7 $M_\odot$ that might be in the Pre-Main Sequence (PMS) phase. These results, if confirmed, imply a more or less continuous star formation process, stretching over 10 million years. Some of these proposed 5-7 $M_\odot$ young stars could be Hα emitters, although only one of them matches with the catalogue of Hα emitters by Kohoutek & Wehmeyer (1999) and two of them are found in Witham et al. (2008).

1.2.1.3 W5, the Soul Nebula

The optical counterpart of W5 is the wide H II region IC 1848. In W5 two distinct ionised shells are visible: W5 East (W5-E) and W5 West (W5-W) (Fig. 1.6). Five O-type stars are known in the area: four of them are in W5-W, and are said to form the IC 1848 cluster, with just one in W5-E. As in W4, Carpenter, Heyer & Snell (2000) found evidence of embedded stars, also described in Karr & Martin (2003) and Thompson et al. (2004).

Koenig et al. (2008), using Spitzer data (with IRAC and MIPS instruments) plus 2MASS H and K_s when IRAC [5.8] and [8.0] photometry was not available, identified 2064 class I and II young stellar objects (YSO) [2]. Analysing the observed spatial distribution of the YSOs only, they found $\sim$ 45-70% to be in clusters of N $\geq$ 10 stars, depending on the applied cut-off distance between cluster members (see the paper for details). The authors proposed at least a fraction of the remaining dispersed population has been ejected after close encounters in the early life of the observed YSO clusterings, citing numerical simulations as supporting evidence. Assuming an average ejection speed of $3\,\mathrm{km\,s^{-1}}$, the typical distance from the nearest clustering, observed by Koenig et al. (2008), could be covered in $\sim$ 3 Myr, in agreement with the 5 Myr age of the oldest O stars in W5 (Karr & Martin, 2003). In Fig. 1.6, positions of class I and class II sources in Koenig et al. (2008) and the five O stars in the area are displayed. It is noteworthy that 68 sources match positions of IPHAS Hα emitters identified by Witham et al. (2008). I anticipate that for 12 of these stars, I obtained low-resolution spectra (Chapter 3). Four are late-type emitters, while eight are early type stars. These stars seem to be young stellar objects, as suggested by Koenig et al. (2008).

Very recently, Chauhan et al. (2011) searched for traces of triggered star formation in the bright rimmed clouds, which are seen at the edge of the W5-E H II. They assessed a distance of 2.1 kpc for the cluster IC 1848 and a median age of 1.3 Myr for the population of PMS stars. They suggested that the induced star formation, in the area, has not lasted for more than 5 Myr, from the estimated ages of the most massive stars in the cluster. The authors found evidence of small-scale star formation, discovering a decreasing age gradient of the PMS stars, from the centre of the cluster to the outside.

[2] YSOs classification scheme was defined by Lada (1987), with the measure of the infrared spectral index $\alpha_{\mathrm{IR}} = d\log(\lambda F_\lambda)/d\log\lambda$, where the derivative is measured in the range 2.2 –10 μm. A class I object has $\alpha_{\mathrm{IR}} > 0$, while a class II object has $-1.5 < \alpha_{\mathrm{IR}} < 0$.

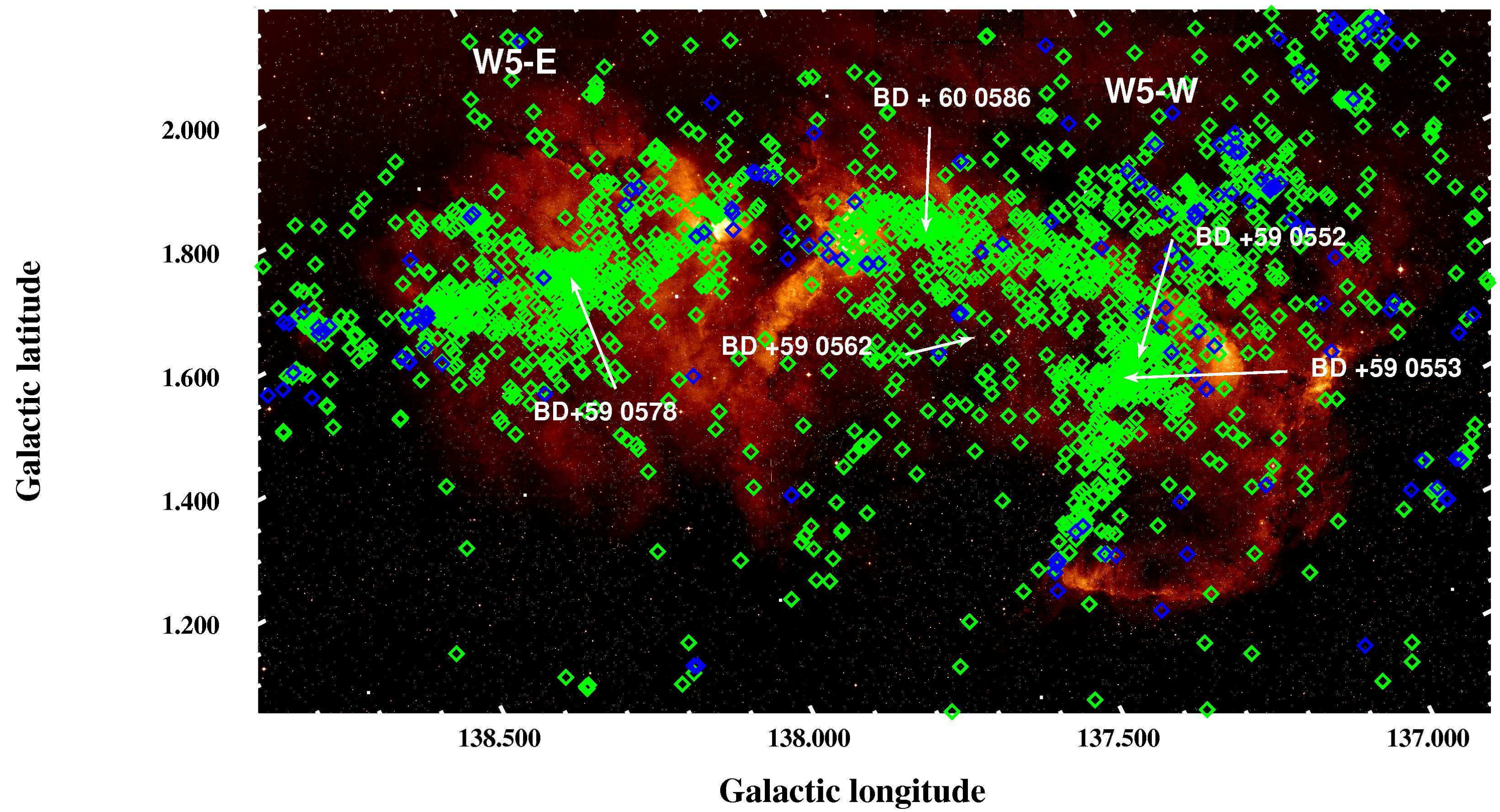

Figure 1.6: Mosaic of IPHAS Hα frames in W5. Arrows point to positions of the five O-type stars, ionising the gas in the area.. YSOs identified in Koenig et al. (2008) are labelled with blue (class I) and green diamonds (class II).

1.2.1.4 CAS OB7

The CAS OB7 Association belongs to the Cas-Per family of Associations (de La Fuente Marcos & de La Fuente Marcos, 2009) along with CAS OB6, which includes W4 and W5. It consists of 32 B-type stars, earlier than B3, and one O6V star (Garmany & Stencel, 1992). The visual magnitudes of these stars are in the range $V = 9.5$ – 11.5, with reddenings in the range of $E(B-V) = 0.6$ – 1.2. Cazzolato & Pineault (2003) collected evidence from neutral hydrogen, CO and IRAS data, indicating arc-like and shell structures surrounding the CAS OB7 members. The structures in the ISM have velocities in agreement with the radial velocities of the stars. The continuum radiation of ionised gas, within the shell, seems to imply a larger UV flux than is measured from the visible OB stars, which implies previous events of star formation and supernovae explosions. The authors are searching for evidence of secondary (more recent) star formation, which could be triggered by the expanding shell surrounding the CAS OB7 Association. The measured distances of the cluster are in the range of 1.9-2.3 kpc (Humphreys, 1976; Garmany & Stencel, 1992), which gives a mean linear diameter on the sky corresponding to $\sim$ 60 pc. Finally, they propose an age greater than the dynamical time computed from the expansion velocity of the shell ($\sim$ 2 Myr), and infer a turn-off age for the association in the range of 8 Myr.

1.2.2 The Outer Arm

The structure of the Outer Arm, seen with stellar tracers seem to be less impressive than it appears from molecular or higher-quality H I observations (see e.g Russeil, 2003; Snell, Carpenter & Heyer, 2002; Levine, Blitz & Heiles, 2006). The first stars noticed beyond the Perseus Arm were reported by Muzzio & Rydgren (1974). They found eight O and B-type stars in the second Quadrant, with distances larger than 4 kpc. Three of these were at distances exceeding 5 kpc, with one deduced to be $\sim$ 10 kpc away. However, these were dispersed over a very large area and the most distant one, is at $b \approx -1^\circ$. At this large distance, the star would be well below the warped galactic plane (Momany et al., 2006). However, this criticism did not allow for the possible mitigating effect of disc flaring at large Galctocentric radii.

Kimeswenger & Weinberger (1989) found what they proposed to be a "very realistic representation" of the gap in structure tracers, between the Perseus and Outer Arms. In the top left panel of Fig. 1.7, I show their Fig 1a, in which the distribution of several reliable tracers are plotted. They excluded isolated OB stars, as these were judged to be not representative of the spiral structure. However, when they considered stars with spectral types earlier than B3, grouped in a more limited area of the sky, the average measured distances were at a heliocentric distance of $\sim$ 4 kpc, i.e. corresponding to the closer edge of their suggested Outer Arm.

More recently, evidence of the stellar population within the Outer arm has been brought forward by Negueruela & Marco (2003). I show, at the top right of Fig. 1.7, their main results. A group of stars, is found at $d \approx 5.3$ kpc around $\ell = 115^\circ$. At larger longitudes, the

Outer Arm seems to approach shorter distances, with 4-5 kpc in the range $\ell = (120^\circ, 140^\circ)$ – this distance is shorter than the ones reported by Vallée (2002) and Russeil (2003), as the authors note.

Finally, the bottom panel of Fig. 1.7 shows the revision of the map of logarithmic spiral arms by Russeil, Adami & Georgelin (2007). The tracers they used, are still much less frequent for the Outer Arm than the Perseus Arm and therefore less compelling. The proposed range of distances covered by the Outer Arm, between $\ell = (120^\circ, 140^\circ)$, is very much unchanged: 4-6 kpc.

Nevertheless, the most compelling and reliable measure within the part of the Galaxy here considered remains the one by Hachisuka et al. (2009), via trigonometric parallaxes of masers. As noted above, this place the SFR at ~ 6 kpc. Recently a more distant section of the Outer Arm was found in the first Galactic quadrant, and trigonometric parallaxes of masers (Sanna et al., 2012) have been obtained there as well, giving a distance of ~ 9 kpc: the studied maser is located within CO complexes suggested by Dame & Thaddeus (2011) to trace the molecular Outer Arm in the first quadrant.

The most concrete evidence, that star formation is happening in an arm-like structure, comes again from molecular and IR studies. Snell, Carpenter & Heyer (2002) identified embedded clusters, within dense clumps in molecular CO emission in SFR seen behind W3/W4/W5 at radial velocities of between -60 and -80 km s^{-1}. The authors reported that the masses of the molecular clouds they identified in the Outer Arm were much lower in comparison to the masses of Perseus Arm clouds, suggesting that the efficiency with which atomic gas is transformed into molecular gas must be much lower. However, they find that the star formation efficiency is similar to that measured for clouds throughout the Milky Way.

Finally, Vázquez et al. (2008) bring forward the evidence of a coherent distribution of open clusters (from Moitinho et al., 2006), blue stars seen in the background of open clusters (Carraro et al., 2005), and molecular clouds (May, Alvarez & Bronfman, 1997), tracing the Outer Arm as parametrised by Vallée (2005) up to a heliocentric distance of ~ 10 kpc, at around $\ell \sim 230^\circ$ in the third Galactic Quadrant. They found that unlike the Local and Outer Arms, which are traced by molecular and optical tracers, the Perseus Arm in the third Quadrant is seen almost only in CO emission, hypothesising a possible disruption of the Perseus Arm due to the crossing of the Local Arm.

In conclusion, the Outer Arm is a less strong feature of the Galaxy, in comparison to the Perseus Arm, although evidence of tracers both in the first and specially in the third Galactic quadrant, would suggest that a number of optical tracers, still not identified, may be present in the second Galactic quadrant and await discovery.

1.3 Emission line stars

The Hα emitters studied in this thesis are all selected from the INT Photometric Hα Survey of the Northern Galactic Plane (IPHAS Drew et al., 2005). IPHAS photometry was collected in two broad band filters, *r* and *i*, and a narrow-band Hα filter. IPHAS has revealed

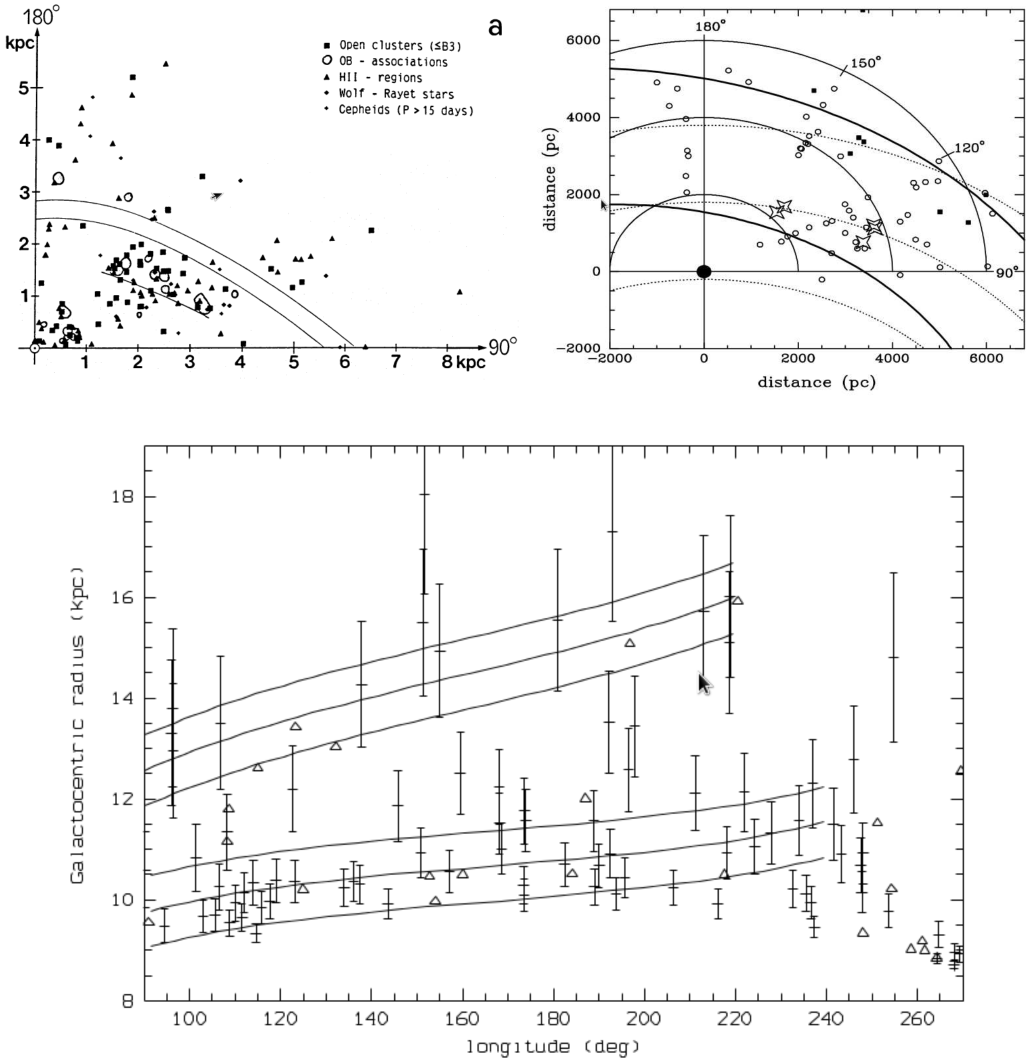

Figure 1.7: Top left panel is Fig. 1a from Kimeswenger & Weinberger (1989), presented by these authors as showing evidence of the Outer Arm in the second Galactic quadrant. The two curves mark the separation between Perseus and Outer Arm. Top right panel is Fig. 7 from Negueruela & Marco (2003). The thick solid curves are the spiral arms locations from Vallée (2002). The stars are open clusters and OB Associations, good tracers of the Perseus Arm. The stars they observed are plotted as empty circles, while squares are background stars of open clusters (Massey, Johnson & Degioia-Eastwood, 1995). Dotted curves are circles of Galactocentric radii 7, 9, and 11 kpc. The thin dark circles, instead, are centred on the Sun and have radii of 2, 4, and 6 kpc. Bottom panel is Fig. 5 from Russeil, Adami & Georgelin (2007). The plot represent the distribution of structure tracers, compared to the location of the fitted arms in the Second Galactic quadrant. Each arm is plotted as three curves, spanning a range 1.4 kpc wide.

itself to be very effective in identifying numerous new emission line objects (see e.g. Viironen et al., 2011; Corradi et al., 2011; Barentsen et al., 2011). Thanks to the different sensitivities of the $(r-i)$ and $(r-\mathrm{H}\alpha)$ colours, the reddening vector moves the stellar loci at a small positive angle with respect to the horizontal in the colour-colour plane (see e.g. Fig. 1.8a) making it possible to easily pick out candidate Hα emitters that are displaced vertically (Witham et al., 2008; Viironen et al., 2009).

Witham et al. (2008) inspected the overlap between IPHAS Hα emitters and sources in the Kohoutek & Wehmeyer (1999) catalogue, which is the most comprehensive previous catalogue of Hα emitters. It is complete down to $V \sim 13$. Only a small number of cross-matches ($\lesssim 10\%$) were found, due to the fact that the range of magnitudes covered by the two samples offers only a small overlap. In Fig. 1.9, I plot the histogram distribution of magnitudes of 311 out of 352 Kohoutek & Wehmeyer (1999), in their original photoelectric V-band magnitudes, and the 560 Witham et al. (2008) Hα emitters found within the surveyed section of the Galactic plane. Cross-matching the two samples, I only find 10 matches. The Kohoutek & Wehmeyer (1999) sample is dominated by early-type emitters, down to $V \sim 13$. The same is true of the Witham et al. (2008) catalogue down to $r \sim 18$ (the authors suggested a fraction of the total as large as 85%, from the analysis of 300 follow-up optical spectra).

Corradi et al. (2008) made an in-depth study of the different populations of the most common point-source Hα emitters that can be identified with IPHAS photometry. Their study focused on the symbiotic stars and aimed at quantifying the contamination from other classes of stars by combining IPHAS photometry with near-IR photometry (2MASS in this instance). One of their main results was that $\sim 46\%$ of the IPHAS-2MASS cross matches are candidate Be stars. They also found that the largest number of contaminants for the selection of symbiotic stars (SySs) comes from the classical T Tauri stars (CTTSs). Their analysis was based on the entire Witham et al. (2008) catalogue, which goes down to a limiting magnitude of $r = 19.5$. The sample of stars I work with, in Section 2, is limited to brighter magnitudes($r \lesssim 17$) and the colour of the observed targets lay in the range $(r-i) \lesssim 1.5$ and $(r-\mathrm{H}\alpha) \lesssim 1.0$. This reduces the number of classes of emitters that are likely to be found. From Fig. 1.8(a) and (b), Be stars, cataclysmic variables (CVs), s-type SySs, compact planetary nebulae (compact PNe or cPNe) and CTTSs (not plotted in figure) make up the pool of likely candidates. Most of the objects above mentioned can present what is known as the B[e] phenomenon (Lamers et al., 1998), i.e. they may present permitted low-ionisation metal emission lines and forbidden emission lines of [Fe II] and [O I] in the optical spectrum, in addition to the Balmer lines in emission and a near-IR excess due to circumstellar dust. This phenomenon is seen in symbiotic Be stars, Herbig Ae/Be stars, cPNe, supergiant Be stars (sgB[e]), and unclassified Be stars (unclB[e]). The last two groups are generally very bright stars (mostly studied in the Magellanic Clouds, Lamers et al., 1998) or rarer stars that do not fit other groups mentioned above.

In the following sections, I will discuss these classes of stars, giving particular emphasis to the classical Be stars (CBe), which are the most frequent object type I identify with the spectroscopic follow-up presented in Chapter 2 (up to 60%).

The second more numerous groups of stars I identify and that are most likely to be

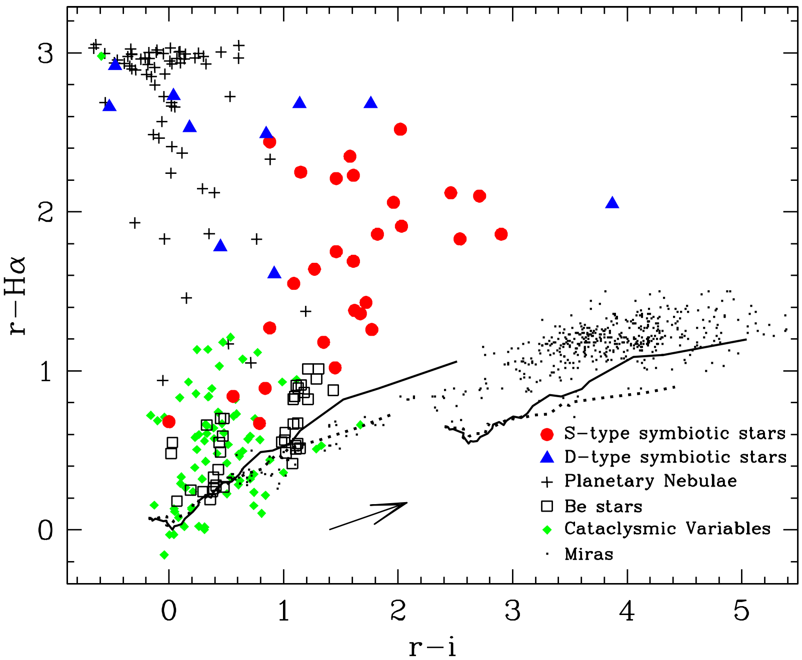

(a)

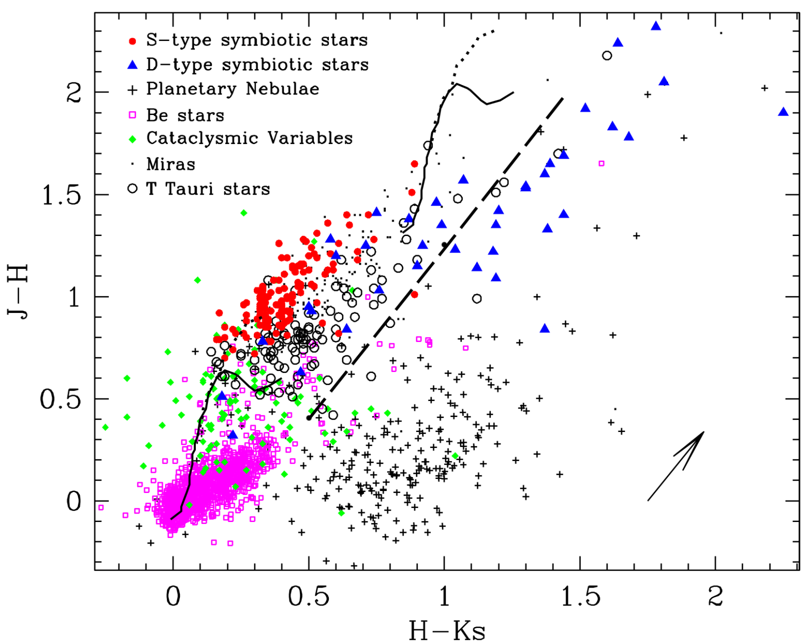

(b)

Figure 1.8: Fig. 1 and Fig. 2 from Corradi et al. (2008). (a) IPHAS colour-colour diagram of different classes of Hα emitters. Stellar loci, with $E(B-V) = 0, 4$, for dwarfs and giants are plotted as solid and dotted lines The arrow shows the direction of the reddening vector, with length corresponding to $E(B-V) = 1$. (b) 2MASS colour-colour diagram of the different classes of Hα emitters. Stellar loci of dwarfs and giants are the solid and dotted lines, which are for $E(B-V) = 0, 4$ as in panel (a). The arrow is the $A_V = 3$ reddening vector. References for the plotted objects can be found in Corradi et al. (2008). The dashed black line, taken from Lee & Chen (2007), roughly separates Herbig Ae/Be stars from classical Be stars and classical T Tauri stars.

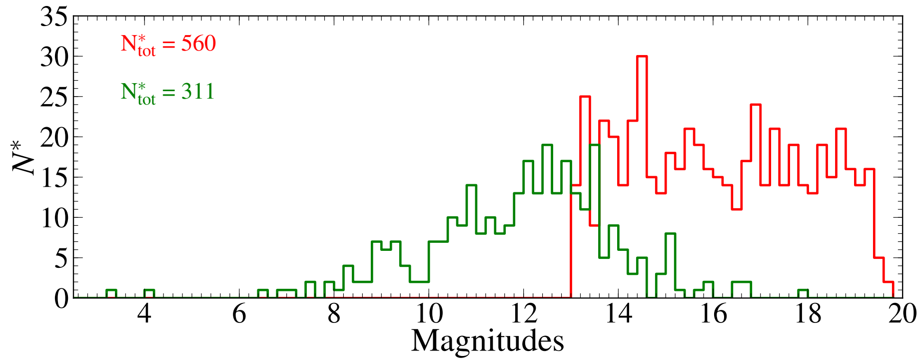

Figure 1.9: Histogram distribution of magnitudes of the point-source Hα emitters identified by Kohoutek & Wehmeyer (1999) (photoelectric V magnitudes), in green, and Witham et al. (2008) (r magnitudes), in red. The number counts represent the stars found along sightlines toward the Perseus arm, between $120° \leq \ell \leq 140°$ and $-1° \leq b \leq +4°$.

found in Galactic plane surveys are YSOs, of which the most numerous are the early-type ones or Herbig Ae/Be (HAeBe) stars, in the brighter range of magnitudes here considered. Differently from CBe stars, HAeBe stars possess generally larger near-IR colour excesses that originate from their dusty circumstellar discs (Lada & Adams, 1992). In the 2MASS colour-colour diagram of Fig. 1.8(b), this class of objects is located on the right hand side of the dashed black line, as found by Lee & Chen (2007), which allows a colour-cut separation both from CBe stars and CTTSs for instance.

The evolved stars are sufficiently uncommon that they do not constitute a significant contaminant in the sample studied – only 1 CV was found. I will begin an overview of the main classes of emission line star with a brief summary of classical Be stars.

1.3.1 Classical Be stars

By definition, these stars are non-supergiant B stars whose spectrum has or had at some time, one or more Balmer lines in emission (Porter & Rivinius, 2003). They possess other distinguishing properties, such as rapid rotation and absence of forbidden emission lines from their spectra. In the HR diagram, they are observed just above the MS (Porter & Rivinius, 2003), and are characterised as being on the terminal age main sequence (TAMS Fabregat & Torrejón, 2000).

In addition to presenting line emission in the Hα and higher order Balmer lines, CBe stars are typified by excess continuum emission at ultraviolet (UV), optical, and IR wavelengths (Fig. 1.10 and Dachs, Kiehling & Engels, 1988; Kaiser, 1989; Zorec & Briot, 1991; Dougherty et al., 1994). The continuum emission of CBe stars is enhanced by the presence of circumstellar envelopes, which have been shown to give rise to free-free and free-bound optically-thin emission (Gehrz, Hackwell & Jones, 1974; Dougherty et al., 1994; Dachs, Kiehling & Engels, 1988, and references therein). The observed correlation between Hα equivalent width, $EW(\text{H}\alpha)$, optical and IR colour excess, suggests that both line and continuum emission are generated within the same regions in the circumstellar envelope (see

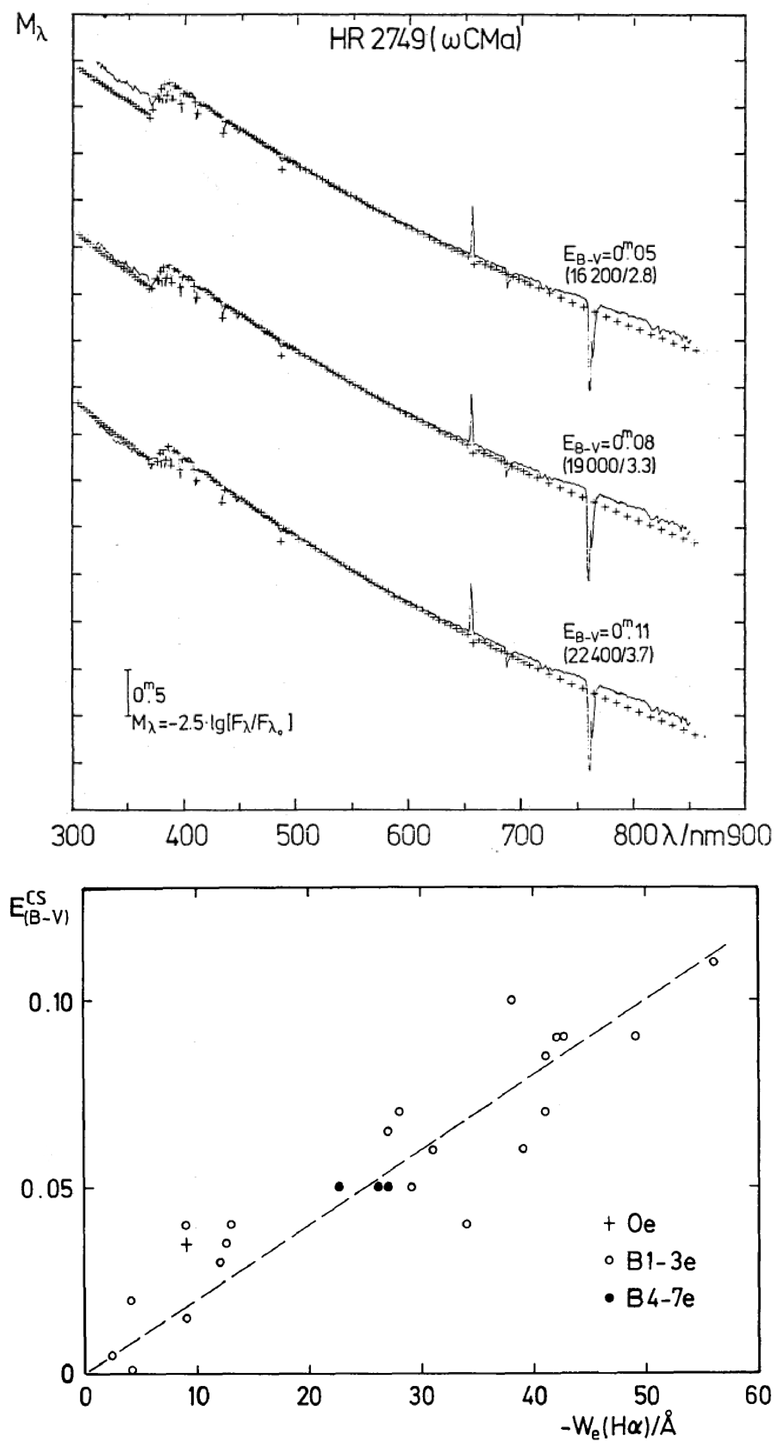

Figure 1.10: Top panel is Fig. 10 from Kaiser (1989) and bottom one is Fig. 11 from Dachs, Kiehling & Engels (1988). Top panel shows the spectrum of the Be star HR 2749 (solid curve), artificially dereddened for three different values of $E(B-V)$, compared to Kurucz (1979) model atmospheres. The continuum excess at red wavelengths is evident. Bottom panel shows the correlation between $E^{cs}(B-V)$ and $EW(\mathrm{H}\alpha)$ found by Dachs, Kiehling & Engels (1988).

e.g. Fig. 1.10 and Dachs et al., 1986; Dachs, Kiehling & Engels, 1988; Howells et al., 2001). Dachs, Kiehling & Engels (1988) showed that the continuum emission is optically thin in visible light, presenting a good correlation between $EW(\mathrm{H}\alpha)$ with the volume emission measure, or the fractional flux originating from the disc (f_D). Measuring Balmer decrements $D_{34} = I_{\mathrm{H}\alpha}/I_{\mathrm{H}\beta}$ and the ratio $EW(\mathrm{H}\alpha)/f_D(\lambda 6563\,\text{Å})$, Dachs, Rohe & Loose (1990) confirmed high electron densities ($n_e \approx 10^{12}$ cm^{-3}) that had been adopted by early CBe models (see e.g. Poeckert & Marlborough, 1978), in order to model the line and continuum emission. In the dense circumstellar environment, collisions are important, but nevertheless the Hα emission is mainly a recombination line (Dachs, Kiehling & Engels, 1988).

The circumstellar envelopes are known to be in the shape of a geometrically thin disc (Dachs, Rohe & Loose, 1990; Waters et al., 1991; Dougherty & Taylor, 1992; Quirrenbach et al., 1997; Porter & Rivinius, 2003, and references therein). From measures of Hα profiles, Dachs et al. (1986) showed that the emission originates from a rotating disc, which has been confirmed by interferometric (Meilland et al., 2007) and spectroastrometric techniques (Oudmaijer et al., 2011) to be in Keplerian rotation and whose extension seems to mildly correlate with the temperature of the underlying star (Tycner et al., 2005). Models describing the disc formation mechanism, which is commonly accepted to be a decretion disc, have invoked in turn radiatively driven winds and stellar pulsation (Porter & Rivinius, 2003). More recently ejection mechanisms due to fast rotation have gained more favour (Townsend, Owocki & Howarth, 2004).

The latest results by Carciofi et al. (2012) confirm the viscous decretion disc model, proposed by Lee, Osaki & Saio (1991), to be a valid approximation that can explain the V-band variation of CBe stars as episodic events of disc formation. Finally, Carciofi & Bjorkman (2006) modelled the radial structure of discs and supported the picture of them as fully ionised – except in the denser parts of the equatorial plane, where Fe II shell lines are thought to originate. They also found that the gas temperature consistent with the observed UV to IR disc emission is $\sim 0.6 T_{\mathrm{eff}}$, as had earlier demonstrated for the winds of hot stars (Drew, 1989).

1.3.1.1 Parameters of CBe stars

CBe stars are known to be fast rotators, which show a typical ratio of equatorial to critical velocity in the range of $v_e/v_c \approx 0.8 - 0.9$ (Townsend, Owocki & Howarth, 2004), where the v_c is the rotation velocity for which the gravitational force is balanced by centrifugal forces (Struve, 1931).

Townsend, Owocki & Howarth (2004) proposed the rotation velocity of CBe stars to have been systematically underestimated from measures of line profiles in previous works (see e.g. Chauville et al., 2001), due to saturation issues originating from gravitational darkening effects (von Zeipel, 1924). It has been pointed out that these effects, induced by structural changes in a fast rotating star, affect spectral lines and the spectral energy distribution (SED) of fast rotating stars, in a way that the real physical parameters can be different from the apparent ones (Townsend, Owocki & Howarth, 2004; Frémat et al.,

Table 1.2: Adopted class V $T_{\rm eff}$ scale, intrinsic colours and absolute magnitude scale. The $T_{\rm eff}$ values are from Kenyon & Hartmann (1995); the intrinsic colours are computed taking the average of Sale et al. (2009), Fabregat (priv. comm.), Kenyon & Hartmann (1995), Siess, Forestini & Dougados (1997). The absolute r magnitudes are conversions of the absolute V magnitudes given by Zorec & Briot (1991). In the final two columns we give class IV and III absolute magnitudes obtained from the same source. Uncertainties on Mr are 50% of the absolute errors given by Zorec & Briot (1991), which more closely resemble the standard deviations at each sub-type than the full range specified by Zorec & Briot (1991).

	dwarfs			subgiants	giants
SpT	$T_{\rm eff}$ (K)	$(r-i)_{\rm o}$ (mag)	$\rm M_r$ (mag)	$\rm M_r$ (mag)	$\rm M_r$ (mag)
B0	30000	−0.17	-3.40 ± 0.30	-3.70 ± 0.25	-4.20 ± 0.35
B1	25400	−0.15	-2.80 ± 0.30	-3.10 ± 0.20	-3.70 ± 0.35
B2	22000	−0.13	-2.10 ± 0.35	-2.50 ± 0.30	-3.30 ± 0.45
B3	18700	−0.12	-1.55 ± 0.25	-2.00 ± 0.20	-2.85 ± 0.50
B4	17000	−0.09	-1.15 ± 0.20	-1.65 ± 0.20	-2.45 ± 0.55
B5	15400	−0.08	-0.70 ± 0.20	-1.20 ± 0.25	-2.30 ± 0.55
B6	14000	−0.07	-0.30 ± 0.20	-0.75 ± 0.25	-1.90 ± 0.55
B7	13000	−0.06	-0.10 ± 0.20	-0.50 ± 0.25	-1.60 ± 0.50
B8	11900	−0.04	0.20 ± 0.25	-0.30 ± 0.25	-1.30 ± 0.50
B9	10500	−0.02	0.60 ± 0.25	0.10 ± 0.30	-0.90 ± 0.60
A0	9520	0.00	1.00 ± 0.25	0.50 ± 0.30	-0.50 ± 0.60

2005). These differences depend on the inclination angle of the rotation axis relative to the line of sight. For physical parameters that are determined from analysis of line profiles, a measure of $T_{\rm eff}$ would increasingly be underestimated for larger rotation speeds and inclination angles, while $\log g$ underestimates correlate with the rotation speed and anticorrelate with the inclination angle (Frémat et al., 2005). With the interpretation given by Townsend, Owocki & Howarth (2004), of CBe stars rotating as rapidly as $v_e/v_c \approx 0.95$, the peculiar location occupied by CBe stars in the HR diagram, i.e. in proximity of the TAMS, could be partly explained as a consequence of the rotation rather than nuclear evolution. After testing models on observed high-resolution spectroscopic data, Frémat et al. (2005) continued to propose that CBe stars rotate at under-critical rotation speeds

Since the underlying star is a B star (Porter & Rivinius, 2003), it has been common practice in the literature to determine physical parameters of CBe stars from the measures of photospheric properties, which are presumed to be typical of normal B-type stars (Kaiser, 1989; Zorec & Briot, 1991; Chauville et al., 2001). Since I will type the CBe stars in this thesis with the standard MK classification (Morgan, Keenan & Kellman, 1943), I supply here the relevant calibrations found in the literature for $T_{\rm eff}$, intrinsic $(r-i)_0$ colours and absolute M_r magnitudes. The adopted values and the sources from which they are derived are given in Table 1.2.

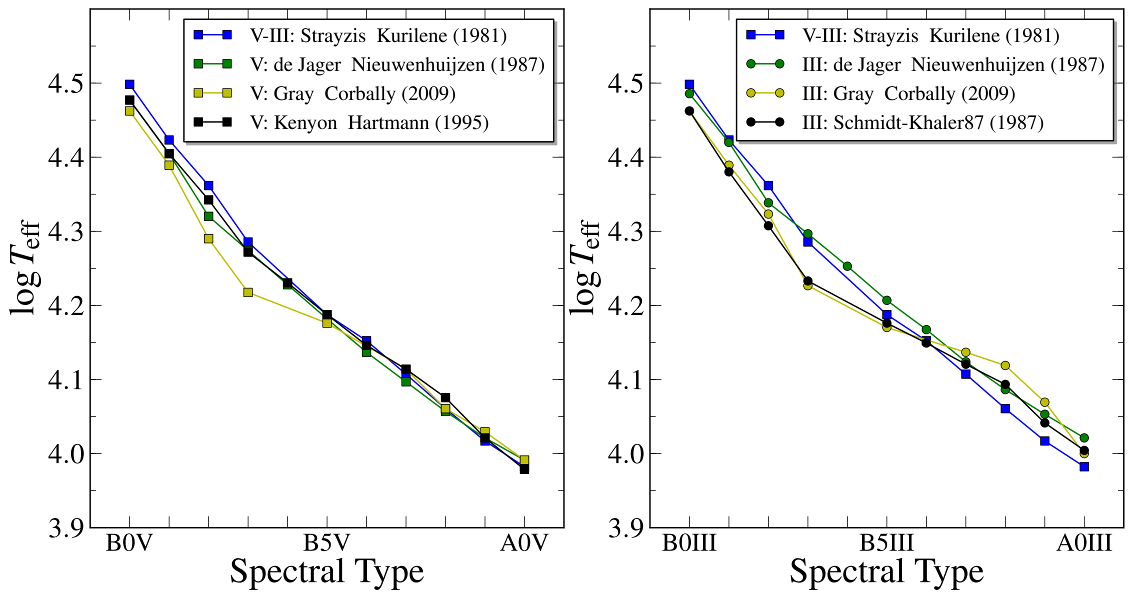

Figure 1.11: The comparison between different temperature calibrations for class V and III stars is shown. The adopted temperature scale for dwarfs is due to Kenyon & Hartmann (1995).

Temperatures. The adopted temperature scale that is used to map spectral types onto model atmospheres is the one from Kenyon & Hartmann (1995). This temperature scale, is not very different from the Straizys & Kuriliene (1981) that is adopted by Munari et al. (2005) for their class V model atmospheres, except that it prefers slightly lower temperatures for early-B. Temperature calibrations for luminosity class III stars present a larger spread. In Fig. 1.11, the available temperature scales are compared.

Intrinsic colours. Intrinsic colours for main sequence stars are plotted in Fig. 1.12. Colours are transformed from Johnson-Cousins values into Sloan colours, using the $(V-R)$ and $(V-I)$, when available. The difference over the broad band filters is minimal, for the present purposes. The adopted curve is in black and is the average of the Kenyon & Hartmann (1995), Siess, Forestini & Dougados (1997), Sale et al. (2009) and Fabregat (priv. comm.) scales. The intrinsic colours of giants and dwarfs differs $\lesssim 20\%$ (see e.g. synthetic colours from Pickles, 1998).

Absolute Magnitudes. The calibration of absolute magnitudes is of a crucial importance when determining distances from spectroscopic parallax. A number of different M_V scales from the literature are plotted in Fig. 1.13. When M_V were supplied, the transformation into M_r was done using the $(V-R_C)$ from Kenyon & Hartmann (1995). The magnitude scale that I adopted in this work is the one given by Zorec & Briot (1991). It is one of the fainter compared to other options. Zorec & Briot (1991) also supply uncertainties with their calibration.

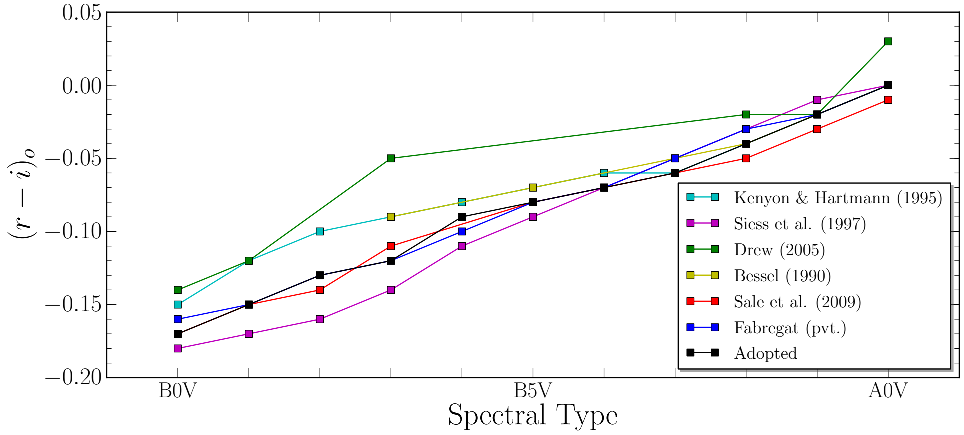

Figure 1.12: Example of the diversity of intrinsic colours $(r-i)_o$ for MS stars. The adopted intrinsic colours are plotted in black.

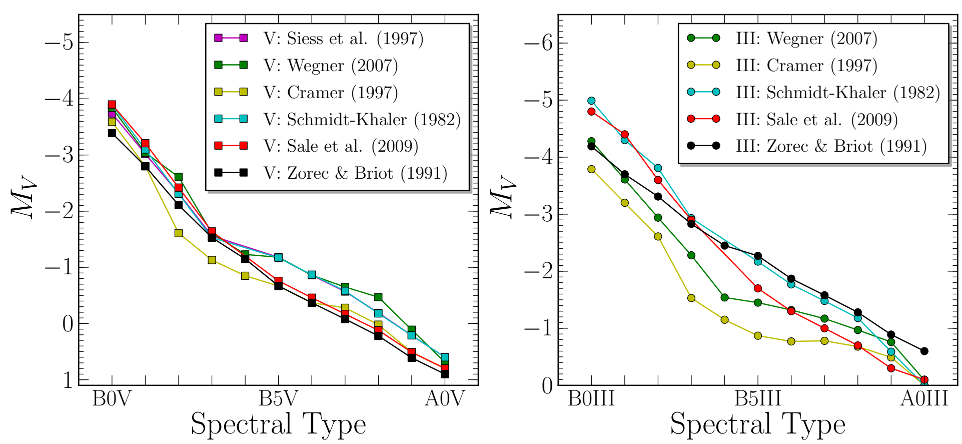

Figure 1.13: The spread of absolute magnitudes available in literature is plotted. The adopted calibration is the one given by Zorec & Briot (1991).

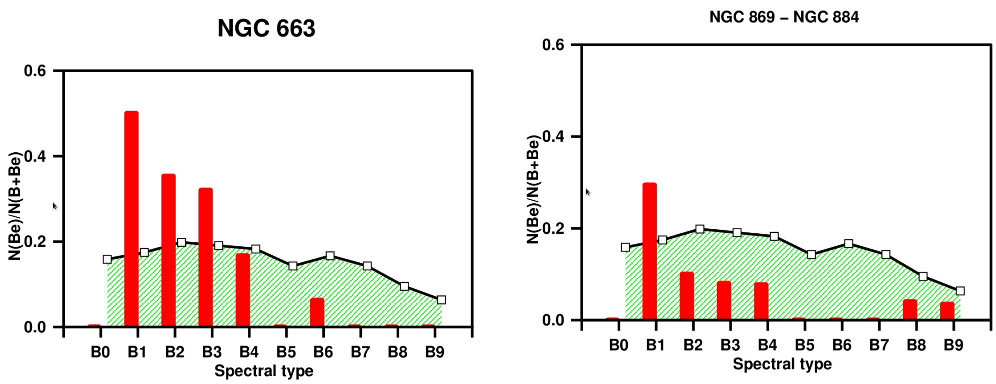

Figure 1.14: Fig. 1 and 2 from Fabregat & Gutierrez-Soto (2005). The spectral type distribution of CBe stars within three open clusters (red histogram bars) is compared to the observed frequencies for field stars (Zorec & Briot, 1997), plotted as a black curve.

1.3.1.2 Where CBe stars are found

The relative number of CBe stars compared to the total number of normal B stars plus CBe stars is around 10% in the Galactic field (see e.g. Zorec & Briot, 1997), while this fraction is larger in open clusters, ranging between 10 – 26% (Mathew, Subramaniam & Bhatt, 2008, and references therein). The observational evidence of large concentrations of CBe within young open clusters (Age $< 10^8$ Myr, Mermilliod, 1982; Slettebak, 1985), suggests CBe stars to be good tracers of the spiral structure of the Milky Way. To establish how far this is true is partly related to the understanding of the causes of the Be phenomenon and its possible link to specific phases of stellar evolution.

In Mermilliod (1982) and Slettebak (1985) the idea that CBe stars represent a restricted evolutionary stage of normal B-type stars was analysed and rejected, based on the observation of CBe stars over a large range of magnitudes, spanning the zero age main sequence (ZAMS) to the TAMS. However, Fabregat & Torrejón (2000) contested Mermilliod's results, noting that the $(U-B)$ colours used in his analysis, would be affected by strong disc emission (Kaiser, 1989). Fabregat & Torrejón (2000), with new observations, identified *bona fide*, CBe stars only in clusters with ages larger than 10 Myr. The peak of the frequency of Be stars was observed in clusters with ages between 13 – 25 Myr, when B1-B2 stars of 9 $M_\odot$ are at the turn-off. The lack of CBe stars in younger clusters, was explained as a result of the evolutionary origin of the Be phenomenon. In addition, the lack of Be stars in clusters with ages $\gtrsim$ 100 Myr is explained as a consequence of absence of B-type stars, since the turn-off age for these clusters corresponds to a spectral type B8 or later.

On the other hand, the spectral type distribution in the field, observed by Zorec & Briot (1997), does not appear as strongly peaked to early spectral types as the distribution found by Fabregat & Gutierrez-Soto (2005) for CBe stars in open clusters (Fig. 1.14). The combination of higher incidence of the Be phenomenon in early-B types and larger presence of CBe stars in clusters younger than $\sim$ 30 Myr (Fabregat & Torrejón, 2000; McSwain & Gies, 2005; Mathew, Subramaniam & Bhatt, 2008) encourages the use of these earlier type CBe stars as structure tracers of the Milky Way disc, either if they are observed in the field or clustered.

The evidence that later type CBe stars may be commonly in the field and may prefer older open clusters (Fabregat & Torrejón, 2000), make them to be less favourable tracers of the spiral structure.

The reason for a relative larger number of later B-types in the field, might be due to e.g. cluster disruption. It is known from simulations, indeed, that the mortality rate of clusters, is expected to be at least 50% for clusters about 50 Myr old (Goodwin & Bastian, 2006). Hence it would be reasonable to expect few clusters with late-type CBe stars. Furthermore an older cluster could not remain within the spiral arms after $\sim$ 100 Myr (Dobbs & Pringle, 2010).

1.3.1.3 More on the evolutionary status of CBe stars

The justification of the Be phenomenon as an evolutionary stage has gained even more ground, with the speculations regarding high rotation speeds. Martayan et al. (2007) found that only stars with high initial equatorial velocities, on the ZAMS, are seen to display the Be character. By comparing the Be populations, both in clusters and field, in the Magellanic Clouds (MC) and the Milky way the authors found that the evolution of rotation speeds, with age, is mass and metallicity dependent. Their main result of relevance here is that the Be phenomenon in the Milky Way appears during the early MS at masses of $\sim 12\ M_{\odot}$, while on the other hand, less massive Be stars ($\sim 5\ M_{\odot}$) appear on the MS at later stages in agreement with the work of Fabregat & Torrejón (2000) - these stellar masses correspond more or less to spectral types B1 and B4 respectively (cf. Frémat et al., 2005; McSwain & Gies, 2005). Mathew, Subramaniam & Bhatt (2008), with observations of CBe stars in open clusters younger than 10 Myr, proposed that some B-type stars can be born already as fast rotators, thereby present with Be phenomenon already on the ZAMS without invoking spin up evolution throughout the MS life. Although, their sample can be contaminated with HAeBe stars.

Finally Fabregat & Gutierrez-Soto (2005) warned that the observed luminosity classes for CBe stars may not link to the evolutionary stage of the star since their determination depends on the inclination angle of the star, as a consequence of gravitational darkening effects on the observed luminosity and colours of fast rotating stars.

1.3.1.4 Known CBe stars

The most complete on-line catalogue of CBe stars is the Be Star Spectra (BeSS) database v1.0[3] (Neiner et al., 2011). The catalogue can be updated by external users and at present consists of 2072 CBe stars over the whole sky. It also contains just 62 HAeBe stars.

Only 64 out of 2072 CBe stars fall within the surveyed part of the Galactic Plane, with 41 of them cross-matching with Kohoutek & Wehmeyer (1999) Hα emitters. For these 64 stars, I plot the histogram distribution of V-magnitudes in Fig. 1.15. Interestingly, 5 of these stars have IPHAS photometry, but only 3 were identified as Hα emitters by Witham

[3] http://basebe.obspm.fr/basebe/

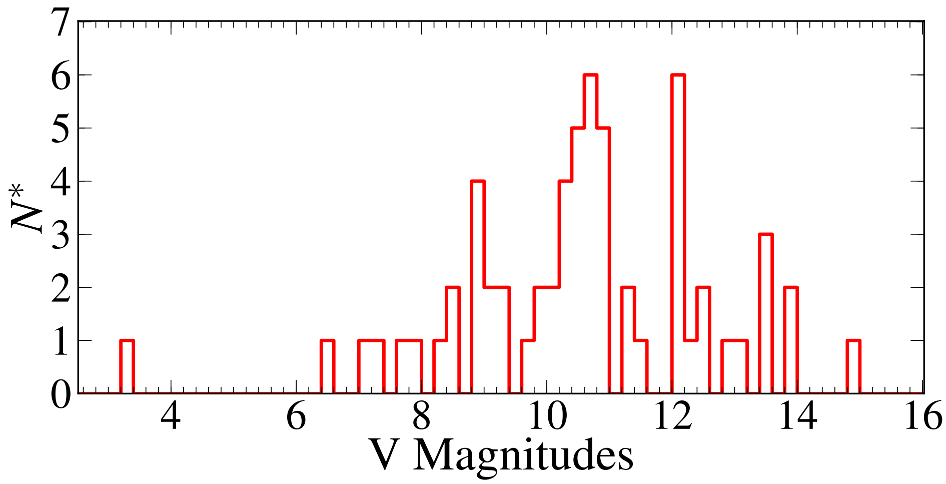

Figure 1.15: Histogram distribution of the visual magnitudes of CBe stars from the BeSS catalogue (Neiner et al., 2011), within the studied strip of the Galactic plane.

et al. (2008), probably due to their lower emission ($EW(\mathrm{H}\alpha) \gtrsim -15$ Å). About half of the 64 CBe stars have spectral types earlier than B3, including a star classified as O6 and two O9 stars. Seventeen stars do not have a spectral type assigned, probably due to their relative faintness (median $V \sim 13$). At least 15 of the 64 stars are seen in proximity of the open cluster NGC 663 at ~ 2.5 kpc (Pandey et al., 2005), which is already known to have a population of CBe stars (Fabregat & Torrejón, 2000), while the majority of them are dispersed across the area.

Among the Kohoutek & Wehmeyer (1999) Hα emitters, I already mentioned 352 stars within this part of the galactic plane, at the beginning of Section 1.3. Among these, 169 are probable CBe stars, because they are classified as early spectral types (O,B,A) and their near IR colours (2MASS) fit the typical colours of CBe stars (Fig. 1.8(b)).

I will come back to the population of known CBe stars seen along sightlines towards the Perseus Arm, in Chapter 9, when I analyse the spatial distribution of the CBe stars I identify in this thesis.

1.3.2 Young stars

YSOs have an obvious association with SFRs and therefore with spiral arms. Their number, among the stars discussed in (Chapter 2), is not very large primarily because they fall beyond the magnitude limit of the considered sample ($r \leq 17$).

Many reviews have provided descriptions of low-mass YSOs or T Tauri stars (e.g. M $< 2\mathrm{M}_\odot$, Bertout, 1989), and intermediate-mass YSOs, or HAeBe ($2\mathrm{M}_\odot \leq \mathrm{M} \leq 10\mathrm{M}_\odot$, Waters & Waelkens, 1998).

CTTSs and HAeBe stars present similar observational properties, which distinguish them from other Hα emitters. These are defined by Waters & Waelkens (1998) for the HAeBe as: i) association with diffuse nebulosity, i.e. proximity to star forming regions (cf. Finkenzeller & Mundt, 1984); ii) IR excess due to circumstellar dust (Hillenbrand et al., 1992); iii) luminosity class from V to III. Weak-line T Tauri stars (WTTSs) are distinguished from CTTSs, even if they lead to the same ZAMS stars, by their smaller $EW(\mathrm{H}\alpha)$ (less than 10 Å), their almost dispersed circumstellar discs and strong X-ray emission (Alcala et al., 1995). Optical spectra of YSOs can show very different features, depending on the amount of circumstellar matter. These range from wavelength-dependent optical veiling, which reduces the depth of absorption lines (Gullbring et al., 1998) in the spectrum, to strong emission in some of the Balmer lines, up to showing all the Balmer series in emission, including the Balmer continuum (see e.g. Fig. 1.16). Optical spectra of CTTSs and HAeBe can show forbidden lines in emission, which are generated in their outflows (Hamann & Persson, 1992; Hartigan, Edwards & Ghandour, 1995). HAeBe stars with forbidden lines may be referred to as HAeB[e] (Lamers et al., 1998). Both WTTSs and CTTSs display spectra with strong Li I (λ 6707 Å) in absorption – a youth indicator (Martin & Claret, 1996). Typical lifetimes of CTTSs are $\sim$5 – 10 Myr (see e.g. Kenyon & Hartmann, 1995; Barentsen et al., 2011), while for HAeBe stars these reduce by up to one order of magnitude (for the most massive ones), as estimated from measures of accretion rates (Hillenbrand et al., 1992)

The standard model used to explain structure of CTTSs and their discs is the accretion of matter through the disc and finally onto the star channelled along magnetic field lines (Camenzind, 1990). In this model, the disc is truncated at the corotation radius, and the gas impacts the photosphere in free-fall, generating shocks in which the plasma emits X-rays and some line emission. Calvet & Gullbring (1998), proposed the re-processed X-rays as the origin of UV and optical veiling, which produces the typical appearance of CTTSs spectra (Fig 1.16). The Hα itself is generated close to the star, where the flux tubes connect the photosphere to the disc. Accretion rates have been estimated in numerous papers to be in the range of $\sim 10^{-6}$ to $10^{-8} M_{\odot}$ yr^{-1} from the observed Hα line flux or other lines, and observational evidence of a strong correlation between line emission and IR colour excess has been established (Kenyon & Hartmann, 1987; Hartigan, Edwards & Ghandour, 1995; Hartmann et al., 1998; Calvet & Gullbring, 1998).

More accurate radiative transfer models, by Kurosawa, Harries & Symington (2006), are able to predict line profiles of several observed features in CTTSs and are proposed to work also for the more massive HAeBe stars. The presence of accretion discs was already proposed for HAeBe stars by Lada & Adams (1992) and by Hillenbrand et al. (1992), from the observation of IR excesses that can be modelled with accretion disc SEDs with $F_{\lambda} \sim \lambda^{-2.3}$. More recently, via a polarimetry study of the Hα lines in a sample of HAeBe, Vink et al. (2002) found that the more massive stars show polarisation consistent with flattened structures, while less massive stars show polarisation consistent with truncated circumstellar discs, like those typical of CTTSs (Vink et al., 2005).

The disappearance of YSO characteristics, such as the IR excess or the strong emission features in optical spectra, is generally interpreted as due to the evolution of these PMS stars onto the ZAMS (Lada & Adams, 1992). Photoevaporation of discs by UV irradiation from massive stars can also play a part (Johnstone, Hollenbach & Bally, 1998). The combination of analysis of optical spectra and IR colours is crucial for distinguishing between

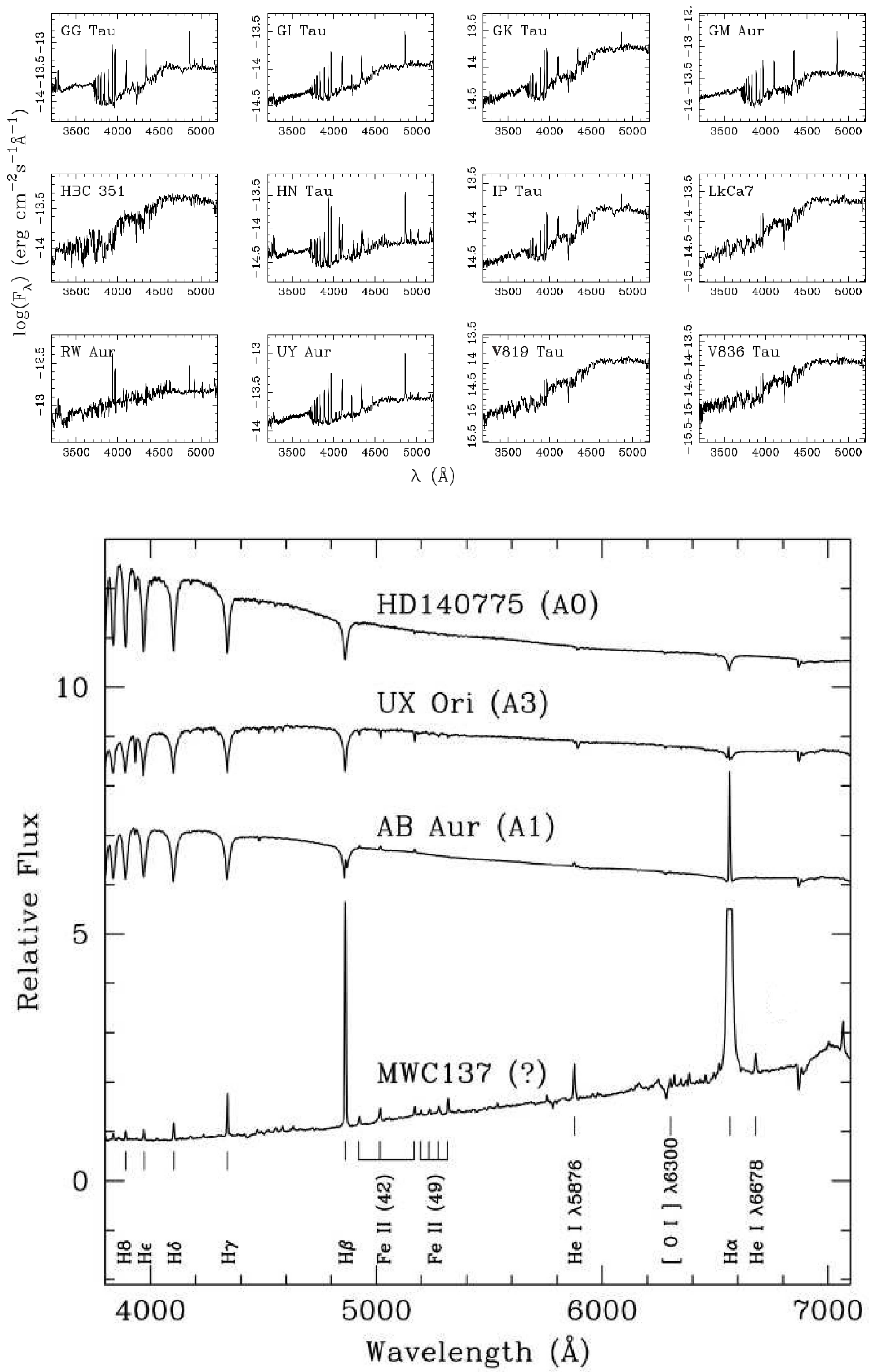

Figure 1.16: Examples of CTTSs from (Gullbring et al., 1998), top panel, and HAeBe stars from (Hernández et al., 2004), bottom panel.

CBe stars and HAeBe stars. However, a neat separation between the two classes becomes difficult when the emission properties of HAeBe stars are less pronounced (cf. Fig. 3 Lada & Adams, 1992).

1.3.3 Evolved stars

The plot in Fig. 1.8, taken from Corradi et al. (2008), shows that a sample of point-sources selected from IPHAS, with $(r-i) \lesssim 1.5$ and $(r-\mathrm{H}\alpha) \lesssim 1.0$, and 2MASS photometry with $(J-H) < 0.6$), would mildly overlap also with CVs, a subset of SySs, and PNe.

These classes of objects are much rarer in the sample considered, due to a combination of causes: i) their space density is not very high, both for CVs ($\rho_0 \sim 10^{-4}$ pc^{-3}, Pretorius et al., 2007) and for PNe ($\rho_0 \sim 10^{-8}$ pc^{-3}, Pottasch, 1996); ii) V-band absolute magnitudes are typically faint ($M_V \sim 10$ for CVs, Pretorius et al., 2007); iii) they are short-lasting ($\sim 10^5$ yr for the PNe phase). Considering the lower frequency of these stars, in the observed sample of Chapter 2, I simply introduce their observed properties that make them mimic those of the CBe stars or YSOs.

CVs and SySs are two different classes of interacting binaries. The first includes classical novae. CV spectra incorporate strong broad emission lines, generated either in nova ejecta or most commonly in optically thin accretion discs encircling the white dwarf (Warner, 2003).

SySs are wide binary systems, with long orbital periods. The central star is generally a hot white dwarf, accreting from the stellar wind of a giant companion (s-type, Corradi et al., 2008). In d-type SySs, the orbiting star is on the asymptotic giant branch (AGB) and the IR colours are reddened, due to the presence of warm dust in the wind of the AGB star.

PNe are the final evolutionary stage of low to intermediate-mass stars before they join the white-dwarf cooling track. The mechanism originating PNe begins during the AGB phase, when the gas of the external loosely-bound layers is detached in response to the increase in luminosity of the star. Here, the radiation pressure of IR photons acts on the dust particles that form within the stellar photosphere and drag it away (Balick & Frank, 2002, and references therein), with typical speeds in the range of ~ 10 – 20 km s^{-1}, as measured from the bright emission lines (Weinberger, 1989). Another formation route is via the creation of a common-envelope phase, in a close binary system (Iben & Livio, 1993). In this phase, the gas flows from the companion onto a white dwarf on a short timescale and engulfs both stars to form the common envelope. The envelope is finally ejected, when the gravitational energy of the spiralling binary system is transferred to the envelope.

In the range of colours that is examined most closely in the follow-up of Hα emitters (Chapters 2 and 3), PNe are even less frequent, due to the fact that their $(r-\mathrm{H}\alpha)$ colours are large. The theoretical maximum for pure Hα emitters, with all the r flux originating from the Hα line, is $(r-\mathrm{H}\alpha) = 3.1$ (Drew et al., 2005). PNe generally are seen close to this limit, while $(r-\mathrm{H}\alpha) \sim 1$ represents a relatively extreme excess for a CBe star (see e.g. Fig. 1.8(a)).

Finally, it is worth mentioning that early spectral-type post-AGB stars could also be detected and mistaken for other types of Be stars. However, their occurrence is extremely rare: in fact, only ~ 50 B/Be stars are found in the catalogue of Galactic post-AGB stars by Szczerba et al. (2007).

Chapter 2

Initial spectroscopic follow-up: lowest-resolution observations

In this chapter, there is a description of the initial lowest-resolution spectroscopic follow-up of candidate Hα emitters. The selection of targets and the observing process are explained in Section 2.2 and 2.3. The data analysis and the objects' properties are discussed in Section 2.4. These observations played a primary role in understanding the different populations of stars that can be picked out by IPHAS. Furthermore, they were used to pave the way to a more in-depth study of the identified Be stars (see e.g. Section 2.5), which will be the core of the discussion in the following chapters.

2.1 Introduction

At the time the initial data release of IPHAS photometry was made available (IDR, González-Solares et al., 2008), Witham et al. (2008) identified $\gtrsim 4500$ candidate Hα emitters, in the northern Galactic Plane, with $13 \leq r \leq 19.5$. The authors selected the objects from the IPHAS ($r-i$, $r-$Hα) plane. The procedure they adopted is shown with an example in Fig. 2.1 (published as Fig. 1 in Witham et al., 2008). The authors applied an iterative σ-clipping technique to identify the main stellar locus in all the available IPHAS fields and picked out the most likely Hα emitters, appearing above the main stellar locus in the colour-colour diagram. This was done before a uniform photometric calibration was available, which meant that the selection could not be made with reference to the unreddened main sequence. An iterative fit to the main stellar locus was used instead as a proxy for the unreddened main sequence.

As was stressed by the authors, spectroscopic follow-up is necessary to confirm whether the sources are emission line stars and then what type they are, since the vast majority of the objects in the catalogue were new to science. They discussed early results of follow-up high success rate in picking out emitters ($\approx 97\%$ of the total observed candidates).

Given the great potential of IPHAS in successfully identifying emission line stars, the core of this project will be the study of the properties and spatial organisation of a

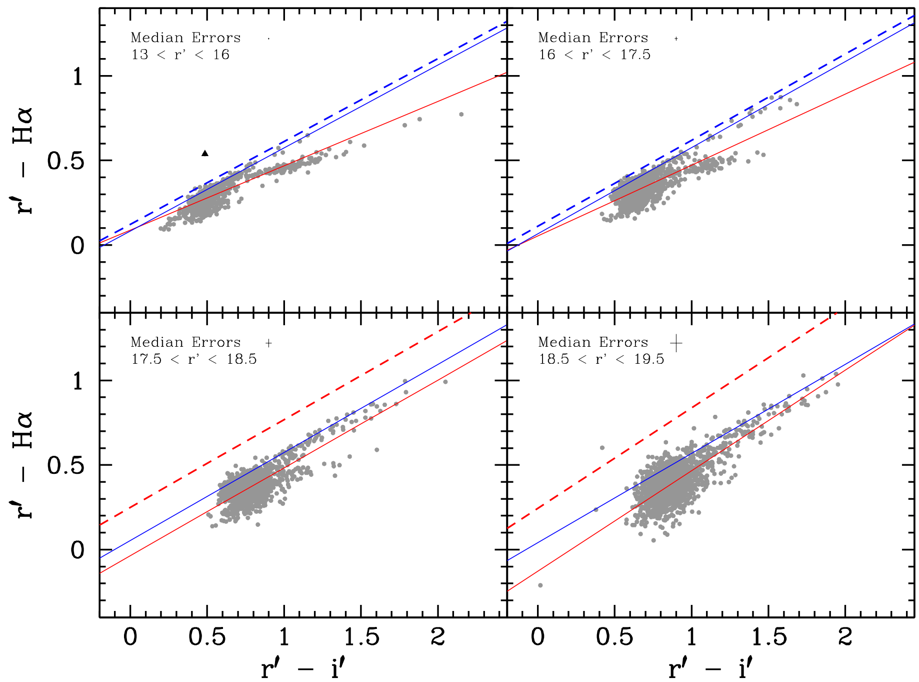

Figure 2.1: The figure, taken from Witham et al. (2008), explains the extraction of Hα emitters from IPHAS photometry. In the four panels, the sources are plotted by applying four different magnitude cuts. Magnitude cuts and typical error are reported on the top left corner of each panel. The red solid line is the initial fit, while the blue one line is the final fit after the σ-clipping iteration. Dashed lines are the delimiting lines above which a star is picked as an emission line candidate. The colour depends on whether the selection was based on the initial or the final fit.

large number of them (≈ 400 stars). The chosen targets are located in a section of the Galactic Plane, in the Perseus Arm direction and enclosed between $120^\circ \leq \ell \leq 140^\circ$ and $-1^\circ \leq b \leq +4^\circ$. The reason for interest in this part of the Galactic Plane, which appears through the literature, were described in the first chapter. However, it is worth stressing again the reason behind the choice of surveying an area that is biased towards positive latitudes: it was indeed shown by Witham et al. (2008) that the denser groups of emitters closely follow the warp of the Galactic disc that is above the 0° latitude in this area. This result goes along with what was an already known evidence, showed by maps of H I and dust (Freudenreich et al., 1994), from the distribution of star forming complexes (Russeil, 2003), and with use of red giant branch stars (Momany et al., 2006).

In Fig. 2.2, the chosen region is shown relative to the location of all the Witham et al. (2008) emission line star candidates, stretching along the northern Galactic Plane. Even at this scale, it is possible to recognise a few denser groups of emitters, which are seen towards more active SFRs, but in the main they are widely dispersed across the 100 deg^2 strip.

The follow-up observations were organised in a two-stage programme. The first stage

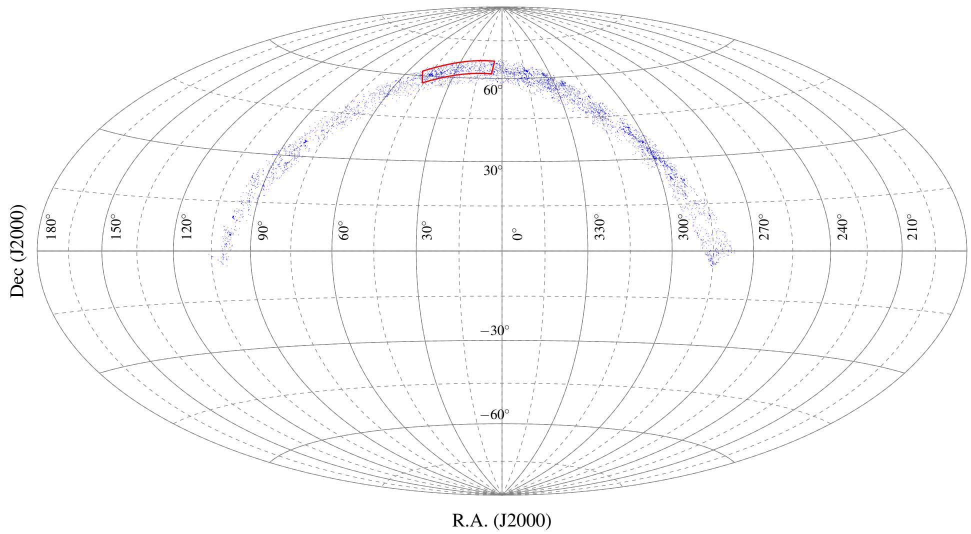

Figure 2.2: All-sky distribution of the $\gtrsim 4500$ Witham et al. (2008) candidate emission line stars (blue points). They stretch along the whole northern Galactic Plane as it is seen from La Palma. The red solid box defines the range of coordinates within the chosen part of the Plane towards the Perseus Arm.

of observations was intended to cover the majority of the candidate emitters with $r \leq 17$, at lower resolution but in a relatively short time. The main goals were the following:

- Confirmation of the emission line nature of the observed target
- By-eye sorting into *broad* groups of objects sharing similar characteristics
- Selection of targets for further observations (e.g. higher resolution and S/N optical spectroscopy)

The present chapter deals with the analysis of this initial spectroscopic follow-up programme. The second phase of follow-up that focused on a group of confirmed CBe stars and YSOs will be described in later chapters.

2.2 Sample selection

The observing strategy was planned on the basis of what is known from the IPHAS photometry. The choice of telescope/instrument for the present follow-up observations has been indeed guided by the magnitude/colour properties of the sample along with the possibility to carry out a large programme of observations. In order to present the observations, it is appropriate to step back to describe the sample selection.

The main source of targets is the Witham et al. (2008) catalogue, whose 560 candidate emission line stars fall within the section of the Galactic Plane that has been chosen. These 560 targets in the area, which are plotted in Fig. 2.3 onto a dust extinction map from

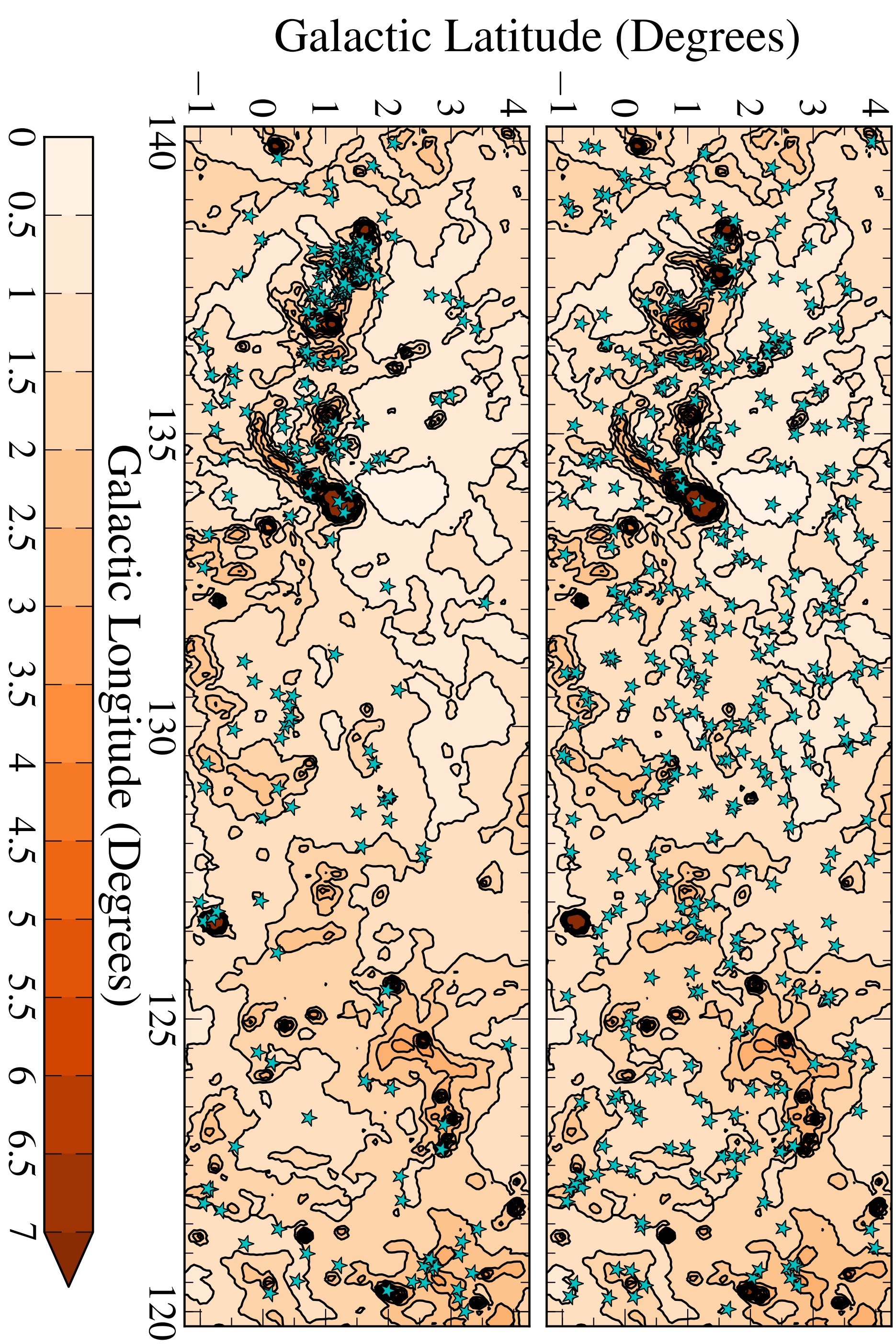

Figure 2.3: The spatial distribution of Witham et al. (2008) candidate emission line stars is shown: in the top panel are the bright sources ($r \leq 17$), while in the bottom one are the fainter ones ($17 < r \leq 19$).

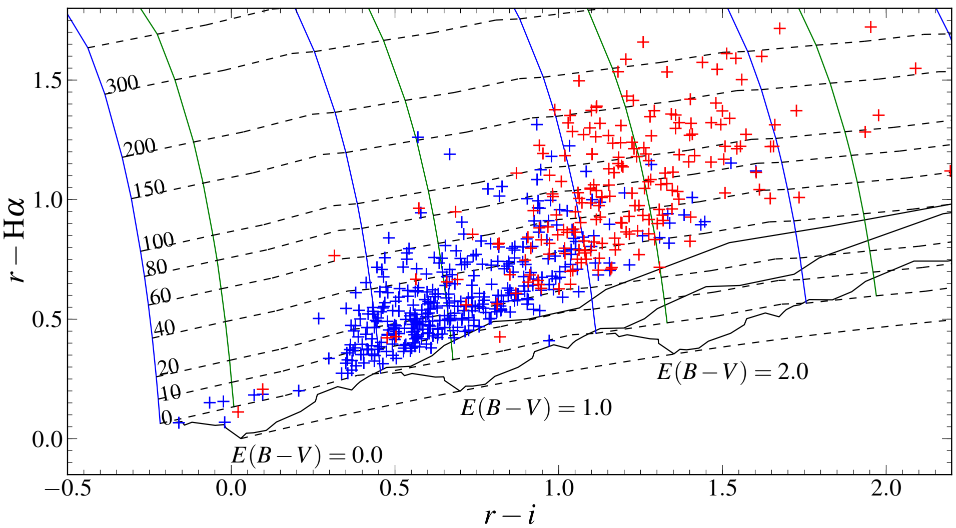

Figure 2.4: IPHAS colour-colour diagram of the Witham et al. (2008) candidate emission line stars. In blue are the bright $(r \leq 17)$ sources and in red the fainter ones $(r > 17)$. Black solid lines are synthetic main sequence loci, at $E(B-V) = 0.0$, 1.0, 2.0 (see e.g. Table 2 in Drew et al., 2005). Dashed curves represent the iso-$EW(\mathrm{H}\alpha)$ curves for a $F_\lambda = \lambda^{-4}$ SED (blue vertical curve; Rayleigh-Jeans) and $F_\lambda = \lambda^{-3} \sim$ A0 SED (green vertical curve) (data tabulated in Table 4 of Drew et al., 2005). The predicted $EW(\mathrm{H}\alpha)$ emission are reported in figure. The early-A reddening line is also plotted as the lowest dashed curve connecting the reddened main sequences.

SFD98. The targets show an evident shift in the character of their spatial distribution, when they are split in two magnitude groups. In the top panel are the objects with $(r \leq 17)$, while in the bottom one are the point sources with $(17 < r \leq 19.5)$. The bright Hα candidate emitters are more dispersed across the area, while the fainter ones clearly favour locations within active sites of star formation. The bright group is likely to be dominated mainly by Be stars that are either in clusters, star associations or in the field (Corradi et al., 2008, suggested that at least 30-50% of the entries in the Witham et al., 2008, catalogue are CBe stars), while the faint selection is more likely to be dominated by YSOs, given the close association to SFRs. In addition to this, there is evidence that the bright group of stars experiences on average smaller amounts of interstellar extinction $(E(B-V) \approx 0.5 - 1.5)$, while the fainter ones are in average more reddened $(E(B-V) \geq 1.5)$. This suggestion is given by Fig.2.4, which is the IPHAS colour-colour diagram of the Witham et al. (2008) candidate emitters in the area. In the same figure, there is indeed a very clear separation between the bright group of stars $(r \leq 17)$ and the fainter ones $(r > 17)$.

In order to reach a compromise between number and quality of data, it was decided to observe targets with a limiting magnitude of $r \approx 17$. The range of r magnitudes that is covered by the observed targets $(12 \lesssim r \lesssim 17)$ is shown in Fig. 2.5, along with the distribution of all Witham et al. (2008) candidates in the area. The two distributions do not exactly match, because about 50 targets more were added to the observing queue, that were derived from IPHAS photometry not available at the time the Witham et al.

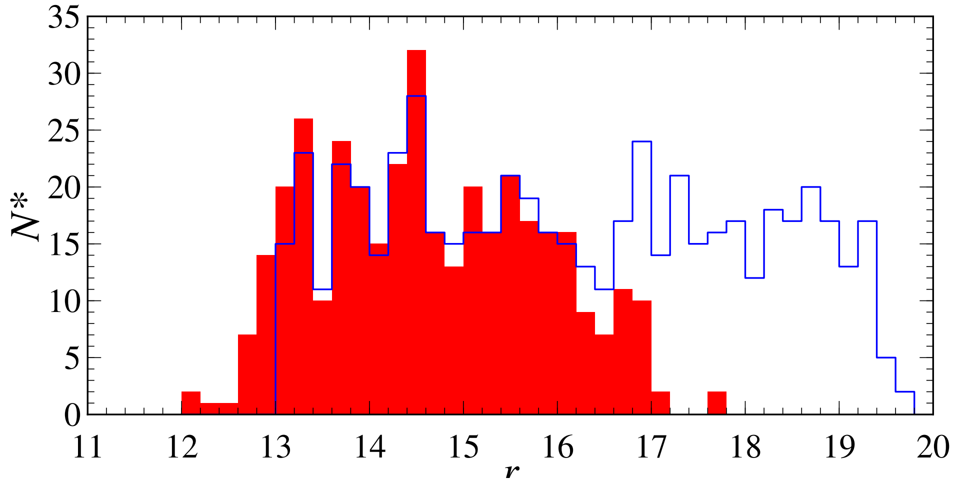

Figure 2.5: The r magnitude distribution of our low-resolution sample is shown (red histograms). The distribution of Witham et al. (2008) candidate emission line stars, in the area, is superimposed in blue.

(2008) catalogue was compiled. At magnitudes fainter than $r = 16$, the distribution of observed targets starts to turn down with respect to Witham et al. (2008) catalogue, due to the increasingly long exposure times that are required for the fainter and more reddened objects.

In Table 2.1, the measured IPHAS photometry is listed, for all the 370 objects observed. Since the IDR, more has been done towards a global calibration of IPHAS photometry and morphological classification of sources can have changed. The photometry that is supplied in Table 2.1 has been corrected using an internal release of the forthcoming global calibration (Farnhill et al. in prep.) and includes only the stellar and probably stellar sources.

In Fig. 2.6, there is a standard IPHAS colour-colour diagram of the 370 observed point sources. All but one of the targets (black crosses) are seen above the synthetic main sequences computed for three different reddenings ($E(B-V) = 0, , 1, 2$). In figure, there are also the lines of constant Hα emission equivalent width, which will be used in Section 2.4.2 to estimate photometric Hα equivalent widths (EW(Hα_{P})).

It would be also desirable to estimate how complete the sample is, down to a given r magnitude and EW(Hα). Considering that the average asymptotic reddening, from SFD98, is $E(B-V) \sim 1.45$ mag in this section of the Galactic plane, the sample is very much complete to $r \approx 17$, as compared to Witham et al. (2008). Very few objects are indeed seen redder than $(r-i) = 1.35$ that corresponds to $E(B-V) = 2$ for an early-A star.

In the chosen area, there are still a few fields that will need to be re-observed, since they are not yet meeting either the required seeing, ellipticity of the sources or magnitude limit. However, the range of magnitudes that is covered in this project lie well above the average magnitude limit ($r \approx 20(10\sigma)$, from Drew et al., 2005), such that all the targets

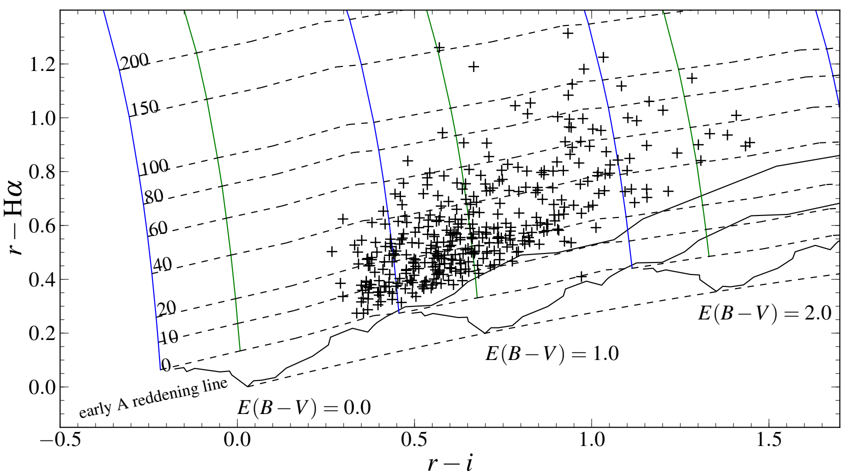

Figure 2.6: The same as in Fig.2.4, but crosses here represent all the targets observed with FLWO/FAST.

have secure photometry, with errors set by the calibration rather than measurement.

Another different matter is to define completeness in terms of $EW(\mathrm{H}\alpha)$. Given the way the minimum detectable $EW(\mathrm{H}\alpha)$ varies with the intrinsic colour $(r-i)$, Witham et al. (2008) did not attempt to confirm the completeness of their selection. To do this rigorously, would require a comprehensive spectroscopy survey of selected sky areas. On the other hand, Barentsen et al. (2011) used a more strict criterion to identify YSOs in IC 1396 and, comparing their selection with data available in literature, assessed their search to be complete down to $EW(\mathrm{H}\alpha) \approx -30$ Å, which is a safe limit for intrinsically red young emitters. It will become evident in Section 2.4.2 that to the chosen magnitude limit, average to strong emitters ($EW(\mathrm{H}\alpha) \lesssim -15$ Å) are identified at the moderate reddenings ($E(B-V) \lesssim 1.5$) encountered, that sets our completeness limits.

2.3 Observations and data reduction

Observations were collected between 2005 and 2011 at the 1.5m Tillinghast telescope of the Fred Lawrence Whipple Observatory with the FAst Spectrograph for the Tillinghast Telescope (FAST, Fabricant et al., 1998) . Three hundred and seventy stars were observed at least once – there are 459 spectra altogether. The grating used is the 300 lines/mm that gives 6 Å resolution and covers the optical range (3500 – 7400 Å). Exposures times ranged from 120s up to 1800s. Given the high flexibility with which the telescope is operated, targets were easily returned to the observing queue when either a better spectrum or a further observation was needed. All the spectra with less than 1000 counts/Å, in the Hα region, were generally queued again for re-observation. The observations' log is coarsely summarised in Fig. 2.7 These data were all obtained in service mode. All the spectra were reduced to one dimension, wavelength calibrated and sky-subtracted via an automated pipeline. Spectrophotometric standards were, in general, observed once

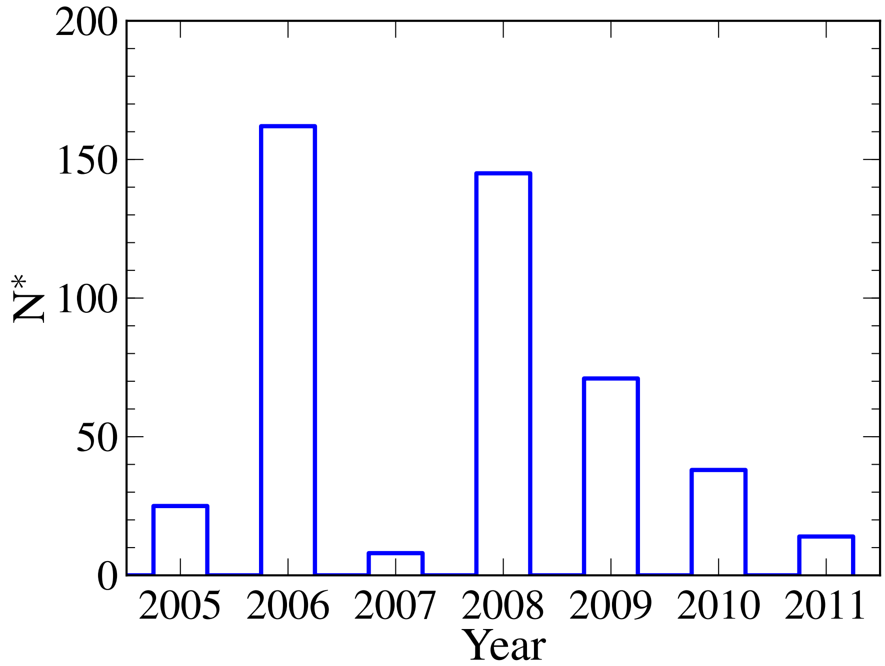

Figure 2.7: A graphic representation of the observing programme. N^{*} is the number of spectra observed per year. The follow-up programme started in 2005 and lasted for 6 years.

or twice per night. An average flux calibration was applied, by using some of the best-behaved standards from across the whole period of observations (by D. Steeghs). This was a pragmatic choice consistent with the first aim that this initial follow-up should confirm the emitter-like nature of the observed objects and the study of the global properties of the sample. From now on, the abbreviation FLWO/FAST will be used in the rest of the thesis, when talking about these first stage lower-resolution spectra.

2.4 Sample properties

In this section, the general properties of the observed sample will be examined. Objects are grouped on the basis of their observed spectrum Combining the spectroscopic information along with the IR photometry and their sky location – which means the association of a star with known galactic structures – it is possible to infer the nature of the target, be it a young star or a more evolved object. The analysis of the sample properties prepared the way for the selection of a number of stars for the next phase of spectroscopic follow-up that is described in the next chapters.

2.4.1 Initial spectral grouping

Visual inspection was carried out for all the 459 FLWO/FAST, looking for distinguishing spectral features, as the first step toward selecting targets for follow-up further. It appears evident that six broad groups are possible:

1. **Early-type spectra (329):** 254 stars displaying well developed higher Balmer lines and no metal lines in absorption, typical of B and A stars. In the first ones, it is possible to recognise also He I lines. This class also shows deep diffuse interstellar bands (DIB) whose intensities are known to be rough proxies for the interstellar reddening. This also means that most of these stars are at large distances. Three examples are plotted in Fig 2.9.

2. **F-type spectra (3):** in this group there are 3 stars I classified as F-type after inspecting their intermediate-resolution spectra (Section 3). These stars show stronger Ca II K-line and the first appearance of the G-Band, typical of F stars, although with lower resolution and S/N they were easily confused with late-A or early-G spectra. More discussion follows in the next chapter.

3. **Late-type spectra (14):** 12 stars showing strong late-type spectral features, such as Ca H & K lines, the G-band and TiO bands. They nevertheless present strong Hα emission, indicating that they are likely T-Tauri stars. Three examples are plotted in Fig 2.10.

4. **Late-type spectra without emission (11):** 11 late-type stars with no Hα emission. Are generally foreground objects, whose colours can be mistaken with emission line stars colours.

5. **Featureless spectra (93):** 81 stars with either an emission dominated spectrum (i.e. all the Balmer lines in emission, including the Balmer continuum) or an extremely high-contrast Hα emission, followed by Hβ and in a few cases weaker higher excitation transitions, but no readily-apparent stellar photospheric absorption lines. Three examples are plotted in Fig 2.11.

6. **Other spectra (3):** this diverse group includes an object with a spectrum typical of a cataclysmic variable, a probable Ap star and another spectrum showing a many likely nebular emission lines. Their spectra are plotted in Fig. 2.12.

7. The remaining 6 spectra are unclassified, since they either have a very poor sky subtraction or simply were mistaken pointings.

A more quantitative spectral-typing will be given in Section 2.5.1.1 for the early-type spectra from the first group. In Fig. 2.8, the IPHAS colour-colour diagram is shown as in Fig. 2.6, but using different symbols for the six groups described above: *early-type* (blue crosses), *F-type* (black crosses), *late-type* (red crosses), *late-type (without emission)* (red squares), *featureless* (cyan circles) and *others* (black triangles). It is worth noticing, the general grouping of the early-type stars and the featureless spectra that is seen on the colour-colour diagram, as compared to the more sparse distribution of the other less frequent objects. This is mostly a selection effect, due to the magnitude limited sample.

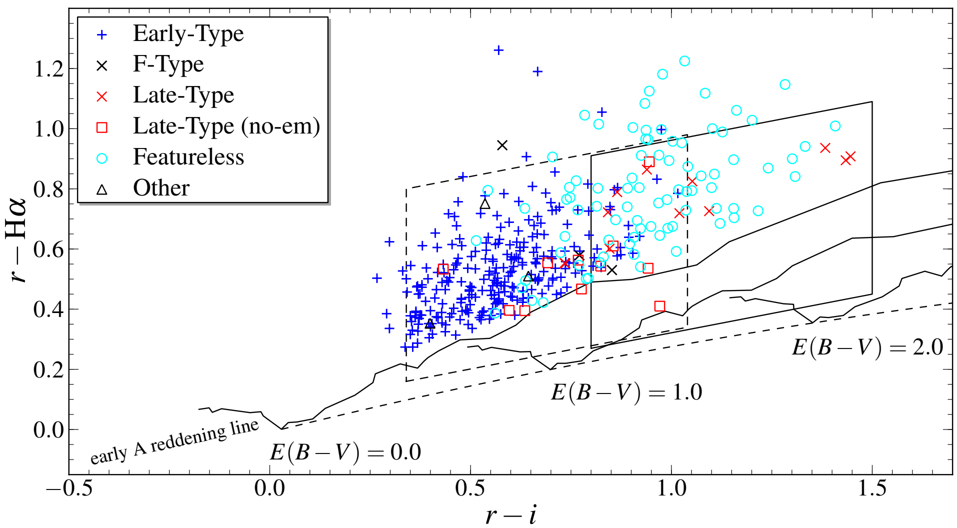

Figure 2.8: IPHAS colour-colour diagram as in Fig. 2.6. The symbols in legend, representing the classification scheme, are explained in the text. The two boxes define the region in which CBe stars with $A_V \sim 4, 6$ can be found (cf Fig. 3 and the discussion in Corradi et al., 2008)

The redder objects are in general the ones whose blue continuum is too noisy to allow a typing with the FLWO/FAST data, while the well exposed ones are mainly B-type bright stars with $A_V \sim 4$ (dashed box in figure, see also Corradi et al., 2008).

The grouping into classes of objects indicates that the view of Corradi et al. (2008), that about an half of the Witham et al. (2008) sample might be made of CBe stars, is an underestimate. Within the observed range of magnitudes ($12 \lesssim r \lesssim 17$), $\sim 70\%$ of the stars have B-type spectrum and some of them may have fallen in the featureless group, for reddening and S/N reasons. The distribution of the stars with *featureless* spectra on the colour-colour plane, indeed, highlights really well the limitation that the combination of larger reddening and faint r magnitudes produce. It is known that, for instance, a typical A0 star, with an observed $(r-i) \sim 0.7$, would experience an interstellar reddening of $E(B-V) \sim 1$ that translates in a $E(B-r) \sim 1.7$, adopting the mean $R_V = 3.1$ extinction law by Fitzpatrick (1999). It is beyond the capability of FAST to deliver ~ 1000 counts in the blue part of the spectrum for $B \gtrsim 16$.

In Fig. 2.8, it is also noticeable that not all the non-emission late-type stars are very close to the main sequence, as it is expected. Two of them (F257, F271) have colours that are typical of strong emitters, but they have filled-in Hα, that may explain the discovery photometry. F257 is an early M-type star seen superposed on W3, but no Li I (λ6707 Å) is visible: it is clearly a less reddened foreground object.

2.4.2 Hα equivalent widths

One of the goals of the follow-up is to confirm the emission line nature of the surveyed objects and/or highlight eventual variability. It is very likely, indeed, that the observed

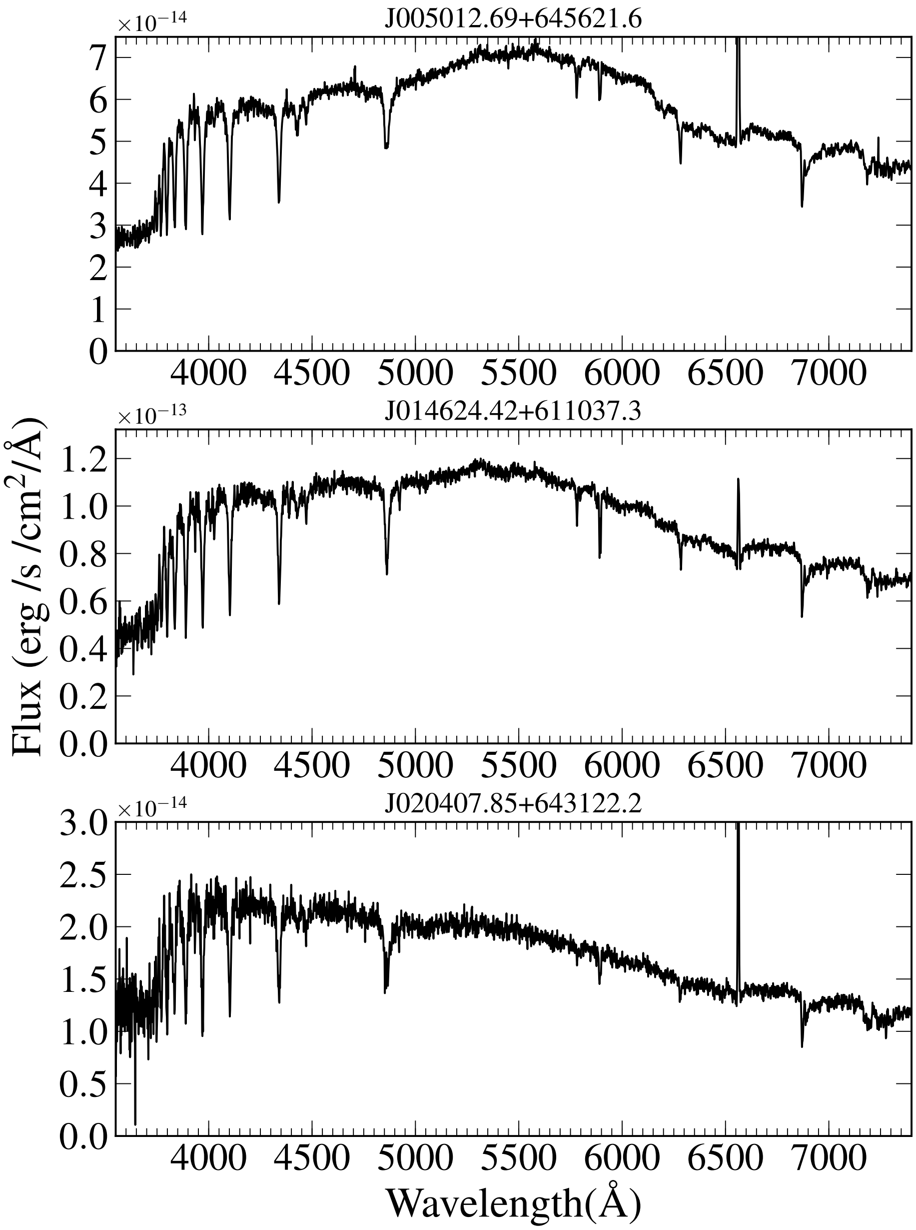

Figure 2.9: Spectra of three typical Be stars observed with FLWO/FAST, from top to bottom: F031, F118, F173.

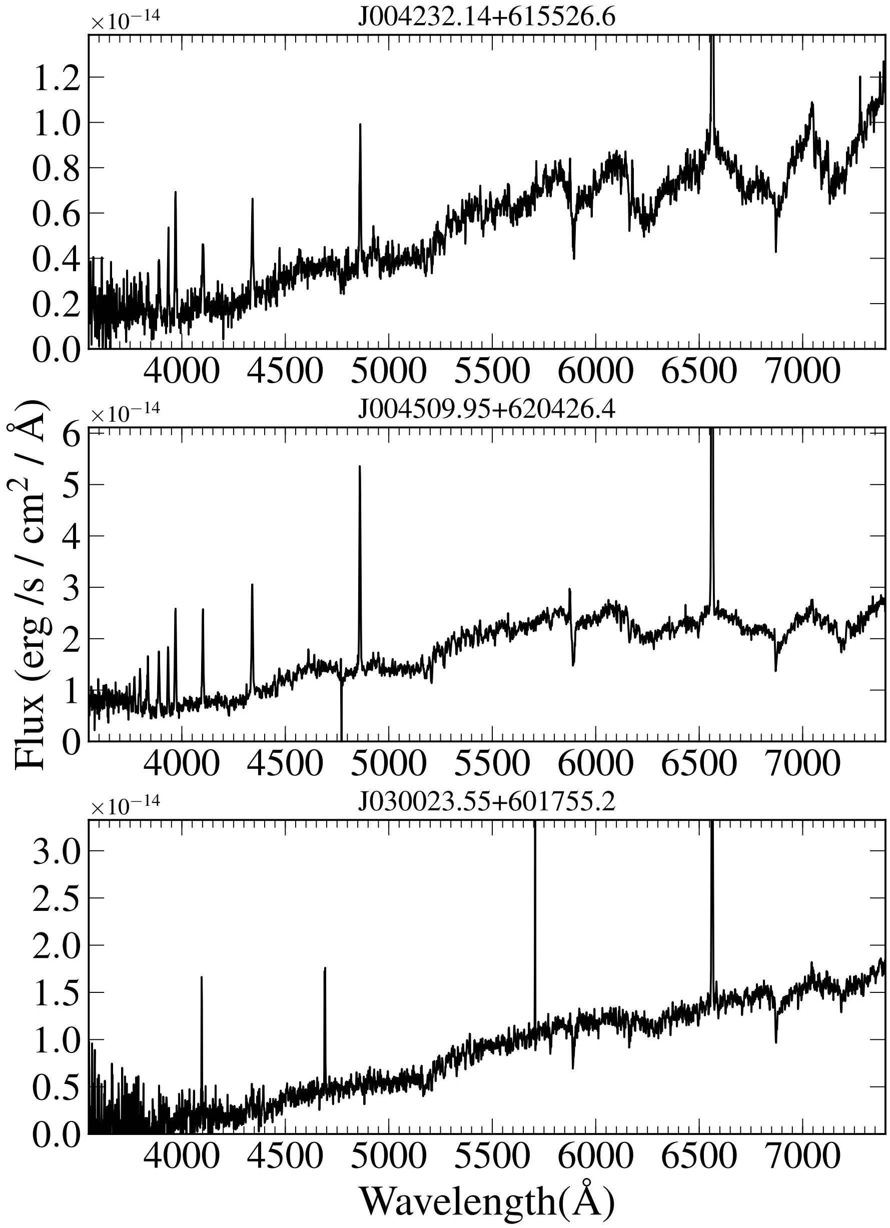

Figure 2.10: Spectra of three late-type stars observed with FLWO/FAST. The first two have all the Balmer lines and the Balmer continuum in emission. From top to bottom: F019, F021, F341

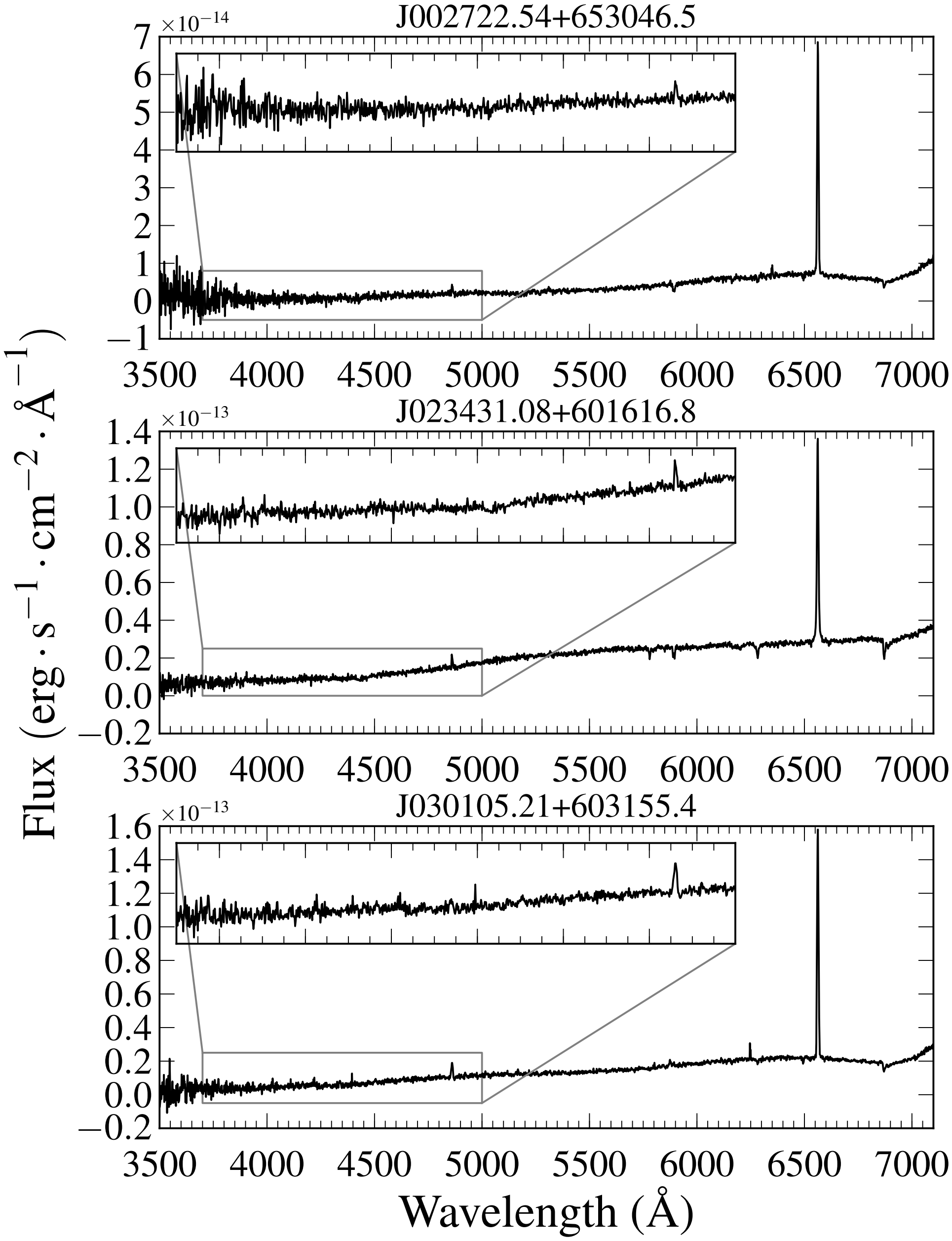

Figure 2.11: Three examples of stars with *featureless* spectra, which are characterised by a very high-contrast Hα line and a blue continuum free of noticeable absorption features. The stars are, from top to bottom, F002, F255, and F344.

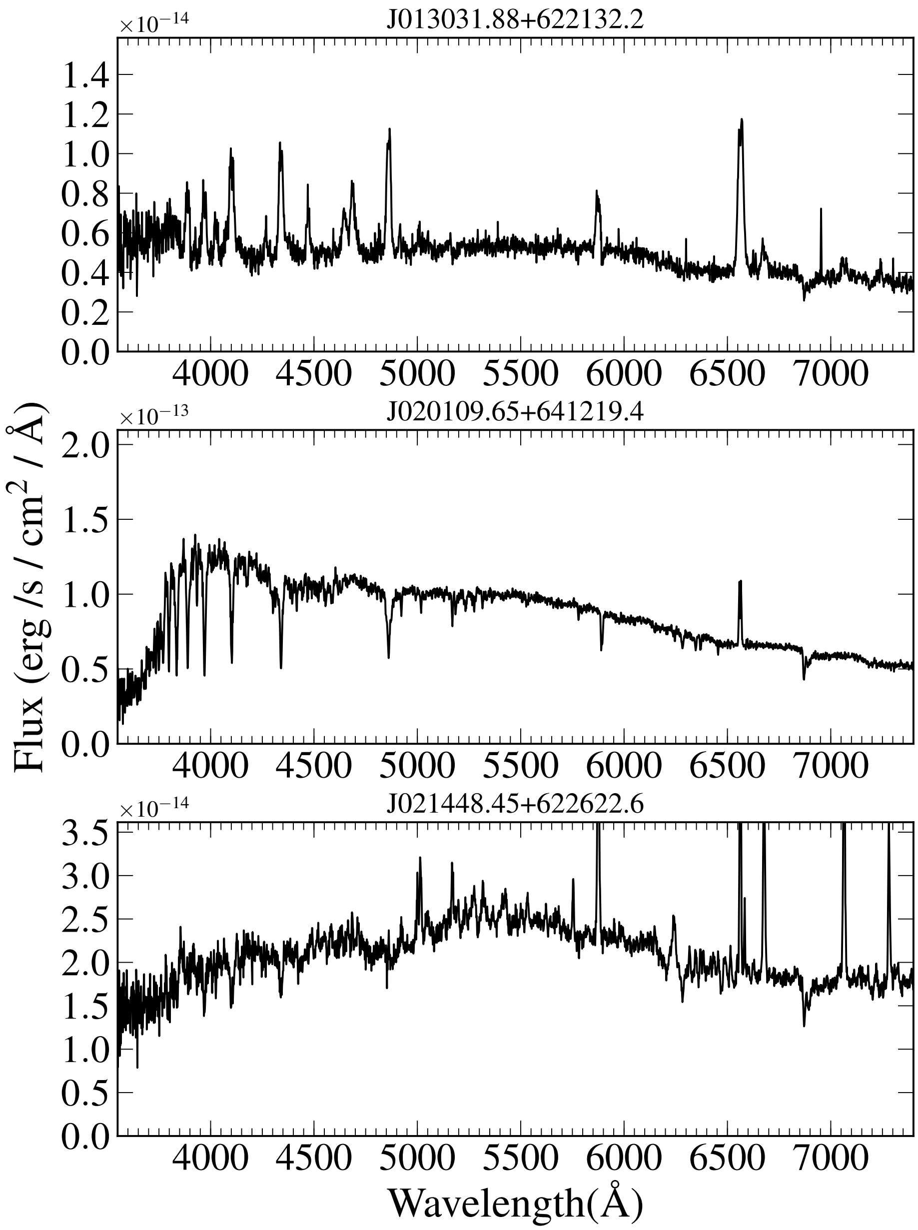

Figure 2.12: Three peculiar FLWO/FAST spectra. Top: a cataclysmic variable (F090). Middle: a probable Ap star (F164), with numerous metallic lines, and a double peaked Hα. Lower: a spectrum with numerous forbidden lines in emission (F207).

objects have variable line emission, since this phenomenon is observed in many classes of stars. For this purpose, the Hα equivalent width that can be estimated from IPHAS photometry is compared with the ones measured from the spectra.

The photometric estimate, $EW(\mathrm{H}\alpha)_\mathrm{P}$, is determined by comparing the observed $(r-i)$ and $(r-\mathrm{H}\alpha)$ colours of the star with the iso-$EW(\mathrm{H}\alpha)$ curves of Fig. 2.6 (see e.g. Table 4 in Drew et al., 2005). These curves are the product of the simulation of curves of growth of $EW(\mathrm{H}\alpha)$ computed for a $F_\lambda \propto \lambda^{-4}$ and $F_\lambda \propto \lambda^{-3}$ – i.e. a Rayleigh-Jeans SED and an A0 SED (Drew et al., 2005). The $EW(\mathrm{H}\alpha)_\mathrm{P}$ are estimated via linear interpolation with the theoretical curves, using the Radial Basis Functions module within the *scipy* package for Python. The values, for each object, are in Table 2.1.

Spectroscopic measures of equivalent widths, $EW(\mathrm{H}\alpha)_\mathrm{S}$, are obtained after normalising the continuum in a sufficiently wide range of wavelengths, centred on the Hα rest wavelength. Errors are estimated allowing the background a $\pm\sigma$ variation. The measure is more uncertain for noisy spectra and later type ones, where the presence of molecular bands significantly affects the continuum normalisation. These, along with $EW(\mathrm{H}\beta)$, are in Table 2.2. When more than one spectrum, for a given star, was available all the measures are listed in the table. Those stars, having more than one $EW(\mathrm{H}\alpha)_\mathrm{S}$ measure, generally agree within the errors, excluding large variations on a short-medium timescale (at most a couple of years; see also Fig. 2.14). A further comparison of the time-dependant Hα variation will be discussed in Chapter 3, including the $EW(\mathrm{H}\alpha)$ measured from intermediate-resolution spectra. In Fig. 2.13, finally, the photometric and spectroscopic measures are compared. Stars are plotted with symbols indicating their group, according to the classification given in the previous section. There is evidence of a small systematic shift of the data-points towards negative values of the difference $\Delta[EW(\mathrm{H}\alpha)] = EW(\mathrm{H}\alpha)_\mathrm{P} - EW(\mathrm{H}\alpha)_\mathrm{S}$. The median of the distribution of the differences, relative to the spectroscopic measure $|\Delta[EW(\mathrm{H}\alpha)]|/EW(\mathrm{H}\alpha)_\mathrm{S}$ is about -0.24. The observed trend may represent a mild bias such that a follow-up observation is more likely to observe a variable star in a lower-activity phase than when first picked out via IPHAS photometry (Barentsen et al., 2011). However, it cannot be excluded a small systematic effect due to the nature of the photometric measurement.

The confirmation success rate of IPHAS, within this sample, is $\sim 93\%$, just considering all the stars with EW(Hα) < 0. This number would be slightly larger if we take into account all the ones with infilled Hα line. Fig.2.15 the distribution of measured $EW(\mathrm{H}\alpha)_\mathrm{S}$ is shown. Its median value is at $EW(\mathrm{H}\alpha)_\mathrm{S} \approx -19$ Å.

2.4.3 Near-IR colour excess

Supplementary information on the observed stars, to add more support to the grouping into classes of Section 2.4.1 and to help out with the study of individual class of objects, can come from the inclusion of IR photometry. Given that these stars are relatively bright, it was possible to collect 2MASS photometry (Skrutskie et al., 2006) for all but 9 of the targets. The accepted photometric quality flags were 'A', 'B', 'C' in all the three bands (JHK_s), or in other words sources with S/N ≥ 5 and photometric uncertainty ≤ 0.21 in all

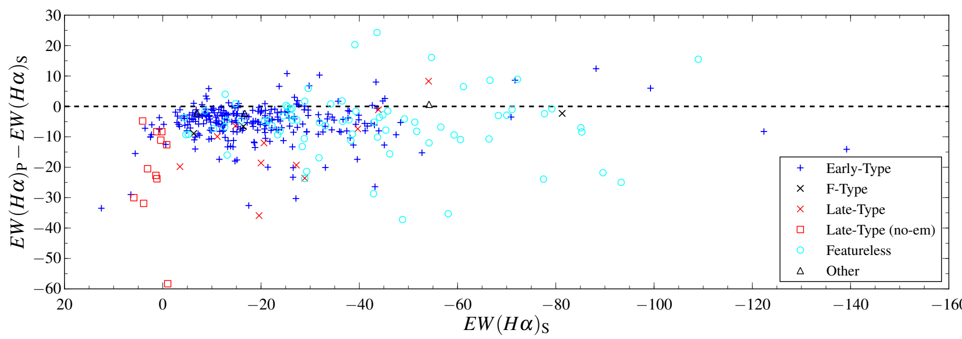

Figure 2.13: The comparison between spectroscopic and photometric measures of $EW(\mathrm{H}\alpha)$ is plotted. Same symbols as in Fig. 2.8 are used. The equality line is drawn as a black dashed line.

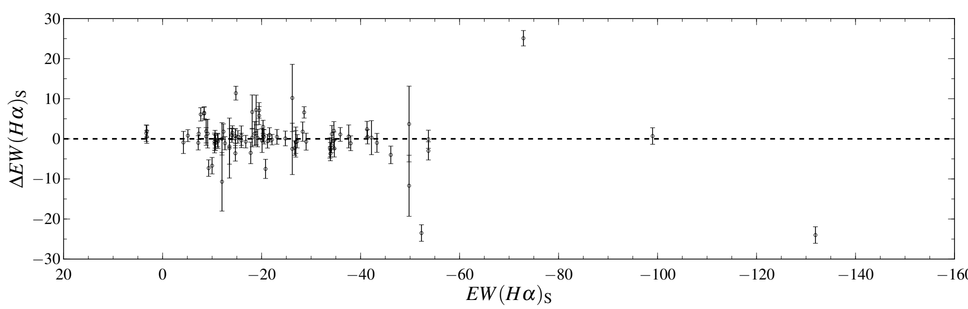

Figure 2.14: The comparison between spectroscopic measures of $EW(\mathrm{H}\alpha)$ at different epochs is plotted for the stars having more than one $EW(\mathrm{H}\alpha)_S$ measure.

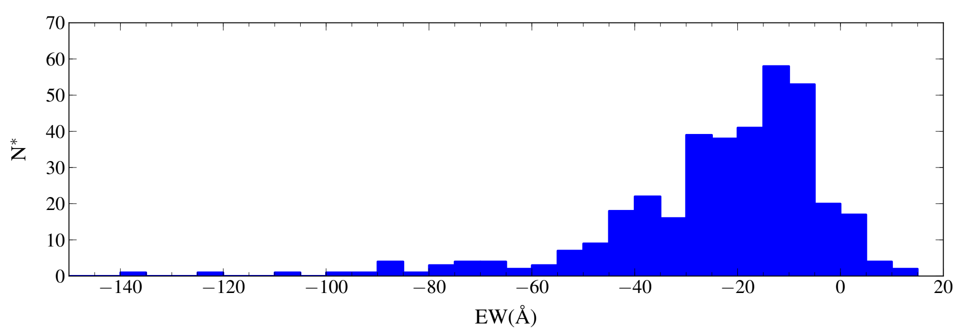

Figure 2.15: The distribution of measured EW(Hα)$_S$, which centres at ~ -19 Å.

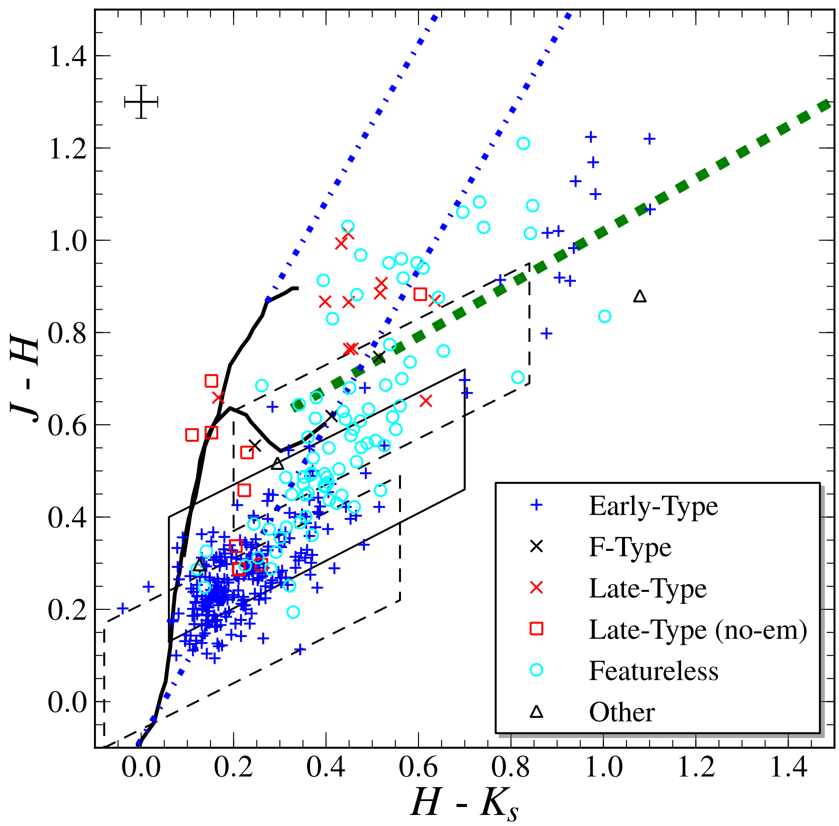

Figure 2.16: Near-IR colour-colour diagram of the observed FLWO/FAST sample, having reliable 2MASS photometry. The dwarf and giant unreddened colours (Bessell & Brett, 1988) are plotted as black solid curves. The blue dashed lines are the reddening vectors from Rieke & Lebofsky (1985). The green dashed line is the unreddened CTTSs locus (Meyer, Calvet & Hillenbrand, 1997). The solid and dashed boxes, starting from the bottom one, delineate the regions where are seen CBe with $A_V \sim 2, 4, 6$ (Corradi et al., 2008). All the plotted curves are converted to the 2MASS system, adopting relationships defined in Carpenter (2001). The typical error bars are plotted in the upper left corner of the figure.

the three bands. In Fig. 2.16, are plotted the 2MASS $(J-H)$ and $(K-S)$ colours. It is noticeable that the majority of early-type stars (blue crosses) are displaced moving parallel to the reddening vectors, They are seen inside the boxes, which enclose the portion of the plane where CBe stars with $A_V = 2, 4$ are typically seen (Corradi et al., 2008). Among these there are the candidate CBe stars that have been chosen for further follow-up and are described in the following chapters.

Furthermore, a similar pattern is seen in the *featureless* group (cyan circles), but displaced to yet larger reddenings ($A_V \approx 6$); this behaviour is further evidence that at least some of these are likely to be more reddened CBe stars. This reinforces the similar conclusion that was drawn in Section 2.4.1.

A few others blue crosses, along with some cyan circles and the majority of red squares gather around the CTT locus, as would be expected of YSOs. The late-type non emitting stars, are seen in very sparse locations of the diagram: a few of them, close to the giant sequence. Others are found among the probable CBe stars, with colours overlap those of lightly reddened late-type MS stars.

2.4.4 Spatial distribution

To complete the picture of group properties of the observed sample, it is necessary to have a closer look again at the spatial distribution of these stars, but with the a posteriori knowledge of their spectra.

In the top panel of Fig. 2.17, the observed targets are plotted with different symbols according to their spectral classification onto the SFD98 extinction map of the area. Their spatial distribution is the same as the one in the top panel of Fig.2.3, but the symbol scheme picks out some more properties. The early-type stars are almost everywhere, since they are the most numerous group and they seem not to prefer any particular location. The *featureless* objects are seen very sparsely across the area as well, except that they are mainly seen in locations showing greater integrated interstellar extinction. The later type emitters (red squares) are even more concentrated towards even denser areas of the ISM (i.e. active SFRs), as expected for young stellar objects. The other groups of stars of Section 2.4.1 are made of too few stars to describe a meaningful spatial distribution.

From the spatial distribution of the stars it is also possible collect some more evidence on what the *featureless* stars are. In the bottom panel of Fig. 2.17, the spatial distribution of stars is binned into strips of width $\Delta\ell = 2°$. The black enclosing histogram specifies the number of stars within each longitude interval. The blue solid bars represent the number of early-type stars, the red ones are the late-type stars and the cyan bars are the stars having featureless spectra, in the same longitude bins.

The general pattern is that the *featureless* objects are a higher fraction of the total number, where the total number is the lowest, in response to typically higher interstellar extinction. This effect is strikingly strong, between $128° \leq \ell \leq 124°$, less so where the reddening wall covers a larger area as compared to the W3/W4/W5 region at greater longitudes.

The suggestion, here, is that the majority of stars with featureless spectra are indeed more reddened CBe stars. Some of these *featureless* stars have been observed in the second-phase follow-up, with higher resolution and S/N, confirming this point.

2.5 Classical Be and Herbig Be stars

The majority of stars in the observed FLWO/FAST sample belong to the *early-type* group. In the literature, numerous studies have focused on several subgroups of Be stars (see e.g. The, de Winter & Perez, 1994; Lamers et al., 1998; Porter & Rivinius, 2003). Their differences have been described in detail in Section 1.3, while, in this section, I will use the shared property of the group, which is the stellar spectral type regardless of whether

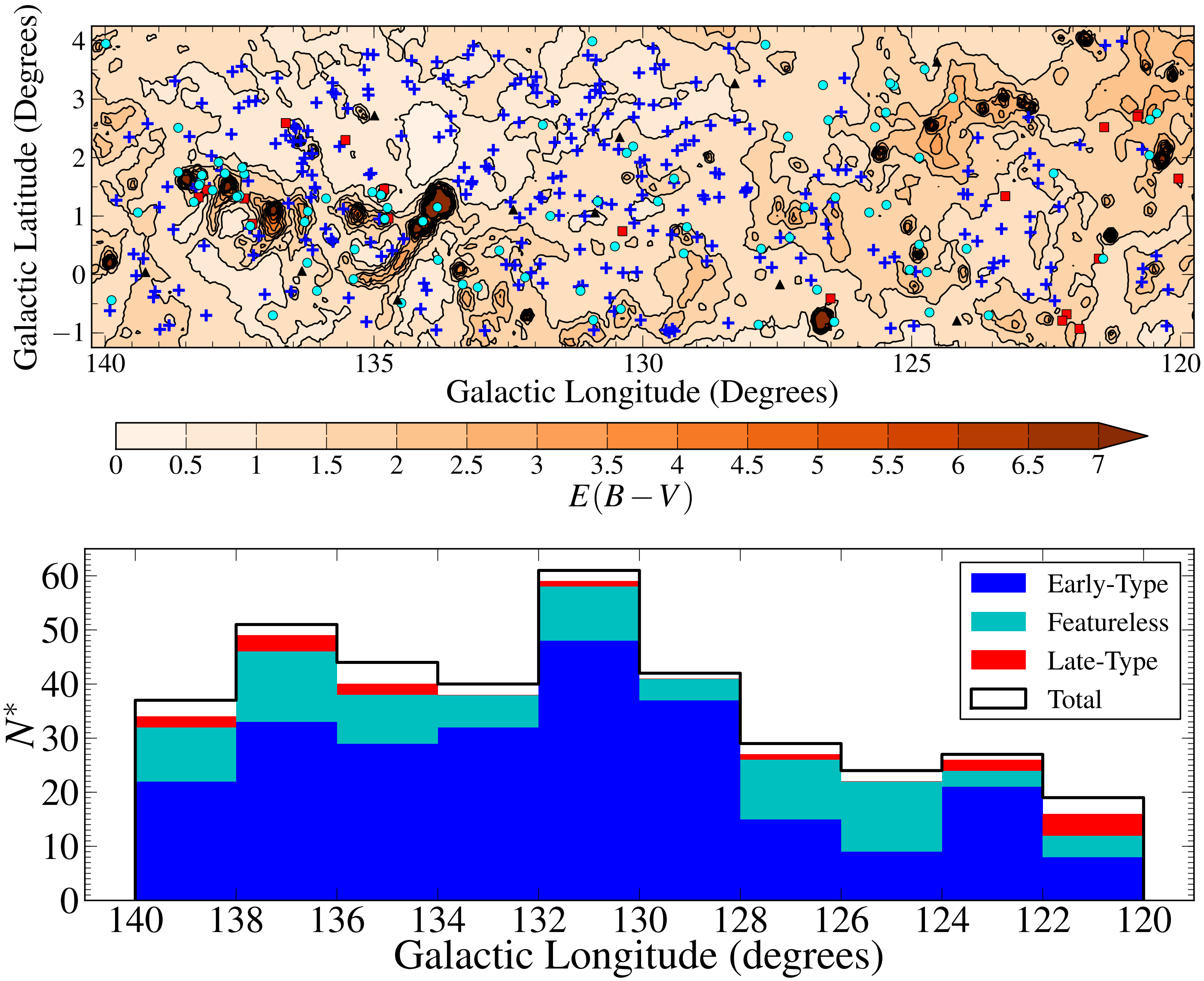

Figure 2.17: (Top): The spatial distribution of the FLWO/FAST observed targets is plotted over the dust-extinction map. Objects are grouped according to the classification give in Section 2.4.1: crosses for the early-type spectra, squares for late-type ones, circles are featureless spectra and triangles are the remaining others. (Bottom): Stars belonging to the same classification group are binned each $\Delta\ell = 2°$ in the Galactic Longitude direction. Colours of histogram bars are explained in the legend.

they are a B[e], a CBe or a HAeBe, in order to classify them. The distinction between the different types of Be stars becomes difficult with the quality of the FLWO/FAST spectra and it is possible only for the spectra with higher S/N ratio. Hence, the principal criterion is photometric and relies on the IR colours of the stars that, in Fig 2.16, have to be found within the three boxes tracing the typical boundaries for CBe stars (Corradi et al., 2008). Willing to be slightly more conservative, here I consider to be candidate CBe stars all the stars with early-type spectra, without presence of forbidden emission lines and with $(J-H) \leq 0.6$ mag. Among the 256 early-type stars, I identified 228 candidate CBe stars. For 47 of them, I also have better quality data observed in La Palma (Chapter 3). The other 28 stars are likely Herbig Be stars, which are generally seen in association with diffuse Hα emission and/or areas with higher extinction. The suggested classification is given in Table 2.2.

Be stars are known to display broader than usual photospheric lines, due either to outflow and/or rapid stellar rotation. In addition to this, they are surrounded by circumstellar discs that affect the line contrast, by adding extra continuum flux, an effect referred to as continuum veiling. How this is generated depends on the disc properties (i.e. temperature gradient, density, dust) or, in other words, on the evolutionary stage of the central star. Furthermore, the present sample suffers from large amounts of extinction ($A_V \gtrsim 4$), which makes it more challenging to acquire well exposed classification-standard blue spectra.

Due to these complications, a standard MK classification can be difficult, if not impossible (e.g. for the stars with *featureless* spectra). In Section 2.4.1, I already mentioned how the S/N of the observed spectra rules the classification scheme and the featureless spectra are just a more extreme case of cooperation between large extinction and veiling – making the detection of photospheric absorption difficult.

A literature search on the subject indicates a few atomic transitions that are suitable for spectral typing in the traditional blue range (3500 – 5000 Å). In the range of temperatures that is covered by B stars, the He I lines are strong enough to be useful for the task. Didelon (1982); Jaschek & Jaschek (1987); Gray & Corbally (2009) supply useful plots and tables that I have adopted as reference. Key absorption lines for spectral type determination are:

- O-type: He II/He I in late O-types; N IV λ4058, and N III $\lambda\lambda$4594 – 4640 – 4642, no He I in early-types
- B-type: He I lines at $\lambda\lambda$4009-4026 Å, $\lambda\lambda$4121-4144 Å and $\lambda\lambda$4387-4471Å compared to the Mg II λ4481 Å
- A-type: Ca II K and Mg II λ4481 Å. The absence of He I

Apparently no O-type stars are seen. He II transitions (as for instance the λ4200 Å) start to appear in B0 stars, but with the current resolution and S/N of the spectra, non have been found.

The above mentioned absorption lines may be affected by infilling (Didelon, 1982) or continuum veiling due to the presence of circumstellar matter, as discussed before, line blending in the fastest rotators, and potentially binarity. However, equivalent widths ratios can still be used, instead of absolute line strengths. It is generally the case that the classification of the B stars in the sample depends heavily on the relative strengths of the He I $\lambda 4471$ and Mg II $\lambda 4481$ features – their ratio is a good $T_{\rm eff}$ indicator, with little sensitivity to $\log g$ within class V-III.

2.5.1 Spectral typing

The spectra in the early-type group have S/N ratios ranging from $\lesssim 10$ to 70, as measured in the continuum between 4445 – 4500 Å , excluding the He I and Mg II lines. In practice to determine the spectral-types, I employed two methods: one relies on the equivalent width ratio of the He ($\lambda 4471$) and Mg II ($\lambda 4481$) lines, for the spectra with higher S/N ratio; the other uses the whole 3600 – 5000 Å range to classify spectra with lower S/N ratio (i.e. S/N < 20).

2.5.1.1 The equivalent width ratio method

In order to test the reliability of the spectral typing based just on the ratio of equivalent widths $W_{\lambda 4471}/W_{\lambda 4481}$, it is important to inspect how this quantity depends on the S/N ratio of the observed spectra. For this purpose, a simple simulation was run, with the aim of determining the expected distribution of equivalent width ratios as measured from synthetic spectra to which random Gaussian noise was added. This was done so to produce a grid of measured line ratios versus spectral type, according to the quality of spectrum.

Stellar atmospheres, with solar metallicity and the typical rotation speed observed in Be stars (~ 300 km s^{-1}), were chosen from the Munari et al. (2005) database (1 Å/pix dispersion) so as to cover the B0 –A0 range. Spectral types, from now on, are mapped onto a $T_{\rm eff}$ scale, given in Table 1.2, to allow a straightforward choice of the necessary model among the available ones. The spectral resolution of the model atmospheres was degraded to match the characteristic resolution of the FLWO/FAST observations ($\Delta\lambda \approx$ 6 Å). Gaussian noise was added to the models, for S/N $= 70, 50, 40, 30$. The line ratio was measured recomputing the random noise 10000 times per each given spectral type and combination of S/N ratio.

In Fig. 2.18 are plotted the $\log W_{\lambda 4471}/W_{\lambda 4481}$ versus spectral type curves for the four S/N ratios considered. The red solid curves represent the median of the corresponding distribution of ratios for each spectral type. The dashed red curves are the 1σ boundaries. The black curve is the line ratio variation as it is measured from a model atmosphere with no noise component being added to it. Comparing the four plots in Fig. 2.18, it is evident how the median of the quantity $\log W_{\lambda 4471}/W_{\lambda 4481}$ becomes less sensitive to $T_{\rm eff}$ for decreasing values of the S/N ratios. The distributions of the measured $W_{\lambda 4471}/W_{\lambda 4481}$ broadens significantly when the S/N ratio decreases. S/N ~ 25 is the limit where the measured line ratio becomes insensitive to the $T_{\rm eff}$ at this degree of spectral resolution. Smaller departures from the zero-noise measure are seen at S/N = 70, 50 and in less extent at S/N = 40. The difference between the black and red curves is still within the 1σ boundaries, at $S/N = 30$. For S/N ratios lower than 25, curves that are reproduced with the same simulation setup

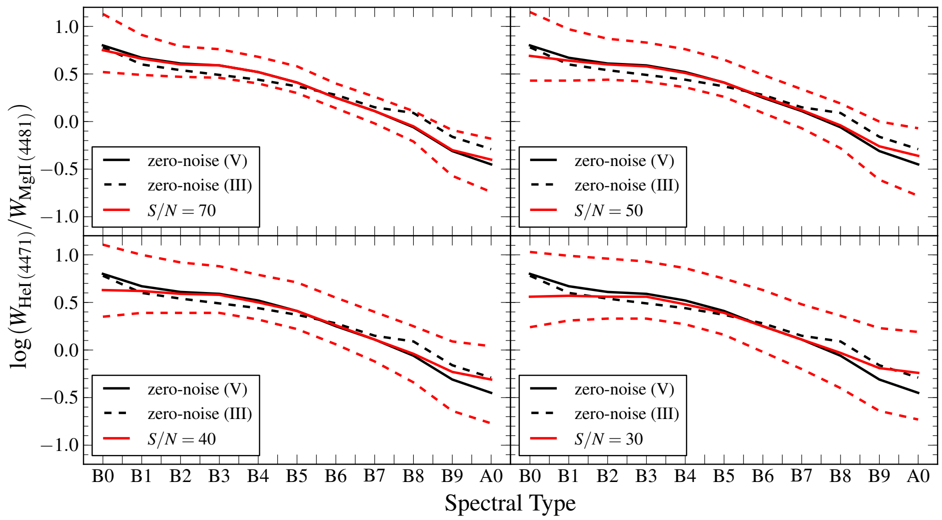

Figure 2.18: The four panels show the $\log W_{\lambda 4471}/W_{\lambda 4481}$ dependence on the spectral type, as measured from Munari et al. (2005) model atmospheres. In each panel the red solid curves represent the median of the distribution of 10000 measures of the line ratio, done for a model atmosphere with added noise. The dashed curves are at the 1σ boundaries. The zero-noise ideal case is traced as black solid (class V) and black dashed (class III) curves.

are basically flat, making the measure of $\log W_{\lambda 4471}/W_{\lambda 4481}$ be a less useful proxy of T_{eff}.

In summary, a spectral typing assignment that is based only on the measure of the quantity $\log W_{\lambda 4471}/\lambda 4481$ would generally produce too large uncertainties, specially when errors on the measure of equivalent widths are large. Since spectral types are defined with the use of a number of reference spectral features, once that the measure of $\log W_{\lambda 4471}/W_{\lambda 4481}$ supplies a first order "guess", the spectral type of a star can be adjusted by visual inspection of the whole spectrum, comparing it by eye with model atmospheres.

To obtain the first order assignment of spectral types, I measured line ratios from the observed spectra and compared them with the simulated distributions. Equivalent widths have been measured for all the 254 stars, whose spectra have been labelled as early-type, by using the ELF package within the STARLINK/DIPSO software. Each equivalent width is measured as the width of the Gaussian fit to the corresponding transition. In Fig. 2.19, there is an example of line-fitting with STARLINK/DIPSO. In Fig. 2.20, I show an example of the initial spectral type assignment, from the measure of $\log W_{\lambda 4471}/W_{\lambda 4481}$, for the spectrum plotted in Fig. 2.19. The measured line ratio favours the B5 spectral type, because its simulated line ratio distribution gives the largest probability in the range $\log W_{\lambda 4471}/W_{\lambda 4481} \pm 1\sigma$ for the star considered. This spectral type also seems to be a reasonable choice from direct comparison with the corresponding model atmosphere (top panel of Fig. 2.19). Visual comparison with B4 and B6 model atmospheres also suggests that the spectral type uncertainty is in the range of ± 1 sub-type..

Spectral types are assigned to spectra with $S/N > 25$ and $\Delta(\log W_{\lambda 4471}/W_{\lambda 4481}) \leq 0.4$, i.e. 81 stars. With this method, the noisier spectra are excluded. For all of them,

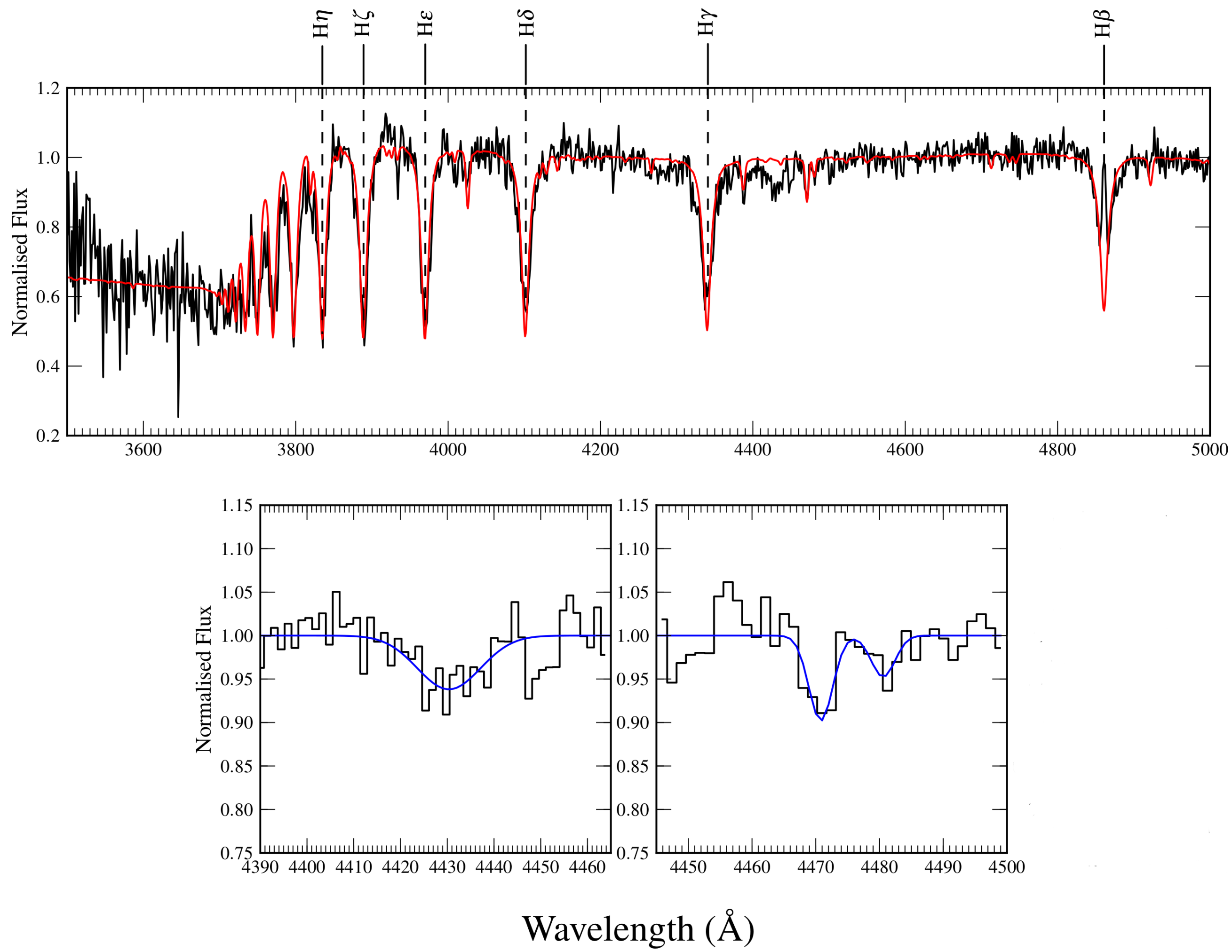

Figure 2.19: In the top panel is the spectrum of the star F029 (B5). In black is the observed spectrum and in red is the best type model atmosphere from Munari et al. (2005), which is determined by measuring the line ratio He I/Mg II. The bottom panels, zoom in two different spectral regions. Left: the DIB(λ4428 Å). Right: the He I and Mg II region. In black, again, are the observed normalised fluxes. In blue are the Gaussians that are fitted with STARLINK/DIPSO.

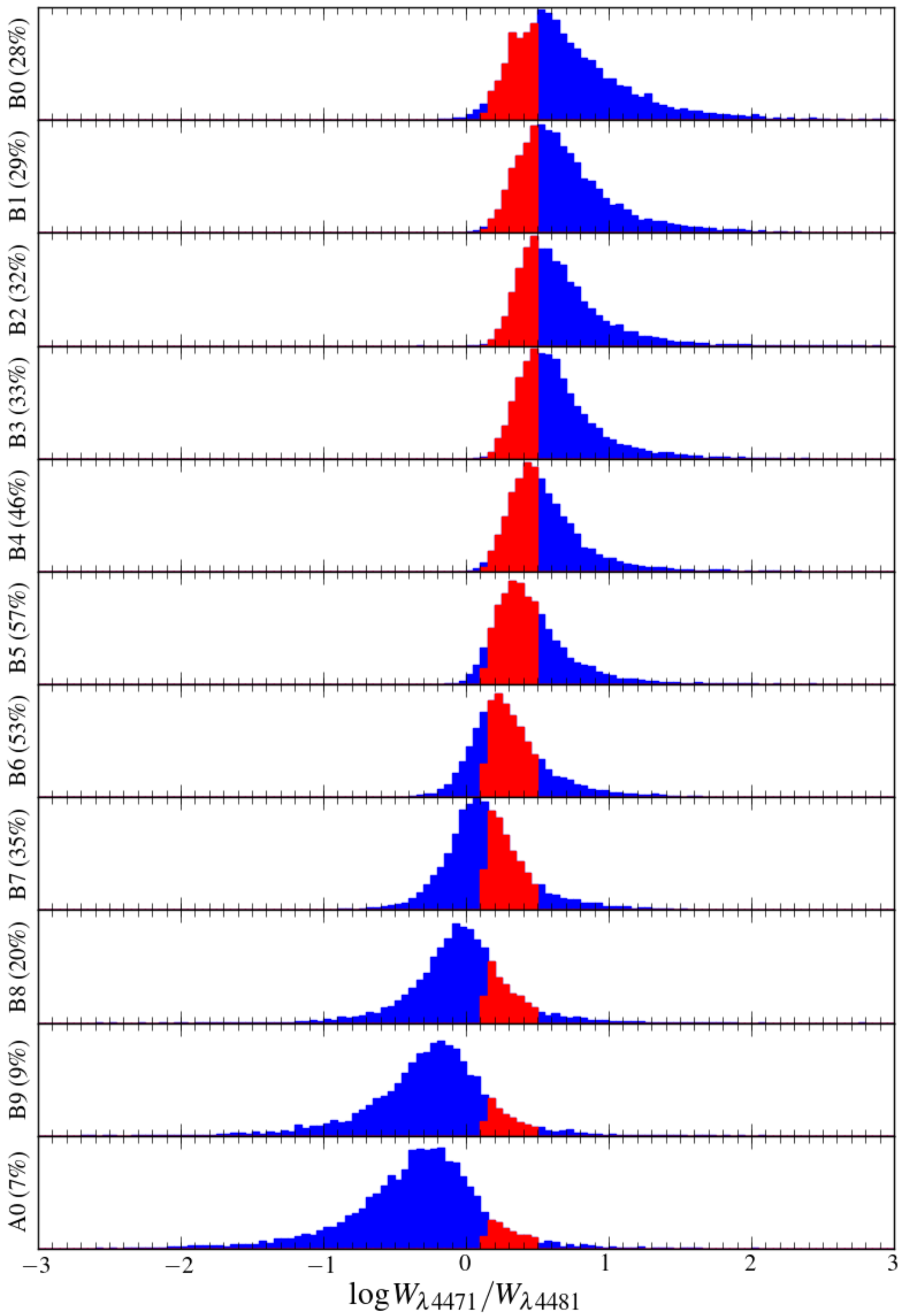

Figure 2.20: Simulated measures of $\log W_{\lambda 4471}/W_{\lambda 4481}$ from model atmospheres with S/N = 40. The red-coloured areas define the range where $\log W_{\lambda 4471}/W_{\lambda 4481} = 0.3 \pm 0.2$, which is measured for the spectrum of object F029. The spectral type is assigned as the most probable one (i.e. B5, with 57%). The uncertainty on the suggested typing for F029 is assessed by eye and it is estimated to be in the range of ± 1 sub-type.

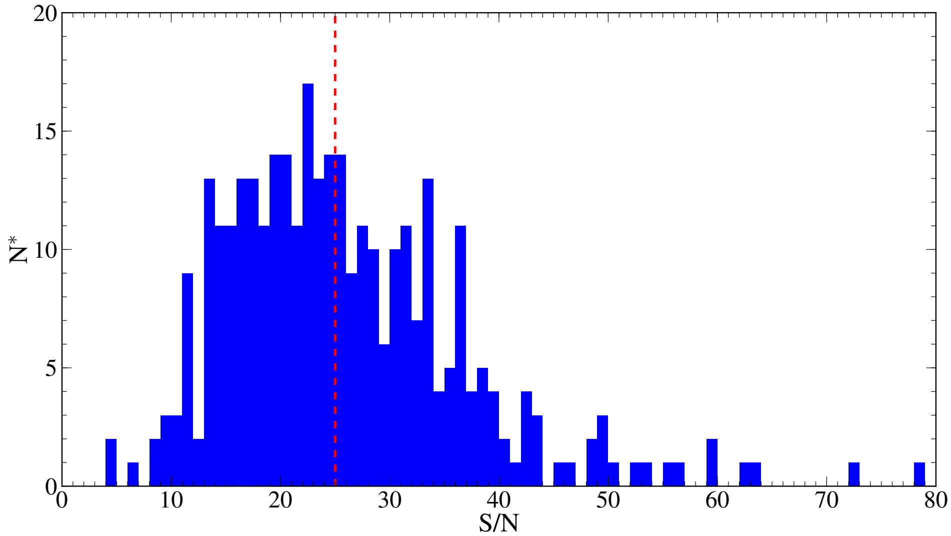

Figure 2.21: Distribution of S/N measured at λ4500 Å, for the Be stars in the FLWO/FAST sample. The vertical dashed line mark the S/N = 25 separation, where the line ratio method was adopted for the spectral typing.

as described before, the probability for a star of having a given spectral type is estimated from the probability density for a spectral type to occur between the measured $\log W_{\lambda 4471}/W_{\lambda 4481} \pm 1\sigma$ and the spectral type is assigned on the basis of the most probable one. The spectral type uncertainty and adjustments to the assigned spectral type, when they appeared necessary, were undertaken by visually comparing the observed spectrum with the corresponding model atmosphere as shown in the top panel of Fig. 2.19. The accuracy of the final typing is estimated to range typically between $\pm$ 1 sub-type for the spectra with S/N > 35, and ± 2 sub-types between $25 <$ S/N ≤ 35 respectively. The spectral types so assigned are listed in Table 2.2. The distribution of measured S/N ratios at λ4500 Å, is displayed in Fig. 2.21. 139 spectra have S/N > 25. The median of the distribution is at S/N = 24, which falls outside of the usable range.

Finally, in Fig.2.22, is the distribution of spectral types that are estimated with this method. When more than one spectrum was taken for each object, the average spectral type is taken into account. No B0 stars are found and B3 appears to be the most frequent spectral type (B2-B3 seems to be the most frequent in the literature as well, see e.g. Zorec & Briot, 1997). A local maximum is seen in the range B5-B7 as well.

2.5.1.2 Fitting the range 3600 –5000 Å

I also made an attempt to estimate the spectral type for the remaining 173 stars that have either noisier spectra (S/N $\leq$ 25) or more uncertain measures of the line ratios (i.e. $\Delta(\log W_{\lambda 4471}/W_{\lambda 4481}) > 0.4$). Since here, uncertainties would well be larger than ± 1 sub-type, I decided to type the spectra, sorting them in larger groups: i) early-B, i.e. B0-B3; ii) mid-B, that is between B4 and B6; iii) late-B, or B7-A0.

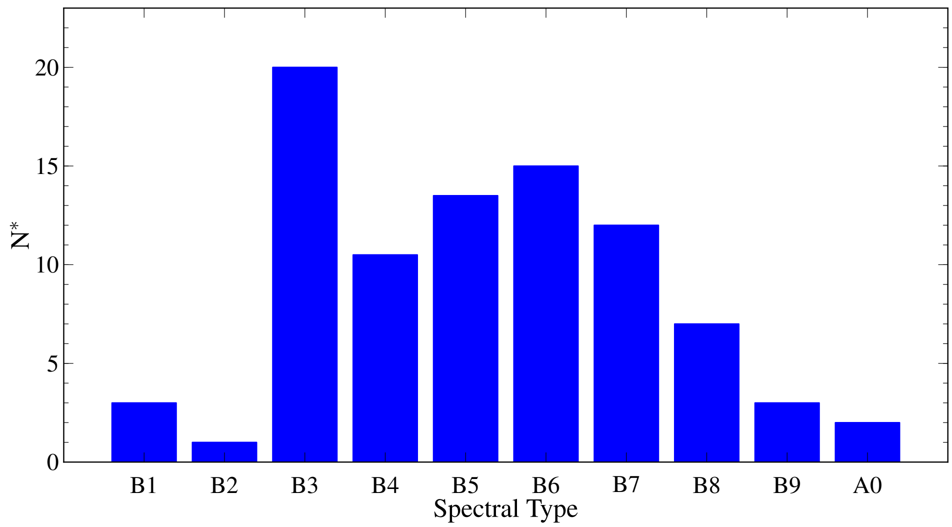

Figure 2.22: Distribution of spectral types, as determined from the use of the correlation between $\log W_{\lambda 4471}/W_{\lambda 4481}$ and spectral type. These are the 81 stars with S/N $>$ 25 and $\Delta(\log W_{\lambda 4471}/W_{\lambda 4481}) \leq 0.4$.

To determine if a spectrum falls within these groups, I used the whole 3600 –5000 Å range. This approach would not be the most correct one, since both Balmer lines and Balmer continuum (i.e. fluxes at $\lambda \lesssim 3700$ Å) of Be stars can be heavily modified with respect to normal B-type stars, as stated in Section 2.5.1.1. However, it is worth trying, because the aim is to have at least a rough classification also for these noisier spectra. To avoid bias from features that are not present in the synthetic spectra, I masked out the regions between $\lambda\lambda 4400 - 4500$ Å and $\lambda\lambda 4820 - 4900$ Å to avoid the DIB at $\lambda 4428$ Å and the Hβ region.

To find the best type, then, I first rebinned the model atmospheres (in the range B0 – A0) and degraded their spectral resolution in order to match the observed spectra. Second, I computed the following variances $\sum_{i=0}^{N}(S_i - M_i)^2$ for each spectral-type, where N is the number of dispersion bins, S is the observed spectrum and M is the corresponding model. The spectrum is assigned to one of the three groups, accordingly to what model atmosphere produces the minimum variance. Two examples of the fits are given in Fig. 2.23. Spectral type groups are reported in Table 2.2.

With this method, the spectra are likely to be typed as earlier than they actually are, when the emission is strong, and later than they are, when the noise is large. However, a visual check of the three groups classification appears to prevent from extremely wrong typing. Generally, strong emission might be observed in hotter early-types, so that the Balmer continuum does not drive the typing too much; also, the wider line wings of late-types help the classification, when the emission is weaker. A better assessment of this method of typing is discussed in Section 3.4.1, with aid of the better quality spectra that were taken in La Palma for some of the stars here typed.

In Fig. 2.24, the pie charts compare the relative fractions of early, mid, and late-B

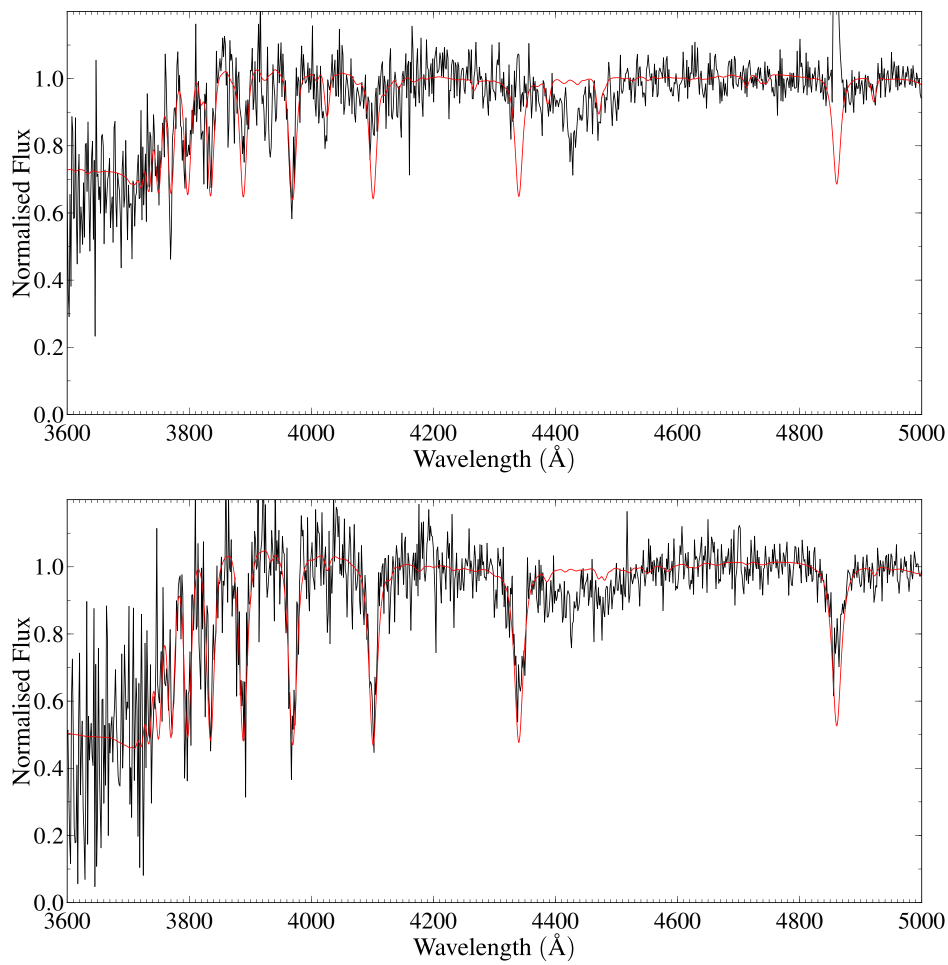

Figure 2.23: Two examples of spectral type determination, via the spectrum fitting over the 3600 – 5000 Å range. Top panel shows the star F089 (S/N = 21), whose best fit is an early-type spectrum. In the bottom panel is the F097, which is a late-type example (S/N = 15). In black are the observed spectra, while in red the model atmospheres.

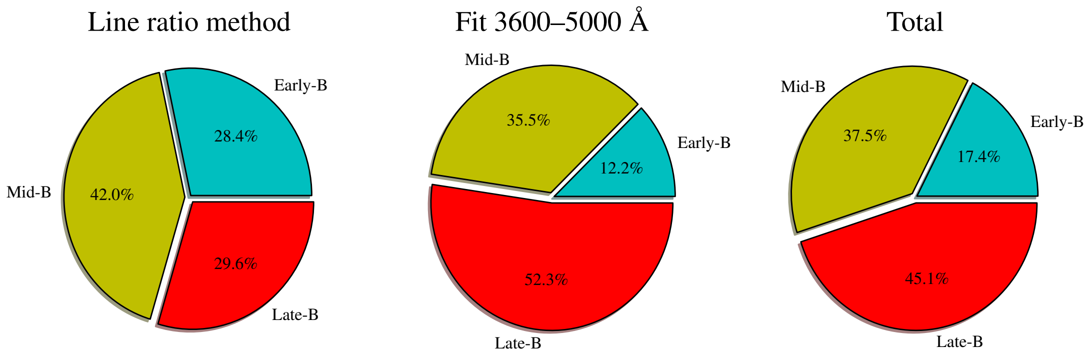

Figure 2.24: Comparison between the two different methods adopted for the spectral typing and the combined fraction of early-B stars (B1-B3), mid-B (B4-B6) and late-B (B7-A0).

types: (i) among 81 stars that I typed with use of the $W_{\lambda 4471}/W_{\lambda 4481}$ ratio, in the previous section; (ii) among the 173 stars presented in this section; (iii) among the total number of stars. When using the whole spectral range 3600 –5000 Å, the classification seem to prefer late-B stars, as compared to the line ratio method. It is worth noting that the distribution of observed r magnitudes is pretty different in the two groups, in a way that higher S/N spectra are in average 1 mag brighter than the others. This information suggest that the observed bias towards later B-types could be not entirely due to the poorer quality of the spectra, but real to a different composition of the two groups.

2.5.2 Diffuse interstellar bands

Among the spectra of the Be stars in the sample, it easy to spot very deep DIBs. These have been studied by many authors, as a tool for estimating the interstellar extinction. Herbig (1995), supplies a useful list of them to compare with. I have chosen two among the deepest ones that are in the blue part of the spectrum (at λ4428 Å and λ5778–5780 Å), to which I have fitted simple Gaussian profiles for measuring the equivalent widths. In Fig. 2.19 there are examples of the fits. The measured equivalent widths are given in Table 8.2. Since the sample studied here is large and measures are available for most of the Be stars, I will discuss the correlation between DIBs equivalent widths and E(B-V) in Section 8.2.

2.6 Late-type stars

In Section 2.4.1, it appeared evident that two groups of late-type stars are present within the sample. The first ones, display Hα in emission and are seen towards known SFRs and therefore are very likely to be YSOs. The others, do not show Hα in emission. The other late-type stars with no-emission are very likely field stars, whose ($r-i$, $r-$Hα) colours mimic the ones of more reddened emission line stars. For two of them (F257, F271) there is evidence of variability, given their $(r-\mathrm{H}\alpha)$ colours and partially infilled Hα lines.

The most interesting ones are, of course, the late-type stars that display Hα emission. These are in general averagely strong emitters with $EW(\mathrm{H}\alpha) < -10$ Å, with many having $EW(\mathrm{H}\alpha) < -20$ Å. Only the star F017 shows a weaker emission $EW(\mathrm{H}\alpha)_\mathrm{S} \sim -3.5$ Å, but it could have been observed in a lower state of activity. Almost the majority of them has all the Balmer lines and the Balmer continuum in emission, but their photospheric absorption is just recognisable so that they do not belong to the group of featureless spectra.

Sharing similar S/N ratio of the Be sample, I can identify typical features that are seen in G to late-K stars, which include the G-Band, the Ca II H & K lines, TiO bands, Fe lines, the Na II doublet, the Li I as a youth indicator (see e.g. Gray & Corbally, 2009, for a detailed list). The identification of the Li I can be problematic due to blending to neighbouring lines and its strength could be highly overestimated. I classified these spectra, visually, by comparing them with spectra from the Indo-US library (Valdes et al., 2004), after degrading the resolution of the latter in order to match the observed spectra's resolution.

I can type 9 stars out of 12, finding 2 late-G, 4 early-K and 3 late-K stars. A more accurate typing, would involve a correction for veiling that severely affect YSOs' spectra (see e.g. Gullbring et al., 1998). However, the present classification does not aim at a very precise typing, since these stars are just a small sub-sample of the total. Spectral types are indicated in Table 2.2.

2.7 Summary

In this chapter, I presented the follow-up spectroscopy of 370 Hα emission line candidate stars, observed low optical dispersion. More than 93% of them confirmed their emission. Among the non confirmed emitters, there are field late-type giants, probable variable emitters and a few stars that were mis-observed.

I found that of the 370 observed stars, 254 are Be stars (CBe and Herbig Be stars), 12 are late-type. A large portion of the observed targets (81 stars) have too low S/N to be put in one of the categories of Section 2.4.1. I collect some evidence, from their observed optical and near-IR photometry along with the analysis of the spatial distribution, that these remaining ones are very likely to be more reddened and fainter Be stars (see e.g. Section 2.4.3).

The Be stars have been studied in larger detail and I propose spectral types for them, with a $\pm$1-2 sub-type precision, for 81 of them. The remaining 173 stars, due to poorer quality of the spectra have been grouped in larger categories: early, mid, late-B types.

This follow-up has satisfied its original role, of initial study of the sample composition and confirmation of the emitter nature of these stars. In the next chapter, I will present the second phase of follow-up, at higher resolution and S/N. The targets in the second phase, were selected from these already observed stars and among the unobserved targets with $r \leq 17$ from the original list of targets.

Table 2.1: IPHAS photometry of the 370 emission line candidates observed with FLWO/FAST. Columns are: ID (#) name; IPHAS point-source name, which includes the J2000 RA and Dec; Galactic Coordinates; r magnitude, $(r-i)$ and $(r-\mathrm{H}\alpha)$ colours from IPHAS; Hα equivalent width being estimated from the IPHAS colour-colour plane; J magnitude, $(J-H)$ and $(H-K)$ colours from 2MASS.

#	IPHAS Jhhmmss.ss+ddmmss.s	ℓ (deg)	b (deg)	r (mag)	$(r-i)$ (mag)	$(r-\mathrm{H}\alpha)$ (mag)	$EW(\mathrm{H}\alpha)_\mathrm{P}$ (Å)	J (mag)	$(J-H)$ (mag)	$(H-K)$ (mag)
F001	J002441.73+642137.5	120.04	1.64	14.76	0.86	0.61	−24	12.51 ± 0.02	0.30 ± 0.04	0.26 ± 0.04
F002	J002722.54+653046.5	120.44	2.76	16.07	1.41	1.01	−63	12.41 ± 0.02	1.03 ± 0.04	0.45 ± 0.04
F003	J002758.97+622906.1	120.23	-0.26	15.08	0.63	0.46	−14	13.30 ± 0.02	0.34 ± 0.04	0.24 ± 0.04
F004	J002843.24+615216.2	120.26	-0.88	14.41	0.49	0.40	−11	13.16 ± 0.02	0.17 ± 0.04	0.20 ± 0.05
F005	J002843.46+652507.3	120.57	2.65	14.36	1.04	0.79	−42	11.52 ± 0.02	0.88 ± 0.03	0.64 ± 0.04
F006	J002921.19+644850.5	120.58	2.04	15.76	1.13	0.99	−69	12.92 ± 0.02	0.46 ± 0.04	0.52 ± 0.04
F007	J002926.93+630450.2	120.45	0.32	14.07	0.35	0.36	−11	13.11 ± 0.02	0.12 ± 0.04	0.18 ± 0.04
F008	J003025.04+645500.0	120.71	2.14	15.93	1.02	0.78	−41	13.15 ± 0.02	0.68 ± 0.04	0.48 ± 0.04
F009	J003037.51+653121.2	120.78	2.74	15.05	1.02	0.72	−33	12.31 ± 0.02	0.87 ± 0.04	0.63 ± 0.04
F010	J003052.95+652859.8	120.80	2.70	14.52	0.94	0.86	−56	12.02 ± 0.02	0.76 ± 0.03	0.45 ± 0.04
F011	J003148.91+625323.2	120.70	0.10	16.27	0.74	0.50	−15	14.45 ± 0.07	0.34 ± 0.11	0.20 ± 0.11
F012	J003210.31+623929.2	120.72	-0.13	13.42	0.49	0.54	−26	12.33 ± 0.02	0.22 ± 0.04	0.15 ± 0.04
F013	J003248.02+664759.6	121.09	3.99	14.46	0.96	0.83	−50	12.11 ± 0.02	0.55 ± 0.03	0.36 ± 0.03
F014	J003559.30+664502.9	121.40	3.92	15.96	0.76	0.61	−27	14.11 ± 0.04	0.40 ± 0.06	0.46 ± 0.06
F015	J003656.80+652044.4	121.42	2.52	16.21	0.97	0.41	−1	13.98 ± 0.03	0.54 ± 0.05	0.23 ± 0.06
F016	J003814.97+630559.7	121.44	0.27	15.53	0.98	1.18	−111	12.50 ± 0.02	1.01 ± 0.04	0.84 ± 0.03
F017	J003856.78+630639.9	121.52	0.27	14.46	0.85	0.60	−23	12.27 ± 0.02	0.66 ± 0.03	0.17 ± 0.04
F018	J004121.36+650413.5	121.87	2.22	13.39	0.74	0.68	−37	12.21 ± 0.02	0.38 ± 0.04	0.38 ± 0.04
F019	J004232.14+615526.6	121.88	-0.93	16.47	1.43	0.89	−45	13.05 ± 0.02	0.87 ± 0.04	0.40 ± 0.03
F020	J004427.40+621046.6	122.12	-0.68	14.49	0.86	0.79	−47	11.98 ± 0.02	0.89 ± 0.04	0.52 ± 0.04
F021	J004509.95+620426.4	122.20	-0.79	15.40	1.05	0.82	−46	12.59 ± 0.02	0.87 ± 0.03	0.45 ± 0.03
F022	J004517.08+640124.1	122.26	1.16	15.62	0.89	0.64	−26	13.37 ± 0.02	0.41 ± 0.04	0.38 ± 0.04
F023	J004607.02+643546.6	122.36	1.73	16.38	0.89	0.74	−39	13.97 ± 0.02	0.44 ± 0.04	0.41 ± 0.04
F024	J004620.80+622503.9	122.34	-0.45	13.21	0.61	0.54	−24	11.98 ± 0.02	0.26 ± 0.04	0.28 ± 0.04
F025	J004651.69+625914.3	122.41	0.12	14.87	0.50	0.45	−16	13.32 ± 0.02	0.22 ± 0.04	0.26 ± 0.05

Table 2.1: Continued

#	IPHAS Jhhmmss.ss+ddmmss.s	ℓ (deg)	b (deg)	r (mag)	$(r-i)$ (mag)	$(r-\mathrm{H}\alpha)$ (mag)	$EW(\mathrm{H}\alpha)_\mathrm{P}$ (Å)	J (mag)	$(J-H)$ (mag)	$(H-K)$ (mag)
F026	J004741.54+624203.3	122.50	-0.17	14.14	0.41	0.44	−18	13.01 ± 0.02	0.20 ± 0.04	0.13 ± 0.04
F027	J004842.93+644411.1	122.64	1.87	14.75	0.58	0.42	−11	13.33 ± 0.03	0.36 ± 0.04	0.09 ± 0.04
F028	J004850.12+642533.7	122.65	1.56	15.63	0.81	0.57	−21	13.92 ± 0.03	0.35 ± 0.05	0.15 ± 0.06
F029	J005011.87+635129.9	122.80	0.99	13.75	0.39	0.50	−25	12.75 ± 0.03	0.19 ± 0.04	0.11 ± 0.04
F030	J005011.89+633525.8	122.79	0.72	15.37	0.62	0.62	−33	13.69 ± 0.02	0.28 ± 0.04	0.37 ± 0.05
F031	J005012.69+645621.6	122.80	2.07	14.16	0.56	0.48	−18	12.65 ± 0.03	0.30 ± 0.05	0.14 ± 0.05
F032	J005029.25+653330.8	122.83	2.69	14.65	0.67	0.65	−35	12.97 ± 0.02	0.26 ± 0.04	0.30 ± 0.04
F033	J005032.31+623155.5	122.83	-0.34	15.42	0.57	0.49	−19	13.95 ± 0.05	0.31 ± 0.08	0.21 ± 0.08
F034	J005425.02+641252.8	123.26	1.34	15.59	0.77	0.56	−21	13.78 ± 0.03	0.34 ± 0.05	0.21 ± 0.05
F035	J005436.84+630549.9	123.29	0.23	14.95	0.62	0.76	−52	13.30 ± 0.03	0.33 ± 0.05	0.36 ± 0.05
F036	J005611.62+630350.5	123.47	0.20	14.37	0.50	0.47	−19	12.95 ± 0.02	0.18 ± 0.03	0.18 ± 0.03
F037	J005619.50+625824.0	123.49	0.11	14.61	0.38	0.38	−13	13.46 ± 0.02	0.23 ± 0.03	0.20 ± 0.04
F038	J005651.72+620943.2	123.57	-0.70	15.84	0.99	0.76	−39	13.27 ± 0.02	0.42 ± 0.04	0.46 ± 0.04
F039	J005743.72+640235.6	123.62	1.18	14.18	0.40	0.39	−13	13.07 ± 0.02	0.20 ± 0.04	0.13 ± 0.04
F040	J005809.86+624412.9	123.70	-0.12	14.63	0.47	0.57	−31	13.32 ± 0.02	0.27 ± 0.04	0.15 ± 0.03
F041	J005859.24+632603.0	123.78	0.57	13.14	0.30	0.62	−45	12.06 ± 0.02	0.30 ± 0.04	0.25 ± 0.03
F042	J005926.64+651157.0	123.77	2.34	13.35	0.45	0.51	−24	12.06 ± 0.02	0.21 ± 0.04	0.14 ± 0.04
F043	J010045.58+631740.2	123.98	0.44	15.42	0.74	0.64	−32	13.53 ± 0.02	0.32 ± 0.04	0.29 ± 0.05
F044	J010051.26+641327.3	123.96	1.37	13.61	0.49	0.40	−11	12.37 ± 0.02	0.19 ± 0.03	0.14 ± 0.04
F045	J010054.58+643729.6	123.95	1.77	12.99	0.56	0.54	−24	11.30 ± 0.03	0.34 ± 0.04	0.19 ± 0.04
F046	J010107.85+633227.0	124.01	0.69	13.84	0.53	0.46	−17	12.47 ± 0.02	0.22 ± 0.03	0.18 ± 0.04
F047	J010138.04+641349.9	124.04	1.38	13.31	0.57	0.67	−41	11.74 ± 0.02	0.34 ± 0.03	0.24 ± 0.03
F048	J010154.04+620332.5	124.16	-0.79	13.04	0.64	0.39	−7	11.43 ± 0.02	0.58 ± 0.03	0.15 ± 0.04
F049	J010406.86+655146.1	124.23	3.02	16.67	1.31	0.84	−41	13.43 ± 0.02	0.63 ± 0.03	0.44 ± 0.03
F050	J010622.54+621031.3	124.67	-0.65	14.54	0.68	0.42	−9	12.98 ± 0.02	0.29 ± 0.03	0.12 ± 0.04
F051	J010707.68+625117.0	124.72	0.04	14.56	0.72	0.59	−26	12.65 ± 0.02	0.39 ± 0.03	0.24 ± 0.03
F052	J010723.34+662742.1	124.53	3.64	14.40	0.94	0.54	−13	12.27 ± 0.02	0.69 ± 0.04	0.15 ± 0.04
F053	J010838.09+631918.6	124.86	0.51	14.19	0.65	0.43	−10	12.59 ± 0.02	0.25 ± 0.03	0.14 ± 0.03

Table 2.1: Continued

#	IPHAS Jhhmmss.ss+ddmmss.s	ℓ (deg)	b (deg)	r (mag)	$(r-i)$ (mag)	$(r-\mathrm{H}\alpha)$ (mag)	$EW(\mathrm{H}\alpha)_\mathrm{P}$ (Å)	J (mag)	$(J-H)$ (mag)	$(H-K)$ (mag)
F054	J010841.17+615511.8	124.96	-0.88	13.62	0.36	0.39	−14	12.84 ± 0.02	0.10 ± 0.03	0.14 ± 0.04
F055	J010859.58+625103.6	124.93	0.05	16.64	0.74	0.55	−21	14.45 ± 0.03	0.91 ± 0.04	0.78 ± 0.04
F056	J010932.61+644814.5	124.86	2.00	14.71	1.11	0.85	−48	12.00 ± 0.02	0.53 ± 0.02	0.37 ± 0.02
F057	J010938.29+661854.0	124.76	3.51	15.16	0.75	0.81	−54	13.33 ± 0.02	0.39 ± 0.04	0.34 ± 0.04
F058	J010958.80+625229.3	125.04	0.08	14.09	0.86	0.70	−35	12.44 ± 0.02	0.47 ± 0.04	0.40 ± 0.04
F059	J011216.30+615051.2	125.39	-0.92	13.52	0.34	0.27	−4	12.65 ± 0.02	0.14 ± 0.03	0.10 ± 0.03
F060	J011234.21+630432.5	125.32	0.30	12.60	0.70	0.59	−27	10.94 ± 0.02	0.27 ± 0.03	0.24 ± 0.03
F061	J011402.43+625735.3	125.50	0.20	12.77	0.66	0.55	−23	11.41 ± 0.02	0.27 ± 0.03	0.25 ± 0.03
F062	J011436.96+635651.7	125.47	1.19	15.54	1.11	0.74	−32	12.80 ± 0.02	0.59 ± 0.03	0.46 ± 0.03
F063	J011458.94+655946.3	125.33	3.23	15.01	0.82	1.01	−86	12.85 ± 0.02	0.45 ± 0.03	0.43 ± 0.03
F064	J011543.94+660116.1	125.40	3.27	14.14	0.93	1.08	−94	11.95 ± 0.02	0.49 ± 0.04	0.40 ± 0.04
F065	J011601.07+653124.8	125.48	2.77	15.55	0.94	0.96	−72	13.13 ± 0.02	0.49 ± 0.03	0.40 ± 0.03
F066	J011604.41+630926.7	125.71	0.42	14.82	0.78	0.53	−17	12.93 ± 0.02	0.31 ± 0.03	0.16 ± 0.03
F067	J011720.92+634727.8	125.79	1.06	14.97	0.90	1.00	−80	12.45 ± 0.02	0.61 ± 0.03	0.47 ± 0.03
F068	J011745.30+651455.1	125.68	2.52	15.36	1.10	1.00	−71	12.77 ± 0.02	0.58 ± 0.03	0.45 ± 0.03
F069	J011918.18+642233.8	125.94	1.67	13.39	0.60	0.69	−43	12.22 ± 0.02	0.29 ± 0.03	0.23 ± 0.03
F070	J012114.50+615139.3	126.44	-0.81	16.19	1.16	1.06	−80	12.99 ± 0.03	0.83 ± 0.04	0.41 ± 0.04
F071	J012158.74+642812.8	126.22	1.79	14.32	0.71	0.73	−44	12.74 ± 0.03	0.29 ± 0.05	0.33 ± 0.05
F072	J012216.48+621448.5	126.51	-0.41	16.62	1.38	0.94	−53	13.35 ± 0.03	1.01 ± 0.04	0.45 ± 0.04
F073	J012320.11+635830.9	126.42	1.32	14.02	0.94	0.97	−72	11.89 ± 0.02	0.47 ± 0.03	0.40 ± 0.03
F074	J012325.80+642638.7	126.37	1.79	16.24	0.71	0.54	−20	14.60 ± 0.03	0.27 ± 0.05	0.11 ± 0.08
F075	J012339.47+631544.2	126.55	0.62	14.98	0.87	0.58	−20	12.97 ± 0.02	0.45 ± 0.03	0.29 ± 0.03
F076	J012339.76+635312.9	126.47	1.24	15.00	0.85	0.74	−41	12.96 ± 0.02	0.41 ± 0.03	0.35 ± 0.03
F077	J012358.07+652615.4	126.31	2.78	13.65	0.50	0.46	−18	12.51 ± 0.02	0.18 ± 0.03	0.14 ± 0.03
F078	J012405.42+660059.9	126.25	3.36	14.98	0.63	0.55	−24	13.45 ± 0.03	0.27 ± 0.04	0.21 ± 0.04
F079	J012416.76+633011.7	126.59	0.86	13.06	0.74	0.47	−12	11.53 ± 0.02	0.31 ± 0.03	0.16 ± 0.02
F080	J012430.74+622156.5	126.76	-0.26	16.62	0.89	0.80	−48	14.30 ± 0.03	0.64 ± 0.04	0.34 ± 0.05
F081	J012540.54+623025.6	126.87	-0.10	13.34	0.55	0.51	−22	12.05 ± 0.02	0.22 ± 0.03	0.19 ± 0.02

Table 2.1: Continued

#	IPHAS	ℓ	b	r	$(r-i)$	$(r-\mathrm{H\alpha})$	$EW(\mathrm{H\alpha})_\mathrm{P}$	J	$(J-H)$	$(H-K)$
	Jhhmmss.ss+ddmmss.s	(deg)	(deg)	(mag)	(mag)	(mag)	(Å)	(mag)	(mag)	(mag)
F082	J012609.27+651617.7	126.55	2.64	14.72	0.91	0.64	−26	12.79 ± 0.03	0.45 ± 0.04	0.36 ± 0.04
F083	J012634.69+641850.9	126.73	1.70	12.78	0.70	0.57	−24	11.07 ± 0.02	0.30 ± 0.04	0.23 ± 0.04
F084	J012703.24+634333.2	126.86	1.13	14.00	0.86	0.80	−49	11.60 ± 0.02	0.37 ± 0.04	0.40 ± 0.04
F085	J012745.08+625154.3	127.06	0.28	13.34	0.50	0.57	−31	12.04 ± 0.02	0.24 ± 0.03	0.21 ± 0.04
F086	J012751.29+655104.0	126.65	3.24	14.50	0.74	0.76	−48	12.77 ± 0.02	0.37 ± 0.04	0.28 ± 0.04
F087	J012812.11+634349.5	126.99	1.15	15.92	1.04	0.73	−33	13.45 ± 0.03	0.47 ± 0.05	0.40 ± 0.05
F088	J012821.12+635754.0	126.97	1.38	14.59	0.64	0.75	−50	12.93 ± 0.07	0.25 ± 0.10	0.29 ± 0.10
F089	J013000.21+631044.6	127.27	0.63	13.68	0.98	1.00	−76	11.33 ± 0.02	0.56 ± 0.03	0.53 ± 0.04
F090	J013031.88+622132.2	127.45	-0.17	16.85	0.54	0.75	−54	15.94 ± 0.10	0.52 ± 0.17	0.29 ± 0.21
F091	J013130.51+630914.3	127.44	0.63	15.04	0.54	0.62	−35	13.64 ± 0.02	0.70 ± 0.04	0.70 ± 0.04
F092	J013213.90+623717.2	127.60	0.12	13.34	0.62	0.43	−11	11.96 ± 0.02	0.22 ± 0.04	0.17 ± 0.04
F093	J013245.66+645233.2	127.30	2.36	15.36	0.78	1.04	−93	13.31 ± 0.03	0.47 ± 0.04	0.40 ± 0.05
F094	J013259.57+613650.6	127.85	-0.86	15.49	0.79	0.50	−14	13.49 ± 0.02	0.76 ± 0.04	0.65 ± 0.04
F095	J013422.61+624459.7	127.82	0.29	12.90	0.42	0.61	−38	11.90 ± 0.02	0.14 ± 0.04	0.26 ± 0.03
F096	J013425.08+625416.3	127.80	0.44	15.13	1.04	0.87	−53	12.65 ± 0.02	0.52 ± 0.04	0.47 ± 0.04
F097	J013739.40+613258.8	128.41	-0.83	14.28	0.67	0.50	−17	12.73 ± 0.03	0.31 ± 0.04	0.16 ± 0.04
F098	J013819.58+635306.0	128.06	1.48	12.96	0.64	0.91	−74	11.50 ± 0.02	0.31 ± 0.04	0.34 ± 0.03
F099	J013825.56+635008.5	128.08	1.43	13.90	0.55	0.46	−16	12.70 ± 0.03	0.24 ± 0.04	0.11 ± 0.04
F100	J013834.27+634841.3	128.10	1.41	15.31	0.66	0.56	−24	14.16 ± 0.03	0.17 ± 0.05	0.15 ± 0.07
F101	J013920.32+662116.0	127.72	3.93	15.29	0.83	0.57	−21	13.34 ± 0.03	0.29 ± 0.04	0.22 ± 0.05
F102	J013920.80+654338.7	127.83	3.31	13.64	0.63	0.46	−14	12.20 ± 0.02	0.24 ± 0.04	0.18 ± 0.04
F103	J013932.59+645302.3	128.01	2.49	12.93	0.54	0.57	−29	11.43 ± 0.02	1.22 ± 0.04	1.10 ± 0.04
F104	J014218.74+624733.5	128.71	0.49	14.53	0.67	0.49	−17	12.90 ± 0.02	0.30 ± 0.04	0.23 ± 0.04
F105	J014221.27+645836.1	128.29	2.64	15.24	0.43	0.39	−12	14.21 ± 0.03	0.25 ± 0.06	0.02 ± 0.07
F106	J014238.73+633753.1	128.58	1.32	13.16	0.50	0.39	−10	12.03 ± 0.02	0.22 ± 0.03	0.12 ± 0.03
F107	J014244.86+623056.2	128.81	0.23	13.15	0.37	0.37	−12	12.06 ± 0.02	0.22 ± 0.03	0.14 ± 0.03
F108	J014322.19+640118.5	128.58	1.72	13.31	0.48	0.49	−22	12.30 ± 0.02	0.16 ± 0.04	0.16 ± 0.04
F109	J014337.23+653607.3	128.29	3.27	13.47	0.78	0.47	−11			

Table 2.1: Continued

#	IPHAS Jhhmmss.ss+ddmmss.s	ℓ (deg)	b (deg)	r (mag)	$(r-i)$ (mag)	$(r-\mathrm{H}\alpha)$ (mag)	$EW(\mathrm{H}\alpha)_\mathrm{P}$ (Å)	J (mag)	$(J-H)$ (mag)	$(H-K)$ (mag)
F110	J014401.85+640124.5	128.65	1.74	15.49	0.63	0.56	−25	14.07 ± 0.03	0.33 ± 0.05	0.18 ± 0.05
F111	J014458.15+633244.0	128.85	1.29	13.97	0.50	0.44	−15	12.89 ± 0.02	0.17 ± 0.04	0.16 ± 0.04
F112	J014458.27+625245.8	128.99	0.64	13.31	0.66	0.60	−30	11.71 ± 0.02	0.34 ± 0.04	0.28 ± 0.04
F113	J014519.02+633559.1	128.88	1.35	13.11	0.46	0.55	−29	12.27 ± 0.02	0.21 ± 0.04	0.22 ± 0.04
F114	J014539.64+611259.1	129.41	-0.97	12.12	0.56	0.57	−28	10.92 ± 0.02	0.19 ± 0.03	0.24 ± 0.03
F115	J014552.19+660933.3	128.40	3.87	16.34	0.72	0.45	−11	14.36 ± 0.03	0.67 ± 0.05	0.71 ± 0.05
F116	J014602.11+611502.2	129.45	-0.93	13.68	0.57	0.71	−47	12.39 ± 0.03	0.26 ± 0.05	0.25 ± 0.04
F117	J014620.44+644802.5	128.74	2.55	14.37	0.48	0.44	−16	13.25 ± 0.02	0.23 ± 0.04	0.17 ± 0.04
F118	J014624.42+611037.3	129.51	-0.99	13.31	0.49	0.35	−6	12.22 ± 0.02	0.17 ± 0.04	0.14 ± 0.04
F119	J014634.08+623317.4	129.24	0.36	15.33	0.99	0.89	−58	13.29 ± 0.02	0.50 ± 0.04	0.43 ± 0.04
F120	J014657.41+630032.2	129.18	0.81	15.60	1.16	0.73	−31	12.84 ± 0.02	0.61 ± 0.04	0.44 ± 0.04
F121	J014807.07+631613.2	129.25	1.10	13.53	0.68	0.69	−40	11.92 ± 0.02	0.25 ± 0.03	0.38 ± 0.03
F122	J014843.39+642854.4	129.05	2.29	13.70	0.44	0.49	−23	12.66 ± 0.02	0.24 ± 0.04	0.15 ± 0.04
F123	J014905.20+624912.3	129.46	0.68	13.72	0.87	0.61	−23	11.49 ± 0.02	0.34 ± 0.04	0.48 ± 0.04
F124	J015001.17+642219.7	129.21	2.22	15.75	0.63	0.44	−11	14.14 ± 0.02	0.29 ± 0.05	0.14 ± 0.06
F125	J015022.92+652743.2	129.01	3.29	13.75	0.50	0.41	−13	12.55 ± 0.02	0.26 ± 0.03	0.28 ± 0.03
F126	J015030.72+634132.5	129.42	1.57	15.68	0.70	0.50	−16	13.84 ± 0.03	0.40 ± 0.04	0.24 ± 0.04
F127	J015037.67+644446.9	129.19	2.60	14.59	0.45	0.37	−10	13.52 ± 0.02	0.21 ± 0.04	0.22 ± 0.04
F128	J015040.88+634526.9	129.42	1.64	15.39	0.76	0.83	−57	13.47 ± 0.03	0.43 ± 0.04	0.42 ± 0.04
F129	J015105.68+611602.6	130.04	-0.78	13.58	0.47	0.37	−8	12.50 ± 0.02	0.24 ± 0.04	0.18 ± 0.03
F130	J015109.13+641421.8	129.36	2.12	15.68	0.58	0.48	−17	14.27 ± 0.03	0.33 ± 0.05	0.08 ± 0.06
F131	J015213.08+624813.6	129.81	0.75	13.04	0.40	0.34	−8	12.11 ± 0.02	0.12 ± 0.03	0.11 ± 0.03
F132	J015221.93+635739.6	129.56	1.88	14.26	0.62	0.60	−31	12.79 ± 0.02	0.27 ± 0.04	0.30 ± 0.04
F133	J015226.33+631840.1	129.72	1.25	15.66	0.79	0.50	−14	13.62 ± 0.02	0.74 ± 0.04	0.58 ± 0.04
F134	J015307.22+650110.4	129.39	2.92	13.98	0.42	0.37	−11	12.97 ± 0.02	0.20 ± 0.04	0.11 ± 0.04
F135	J015314.56+620241.5	130.11	0.04	12.85	0.40	0.30	−5	11.88 ± 0.02	0.17 ± 0.04	0.07 ± 0.03
F136	J015329.19+643128.1	129.54	2.45	13.98	0.36	0.27	−3	13.12 ± 0.02	0.11 ± 0.03	0.11 ± 0.04
F137	J015427.15+612204.7	130.41	-0.59	14.28	1.07	0.84	−48	11.55 ± 0.02	0.57 ± 0.03	0.51 ± 0.02

Table 2.1: Continued

#	IPHAS	ℓ	b	r	$(r-i)$	$(r-\mathrm{H}\alpha)$	$EW(\mathrm{H}\alpha)_\mathrm{P}$	J	$(J-H)$	$(H-K)$
	Jhhmmss.ss+ddmmss.s	(deg)	(deg)	(mag)	(mag)	(mag)	(Å)	(mag)	(mag)	(mag)
F138	J015510.44+632108.5	130.01	1.36	15.81	0.53	0.39	−10	14.46 ± 0.02	0.14 ± 0.05	0.20 ± 0.07
F139	J015520.62+611752.8	130.53	-0.63	13.37	0.48	0.43	−15	12.24 ± 0.02	0.17 ± 0.03	0.14 ± 0.02
F140	J015524.75+615836.1	130.37	0.03	14.95	0.56	0.44	−13			
F141	J015526.12+625056.4	130.16	0.88	14.31	0.56	0.62	−34	13.11 ± 0.02	0.25 ± 0.03	0.28 ± 0.03
F142	J015601.25+633944.1	130.02	1.68	14.59	0.59	0.51	−20	13.14 ± 0.02	0.18 ± 0.03	0.22 ± 0.04
F143	J015613.22+635623.8	129.97	1.96	14.05	0.47	0.63	−39	12.82 ± 0.03	0.31 ± 0.04	0.33 ± 0.04
F144	J015627.82+612939.2	130.61	-0.40	12.62	0.43	0.49	−23	11.49 ± 0.02	0.23 ± 0.03	0.17 ± 0.03
F145	J015630.87+630307.5	130.23	1.11	13.27	0.27	0.50	−30	12.52 ± 0.02	0.10 ± 0.03	0.08 ± 0.03
F146	J015644.71+653640.6	129.61	3.59	14.99	0.53	0.37	−7	13.70 ± 0.02	0.14 ± 0.03	0.11 ± 0.04
F147	J015645.75+635259.8	130.05	1.92	13.11	0.58	0.54	−24	11.67 ± 0.02	0.27 ± 0.02	0.22 ± 0.02
F148	J015650.51+645341.1	129.80	2.90	15.46	0.43	0.42	−15	14.31 ± 0.03	0.20 ± 0.05	-0.04 ± 0.06
F149	J015701.97+623930.5	130.38	0.74	16.70	1.45	0.91	−47	12.95 ± 0.02	0.99 ± 0.03	0.43 ± 0.03
F150	J015738.22+622231.1	130.52	0.48	17.13	1.30	0.90	−50	13.67 ± 0.02	1.06 ± 0.03	0.70 ± 0.03
F151	J015741.35+605313.7	130.91	-0.95	14.75	0.72	0.51	−16	13.06 ± 0.02	0.31 ± 0.03	0.17 ± 0.03
F152	J015804.46+653020.6	129.77	3.52	13.06	0.37	0.33	−7	12.15 ± 0.02	0.12 ± 0.03	0.17 ± 0.03
F153	J015808.43+610256.8	130.92	-0.78	16.17	1.22	0.73	−28	12.98 ± 0.02	0.66 ± 0.03	0.38 ± 0.03
F154	J015809.04+615813.6	130.68	0.11	14.55	0.70	0.57	−25	12.92 ± 0.02	0.29 ± 0.03	0.24 ± 0.03
F155	J015832.88+640633.9	130.18	2.19	16.00	0.51	0.63	−37	14.60 ± 0.02	0.29 ± 0.05	0.28 ± 0.06
F156	J015918.32+654955.8	129.81	3.87	15.14	0.53	0.50	−21	13.80 ± 0.02	0.24 ± 0.03	0.16 ± 0.04
F157	J015919.69+645053.4	130.07	2.92	12.78	0.37	0.48	−24	11.88 ± 0.02	0.24 ± 0.03	0.16 ± 0.03
F158	J015922.53+635829.3	130.30	2.08	15.06	0.54	0.79	−60	13.37 ± 0.02	0.45 ± 0.03	0.36 ± 0.03
F159	J015938.99+643615.4	130.17	2.69	13.24	0.43	0.52	−27	12.10 ± 0.02	0.27 ± 0.03	0.22 ± 0.03
F160	J015945.33+630314.9	130.58	1.20	14.62	0.53	0.39	−9	13.04 ± 0.02	0.25 ± 0.04	0.12 ± 0.04
F161	J020037.84+652133.9	130.07	3.45	13.08	0.37	0.29	−4	12.11 ± 0.02	0.21 ± 0.03	0.14 ± 0.03
F162	J020049.43+635944.0	130.45	2.14	14.01	0.65	0.64	−34	12.39 ± 0.02	0.28 ± 0.03	0.31 ± 0.03
F163	J020105.33+613403.0	131.12	-0.19	14.47	0.66	0.68	−39	12.78 ± 0.02	0.37 ± 0.03	0.31 ± 0.03
F164	J020109.65+641219.4	130.43	2.35	14.53	0.40	0.35	−9	13.42 ± 0.02	0.30 ± 0.03	0.13 ± 0.04
F165	J020111.63+612826.7	131.16	-0.28	15.17	0.64	0.73	−48	13.38 ± 0.03	0.35 ± 0.04	0.30 ± 0.04

Table 2.1: Continued

#	IPHAS	ℓ	b	r	$(r-i)$	$(r-\mathrm{H}\alpha)$	$EW(\mathrm{H}\alpha)_\mathrm{P}$	J	$(J-H)$	$(H-K)$
	Jhhmmss.ss+ddmmss.s	(deg)	(deg)	(mag)	(mag)	(mag)	(Å)	(mag)	(mag)	(mag)
F166	J020121.79+630117.3	130.77	1.22	13.34	0.44	0.35	-8	12.26 ± 0.02	0.14 ± 0.04	0.13 ± 0.04
F167	J020136.00+613207.6	131.19	-0.21	13.15	0.45	0.38	-11	11.93 ± 0.02	0.19 ± 0.04	0.15 ± 0.04
F168	J020202.55+625018.2	130.89	1.06	16.80	0.82	0.54	-17	14.58 ± 0.05	0.46 ± 0.08	0.22 ± 0.09
F169	J020203.16+630213.4	130.84	1.25	13.42	0.77	0.73	-42	11.62 ± 0.02	0.40 ± 0.04	0.36 ± 0.04
F170	J020252.26+620926.0	131.17	0.43	15.22	0.61	0.57	-27	12.91 ± 0.03	0.45 ± 0.05	0.28 ± 0.06
F171	J020326.01+635943.1	130.72	2.22	14.41	0.56	0.49	-19	13.00 ± 0.02	0.22 ± 0.04	0.22 ± 0.04
F172	J020328.03+624333.8	131.08	1.00	13.76	0.46	0.40	-13	12.55 ± 0.02	0.15 ± 0.04	0.14 ± 0.04
F173	J020407.85+643122.2	130.65	2.75	13.94	0.36	0.39	-14	12.98 ± 0.02	0.19 ± 0.03	0.12 ± 0.04
F174	J020504.17+630216.1	131.17	1.35	15.10	0.60	0.44	-13	13.68 ± 0.03	0.36 ± 0.05	0.13 ± 0.04
F175	J020547.47+641051.7	130.92	2.47	12.63	0.38	0.38	-13	11.80 ± 0.02	0.17 ± 0.03	0.12 ± 0.03
F176	J020618.67+644945.1	130.79	3.11	14.79	0.39	0.54	-30	13.85 ± 0.03	0.20 ± 0.05	0.15 ± 0.06
F177	J020649.26+645826.9	130.80	3.26	14.42	0.55	0.37	-7			
F178	J020707.67+612422.7	131.86	-0.15	13.25	0.40	0.32	-5	12.27 ± 0.02	0.09 ± 0.03	0.16 ± 0.04
F179	J020717.23+645046.2	130.88	3.15	12.51	0.34	0.50	-27	11.63 ± 0.02	0.18 ± 0.04	0.16 ± 0.04
F180	J020731.12+634520.4	131.22	2.12	14.58	0.71	0.45	-11	12.78 ± 0.02	0.36 ± 0.04	0.18 ± 0.04
F181	J020734.24+623601.1	131.56	1.01	14.42	0.60	0.44	-12	12.98 ± 0.02	0.27 ± 0.04	0.18 ± 0.04
F182	J020753.51+644148.9	130.99	3.03	15.89	0.36	0.33	-8	14.89 ± 0.04	0.19 ± 0.07	0.08 ± 0.12
F183	J020817.76+614220.1	131.91	0.18	13.39	0.56	0.56	-27	11.82 ± 0.02	0.32 ± 0.03	0.26 ± 0.04
F184	J020826.27+625745.9	131.55	1.39	14.39	0.68	0.53	-20	12.64 ± 0.02	0.28 ± 0.04	0.24 ± 0.04
F185	J020837.59+652028.2	130.87	3.67	14.69	0.56	0.52	-23	13.34 ± 0.02	0.25 ± 0.04	0.17 ± 0.04
F186	J020850.76+623246.6	131.72	1.00	14.26	0.75	0.77	-49	12.35 ± 0.02	0.38 ± 0.04	0.31 ± 0.04
F187	J020855.24+631501.1	131.52	1.68	12.35	0.35	0.38	-13	11.60 ± 0.03	0.16 ± 0.04	0.16 ± 0.04
F188	J020859.72+635536.1	131.33	2.33	15.00	0.53	0.38	-8	13.68 ± 0.03	0.19 ± 0.05	0.18 ± 0.05
F189	J020917.87+613045.2	132.08	0.03	13.84	0.82	0.54	-17	11.91 ± 0.02	0.34 ± 0.04	0.23 ± 0.03
F190	J021000.05+640838.5	131.37	2.57	12.79	0.37	0.35	-10	11.84 ± 0.02	0.17 ± 0.03	0.13 ± 0.03
F191	J021002.71+612413.5	132.19	-0.05	16.20	0.92	0.54	-14	13.92 ± 0.02	0.49 ± 0.04	0.35 ± 0.04
F192	J021005.63+631100.3	131.67	1.65	16.06	0.57	0.38	-8	14.64 ± 0.02	0.27 ± 0.05	0.08 ± 0.08
F193	J021008.60+653741.4	130.94	3.99	16.54	1.01	0.59	-18	14.15 ± 0.02	0.61 ± 0.04	0.38 ± 0.05

Table 2.1: Continued

#	IPHAS	ℓ	b	r	$(r-i)$	$(r-\mathrm{H}\alpha)$	$EW(\mathrm{H}\alpha)_\mathrm{P}$	J	$(J-H)$	$(H-K)$
	Jhhmmss.ss+ddmmss.s	(deg)	(deg)	(mag)	(mag)	(mag)	(Å)	(mag)	(mag)	(mag)
F194	J021011.09+652230.2	131.02	3.75	13.78	0.60	0.53	−22	12.37 ± 0.02	0.27 ± 0.03	0.14 ± 0.03
F195	J021036.32+611444.0	132.31	-0.18	13.07	0.56	0.42	−11	11.66 ± 0.02	0.26 ± 0.03	0.17 ± 0.03
F196	J021057.06+624700.8	131.88	1.30	13.98	0.50	0.34	−5	12.73 ± 0.02	0.29 ± 0.03	0.08 ± 0.03
F197	J021121.67+624707.5	131.92	1.32	15.54	0.67	0.50	−18	13.93 ± 0.03	0.35 ± 0.05	0.25 ± 0.05
F198	J021128.86+634604.0	131.64	2.26	13.95	0.56	0.40	−10	12.54 ± 0.02	0.22 ± 0.03	0.15 ± 0.03
F199	J021159.14+615639.9	132.25	0.54	14.99	0.89	0.68	−31	12.79 ± 0.02	0.43 ± 0.03	0.27 ± 0.03
F200	J021202.03+613230.4	132.38	0.16	15.44	0.90	0.59	−20	13.27 ± 0.02	0.39 ± 0.03	0.36 ± 0.03
F201	J021210.42+623242.3	132.09	1.12	12.17	0.37	0.45	−20	11.33 ± 0.02	0.13 ± 0.03	0.17 ± 0.03
F202	J021320.12+613003.1	132.54	0.17	12.97	0.61	0.57	−27	11.26 ± 0.02	0.28 ± 0.03	0.23 ± 0.03
F203	J021325.98+622043.1	132.29	0.97	14.46	0.77	0.59	−25	12.56 ± 0.02	0.49 ± 0.03	0.37 ± 0.03
F204	J021336.53+601829.1	132.94	-0.96	13.73	0.61	0.38	−6	12.18 ± 0.02	0.26 ± 0.03	0.15 ± 0.03
F205	J021352.00+642520.3	131.68	2.96	15.03	0.48	0.39	−11	13.96 ± 0.03	0.20 ± 0.04	0.19 ± 0.05
F206	J021415.12+635857.1	131.86	2.56	16.02	0.64	0.49	−18	14.33 ± 0.03	0.19 ± 0.05	0.33 ± 0.07
F207	J021448.45+622622.6	132.41	1.11	12.86	0.64	0.51	−19	11.13 ± 0.02	0.88 ± 0.03	1.08 ± 0.02
F208	J021500.45+614141.5	132.67	0.41	16.12	0.92	0.67	−29	13.41 ± 0.02	0.49 ± 0.03	0.37 ± 0.03
F209	J021532.96+623236.9	132.46	1.24	13.05	0.63	0.61	−31	11.45 ± 0.02	0.32 ± 0.03	0.25 ± 0.03
F210	J021630.48+605758.6	133.07	-0.22	15.02	1.03	0.95	−66	12.30 ± 0.02	0.59 ± 0.03	0.55 ± 0.03
F211	J021647.40+642812.9	131.97	3.11	14.56	0.50	0.46	−18	13.28 ± 0.02	0.20 ± 0.04	0.23 ± 0.04
F212	J021744.41+644335.2	131.98	3.38	13.71	0.57	0.63	−36	12.22 ± 0.02	0.29 ± 0.03	0.27 ± 0.03
F213	J021747.84+643419.9	132.04	3.24	14.65	0.57	0.62	−34	13.14 ± 0.03	0.28 ± 0.04	0.27 ± 0.03
F214	J021809.82+635254.9	132.30	2.60	14.27	0.68	0.45	−12			
F215	J021848.02+605515.5	133.35	-0.17	14.54	0.92	0.80	−47	11.95 ± 0.03	0.68 ± 0.04	0.45 ± 0.04
F216	J022009.76+643605.9	132.27	3.35	15.67	0.57	0.43	−13	14.27 ± 0.03	0.29 ± 0.05	0.17 ± 0.07
F217	J022025.02+600114.0	133.84	-0.95	13.28	0.44	0.49	−23			
F218	J022033.45+625717.4	132.86	1.81	15.75	0.71	0.86	−63	13.90 ± 0.02	0.40 ± 0.04	0.45 ± 0.04
F219	J022045.25+631642.8	132.78	2.13	15.07	0.50	0.48	−19	13.85 ± 0.03	0.22 ± 0.04	0.22 ± 0.05
F220	J022053.65+642835.6	132.38	3.26	15.96	0.51	0.53	−26	14.28 ± 0.03	0.31 ± 0.05	0.20 ± 0.06
F221	J022100.28+635435.2	132.59	2.73	13.15	0.42	0.38	−11	12.11 ± 0.02	0.13 ± 0.04	0.13 ± 0.04

Table 2.1: Continued

#	IPHAS	ℓ	b	r	$(r-i)$	$(r-\mathrm{H}\alpha)$	$EW(\mathrm{H}\alpha)_\mathrm{P}$	J	$(J-H)$	$(H-K)$
	Jhhmmss.ss+ddmmss.s	(deg)	(deg)	(mag)	(mag)	(mag)	(Å)	(mag)	(mag)	(mag)
F222	J022107.83+625754.6	132.92	1.85	14.96	0.68	0.58	−26	13.23 ± 0.03	0.31 ± 0.04	0.36 ± 0.05
F223	J022222.78+623841.9	133.17	1.59	15.27	0.64	0.44	−11	13.54 ± 0.02	0.33 ± 0.04	0.20 ± 0.04
F224	J022227.73+623530.6	133.19	1.55	14.39	0.46	0.71	−50	13.12 ± 0.03	0.23 ± 0.04	0.16 ± 0.04
F225	J022242.60+622334.5	133.29	1.37	16.06	0.62	0.49	−18	14.34 ± 0.05	0.31 ± 0.08	0.24 ± 0.09
F226	J022333.64+610950.6	133.81	0.25	15.96	0.90	0.62	−24	13.42 ± 0.02	0.83 ± 0.03	1.00 ± 0.02
F227	J022337.05+601602.8	134.13	-0.59	14.00	0.57	0.50	−20	12.54 ± 0.02	0.25 ± 0.02	0.16 ± 0.03
F228	J022343.45+603545.6	134.02	-0.27	12.98	0.69	0.48	−14	11.24 ± 0.02	0.26 ± 0.04	0.19 ± 0.05
F229	J022420.68+624842.5	133.32	1.83	13.52	0.65	0.52	−19	11.74 ± 0.02	0.32 ± 0.03	0.18 ± 0.03
F230	J022423.64+604156.7	134.07	-0.15	16.26	0.81	0.53	−17	13.71 ± 0.02	1.03 ± 0.03	0.93 ± 0.03
F231	J022431.47+623334.4	133.43	1.60	15.45	0.60	0.52	−22	13.35 ± 0.02	0.80 ± 0.03	0.88 ± 0.02
F232	J022502.69+644947.6	132.68	3.74	13.32	0.58	0.46	−15	11.80 ± 0.02	0.26 ± 0.03	0.19 ± 0.03
F233	J022618.80+615952.8	133.82	1.15	14.84	0.77	0.55	−19	12.44 ± 0.02	0.70 ± 0.03	0.81 ± 0.03
F234	J022635.99+601401.8	134.49	-0.49	14.54	0.94	0.99	−77	12.13 ± 0.02	0.56 ± 0.02	0.49 ± 0.03
F235	J022718.63+601525.1	134.56	-0.43	13.06	0.60	0.40	−8	11.46 ± 0.02	0.58 ± 0.02	0.11 ± 0.03
F236	J022744.58+614030.0	134.09	0.91	15.51	1.33	0.94	−55	12.10 ± 0.02	0.69 ± 0.03	0.53 ± 0.03
F237	J022821.67+641216.0	133.24	3.29	15.80	0.58	0.49	−18	14.16 ± 0.02	0.22 ± 0.04	0.27 ± 0.05
F238	J022823.86+631834.8	133.57	2.46	12.82	0.54	0.64	−38	11.45 ± 0.02	0.28 ± 0.02	0.30 ± 0.02
F239	J022913.58+633224.5	133.57	2.71	13.79	0.74	0.54	−19	11.61 ± 0.02	0.64 ± 0.02	0.28 ± 0.02
F240	J022935.91+611556.8	134.45	0.61	13.78	0.83	1.05	−93	11.14 ± 0.02	1.22 ± 0.03	0.97 ± 0.02
F241	J022942.32+644857.2	133.15	3.91	13.83	0.65	0.81	−58	12.20 ± 0.02	0.34 ± 0.03	0.30 ± 0.03
F242	J022953.82+630742.3	133.79	2.35	14.31	0.66	0.50	−17	12.85 ± 0.02	0.22 ± 0.03	0.15 ± 0.03
F243	J023003.21+643829.4	133.25	3.76	15.30	0.55	0.53	−24	13.84 ± 0.02	0.17 ± 0.04	0.24 ± 0.05
F244	J023031.39+594127.1	135.14	-0.81	14.49	0.57	0.43	−12	12.96 ± 0.02	0.31 ± 0.04	0.17 ± 0.04
F245	J023035.11+610005.9	134.66	0.41	14.54	0.65	0.46	−14	12.61 ± 0.02	0.42 ± 0.03	0.39 ± 0.03
F246	J023150.04+604952.4	134.86	0.31	13.88	0.44	0.32	−5	12.75 ± 0.02	0.19 ± 0.03	0.12 ± 0.03
F247	J023202.89+641033.2	133.62	3.41	16.19	0.63	0.42	−10	14.47 ± 0.03	0.25 ± 0.05	0.32 ± 0.07
F248	J023235.10+640522.7	133.71	3.35	13.48	0.70	0.75	−48	11.62 ± 0.02	0.33 ± 0.02	0.27 ± 0.03
F249	J023250.45+612857.4	134.73	0.96	14.45	0.85	0.53	−15	12.17 ± 0.02	0.75 ± 0.02	0.51 ± 0.02

Table 2.1: Continued

#	IPHAS Jhhmmss.ss+ddmmss.s	ℓ (deg)	b (deg)	r (mag)	$(r-i)$ (mag)	$(r-\mathrm{H}\alpha)$ (mag)	$EW(\mathrm{H}\alpha)_\mathrm{P}$ (Å)	J (mag)	$(J-H)$ (mag)	$(H-K)$ (mag)
F250	J023322.55+612718.2	134.80	0.95	16.49	1.16	0.90	−53	13.35 ± 0.02	1.08 ± 0.03	0.73 ± 0.02
F251	J023336.63+613848.4	134.75	1.14	16.45	0.97	0.65	−25	13.88 ± 0.02	0.96 ± 0.04	0.56 ± 0.03
F252	J023404.70+605914.4	135.06	0.55	12.91	0.62	0.66	−38	11.30 ± 0.02	0.42 ± 0.03	0.51 ± 0.03
F253	J023410.28+612440.4	134.90	0.95	13.64	0.67	1.19	−131	11.44 ± 0.02	1.02 ± 0.03	0.90 ± 0.03
F254	J023411.97+595634.2	135.47	-0.40	13.17	0.60	0.56	−27	11.65 ± 0.02	0.28 ± 0.03	0.23 ± 0.03
F255	J023431.08+601616.8	135.38	-0.08	13.62	1.10	0.80	−42	10.77 ± 0.02	0.55 ± 0.03	0.48 ± 0.04
F256	J023439.79+641813.4	133.83	3.64	16.95	0.70	0.50	−17	15.11 ± 0.04	0.28 ± 0.09	0.26 ± 0.11
F257	J023503.66+615452.4	134.81	1.46	16.77	0.94	0.89	−59	14.06 ± 0.03	0.88 ± 0.04	0.60 ± 0.04
F258	J023515.33+614803.3	134.87	1.36	16.74	1.08	1.12	−94	13.54 ± 0.03	1.03 ± 0.04	0.74 ± 0.04
F259	J023536.82+625251.7	134.49	2.37	16.71	0.57	0.46	−15	14.96 ± 0.06	0.31 ± 0.11	0.23 ± 0.13
F260	J023558.18+604457.8	135.36	0.43	16.10	0.84	0.63	−27			
F261	J023629.19+634245.8	134.25	3.17	15.64	0.60	0.61	−33	13.92 ± 0.02	0.32 ± 0.04	0.37 ± 0.05
F262	J023642.66+614714.9	135.03	1.41	15.44	0.56	0.39	−8	13.95 ± 0.05	0.33 ± 0.07	0.14 ± 0.06
F263	J023753.78+620410.0	135.05	1.73	12.98	0.52	0.37	−8	11.58 ± 0.02	0.27 ± 0.03	0.26 ± 0.03
F264	J023758.11+634635.6	134.38	3.30	13.28	0.30	0.34	−11	12.34 ± 0.02	0.18 ± 0.03	0.07 ± 0.03
F265	J023809.91+620224.6	135.09	1.71	13.16	0.56	0.45	−15	11.71 ± 0.02	0.30 ± 0.02	0.19 ± 0.02
F266	J023841.80+640826.3	134.30	3.66	14.03	0.58	0.48	−17	12.38 ± 0.02	0.30 ± 0.03	0.17 ± 0.03
F267	J023853.36+594924.4	136.06	-0.28	16.09	1.00	0.68	−28	13.46 ± 0.02	0.49 ± 0.02	0.31 ± 0.03
F268	J023923.65+604247.4	135.76	0.56	13.35	0.46	0.53	−27			
F269	J023948.17+604505.1	135.79	0.61	13.30	0.39	0.43	−17	12.28 ± 0.02	0.21 ± 0.03	0.12 ± 0.03
F270	J023950.94+611829.2	135.57	1.12	13.96	0.48	0.61	−36	12.08 ± 0.02	1.02 ± 0.03	0.88 ± 0.02
F271	J024054.96+630009.7	134.99	2.72	15.72	0.43	0.53	−28	14.36 ± 0.02	0.29 ± 0.05	0.21 ± 0.07
F272	J024111.95+605125.4	135.90	0.78	15.88	0.60	0.47	−16	13.74 ± 0.03	1.13 ± 0.04	0.94 ± 0.03
F273	J024146.73+602532.5	136.14	0.42	14.06	0.64	0.70	−42	12.31 ± 0.02	0.30 ± 0.03	0.25 ± 0.03
F274	J024147.73+601109.1	136.24	0.20	16.08	1.28	1.15	−92	12.53 ± 0.02	0.70 ± 0.03	0.56 ± 0.03
F275	J024159.21+600106.0	136.34	0.06	14.56	0.69	0.55	−23	12.80 ± 0.02	0.29 ± 0.03	0.21 ± 0.03
F276	J024221.54+593716.4	136.54	-0.29	13.36	0.61	0.47	−16	11.67 ± 0.02	0.23 ± 0.03	0.26 ± 0.03
F277	J024252.58+611953.8	135.89	1.30	15.75	0.70	0.91	−72	13.95 ± 0.03	0.36 ± 0.05	0.37 ± 0.05

Table 2.1: Continued

#	IPHAS Jhhmmss.ss+ddmmss.s	ℓ (deg)	b (deg)	r (mag)	$(r-i)$ (mag)	$(r-\mathrm{H}\alpha)$ (mag)	$EW(\mathrm{H}\alpha)_\mathrm{P}$ (Å)	J (mag)	$(J-H)$ (mag)	$(H-K)$ (mag)
F278	J024305.60+631614.7	135.10	3.07	14.59	0.45	0.62	−38	13.27 ± 0.02	0.27 ± 0.03	0.31 ± 0.04
F279	J024317.67+603205.6	136.27	0.59	13.69	0.67	0.71	−43	11.98 ± 0.03	0.32 ± 0.04	0.26 ± 0.04
F280	J024326.34+590631.1	136.88	-0.70	16.57	1.03	1.22	−118	13.68 ± 0.03	0.95 ± 0.04	0.54 ± 0.03
F281	J024332.05+632150.1	135.11	3.17	14.22	0.37	0.47	−23	12.98 ± 0.02	0.21 ± 0.03	0.14 ± 0.03
F282	J024339.29+622328.8	135.53	2.30	14.24	0.77	0.58	−23	12.02 ± 0.02	0.56 ± 0.03	0.25 ± 0.02
F283	J024405.38+621448.6	135.64	2.19	15.24	0.44	0.46	−20	13.80 ± 0.02	0.49 ± 0.03	0.49 ± 0.04
F284	J024430.40+604829.2	136.29	0.90	15.56	0.92	0.69	−33	12.91 ± 0.02	0.49 ± 0.03	0.37 ± 0.03
F285	J024439.54+605954.8	136.23	1.08	16.16	0.94	1.13	−101	13.17 ± 0.03	1.07 ± 0.04	0.85 ± 0.04
F286	J024454.00+635608.0	135.01	3.76	15.76	0.51	0.59	−33	14.25 ± 0.02	0.23 ± 0.05	0.22 ± 0.06
F287	J024504.86+612502.1	136.09	1.48	15.38	0.59	0.58	−29	13.81 ± 0.02	0.35 ± 0.04	0.21 ± 0.04
F288	J024506.09+611409.1	136.17	1.32	15.97	0.69	0.79	−53	14.12 ± 0.02	0.35 ± 0.03	0.31 ± 0.04
F289	J024509.54+612523.5	136.10	1.49	15.05	0.54	0.78	−57	13.37 ± 0.02	0.41 ± 0.04	0.38 ± 0.04
F290	J024519.10+633755.1	135.18	3.50	14.04	0.46	0.68	−46	12.74 ± 0.02	0.30 ± 0.03	0.26 ± 0.03
F291	J024521.28+625416.2	135.49	2.84	13.65	0.37	0.45	−20	12.48 ± 0.02	0.19 ± 0.03	0.16 ± 0.03
F292	J024540.61+592151.2	137.03	-0.34	13.26	0.43	0.55	−30	11.99 ± 0.02	0.23 ± 0.03	0.20 ± 0.04
F293	J024553.87+635414.7	135.12	3.77	14.20	0.60	0.57	−28	12.48 ± 0.02	0.34 ± 0.03	0.30 ± 0.03
F294	J024618.12+613514.8	136.15	1.70	15.60	0.47	0.55	−29	14.33 ± 0.03	0.27 ± 0.04	0.13 ± 0.05
F295	J024735.56+615530.9	136.15	2.07	13.46	0.36	0.37	−12	12.29 ± 0.02	0.23 ± 0.03	0.12 ± 0.03
F296	J024748.62+605750.5	136.59	1.22	13.94	0.48	0.84	−70	12.04 ± 0.02	1.10 ± 0.03	0.98 ± 0.03
F297	J024753.07+613405.8	136.33	1.76	14.35	0.63	0.62	−33	12.61 ± 0.02	0.40 ± 0.03	0.27 ± 0.03
F298	J024758.73+630156.8	135.71	3.09	14.74	0.52	0.72	−49	13.24 ± 0.02	0.36 ± 0.03	0.30 ± 0.03
F299	J024823.01+614728.1	136.29	1.99	12.86	0.38	0.48	−24	11.72 ± 0.02	0.23 ± 0.03	0.13 ± 0.03
F300	J024823.69+614107.2	136.34	1.90	13.92	0.35	0.54	−32	12.75 ± 0.02	0.29 ± 0.03	0.24 ± 0.03
F301	J024838.04+630153.0	135.77	3.12	15.25	0.41	0.65	−44	13.89 ± 0.03	0.23 ± 0.05	0.18 ± 0.06
F302	J024913.93+631042.4	135.77	3.28	13.20	0.33	0.53	−31	12.04 ± 0.03	0.25 ± 0.05	0.27 ± 0.06
F303	J024928.47+595248.4	137.24	0.33	13.34	0.79	0.73	−41	11.25 ± 0.02	0.47 ± 0.03	0.41 ± 0.03
F304	J024940.66+621424.8	136.23	2.46	13.06	0.29	0.38	−16	12.36 ± 0.02	0.13 ± 0.04	0.12 ± 0.04
F305	J024953.34+601328.3	137.14	0.66	16.70	0.93	1.31	−145	13.72 ± 0.03	0.99 ± 0.05	0.77 ± 0.04

Table 2.1: Continued

#	IPHAS Jhhmmss.ss+ddmmss.s	ℓ (deg)	b (deg)	r (mag)	$(r-i)$ (mag)	$(r-\mathrm{H}\alpha)$ (mag)	$EW(\mathrm{H}\alpha)_\mathrm{P}$ (Å)	J (mag)	$(J-H)$ (mag)	$(H-K)$ (mag)
F306	J025002.27+620135.9	136.36	2.29	15.86	0.57	1.26	−153	14.01 ± 0.03	0.42 ± 0.05	0.44 ± 0.05
F307	J025016.66+624435.6	136.07	2.94	14.53	0.40	0.35	−9	13.21 ± 0.02	0.24 ± 0.04	0.11 ± 0.04
F308	J025059.14+615648.7	136.50	2.27	15.32	0.38	0.61	−40	14.16 ± 0.03	0.21 ± 0.04	0.22 ± 0.05
F309	J025102.22+615733.8	136.50	2.28	14.10	0.44	0.72	−52	12.70 ± 0.02	0.30 ± 0.04	0.37 ± 0.04
F310	J025129.48+602122.1	137.26	0.87	16.94	0.84	0.72	−39			
F311	J025130.43+621052.2	136.45	2.50	15.85	0.47	0.76	−57	13.98 ± 0.03	0.91 ± 0.04	0.93 ± 0.04
F312	J025136.03+601557.5	137.31	0.79	15.72	0.42	0.46	−21	14.16 ± 0.03	0.50 ± 0.05	0.37 ± 0.05
F313	J025138.00+601824.9	137.30	0.83	16.84	0.90	0.84	−53	13.90 ± 0.03	0.88 ± 0.04	0.47 ± 0.04
F314	J025200.23+621145.2	136.49	2.54	13.88	0.38	0.47	−23	12.65 ± 0.02	0.22 ± 0.04	0.16 ± 0.04
F315	J025204.14+583423.4	138.12	-0.70	12.96	0.34	0.46	−22	11.84 ± 0.02	0.17 ± 0.03	0.17 ± 0.03
F316	J025233.25+615902.2	136.64	2.38	14.82	0.43	0.35	−8	13.60 ± 0.03	0.14 ± 0.05	0.22 ± 0.06
F317	J025324.51+614622.9	136.83	2.24	15.47	0.54	0.60	−32	13.79 ± 0.03	0.29 ± 0.05	0.42 ± 0.06
F318	J025409.07+604035.9	137.41	1.30	15.28	0.74	0.55	−21	13.14 ± 0.02	0.77 ± 0.04	0.46 ± 0.04
F319	J025448.84+605832.0	137.34	1.60	16.13	0.76	0.55	−21	13.90 ± 0.03	0.41 ± 0.05	0.32 ± 0.05
F320	J025500.93+603843.9	137.51	1.32	16.85	0.92	0.91	−63	14.26 ± 0.02	0.91 ± 0.04	0.39 ± 0.05
F321	J025502.19+604017.5	137.50	1.35	16.87	0.81	0.74	−42	14.51 ± 0.03	0.77 ± 0.05	0.54 ± 0.05
F322	J025516.98+603802.2	137.55	1.33	16.55	0.97	0.75	−39	13.72 ± 0.03	0.95 ± 0.04	0.60 ± 0.04
F323	J025544.62+610311.0	137.41	1.72	16.85	0.82	0.80	−51	14.41 ± 0.03	0.55 ± 0.05	0.41 ± 0.06
F324	J025610.40+580629.6	138.81	-0.87	13.79	0.55	0.45	−15	12.30 ± 0.02	0.20 ± 0.03	0.15 ± 0.03
F325	J025625.38+610732.2	137.45	1.83	14.44	0.97	0.91	−62	11.86 ± 0.02	0.63 ± 0.03	0.49 ± 0.03
F326	J025631.47+593648.4	138.16	0.49	15.01	0.72	0.74	−45	13.26 ± 0.02	0.36 ± 0.03	0.36 ± 0.03
F327	J025700.49+575742.8	138.98	-0.94	14.26	0.62	0.59	−29	12.60 ± 0.02	0.24 ± 0.03	0.15 ± 0.03
F328	J025704.88+584311.7	138.63	-0.27	16.22	0.80	0.54	−18	14.13 ± 0.02	0.43 ± 0.03	0.21 ± 0.04
F329	J025737.78+624703.4	136.80	3.36	14.70	0.46	0.31	−4	13.53 ± 0.02	0.23 ± 0.04	0.15 ± 0.05
F330	J025825.01+605331.8	137.77	1.73	16.58	0.95	0.68	−29	14.01 ± 0.03	0.69 ± 0.05	0.26 ± 0.05
F331	J025859.45+603118.5	138.00	1.44	16.91	0.99	0.67	−27	14.08 ± 0.03	0.92 ± 0.04	0.57 ± 0.04
F332	J025904.88+621459.5	137.20	2.97	15.60	0.40	0.35	−9	14.48 ± 0.03	0.21 ± 0.07	0.17 ± 0.09
F333	J025905.15+605404.2	137.84	1.78	12.93	0.58	0.78	−57	10.82 ± 0.02	1.17 ± 0.03	0.98 ± 0.03

Table 2.1: Continued

#	IPHAS	ℓ	b	r	$(r-i)$	$(r-\mathrm{H}\alpha)$	$EW(\mathrm{H}\alpha)_\mathrm{P}$	J	$(J-H)$	$(H-K)$
	Jhhmmss.ss+ddmmss.s	(deg)	(deg)	(mag)	(mag)	(mag)	(Å)	(mag)	(mag)	(mag)
F334	J025935.04+603207.2	138.06	1.48	13.88	0.42	0.52	−27	12.52 ± 0.02	0.27 ± 0.04	0.21 ± 0.04
F335	J025946.50+602906.6	138.11	1.45	15.02	0.73	0.55	−21	12.96 ± 0.02	0.65 ± 0.04	0.62 ± 0.04
F336	J025950.85+582333.1	139.10	-0.39	14.00	0.58	0.95	−84	12.09 ± 0.02	0.62 ± 0.03	0.41 ± 0.03
F337	J025959.45+582929.5	139.07	-0.29	13.23	0.57	0.48	−18	11.69 ± 0.02	0.31 ± 0.03	0.13 ± 0.03
F338	J030001.93+610013.4	137.89	1.92	14.70	1.05	0.79	−42	11.71 ± 0.02	0.62 ± 0.03	0.54 ± 0.04
F339	J030002.63+621036.3	137.33	2.96	17.20	0.48	0.42	−14			
F340	J030010.27+613223.2	137.65	2.40	13.70	0.51	0.44	−15	12.49 ± 0.02	0.11 ± 0.04	0.34 ± 0.04
F341	J030023.55+601755.2	138.26	1.32	16.61	1.09	0.73	−31	13.38 ± 0.02	0.91 ± 0.04	0.52 ± 0.04
F342	J030042.46+601106.0	138.35	1.24	16.93	0.63	0.47	−15	15.20 ± 0.05	0.25 ± 0.11	0.32 ± 0.14
F343	J030056.68+615940.7	137.51	2.85	13.04	0.35	0.32	−7	12.17 ± 0.02	0.13 ± 0.03	0.10 ± 0.04
F344	J030105.21+603155.4	138.23	1.57	15.78	1.00	0.96	−68	12.85 ± 0.02	0.94 ± 0.03	0.61 ± 0.03
F345	J030107.75+602921.8	138.25	1.53	17.79	1.24	0.87	−47	14.25 ± 0.03	1.21 ± 0.04	0.83 ± 0.04
F346	J030120.82+602444.9	138.31	1.48	14.36	0.56	0.50	−20	12.83 ± 0.02	0.23 ± 0.04	0.25 ± 0.04
F347	J030121.61+602856.6	138.28	1.54	13.89	0.67	0.57	−25	11.79 ± 0.02	0.98 ± 0.04	0.94 ± 0.03
F348	J030122.83+603940.3	138.20	1.70	17.66	1.02	0.80	−43	14.67 ± 0.04	0.97 ± 0.05	0.47 ± 0.05
F349	J030124.02+610221.3	138.02	2.03	14.81	0.68	0.65	−34	13.02 ± 0.02	0.32 ± 0.04	0.35 ± 0.04
F350	J030133.63+593518.5	138.73	0.77	14.05	0.70	0.73	−44	12.42 ± 0.02	0.40 ± 0.03	0.33 ± 0.02
F351	J030225.78+584156.8	139.25	0.04	16.03	0.88	0.61	−23	13.71 ± 0.02	0.41 ± 0.03	0.30 ± 0.03
F352	J030317.45+583402.0	139.42	-0.02	14.46	0.74	0.56	−22	12.51 ± 0.02	0.34 ± 0.03	0.22 ± 0.03
F353	J030331.33+585234.6	139.29	0.27	14.62	0.76	0.52	−17	12.60 ± 0.03	0.37 ± 0.05	0.16 ± 0.04
F354	J030332.31+623856.7	137.46	3.56	14.31	0.57	0.42	−12	12.80 ± 0.02	0.27 ± 0.04	0.17 ± 0.04
F355	J030422.01+574820.4	139.91	-0.62	14.32	0.62	0.57	−26	12.91 ± 0.02	0.26 ± 0.03	0.17 ± 0.03
F356	J030423.32+622900.9	137.63	3.47	13.72	0.66	0.59	−28	12.10 ± 0.02	0.31 ± 0.03	0.22 ± 0.03
F357	J030442.30+602926.7	138.64	1.75	13.67	1.20	1.03	−73	10.75 ± 0.01	0.64 ± 0.02	0.56 ± 0.02
F358	J030447.01+575832.2	139.88	-0.44	16.74	1.12	0.68	−26	13.93 ± 0.02	0.47 ± 0.04	0.35 ± 0.04
F359	J030451.26+594758.8	138.99	1.15	15.08	0.79	0.82	−54	13.06 ± 0.02	0.44 ± 0.05	0.38 ± 0.05
F360	J030501.73+585146.8	139.47	0.35	13.41	0.82	0.60	−24	11.00 ± 0.02	0.35 ± 0.03	0.32 ± 0.03
F361	J030510.86+601022.7	138.84	1.50	16.34	0.92	0.64	−26	13.47 ± 0.02	0.92 ± 0.03	0.91 ± 0.03

Table 2.1: Continued

#	IPHAS	ℓ	b	r	$(r-i)$	$(r-\mathrm{H}\alpha)$	$EW(\mathrm{H}\alpha)_{\mathrm{P}}$	J	$(J-H)$	$(H-K)$
	Jhhmmss.ss+ddmmss.s	(deg)	(deg)	(mag)	(mag)	(mag)	(Å)	(mag)	(mag)	(mag)
F362	J030539.90+610725.6	138.43	2.36	14.39	0.85	0.73	−40	12.21 ± 0.02	0.55 ± 0.03	0.32 ± 0.03
F363	J030625.00+614359.0	138.20	2.93	15.90	0.74	0.59	−26	13.90 ± 0.03	0.40 ± 0.04	0.24 ± 0.05
F364	J030711.55+593116.1	139.39	1.06	16.01	0.82	0.55	−19	13.98 ± 0.02	0.31 ± 0.04	0.25 ± 0.04
F365	J030750.47+610859.5	138.64	2.51	16.05	1.16	0.70	−27	13.48 ± 0.02	0.57 ± 0.03	0.36 ± 0.03
F366	J031046.28+593003.7	139.79	1.27	15.46	0.87	0.80	−49	12.82 ± 0.02	1.07 ± 0.04	1.10 ± 0.04
F367	J031141.73+614847.9	138.70	3.31	15.51	0.55	0.38	−8	14.00 ± 0.02	0.24 ± 0.04	0.18 ± 0.05
F368	J031208.90+605534.3	139.21	2.58	15.12	0.80	0.65	−30	12.90 ± 0.02	0.45 ± 0.03	0.41 ± 0.03
F369	J031333.27+603307.1	139.55	2.35	15.76	0.86	0.58	−20	13.69 ± 0.03	0.44 ± 0.05	0.36 ± 0.05
F370	J032342.40+613959.1	139.99	3.95	15.99	0.91	0.58	−19	13.72 ± 0.02	0.45 ± 0.04	0.33 ± 0.04

Table 2.2: Spectral classification and measures of equivalent widths from the FLWO/FAST spectra. Columns are: ID number; date of observation; Spectral classification; spectroscopic Hα equivalent width; Hβ equivalent widths; S/N at 4500 Å; measures of line ratios $W_{\lambda 4471}/W_{\lambda 4481}$. spectral type as determined from the $\log(W_{\lambda 4471}/W_{\lambda 4481})$; for the early-type stars.

#	Date Obs. yyyy-mm-dd	Group	$EW(\mathrm{H}\alpha)_S$ (Å)	$EW(\mathrm{H}\beta)$ (Å)	S/N	$\log(W_{\lambda 4471}/W_{\lambda 4481})$	SpT	CBe
F001	2009-12-11	Late(no-em)	5.9 ± 1.2	7.8 ± 2.0				
F002	2010-01-18	Featureless	-72.2 ± 2.7	-6.2 ± 9.8				
F003	2010-01-06	Early	-14.1 ± 1.3	6.0 ± 1.6	22	0.2 ± 0.2	Mid-B	✓
F004	2010-01-18	Early	-10.3 ± 1.5	8.7 ± 1.5	15	0.6 ± 0.7	Late-B	✓
F005	2010-01-18	Featureless	-36.6 ± 2.0	-2.0 ± 3.9				
F006	2010-01-18	Featureless	-59.3 ± 3.7	3.7 ± 8.7				
F007	2006-09-26	Early	-5.1 ± 1.0	8.7 ± 1.0	59	0.2 ± 0.1	B6	✓
F008	2010-09-05	Early	-21.4 ± 3.3	2.4 ± 3.3	16		Early-B	
F009	2010-09-05	Late	-20.6 ± 1.5	-4.2 ± 2.8			early-K	
F010	2010-09-05	Late	-19.6 ± 1.4	-1.8 ± 2.8			early-K	
F011[1]	2010-10-09		3.1 ± 1.3	4.6 ± 0.6				
F012	2006-09-26	Early	-20.8 ± 1.0	4.3 ± 1.0	33	0.2 ± 0.1	B6	✓
F013	2010-09-05	Early	-26.5 ± 0.8	-0.5 ± 1.0	32		Early-B	✓
F014	2010-09-05	Early	-13.8 ± 1.5	15.4 ± 1.9	19		Late-B	✓
F015	2010-10-09	Late(no-em)	4.1 ± 1.9	5.1 ± 2.8				
F016	2010-09-08	Featureless	-89.6 ± 1.8	-27.8 ± 4.4				
F017	2010-09-10	Late	-3.5 ± 1.6	2.3 ± 2.6			early-K	
F018	2006-09-26	Early	-28.6 ± 1.0	1.0 ± 1.2	33	1.7 ± 2.5	Early-B	✓
	2009-11-11	Early	-35.2 ± 1.0	1.0 ± 1.2	33	1.2 ± 1.3	Early-B	✓
F019	2010-10-09	Late	-43.9 ± 2.6	-11.3 ± 5.0			mid-G	
F020	2010-09-12	Late	-39.7 ± 1.9	-9.4 ± 2.8			mid-K	
F021	2010-10-03	Late	-54.1 ± 1.7	-19.4 ± 4.5			late-G	
F022	2010-10-07	Early	-27.2 ± 2.4	4.1 ± 1.9	16	-0.2 ± 0.7	Early-B	✓
F023	2009-11-15	Featureless	-28.8 ± 2.2	6.4 ± 4.9				

Table 2.2: Continued

#	Date Obs. yyyy-mm-dd	Group	$EW(H\alpha)_S$ (Å)	$EW(H\beta)$ (Å)	S/N	$\log(W_{\lambda 4471}/W_{\lambda 4481})$	SpT	CBe
F024	2006-09-26	Early	-22.8 ± 1.1	4.5 ± 1.2	36	1.0 ± 0.6	Mid-B	✓
F025	2010-10-02	Early	-10.8 ± 1.7	8.7 ± 1.2	35		Late-B	✓
F026	2006-09-26	Early	-13.1 ± 1.2	7.7 ± 1.1	32	0.1 ± 0.1	B7	✓
F027	2010-10-07	Early	-4.5 ± 1.1	8.0 ± 1.0	36	0.2 ± 0.1	B6	✓
F028	2010-10-07	Early	-19.4 ± 1.3	6.8 ± 1.5	19	-0.2 ± 0.3	Late-B	✓
F029	2006-09-26	Early	-23.3 ± 1.2	6.9 ± 1.4	36	0.3 ± 0.2	B5	✓
F030	2010-10-07	Early	-21.8 ± 1.1	6.1 ± 1.3	23	0.1 ± 0.1	Mid-B	✓
F031	2010-10-07	Early	-9.9 ± 0.7	7.4 ± 0.7	45	0.3 ± 0.1	B5	✓
F032	2010-10-07	Early	-26.6 ± 0.8	4.6 ± 0.9	36	1.3 ± 1.2	Mid-B	✓
F033	2009-12-13	Early	-12.1 ± 1.9	6.7 ± 2.2	15		Late-B	✓
F034	2009-12-13	Late(no-em)	1.4 ± 1.5	1.9 ± 3.3				
F035	2009-12-18	Early	-38.8 ± 1.2	2.2 ± 1.4	23	0.2 ± 0.3	Mid-B	✓
F036	2009-12-18	Early	-12.6 ± 1.2	7.8 ± 1.1	27	1.0 ± 1.3	Late-B	✓
F037	2009-12-18	Early	-9.5 ± 1.8	7.1 ± 1.3	22	0.3 ± 0.2	Late-B	✓
F038	2009-12-18	Featureless	-33.1 ± 2.2	3.5 ± 4.0				
F039	2006-09-26	Early	-8.9 ± 1.1	11.2 ± 1.1	38	0.3 ± 0.3	B5	✓
F040	2009-11-19	Early	-23.5 ± 1.6	7.5 ± 1.7	24	-0.4 ± 0.3	Late-B	✓
F041	2009-01-31	Early	-35.9 ± 1.0	5.7 ± 1.0	41	0.7 ± 0.2	B3	✓
	2006-09-27	Early	-37.0 ± 1.4	5.7 ± 1.0	41	0.6 ± 0.2	B3	✓
F042	2006-09-27	Early	-21.8 ± 1.0	5.8 ± 1.0	33	-0.0 ± 0.1	B8	✓
F043	2008-09-28	Featureless	-27.3 ± 2.3	4.3 ± 4.0				✓
F044	2006-09-27	Early	-8.6 ± 1.2	8.6 ± 1.2	42	1.0 ± 1.2	Late-B	✓
F045	2006-09-27	Early	-19.3 ± 1.2	6.5 ± 1.3	25	0.1 ± 0.1	Late-B	✓
F046	2006-09-27	Early	-12.6 ± 1.0	6.8 ± 1.1	40		Late-B	✓
F047	2006-09-27	Early	-32.6 ± 1.1	5.2 ± 1.2	35	0.7 ± 0.5	Late-B	✓
F048	2006-09-27	Late(no-em)	1.2 ± 1.7	0.8 ± 4.0				

Table 2.2: Continued

#	Date Obs. yyyy-mm-dd	Group	$EW(\mathrm{H}\alpha)_S$ (Å)	$EW(\mathrm{H}\beta)$ (Å)	S/N	$\log(W_{\lambda4471}/W_{\lambda4481})$	SpT	CBe
F049	2010-10-09	Featureless	-39.3 ± 2.6	1.8 ± 5.5				
F050	2008-09-28	Featureless	-12.7 ± 2.2	7.9 ± 3.8				
F051	2008-09-28	Featureless	-20.7 ± 2.0	6.0 ± 3.5				✓
F052	2009-11-19	Late(no-em)	-0.8 ± 2.3	1.6 ± 4.4				
F053	2008-10-01	Featureless	-8.6 ± 1.6	7.6 ± 2.4				
F054	2006-09-27	Early	-12.4 ± 1.9	9.0 ± 1.0	46	0.2 ± 0.1	B6	✓
F055	2009-10-21	Early	12.5 ± 2.4	17.5 ± 3.3	16		Late-B	
F056	2008-10-01	Featureless	-44.8 ± 2.0	5.2 ± 5.5				
F057	2008-10-01	Featureless	-43.7 ± 2.4	0.0 ± 4.9				
F058	2008-10-01	Featureless	-36.5 ± 1.6	-0.1 ± 2.6				✓
F059	2008-10-01	Early	3.6 ± 1.4	8.9 ± 1.3	30		Late-B	✓
F060	2006-09-27	Early	-23.4 ± 0.9	6.0 ± 1.1	30	-0.2 ± 0.1	B9	✓
F061	2006-09-27	Early	-22.1 ± 0.9	4.7 ± 1.0	37	0.9 ± 0.4	B1	✓
F062	2008-10-30	Featureless	-23.9 ± 1.6	2.5 ± 3.4				
F063	2008-10-30	Featureless	-48.8 ± 1.4	2.5 ± 2.5				
F064	2008-10-30	Featureless	-85.3 ± 1.4	-2.9 ± 2.2				✓
F065	2008-10-30	Featureless	-60.6 ± 1.7	1.7 ± 3.4				
F066	2008-10-30	Early	-23.7 ± 1.5	6.6 ± 2.4	13		Late-B	✓
F067	2008-10-30	Featureless	-77.7 ± 2.0	0.9 ± 3.5				
F068	2008-11-02	Featureless	-68.3 ± 1.6	-0.1 ± 3.6				
F069	2006-09-27	Early	-45.2 ± 1.1	3.0 ± 1.1	33		Mid-B	✓
F070	2011-01-10	Featureless	-79.2 ± 2.4	-20.2 ± 5.6				
F071	2008-11-03	Early	-43.6 ± 1.8	2.5 ± 2.6	13	0.3 ± 0.5	Mid-B	✓
F072	2009-10-22	Late	-28.9 ± 2.8	-7.9 ± 9.2			early-K	
F073	2006-09-27	Featureless	-71.1 ± 1.3	-1.5 ± 1.8				✓
F074	2009-11-12	Early	-16.7 ± 1.9	8.6 ± 3.1	14		Late-B	✓

Table 2.2: Continued

#	Date Obs. yyyy-mm-dd	Group	$EW(H\alpha)_S$ (Å)	$EW(H\beta)$ (Å)	S/N	$\log(W_{\lambda 4471}/W_{\lambda 4481})$	SpT	CBe
F075	2008-11-03	Early	-9.4 ± 1.8	6.1 ± 2.8	14		Late-B	✓
F076	2008-11-03	Early	-36.7 ± 1.7	6.7 ± 2.6	14		Late-B	✓
F077	2006-09-27	Early	-15.0 ± 1.0	6.2 ± 1.2	33	0.0 ± 0.1	B7	✓
F078	2008-11-03	Early	-18.9 ± 2.3	5.7 ± 2.3	22	0.9 ± 1.1	Late-B	✓
F079	2008-10-24	Early	-12.6 ± 1.3	6.3 ± 2.0	23	0.6 ± 0.3	Mid-B	✓
	2006-09-27	Early	-11.5 ± 1.0	6.3 ± 2.0	23	0.6 ± 0.2	B3	✓
F080	2009-11-12	Featureless	-42.2 ± 3.5	1.1 ± 5.6				
	2009-10-23	Featureless	-42.5 ± 2.4	1.1 ± 5.6				
F081	2008-10-24	Early	-21.2 ± 1.2	7.1 ± 1.6	28		Late-B	✓
	2006-09-27	Early	-20.6 ± 1.2	7.1 ± 1.6	28	0.3 ± 0.1	B5	✓
F082	2008-10-24	Featureless	-21.4 ± 2.1	5.3 ± 3.1				✓
F083	2006-09-27	Early	-18.2 ± 1.0	2.1 ± 1.1	39	0.8 ± 0.3	B3	✓
F084	2008-10-24	Early	-52.3 ± 1.6	0.6 ± 2.7	15	0.8 ± 0.8	Mid-B	✓
	2006-09-27	Early	-28.8 ± 1.3	0.6 ± 2.7	15		Mid-B	✓
F085	2006-09-27	Early	-26.8 ± 1.3	5.4 ± 1.4	31	0.8 ± 0.4	B3	✓
F086	2008-10-24	Featureless	-43.0 ± 1.9	2.5 ± 3.1				
F087	2008-10-24	Featureless	-34.2 ± 3.1	4.2 ± 5.9				
F088[1]	2008-10-24		1.7 ± 0.7	3.5 ± 0.8				
F089	2008-10-24	Featureless	-72.9 ± 1.5	-3.4 ± 2.2				✓
	2006-09-26	Early	-98.0 ± 1.2	-3.4 ± 2.2		1.0 ± 1.3	Early-B	✓
F090	2010-10-09	CV	-54.2 ± 3.4	-22.7 ± 5.3				
F091	2008-10-31	Early	-43.4 ± 2.2	10.1 ± 1.7	26		Late-B	
F092	2008-10-31	Early	-7.3 ± 1.1	7.0 ± 1.2	32		Late-B	✓
	2006-09-26	Early	-8.6 ± 1.0	7.0 ± 1.2	32	0.5 ± 0.2	B4	✓
F093	2008-10-31	Featureless	-58.1 ± 1.3	0.2 ± 3.5				✓
F094	2008-10-31	Featureless	-14.8 ± 1.6	3.8 ± 2.5				

Table 2.2: Continued

#	Date Obs. yyyy-mm-dd	Group	$EW(\mathrm{H}\alpha)_\mathrm{S}$ (Å)	$EW(\mathrm{H}\beta)$ (Å)	S/N	$\log(W_{\lambda 4471}/W_{\lambda 4481})$	SpT	CBe
F095	2006-09-26	Early	-33.5 ± 1.1	3.6 ± 1.0	32	0.2 ± 0.1	B6	✓
F096	2008-10-31	Featureless	-49.2 ± 1.9	0.7 ± 3.7				
F097	2008-11-02	Early	-7.5 ± 1.5	7.0 ± 1.7	15	-0.4 ± 0.1	Late-B	✓
F098	2006-09-26	Early	-70.9 ± 1.1	0.4 ± 1.2	27	0.5 ± 0.2	B3	✓
F099	2008-11-02	Early	-13.4 ± 1.3	5.5 ± 1.9	17	0.1 ± 0.1	Mid-B	✓
F100	2008-10-24	Early	-26.8 ± 1.8	4.1 ± 2.7	16	0.7 ± 0.5	Mid-B	✓
F101	2009-11-19	Featureless	-15.9 ± 1.5	5.0 ± 2.8				
F102	2006-09-26	Early	-9.6 ± 1.0	9.4 ± 1.3	33	0.1 ± 0.1	B6	✓
F103	2006-09-27	Early	-28.9 ± 1.4	14.0 ± 1.9	19	0.1 ± 0.1	Late-B	
F104	2009-11-23	Early	-14.3 ± 1.1	5.8 ± 1.4	25		Late-B	✓
F105	2009-11-23	Early	-8.9 ± 1.5	9.1 ± 1.5	25	0.5 ± 0.4	Late-B	
F106	2006-09-27	Early	-3.4 ± 1.1	7.0 ± 1.1	31		Late-B	✓
F107	2006-09-27	Early	-10.2 ± 1.4	6.5 ± 1.4	28	0.2 ± 0.1	B6	✓
F108	2006-09-27	Early	-20.0 ± 1.5	5.9 ± 1.6	28	0.1 ± 0.1	B7	✓
F109	2006-09-27	Late(no-em)	0.4 ± 1.8	0.4 ± 3.9				
F110	2009-11-23	Early	-13.3 ± 1.4	6.2 ± 1.8	18	0.5 ± 0.5	Late-B	✓
F111	2006-09-27	Early	-12.1 ± 1.3	7.1 ± 1.4	23	-0.1 ± 0.1	Late-B	✓
F112	2006-09-27	Early	-25.7 ± 1.4	3.6 ± 1.5	20		Early-B	✓
F113	2006-09-27	Early	-23.9 ± 1.1	3.6 ± 1.1	31		Mid-B	✓
F114	2006-09-27	Early	-20.7 ± 0.8	2.9 ± 0.9	50	0.7 ± 0.2	B2	✓
F115	2009-11-12	Early	-8.4 ± 2.0	16.7 ± 4.5	9		Late-B	
F116	2006-09-27	Early	-41.1 ± 1.0	4.4 ± 1.1	40	0.4 ± 0.1	B4	✓
F117	2009-11-24	Early	-13.0 ± 1.1	6.3 ± 1.0	26	0.3 ± 0.1	B5	✓
F118	2009-11-24	Early	-0.2 ± 0.8	7.5 ± 0.9	36	0.6 ± 0.2	B3	✓
F119	2009-11-24	Featureless	-66.6 ± 1.3	-0.1 ± 2.1				
F120	2009-11-24	Featureless	-26.4 ± 1.5	2.5 ± 2.9				

Table 2.2: Continued

#	Date Obs. yyyy-mm-dd	Group	$EW(\mathrm{H}\alpha)_S$ (Å)	$EW(\mathrm{H}\beta)$ (Å)	S/N	$\log(W_{\lambda 4471}/W_{\lambda 4481})$	SpT	CBe
F121	2006-09-27	Early	-38.0 ± 1.2	1.9 ± 1.5	26	1.0 ± 0.7	Mid-B	✓
F122	2006-09-27	Early	-18.4 ± 1.1	6.5 ± 1.0	28		Late-B	✓
F123	2006-09-27	Early	-29.8 ± 1.4	3.4 ± 1.9	31		Mid-B	✓
F124	2009-11-24	Early	-9.2 ± 1.9	8.5 ± 2.3	17	0.1 ± 0.3	Late-B	✓
F125	2006-09-27	Early	-5.6 ± 1.1	3.1 ± 1.4	27	0.2 ± 0.1	B6	✓
F126	2010-10-08	Early	-13.1 ± 1.3	7.7 ± 1.5	27	-0.2 ± 0.1	B9	✓
F127	2009-12-12	Early	5.6 ± 1.4	8.2 ± 1.4	25	0.6 ± 0.3	Mid-B	✓
F128	2009-12-12	Featureless	-51.3 ± 1.5	1.8 ± 2.1				
F129	2006-10-21	Early	-6.1 ± 0.9	7.6 ± 1.0	49	0.1 ± 0.1	B7	✓
F130	2009-12-12	Early	-9.6 ± 1.6	8.0 ± 2.3	17	-0.1 ± 0.1	Mid-B	✓
F131	2006-10-21	Early	-6.8 ± 0.7	8.9 ± 0.8	72	0.1 ± 0.1	B7	✓
F132	2009-12-12	Early	-29.6 ± 1.6	3.0 ± 1.9	20	0.6 ± 0.5	Mid-B	✓
F133	2009-12-12	Featureless	-4.7 ± 1.7	2.3 ± 3.0				
F134	2006-10-21	Early	-7.3 ± 1.2	6.7 ± 1.4	34	0.3 ± 0.2	B5	✓
F135	2006-09-27	Early	-2.6 ± 1.0	8.7 ± 0.9	35	0.1 ± 0.1	B6	✓
F136	2006-09-27	Early	0.7 ± 1.5	10.8 ± 1.4	26	0.0 ± 0.4	B7	✓
F137	2009-12-12	Featureless	-44.1 ± 1.2	0.1 ± 1.9				✓
F138	2009-12-12	Early	-7.0 ± 1.6	8.3 ± 2.3	16		Late-B	✓
F139	2006-10-21	Early	-14.7 ± 0.9	8.5 ± 0.9	53	0.7 ± 0.3	B3	✓
F140	2009-12-18	Early	-7.3 ± 1.2	9.1 ± 1.3	27	-0.6 ± 0.2	A0	
F141	2009-12-18	Early	-35.7 ± 1.3	3.2 ± 1.3	30	0.7 ± 0.2	B3	✓
F142	2008-11-03	Early	-12.2 ± 1.6	7.3 ± 2.2	13		Late-B	✓
F143	2008-11-03	Early	-34.2 ± 1.6	1.4 ± 1.9	20	0.1 ± 0.2	Early-B	✓
	2006-10-21	Early	-35.4 ± 1.4	1.4 ± 1.9	20	0.6 ± 0.2	B3	✓
F144	2006-10-21	Early	-12.7 ± 0.7	6.0 ± 0.8	63	0.9 ± 0.3	B1	✓
F145	2008-11-03	Early	-27.2 ± 1.4	6.0 ± 1.1	34	0.5 ± 0.2	B4	✓

Table 2.2: Continued

#	Date Obs. yyyy-mm-dd	Group	$EW(\mathrm{H}\alpha)_S$ (Å)	$EW(\mathrm{H}\beta)$ (Å)	S/N	$\log(W_{\lambda4471}/W_{\lambda4481})$	SpT	CBe
	2006-10-21	Early	-26.6 ± 0.9	6.0 ± 1.1	34	0.4 ± 0.1	B5	✓
F146	2008-11-03	Early	0.7 ± 1.4	5.9 ± 1.9	15	0.3 ± 0.3	Mid-B	✓
F147	2008-11-03	Early	-20.3 ± 1.3	4.7 ± 1.4	24	0.3 ± 0.1	Mid-B	✓
	2006-10-21	Early	-21.1 ± 0.9	4.7 ± 1.4	24	0.8 ± 0.2	B3	✓
F148	2008-11-03	Early	-15.3 ± 2.1	8.2 ± 2.5	15		Late-B	
F149	2011-02-07	Late	-27.2 ± 2.7	-4.2 ± 8.9				
F150	2010-10-09	Featureless	-38.3 ± 3.9	-4.8 ± 11.8				
F151	2008-11-03	Early	-11.4 ± 1.5	9.9 ± 2.0	14	0.5 ± 0.5	Late-B	✓
F152	2006-10-21	Early	-8.0 ± 0.8	4.2 ± 0.9	56	0.4 ± 0.1	B4	✓
F153	2009-10-19	Featureless	-22.2 ± 2.6	2.6 ± 6.7				
F154	2008-11-03	Early	-20.8 ± 1.2	5.2 ± 2.0	16	-0.2 ± 0.2	Mid-B	✓
F155	2009-10-19	Featureless	-31.9 ± 2.8	6.9 ± 3.1				
F156	2008-11-03	Early	-17.5 ± 2.2	6.0 ± 2.8	13		Late-B	✓
F157	2006-10-21	Early	-15.1 ± 0.7	5.7 ± 0.8	62	0.5 ± 0.1	B4	✓
F158	2008-11-03	Featureless	-51.7 ± 2.1	1.7 ± 2.7				✓
F159	2008-11-03	Early	-20.3 ± 1.1	4.1 ± 1.1	30	0.1 ± 0.1	B6	✓
	2006-10-21	Early	-23.3 ± 1.2	4.1 ± 1.1	30	0.4 ± 0.3	B4	✓
F160	2008-11-03	Early	-6.6 ± 1.5	9.3 ± 1.8	19	-1.3 ± 7.5	Late-B	✓
F161	2008-11-01	Early	3.3 ± 1.8	6.1 ± 2.0	17	0.8 ± 0.8	Late-B	✓
	2006-10-31	Early	1.9 ± 1.0	6.1 ± 2.0	17	1.2 ± 0.9	Mid-B	✓
F162	2008-11-01	Early	-33.8 ± 2.4	3.0 ± 1.5	20	0.4 ± 0.2	Mid-B	✓
	2005-01-17	Early	-31.5 ± 0.7	3.0 ± 1.5	20	0.6 ± 0.3	B3	✓
F163	2005-01-17	Early	-37.7 ± 0.9	2.4 ± 1.2	22	0.6 ± 0.2	Mid-B	✓
F164	2005-01-17	Ap(?)	-7.0 ± 1.1	9.8 ± 1.2				
F165	2008-11-01	Featureless	-38.6 ± 1.4	5.1 ± 2.1				
F166	2006-10-31	Early	2.5 ± 1.4	7.9 ± 1.2	23	-0.0 ± 0.1	Mid-B	✓

Table 2.2: Continued

#	Date Obs. yyyy-mm-dd	Group	$EW(\mathrm{H}\alpha)_S$ (Å)	$EW(\mathrm{H}\beta)$ (Å)	S/N	$\log(W_{\lambda 4471}/W_{\lambda 4481})$	SpT	CBe
F167	2005-01-17	Early	-7.3 ± 0.5	7.4 ± 0.5	78	0.1 ± 0.1	B7	✓
F168	2011-03-11	Late(no-em)	3.1 ± 0.9	6.0 ± 1.7				
F169	2008-11-01	Featureless	-43.3 ± 1.9	0.5 ± 2.7				✓
	2006-10-31	Early	-42.3 ± 1.4	0.5 ± 2.7			Early-B	✓
F170	2005-01-17	Early	-22.3 ± 1.2	5.6 ± 1.4	20	0.1 ± 0.2	Mid-B	✓
F171	2008-11-01	Early	-16.8 ± 1.2	5.2 ± 1.4	24	1.2 ± 1.5	Mid-B	✓
	2005-01-17	Early	-16.1 ± 1.0	5.2 ± 1.4	24	0.7 ± 0.7	Mid-B	✓
F172	2008-11-01	Early	-10.6 ± 2.1	6.3 ± 2.2	16	0.6 ± 1.4	Late-B	✓
	2005-01-18	Early	-10.5 ± 0.7	6.3 ± 2.2	16	0.0 ± 0.2	B8	✓
F173	2008-11-01	Early	-11.2 ± 1.5	7.7 ± 1.3	28	0.4 ± 0.2	B4	✓
	2005-01-18	Early	-10.6 ± 1.0	7.7 ± 1.3	28	0.2 ± 0.1	B6	✓
F174	2005-01-18	Early	-9.3 ± 1.6	6.3 ± 1.9	13	0.0 ± 0.2	Mid-B	✓
	2008-12-19	Early	-2.0 ± 1.3	6.3 ± 1.9	13		Late-B	✓
F175	2005-01-18	Early	-9.5 ± 0.7	3.4 ± 0.9	38	0.9 ± 0.3	B1	✓
F176	2005-01-18	Early	-28.8 ± 1.1	5.9 ± 1.1	33	1.5 ± 2.0	Mid-B	✓
F177	2009-11-18	Early	-9.0 ± 1.4	5.8 ± 1.7	22	-0.2 ± 0.2	Late-B	
F178	2005-01-18	Early	-8.8 ± 1.1	7.1 ± 0.7	42		Mid-B	✓
F179	2006-10-31	Early	-25.5 ± 0.9	4.6 ± 1.1	49	0.6 ± 0.3	B3	✓
F180	2005-01-18	Early	-6.2 ± 1.1	6.1 ± 3.0	20		Late-B	✓
F181	2009-11-18	Early	-11.4 ± 1.4	5.4 ± 1.5	22		Late-B	✓
F182	2009-11-18	Early	-2.9 ± 2.0	8.3 ± 2.2	17	0.4 ± 0.4	Late-B	✓
F183	2006-10-31	Early	-27.7 ± 1.2	5.3 ± 1.6	32	0.6 ± 0.4	B3	✓
F184	2009-11-18	Early	-18.3 ± 1.4	7.6 ± 1.6	27	-1.0 ± 0.1	A0	✓
F185	2009-11-18	Early	-17.2 ± 1.6	2.7 ± 1.9	17	0.7 ± 1.0	Late-B	✓
F186	2009-11-18	Featureless	-31.8 ± 1.5	0.8 ± 2.1				
F187	2006-10-31	Early	-0.6 ± 1.0	6.4 ± 0.9	48	0.6 ± 0.1	B3	✓

Table 2.2: Continued

#	Date Obs. yyyy-mm-dd	Group	$EW(\text{H}\alpha)_S$ (Å)	$EW(\text{H}\beta)$ (Å)	S/N	$\log(W_{\lambda 4471}/W_{\lambda 4481})$	SpT	CBe
F188	2009-11-18	Early	-5.4 ± 1.7	9.6 ± 1.9	23	0.2 ± 0.4	Late-B	✓
F189	2008-12-19	Early	-14.1 ± 0.9	5.8 ± 1.3	27	-0.3 ± 0.2	B9	✓
	2006-10-31	Early	-15.6 ± 1.5	5.8 ± 1.3	27	0.5 ± 0.6	Mid-B	✓
F190	2006-10-31	Early	-6.5 ± 0.8	8.5 ± 0.9	38	-0.0 ± 0.1	B8	✓
F191	2009-10-21	Featureless	-5.2 ± 2.6	7.4 ± 3.8				
F192	2009-10-21	Early	-4.3 ± 2.4	7.9 ± 2.7	14		Late-B	✓
F193	2011-02-07	Featureless	-10.3 ± 2.2	4.8 ± 4.1				
F194	2006-10-31	Early	-19.9 ± 1.2	4.8 ± 1.5	18	-0.1 ± 0.2	Mid-B	✓
F195	2006-10-31	Early	-8.6 ± 0.9	7.8 ± 1.0	36	-0.1 ± 0.1	B8	✓
F196	2009-11-22	Early	-3.5 ± 1.0	7.3 ± 1.1	43	0.3 ± 0.3	B6	✓
F197	2009-11-22	Early	-15.2 ± 1.4	5.9 ± 1.6	20		Mid-B	✓
F198	2006-11-16	Early	-8.8 ± 1.1	7.4 ± 1.2	32	0.2 ± 0.1	B6	✓
F199	2009-11-22	Early	-24.2 ± 1.4	6.4 ± 2.4	13		Late-B	✓
F200	2009-11-22	Early	-20.8 ± 1.5	4.4 ± 2.4	11		Mid-B	✓
F201	2006-11-16	Early	-17.1 ± 0.8	6.1 ± 0.8	55	0.4 ± 0.2	B5	✓
F202	2006-11-16	Early	-21.0 ± 1.0	5.6 ± 1.1	39		Mid-B	✓
F203	2008-10-22	Early	-18.6 ± 2.5	2.3 ± 3.4	11		Mid-B	✓
	2006-11-26	Early	-19.9 ± 1.6	2.3 ± 3.4	11		Early-B	✓
F204	2008-10-22	Early	-3.0 ± 1.1	9.4 ± 1.5	24		Late-B	✓
F205	2006-11-26	Early	-9.9 ± 1.3	9.3 ± 1.8	29	0.0 ± 0.1	B7	✓
F206	2011-02-03	Featureless	-12.9 ± 3.1	7.7 ± 3.5				
F207	2006-11-16	Neb	-16.7 ± 4.8	4.7 ± 3.8				
F208	2009-11-12	Featureless	-26.1 ± 2.2	4.9 ± 4.9				
F209	2008-10-22	Early	-14.8 ± 1.0	0.7 ± 1.3	36		Early-B	✓
	2006-11-16	Early	-26.2 ± 1.4	0.7 ± 1.3	36		Early-B	✓
F210	2008-10-22	Featureless	-54.2 ± 1.5	1.7 ± 4.0				

Table 2.2: Continued

#	Date Obs. yyyy-mm-dd	Group	$EW(\mathrm{H}\alpha)_S$ (Å)	$EW(\mathrm{H}\beta)$ (Å)	S/N	$\log(W_{\lambda4471}/W_{\lambda4481})$	SpT	CBe
F211	2008-10-22	Early	-15.0 ± 1.4	6.5 ± 1.6	18		Late-B	✓
	2008-10-22	Early	-19.5 ± 1.6	3.2 ± 2.0	17	-0.0 ± 0.2	Late-B	✓
F212	2006-11-16	Early	-25.3 ± 1.6	3.2 ± 2.0	17	0.3 ± 0.3	Mid-B	✓
	2006-11-24	Early	-26.6 ± 1.1	3.2 ± 2.0	17	0.4 ± 0.2	B4	✓
F213	2008-10-22	Early	-27.4 ± 1.5	3.7 ± 2.1	22		Mid-B	✓
F214	2008-10-22	Early	-8.8 ± 1.5	5.5 ± 1.9	18		Mid-B	
F215	2008-10-22	Featureless	-45.8 ± 1.7	2.2 ± 2.6				
	2008-10-25	Early	-8.8 ± 1.5	7.2 ± 1.8	14		Late-B	✓
F216	2008-10-25	Early	-10.7 ± 2.5	7.2 ± 1.8	14	0.3 ± 0.3	Late-B	✓
	2006-11-26	Early	-9.4 ± 1.6	7.2 ± 1.8	14		Late-B	✓
F217	2008-10-25	Early	6.5 ± 1.5	9.8 ± 1.6	20	0.1 ± 0.1	Late-B	
F218	2008-10-25	Early	-71.7 ± 1.5	-0.2 ± 2.5	18	0.5 ± 0.7	Mid-B	✓
F219	2008-10-25	Early	-16.1 ± 1.5	5.9 ± 1.5	21		Late-B	✓
F220	2009-11-12	Early	-14.4 ± 1.8	6.6 ± 2.2	15	-0.3 ± 0.2	Late-B	✓
F221	2006-11-16	Early	-8.1 ± 1.1	7.9 ± 1.2	31		Late-B	✓
F222	2008-10-25	Early	-27.4 ± 1.2	3.8 ± 2.0	22	0.5 ± 0.7	Mid-B	✓
F223	2008-10-25	Early	-8.1 ± 1.5	6.4 ± 2.2	18	0.3 ± 0.4	Late-B	✓
F224	2008-10-25	Early	-17.5 ± 1.1	17.3 ± 1.4	28	-0.1 ± 0.3	B8	✓
F225[2]	2011-02-05		-0.2 ± 2.2	7.2 ± 2.5				
F226	2008-09-28	Featureless	-29.6 ± 2.3	11.4 ± 4.4				
F227	2008-09-28	Early	-12.4 ± 1.6	6.8 ± 1.8	4		Late-B	✓
F228	2006-11-16	Early	-8.3 ± 1.0	7.5 ± 1.2	30	0.0 ± 0.3	B7	✓
F229	2008-09-28	Early	-14.7 ± 1.9	6.8 ± 3.1	12		Mid-B	✓
	2006-11-16	Early	-14.8 ± 1.4	6.8 ± 3.1	12		Late-B	✓
F230[2]	2011-02-05		5.4 ± 1.4	14.9 ± 1.8				
F231	2008-09-28	Early	-31.9 ± 3.0	9.6 ± 3.8	8		Late-B	

Table 2.2: Continued

#	Date Obs. yyyy-mm-dd	Group	$EW(H\alpha)_S$ (Å)	$EW(H\beta)$ (Å)	S/N	$\log(W_{\lambda4471}/W_{\lambda4481})$	SpT	CBe
	2008-09-28	Early	-10.5 ± 1.9	5.4 ± 2.6	13	1.6 ± 0.6	Late-B	✓
F232	2006-11-24	Early	-9.8 ± 1.0	5.4 ± 2.6	13	0.3 ± 0.2	B5	✓
	2006-11-16	Early	-9.3 ± 1.3	5.4 ± 2.6	13	-0.2 ± 0.1	Late-B	✓
F233	2008-09-28	Featureless	-43.6 ± 2.2	7.2 ± 3.8				
F234	2008-09-28	Featureless	-66.4 ± 2.3	-1.3 ± 4.0				✓
F235	2008-09-28	Late(no-em)	0.2 ± 2.2	-0.4 ± 4.6				
F236	2008-09-29	Featureless	-61.2 ± 1.7	3.9 ± 5.0				
F237	2008-09-29	Early	-12.2 ± 2.7	6.2 ± 3.6	9	0.2 ± 0.3	Late-B	✓
F238	2006-11-16	Early	-29.3 ± 1.0	3.5 ± 1.2	33	0.5 ± 0.1	B3	✓
	2006-11-24	Early	-14.7 ± 1.1	4.3 ± 1.6	19	0.7 ± 0.8	Mid-B	
F239	2006-11-16	Early	-11.1 ± 1.6	4.3 ± 1.6	19		Mid-B	
	2008-09-29	Early	-15.4 ± 1.5	4.3 ± 1.6	19	-1.1 ± 0.1	Late-B	
F240	2008-09-29	Early	-99.0 ± 1.3	-2.5 ± 1.9	22	0.6 ± 0.8	Early-B	
	2006-11-16	Early	-99.7 ± 1.6	-2.5 ± 1.9	22		Early-B	
F241	2006-11-16	Early	-45.1 ± 1.5	2.1 ± 2.2	18	$1.5 \pm$		
F242	2008-09-29	Early	-10.0 ± 1.5	3.2 ± 1.6	19		Early-B	✓
	2006-11-24	Early	-3.3 ± 1.4	3.2 ± 1.6	19	0.6 ± 0.5	Mid-B	✓
F243	2008-09-29	Early	-16.4 ± 1.4	6.3 ± 2.0	16	0.4 ± 0.3	Late-B	✓
F244	2008-09-29	Early	-8.9 ± 1.3	7.6 ± 1.9	22		Late-B	✓
F245	2008-09-29	Early	-11.8 ± 1.3	5.1 ± 1.8	21	1.0 ± 1.3	Early-B	✓
F246	2008-09-29	Early	-6.3 ± 2.5	9.6 ± 1.1	31	0.5 ± 0.4	B4	✓
F247	2010-10-10	Early	-5.9 ± 1.5	7.2 ± 1.4	22	0.3 ± 0.3	Late-B	✓
F248	2008-09-29	Early	-41.4 ± 1.2	1.0 ± 1.8	21		Late-B	✓
	2006-11-16	Early	-41.9 ± 1.3	1.0 ± 1.8	21	0.5 ± 0.6	Mid-B	✓
F249	2008-09-29	F-type	-6.3 ± 1.4	3.7 ± 2.7				
F250	2009-01-29	Featureless	-45.4 ± 2.1	-9.9 ± 6.3				

Table 2.2: Continued

#	Date Obs. yyyy-mm-dd	Group	$EW(\mathrm{H\alpha})_S$ (Å)	$EW(\mathrm{H\beta})$ (Å)	S/N	$\log(W_{\lambda4471}/W_{\lambda4481})$	SpT	CBe
F251	2009-01-29	Featureless	-25.1 ± 2.8	4.8 ± 9.8				
F252	2006-11-16	Early	-34.5 ± 1.1	5.5 ± 1.5	25		Mid-B	✓
F253	2008-09-29	Early	-131.9 ± 1.3	-5.6 ± 1.9	24		Mid-B	
	2006-11-16	Early	-107.9 ± 1.6	-5.6 ± 1.9	24	0.1 ± 0.3	Mid-B	
F254	2008-09-29	Early	-8.4 ± 1.2	4.7 ± 1.6	21	1.0 ± 0.9	Late-B	✓
	2006-11-16	Early	-14.7 ± 1.1	4.7 ± 1.6	21	0.6 ± 0.3	B3	✓
	2006-11-24	Early	-14.9 ± 0.9	4.7 ± 1.6	21	0.6 ± 0.2	B3	✓
F255	2006-11-24	Featureless	-37.6 ± 1.2	-0.4 ± 2.1				✓
	2006-11-17	Featureless	-38.2 ± 2.6	-0.4 ± 2.1				✓
F256	2010-10-10	Early	-11.0 ± 2.2	7.8 ± 2.6	12		Mid-B	✓
F257	2011-02-07	Late(no-em)	-1.0 ± 2.3	2.6 ± 5.0				
F258	2011-03-09	Featureless	-109.0 ± 3.1	-22.7 ± 7.3				
F259	2011-03-09	Early	-12.1 ± 2.7	10.3 ± 2.7	11	0.3 ± 0.5	Late-B	✓
F260	2009-01-29	Featureless	-25.9 ± 1.7	4.4 ± 3.4				
F261	2008-09-29	Early	-15.1 ± 1.5	6.0 ± 2.4	17		Mid-B	✓
F262	2008-10-01	Featureless	-4.4 ± 2.6	7.6 ± 3.8				✓
F263	2006-11-24	Early	2.5 ± 2.4	5.1 ± 2.3	22		Early-B	✓
F264	2006-11-24	Early	-5.1 ± 1.0	8.9 ± 1.1	36	0.0 ± 0.1	B7	✓
	2006-11-17	Early	-5.9 ± 1.1	8.9 ± 1.1	36		Late-B	✓
F265	2006-11-24	Early	-15.2 ± 1.1	4.8 ± 1.3	33	0.5 ± 0.4	B4	✓
	2006-11-17	Early	-15.7 ± 1.1	4.8 ± 1.3	33	0.3 ± 0.2	B6	✓
F266	2006-11-17	Early	-10.7 ± 1.7	7.0 ± 2.0	25		Late-B	✓
	2008-12-19	Early	-9.7 ± 0.8	7.0 ± 2.0	25	0.5 ± 0.6	Late-B	✓
F267	2009-02-03	Featureless	-24.5 ± 3.8	4.4 ± 12.4				
F268	2008-10-01	Early	-24.8 ± 1.4	5.9 ± 1.6	18	-0.0 ± 0.1	Late-B	
	2006-11-17	Early	-24.9 ± 1.2	5.9 ± 1.6	18	1.2 ± 1.6	Late-B	

Table 2.2: Continued

#	Date Obs. yyyy-mm-dd	Group	$EW(\mathrm{H\alpha})_S$ (Å)	$EW(\mathrm{H\beta})$ (Å)	S/N	$\log(W_{\lambda4471}/W_{\lambda4481})$	SpT	CBe
F269	2006-11-17	Early	-11.3 ± 1.2	8.0 ± 1.1	29		Late-B	✓
F270	2006-11-24	Early	-34.7 ± 1.4	12.6 ± 1.6	33		Late-B	
	2006-11-17	Early	-32.3 ± 1.6	12.6 ± 1.6	33		Late-B	
F271	2009-11-22	Late(no-em)	3.9 ± 1.0	4.2 ± 1.8				
F272	2009-11-22	Early	-7.2 ± 2.1	18.9 ± 2.4	18		Late-B	
F273	2006-11-17	Early	-34.6 ± 1.5	5.3 ± 2.4	16	0.3 ± 0.4	Late-B	✓
	2006-11-26	Early	-34.2 ± 1.5	5.3 ± 2.4	16	-0.3 ± 0.2	Late-B	✓
F274	2009-02-05	Featureless	-85.1 ± 2.3	-0.2 ± 13.8				
F275	2008-11-04	Late(no-em)	1.2 ± 1.8	3.7 ± 5.5				
F276	2006-11-26	Early	-11.1 ± 1.2	7.8 ± 1.5	27	1.2 ± 2.1	Late-B	✓
	2006-11-17	Early	-10.8 ± 1.2	7.8 ± 1.5	27		Late-B	✓
F277	2008-11-04	Featureless	-42.9 ± 1.9	3.9 ± 3.1				✓
F278	2008-10-01	Early	-28.3 ± 1.8	2.6 ± 3.1	11		Mid-B	✓
	2006-11-26	Early	-30.1 ± 1.6	2.6 ± 3.1	11	1.3 ± 1.1	Early-B	✓
F279	2006-11-17	Early	-39.9 ± 1.5	3.7 ± 2.0	20		Mid-B	✓
F280	2009-02-05	Featureless	-93.3 ± 6.8	-16.2 ± 39.2				
	2008-11-04	Early	-15.9 ± 1.5	6.1 ± 1.8	23	1.6 ± 0.6	Late-B	✓
F281	2006-11-26	Early	-15.5 ± 1.0	6.1 ± 1.8	23	0.5 ± 0.2	B3	✓
	2006-11-17	Early	-16.7 ± 1.9	6.1 ± 1.8	23	0.1 ± 0.3	Late-B	✓
F282	2006-11-17	F-type	-16.4 ± 2.0	2.8 ± 3.2				
F283	2006-11-26	Early	-19.6 ± 3.3	16.9 ± 3.1	13	-0.4 ± 0.2	Late-B	✓
F284	2009-11-22	Featureless	-23.4 ± 2.6	6.9 ± 2.9				
F285	2009-02-05	Featureless	-77.5 ± 2.6	-10.4 ± 7.2				
F286	2009-12-18	Early	-14.7 ± 2.8	6.3 ± 2.8	10		Mid-B	✓
F287	2006-11-26	Early	-11.5 ± 2.5	7.5 ± 2.7	17		Late-B	✓
F288	2009-12-18	Early	-33.1 ± 1.9	5.9 ± 2.7	14	0.1 ± 0.2	Late-B	✓

Table 2.2: Continued

#	Date Obs. yyyy-mm-dd	Group	$EW(\mathrm{H}\alpha)_S$ (Å)	$EW(\mathrm{H}\beta)$ (Å)	S/N	$\log(W_{\lambda4471}/W_{\lambda4481})$	SpT	CBe
F289	2006-11-26	Early	-27.1 ± 1.8	3.3 ± 2.4	20	1.6 ± 4.0	Early-B	✓
F290	2006-11-17	Early	-38.0 ± 1.3	3.3 ± 1.4	31	0.9 ± 0.4	Early-B	✓
	2008-11-02	Early	-36.9 ± 1.3	3.3 ± 1.4	31	0.4 ± 0.3	Mid-B	✓
F291	2006-11-17	Early	-15.0 ± 1.2	5.9 ± 1.4	35		Mid-B	✓
F292	2006-11-27	Early	-22.1 ± 0.7	5.0 ± 0.9	49	0.8 ± 0.3	B1	✓
	2006-11-17	Early	-21.9 ± 1.1	5.0 ± 0.9	49	0.1 ± 0.1	B7	✓
F293	2006-11-17	Early	-14.3 ± 1.3	6.2 ± 1.9	24	0.8 ± 1.0	Mid-B	✓
F294	2006-11-27	Early	-22.2 ± 2.0	6.8 ± 2.2	19	0.6 ± 0.6	Mid-B	✓
F295	2008-10-23	Early	-12.3 ± 1.5	6.9 ± 2.0	20	0.1 ± 0.1	Late-B	✓
	2006-11-17	Early	-14.1 ± 1.2	6.9 ± 2.0	20	0.3 ± 0.2	B5	✓
F296	2006-11-17	Early	-43.2 ± 1.4	11.7 ± 1.7	26	-0.0 ± 0.1	B8	
F297	2006-11-27	Early	-29.6 ± 1.1	3.2 ± 1.4	29	0.5 ± 0.2	B3	✓
F298	2008-10-23	Early	-41.3 ± 1.7	1.8 ± 2.4	16		Early-B	✓
	2006-11-27	Early	-43.7 ± 1.0	1.8 ± 2.4	16		Early-B	✓
F299	2006-11-17	Early	-18.4 ± 0.9	6.0 ± 0.9	42	0.4 ± 0.2	B5	✓
F300	2006-11-27	Early	-26.7 ± 1.1	4.5 ± 1.3	29	0.3 ± 0.1	B5	✓
	2006-11-17	Early	-24.4 ± 1.4	4.5 ± 1.3	29	0.6 ± 0.3	B3	✓
F301	2008-10-23	Early	-34.6 ± 1.9	6.3 ± 2.7	14	0.1 ± 0.1	Mid-B	✓
	2006-11-27	Early	-36.6 ± 1.3	6.3 ± 2.7	14	1.2 ± 1.5	Mid-B	✓
F302	2006-12-13	Early	-23.1 ± 1.6	5.8 ± 1.6	25	0.5 ± 0.2	Mid-B	✓
	2008-10-23	Early	-33.9 ± 1.3	-0.2 ± 2.2	15	0.8 ± 0.5	Early-B	✓
F303	2006-12-13	Early	-30.2 ± 1.2	-0.2 ± 2.2	15		Early-B	✓
	2006-11-17	Early	-31.2 ± 1.2	-0.2 ± 2.2	15		Early-B	✓
F304	2006-12-13	Early	-15.3 ± 1.2	9.0 ± 1.1	42	0.4 ± 0.1	B5	✓
F305[3]	2011-02-07		11.0 ± 0.6	15.2 ± 0.6	85	-0.6 ± 0.1	B9	
F306	2011-03-08	Early	-139.2 ± 1.8	-1.4 ± 2.2	17		Early-B	✓

Table 2.2: Continued

#	Date Obs. yyyy-mm-dd	Group	$EW(\mathrm{H}\alpha)_\mathrm{S}$ (Å)	$EW(\mathrm{H}\beta)$ (Å)	S/N	$\log(W_{\lambda 4471}/W_{\lambda 4481})$	SpT	CBe
F307	2008-10-23	Early	-5.0 ± 1.2	8.0 ± 1.6	20		Late-B	✓
	2008-10-23	Early	-26.9 ± 2.1	5.6 ± 2.2	16	-0.1 ± 0.1	Mid-B	✓
F308	2008-10-23	Early	-26.1 ± 1.9	5.6 ± 2.2	16		Mid-B	✓
	2006-12-13	Early	-26.1 ± 3.1	5.6 ± 2.2	16		Mid-B	✓
F309	2008-10-26	Early	-46.1 ± 1.6	2.0 ± 1.6	24	1.9 ± 8.5	Mid-B	✓
	2006-12-13	Early	-42.1 ± 1.5	2.0 ± 1.6	24	0.8 ± 0.5	Mid-B	✓
F310	2010-10-10	Late	-20.0 ± 1.6	2.5 ± 3.7			mid-K	
F311	2006-12-13	Early	-39.6 ± 1.9	5.5 ± 2.1	25		Late-B	
F312	2008-10-26	Early	-6.6 ± 2.1	18.7 ± 2.0	23		Late-B	✓
F313	2011-02-07	Featureless	-28.9 ± 2.7	1.2 ± 7.0				
F314	2006-12-13	Early	-14.0 ± 1.1	5.6 ± 1.1	30	-0.0 ± 0.1	B8	✓
	2006-11-17	Early	-14.9 ± 1.4	5.6 ± 1.1	30	0.3 ± 0.2	B5	✓
F315	2006-12-13	Early	-15.3 ± 1.0	7.5 ± 0.9	38	0.1 ± 0.1	B7	✓
F316	2008-10-26	Early	-4.4 ± 1.6	8.1 ± 1.6	25	0.4 ± 0.3	Late-B	✓
	2008-10-26	Early	-18.1 ± 1.9	5.3 ± 2.6	15		Late-B	✓
F317	2005-01-20	Early	-24.8 ± 3.8	5.3 ± 2.6	15	-0.0 ± 0.3	Mid-B	✓
	2006-12-13	Early	-18.4 ± 1.3	5.3 ± 2.6	15	0.4 ± 0.2	Mid-B	✓
F318	2008-10-26	Late	-11.1 ± 1.8	4.0 ± 3.0			mid-K	
F319	2010-10-10	Early	-9.9 ± 1.6	6.1 ± 2.2	17	0.7 ± 1.1	Late-B	✓
F320	2011-01-04	Featureless	-56.6 ± 3.2	-12.4 ± 4.7				
F321	2010-10-10	Featureless	-37.9 ± 2.4	-7.2 ± 5.7				
F322	2010-10-09	Featureless	-54.7 ± 2.9	-9.1 ± 4.2				
F323	2010-10-10	Featureless	-29.3 ± 2.0	3.9 ± 3.0				
F324	2009-11-18	Early	-25.3 ± 1.3	5.7 ± 1.7	23		Mid-B	✓
F325	2009-11-18	Featureless	-46.2 ± 2.2	1.8 ± 3.2				
F326	2009-11-19	Early	-39.3 ± 1.2	0.6 ± 1.9	17	0.3 ± 0.2	Mid-B	✓

Table 2.2: Continued

#	Date Obs. yyyy-mm-dd	Group	$EW(\mathrm{H}\alpha)_S$ (Å)	$EW(\mathrm{H}\beta)$ (Å)	S/N	$\log(W_{\lambda4471}/W_{\lambda4481})$	SpT	CBe
F327	2008-10-24	Early	-20.5 ± 1.4	6.7 ± 2.0	19	0.9 ± 0.9	Mid-B	✓
	2006-12-13	Early	-21.0 ± 1.1	6.7 ± 2.0	19	0.5 ± 0.3	Mid-B	✓
F328	2010-10-09	Early	-12.0 ± 2.0	7.9 ± 2.8	14		Mid-B	✓
F329	2008-10-24	Early	-9.1 ± 1.6	8.4 ± 2.0	21	1.2 ± 2.2	Late-B	✓
	2008-10-24	Early	-10.4 ± 3.2	8.4 ± 2.0	21		Late-B	✓
F330	2010-10-09	Featureless	-13.1 ± 1.8	2.7 ± 4.2				
F331	2010-10-09	Featureless	-28.9 ± 3.8	-1.6 ± 4.8				
F332	2008-10-24	Early	-3.2 ± 1.9	8.3 ± 2.4	19	0.1 ± 0.5	Late-B	✓
F333	2006-11-17	Early	-47.5 ± 0.9	6.8 ± 1.1	43	0.3 ± 0.1	B6	
F334	2008-10-24	Early	-19.2 ± 1.6	8.5 ± 1.9	22		Late-B	✓
	2006-11-17	Early	-19.4 ± 1.5	8.5 ± 1.9	22		Late-B	✓
F335	2008-10-24	Late	-14.8 ± 1.4	3.2 ± 2.5				
F336	2008-10-24	F-type	-81.3 ± 1.9	2.3 ± 2.0				
F337	2006-11-26	Early	-12.2 ± 1.3	6.3 ± 1.6	24		Late-B	✓
F338	2005-01-17	Featureless	-28.4 ± 1.0	0.8 ± 1.4				
	2008-12-21	Early	-12.0 ± 2.7	17.2 ± 3.5	10	1.8 ± 2.0	Late-B	
F339	2007-01-15	Early	-1.3 ± 6.8	17.2 ± 3.5	10		Late-B	
	2008-12-21	Early	-12.0 ± 3.0	17.2 ± 3.5	10		Late-B	
F340	2008-02-06	Early	-7.7 ± 1.5	4.4 ± 1.8	25	3.1 ± 108.9	Early-B	✓
	2005-01-17	Early	-13.8 ± 0.7	4.4 ± 1.8	25		Early-B	✓
	2008-12-21	Late	-18.9 ± 2.2	-1.1 ± 8.7			mid-K	
F341	2007-01-15	Late	-26.1 ± 3.0	-1.1 ± 8.7			mid-K	
	2008-12-21	Late	-20.3 ± 1.9	-1.1 ± 8.7			mid-K	
	2007-01-15	Featureless	-13.5 ± 3.7	7.8 ± 4.9				
F342	2008-12-21	Featureless	-11.2 ± 6.5	7.8 ± 4.9				
	2008-12-21	Featureless	-11.6 ± 2.4	7.8 ± 4.9				

Table 2.2: Continued

#	Date Obs. yyyy-mm-dd	Group	$EW(\mathrm{H}\alpha)_S$ (Å)	$EW(\mathrm{H}\beta)$ (Å)	S/N	$\log(W_{\lambda 4471}/W_{\lambda 4481})$	SpT	CBe
	2008-02-06	Early	3.2 ± 1.1	6.9 ± 1.4	43		Mid-B	✓
F343	2007-01-15	Early	2.7 ± 1.2	6.9 ± 1.4	43		Mid-B	✓
	2006-11-17	Early	1.3 ± 1.0	6.9 ± 1.4	43		Mid-B	✓
	2008-12-22	Featureless	-53.7 ± 1.5	-3.7 ± 3.8				
F344	2008-12-22	Featureless	-53.6 ± 1.7	-3.7 ± 3.8				
	2006-01-21	Featureless	-50.7 ± 1.7	-3.7 ± 3.8				
	2007-01-15	Featureless	-26.2 ± 5.3	-10.4 ± 23.3				
F345	2008-12-22	Featureless	-36.4 ± 6.5	-10.4 ± 23.3				
	2008-12-22	Featureless	-23.7 ± 3.6	-10.4 ± 23.3				
F346	2009-11-19	Early	-11.6 ± 1.8	6.7 ± 2.5	15		Mid-B	✓
F347	2005-01-17	Early	-18.4 ± 0.8	8.8 ± 0.9	23	-0.5 ± 0.1	Late-B	
	2008-12-28	Featureless	-49.8 ± 6.0	-10.6 ± 22.2				
F348	2007-01-15	Featureless	-38.1 ± 4.7	-10.6 ± 22.2				
	2008-12-28	Featureless	-53.5 ± 7.3	-10.6 ± 22.2				
F349	2008-02-06	Early	-29.0 ± 1.8	4.9 ± 2.2	19	0.4 ± 0.2	Mid-B	✓
	2005-01-17	Early	-28.3 ± 1.1	4.9 ± 2.2	19	0.5 ± 0.2	Mid-B	✓
F350	2005-01-17	Early	-39.9 ± 0.8	1.9 ± 1.0	28	0.5 ± 0.2	B3	✓
F351[4]	2006-02-03		-19.6 ± 2.9	5.2 ± 2.5				
F352	2005-01-17	Early	-20.1 ± 1.0	6.2 ± 1.3	25		Late-B	✓
F353	2005-01-17	Early	-6.6 ± 1.1	4.4 ± 1.3	21	0.6 ± 0.3	Mid-B	✓
F354	2008-02-06	Early	-7.2 ± 1.3	8.5 ± 1.6	22	-0.1 ± 0.1	Late-B	✓
	2006-02-03	Early	-6.2 ± 1.2	8.5 ± 1.6	22	-0.1 ± 0.3	Late-B	✓
F355	2008-02-06	Early	-21.6 ± 1.4	7.8 ± 1.6	23	1.7 ± 7.0	Late-B	✓
	2006-02-03	Early	-22.6 ± 1.1	7.8 ± 1.6	23	0.7 ± 0.5	Late-B	✓
F356	2008-02-06	Early	-23.1 ± 1.6	5.0 ± 1.3	27		Mid-B	✓
	2005-01-17	Early	-23.6 ± 0.9	5.0 ± 1.3	27	0.3 ± 0.2	Mid-B	✓

Table 2.2: Continued

#	Date Obs. yyyy-mm-dd	Group	$EW(\mathrm{H}\alpha)_S$ (Å)	$EW(\mathrm{H}\beta)$ (Å)	S/N	$\log(W_{\lambda 4471}/W_{\lambda 4481})$	SpT	CBe
F357	2006-02-03	Featureless	-70.0 ± 0.9	-1.1 ± 1.7				
F358	2007-01-17	Featureless	-25.4 ± 3.5	9.2 ± 10.8				
F359	2005-01-20	Early	-48.4 ± 1.1	0.2 ± 2.4	13	0.4 ± 0.4	Early-B	✓
F360	2005-03-09	Early	-16.2 ± 0.9	4.0 ± 1.4	24	0.5 ± 0.4	Mid-B	✓
F361	2006-02-03	Early	-24.1 ± 1.9	13.4 ± 3.5	9	0.9 ± 1.4	Late-B	
F362	2008-02-06	Early	-34.1 ± 1.5	4.2 ± 2.2	16		Late-B	✓
	2006-02-03	Early	-32.5 ± 1.1	4.2 ± 2.2	16	0.6 ± 0.4	Mid-B	✓
F363	2008-02-06	Early	-20.1 ± 2.4	9.8 ± 3.3	11		Late-B	✓
	2006-02-06	Early	-19.7 ± 1.8	9.8 ± 3.3	11	0.3 ± 0.3	Mid-B	✓
F364	2009-12-18	Featureless	-39.1 ± 2.1	2.7 ± 2.6				
F365	2006-02-06	Featureless	-26.3 ± 2.5	3.3 ± 5.4				
F366	2006-02-06	Early	-41.2 ± 1.7	7.6 ± 2.1	11	0.1 ± 0.2	Late-B	
F367	2008-02-07	Early	-4.2 ± 1.9	9.5 ± 2.1	26		Late-B	✓
	2007-02-21	Early	-3.3 ± 2.0	9.5 ± 2.1	26	-0.0 ± 0.2	Late-B	✓
F368	2006-02-06	Early	-20.8 ± 1.3	1.5 ± 2.3	13		Early-B	✓
	2008-02-07	Early	-13.3 ± 2.0	1.5 ± 2.3	13	0.5 ± 0.5	Early-B	✓
F369	2008-02-07	Early	-17.8 ± 1.9	5.2 ± 3.4	11		Late-B	✓
	2006-02-06	Early	-14.3 ± 1.9	5.2 ± 3.4	11		Early-B	✓
F370	2009-12-15	Featureless	-12.6 ± 1.8	6.9 ± 4.0				

[1] Two stars with small angular separation were observed.
[2] The Hα was wrongly clipped.
[3] More probably a brighter B-type star was observed, instead of the fainter proposed target.
[4] Poor sky subtraction.

Chapter 3

Second stage spectroscopic follow-up: intermediate-resolution spectra

Here, I introduce the second phase of follow-up, which has targeted 91 IPHAS Hα emitters. The sample selection, observations and data reduction are described. The discussion regarding the spectral typing is organised in two parts. The first part focuses on a sample of 68 CBe stars, which have been studied further (see Chapters 4 and 5 and 6). The second part describes the remaining stars, that are mainly young stellar objects.

3.1 Introduction

While the FLWO/FAST observations were acquired, the IPHAS collaboration was awarded an International Time Programme (ITP) 2006-2008 at the Observatory of Roque de Los Muchachos in La Palma. Some of the allocated time was used for follow-up spectroscopy in the Perseus Arm. During these observations and two further runs (in 2009 and 2010), 91 stars were reobserved at higher resolution and with superior signal-to-noise ratio. Given the immense potential of IPHAS, for picking out distant or faint emission line objects, the La Palma observations aimed at studying some of the most “likely to be” distant stars covering a range of diverse environments in the surveyed area. A group of possible CBe stars has been identified, along with a selection of more likely YSOs. The choice of suitable targets took place while FLWO/FAST observations were still ongoing, and some targets were selected on the basis of the available spectroscopic information, while others were chosen using their inferred properties from IPHAS and 2MASS photometry, along with inspection of their spatial distribution.

3.2 Sample selection

The wider aim of these observing programmes was to achieve comprehensive spectroscopic coverage of the emission line star population, as revealed by IPHAS, over a well-defined section of the northern Plane. In the expectation (now supported) that the brighter

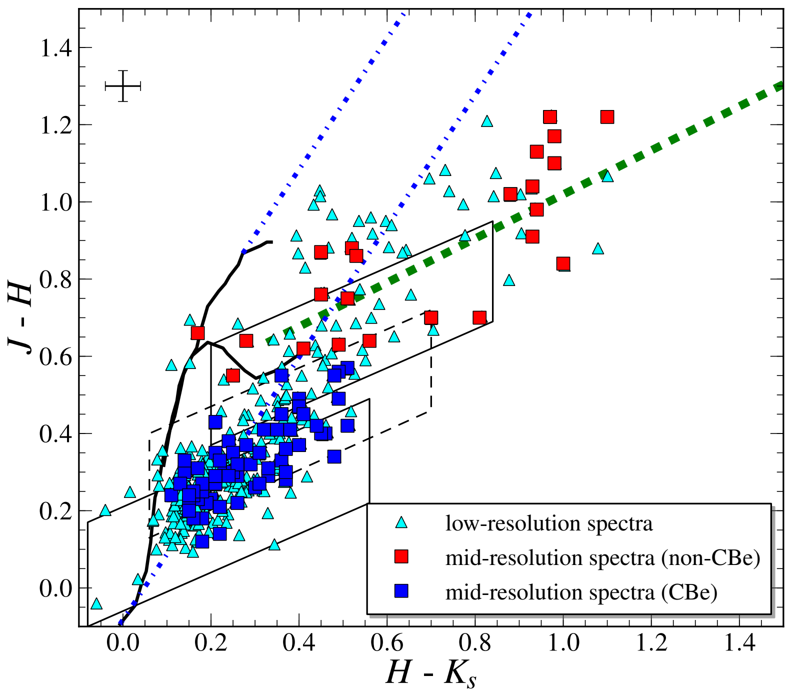

Figure 3.1: 2MASS near-IR colour-colour diagram of the observed sample of emission line stars. The colour scheme is defined in the legend. The solid line follows the dwarf and giant unreddened sequences (Bessell & Brett, 1988). The blue dot-dashed lines are the reddening vectors from Rieke & Lebofsky (1985). The boxes drawn are due to Corradi et al. (2008) and roughly delineates the region CBe stars with $A_V \sim 2, 4, 6$ would occupy, while the green dashed line is the unreddened CTTSs locus (Meyer, Calvet & Hillenbrand, 1997). All the plotted curves are converted to the 2MASS system, adopting relationships defined in Carpenter (2001). Typical error bars, for the stars that have got intermediate-resolution spectra, are in the upper left corner of the diagram

population ($r \leq 17$) would be dominated by CBe stars, a second aim was to use these relatively luminous objects as probes of the Perseus Arm and the Outer Arm beyond, and as test of the knowledge of extinction in the area.

The available FLWO/FAST observations played an exploratory role, prior to the second follow-up phase and the knowledge gained from them aided the choice of suitable targets for more in-depth follow-up. The approach taken to building up the final higher resolution sample, in the 2009/10 sample was to chose additional targets, to add to those observed during the ITP such that the parameter space in the 2MASS ($J-H$, $H-K$) was sampled in a uniform way, or in other words, in the less biased way possible.

From the initial follow-up appeared evident that more than 60% of the emitters with $r \leq 17$ are Be stars, and that most of them are CBe stars. The remaining Be stars are likely to be Herbig Be stars, as they also show forbidden emission lines and larger IR excess (see e.g. Section 2.4 and 2.5). Furthermore, a minor number of low-mass YSOs are also found, but they are less frequent due to the magnitude cut. In 2009/10 the aim was to obtain spectra of targets making use of this acquired knowledge. Fig. 3.1 and 3.2

are the additional tools that drove the selection. Ninety-one stars have been observed in La Palma: these are represented in the figures by blue and red squares. The triangles are used to display the stars with FLWO/FAST spectra, for comparison.

Seventy-eight stars are picked among the emitters that are seen enclosed within the three boxes of Fig. 3.1. As noted before, these represent the colour ranges in the near-IR diagram where typical CBe are found (Corradi et al., 2008). Following the spectral classification of Section 3.4, 9 of the stars within the $A_V = 6$ box, which are the ones with $(J-H) \gtrsim 0.6$, are dismissed from the CBe group (this is also anticipated by the colour code used in Fig. 3.1 and 3.2). The remaining stars are seen above the CTTS locus or in its proximity. This approach granted a mixed but representative population of Be stars (even when from the low-resolution spectra it was not definitely clear which class of emitters they belonged to). Among the observed stars, I identified a few late-type stars. As it is evident from Fig. 3.2, no particular location has been preferred and the area has been surveyed quite uniformly. Although in figure a group of stars, which can be seen at about $\ell = 136°$, forms a line perpendicular to the Galactic plane that follows the left edge of the W4 H II region, not all of them are in the Perseus Arm, as the spectroscopic parallaxes of Chapter 6 confirm.

In Fig. 3.3, is the IPHAS colour-colour diagram. The CBe stars observed in La Palma have colour excesses that range between 0.6 – 1.6 mag, as will be demonstrated clearly in Chapter 4, consistent with the majority of them falling within the $A_V = 4$ box from Corradi et al. (2008). In Table 3.2, the IPHAS and 2MASS magnitudes of the stars, for which intermediate-resolution spectra have been collected, are provided.

3.3 Observations and data reduction

The intermediate-resolution higher quality spectra of the 91 selected targets were obtained on La Palma at the Isaac Newton Telescope (INT), using the Intermediate Dispersion Spectrograph (IDS), and on the Nordic Optical Telescope (NOT) using the Andalucia Faint Object Spectrograph and Camera (ALFOSC). The data were obtained over 18 nights between the years of 2006 and 2010.

Relevant information about spectrograph set-ups for these observations is listed in Table 3.1. The main point of contrast between the INT and NOT data is that a bluer, higher resolution grating was chosen for the latter, offering better opportunities for traditional

Table 3.1: La Palma observations and relevant telescope set-up information, sorted by date of observation.

Run	Telescope/Instrument	Grating	Wavelength interval	$\Delta\lambda$	Observed	Apparent magnitude (r)
2006-08-27/29 2006-09-08	INT/IDS	R300V	3500-7500 Å	$\sim$ 4Å	35	$\sim$ 14.0 – 16.0
2007-12-04/07	NOT/ALFOSC	#16	3500-5000 Å	$\sim$ 2Å	39	$\sim$ 13.5 – 17.0
2009-11-27/30	INT/IDS	R400V	3500-7500 Å	$\sim$ 3Å	11	$\sim$ 13.0 – 14.0
2010-10-21/26	INT/IDS	R400V	3500-7500 Å	$\sim$ 3Å	10	$\sim$ 13.0 – 16.0

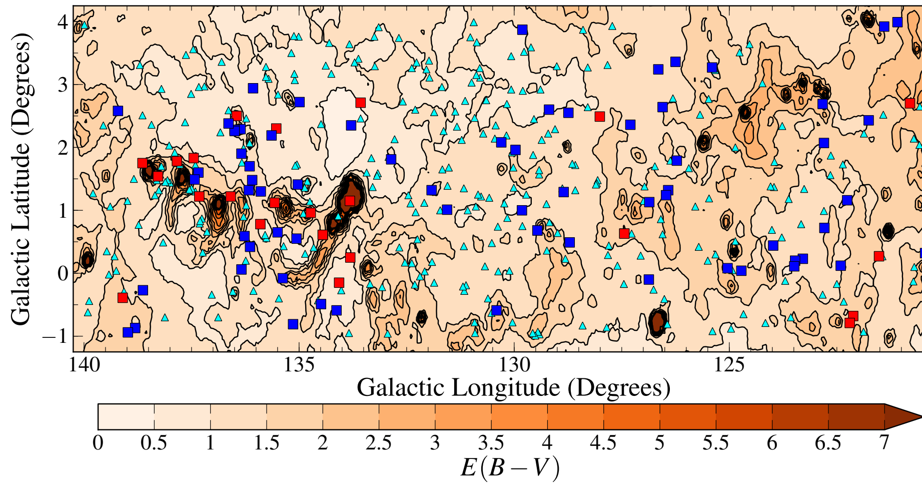

Figure 3.2: The contour map of integrated dust column across the area, from Schlegel, Finkbeiner & Davis (1998). Symbols and colour scheme are the same as in Fig. 3.1.

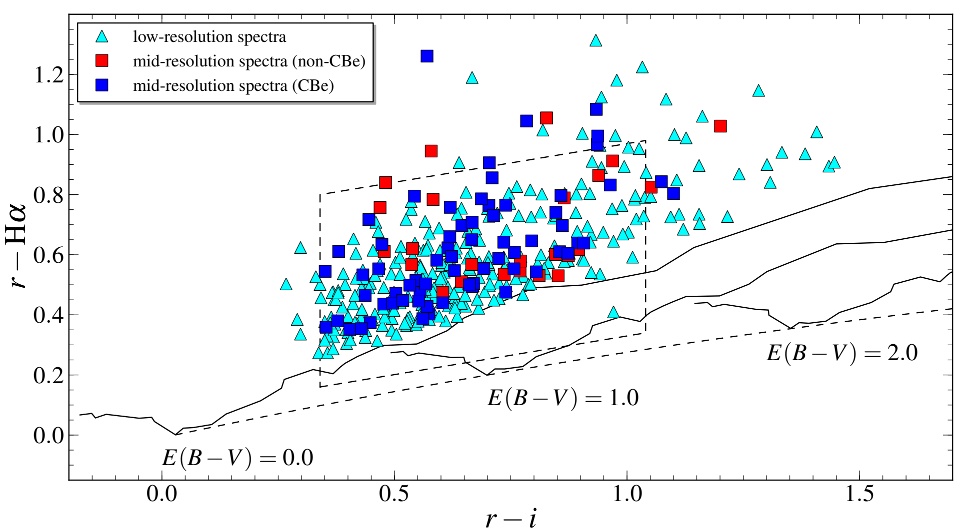

Figure 3.3: IPHAS colour-colour diagram of the observed targets. Colours and symbols are explained in the legend. Black solid lines are synthetic main sequence loci, at $E(B-V) = 0.0$, 1.0, 2.0 (see e.g. Table 2 in Drew et al., 2005). These move parallel to the reddening vector that is plotted as the early-A reddening curve (dashed lower curve). The box drawn above the unreddened main sequence defines the region in which CBe stars with $A_v \sim 4$ are likely to be located (cf Fig. 3.1 and the discussion to be found in Corradi et al. (2008). The CBe stars, for which I have obtained intermediate-resolution spectra, are picked out as blue squares.

blue-range spectral-typing – at the price of no coverage of the Hα region.

A further practical criterion that came into play in deciding which of the target stars to prioritise for intermediate-resolution spectroscopy was to prefer objects for which $(B-r) \lesssim 1.7$ was anticipated, giving a better prospect of a blue spectrum of usable quality. Four targets were observed twice using different telescopes and/or instrument set-ups.

To break this down a little further, three runs took place at the INT (semester B, 2006, 2009 and 2010), observing respectively 38, 12, and 10 objects with the IDS. In 2006, the R300V grating was used, with a dispersion of 1.87 Å/pix, while in the other two runs the R400V was preferred, giving 1.41 Å/pix. During each run, the slit width was 1" so as to achieve spectral resolutions of, respectively, $\Delta\lambda \approx 4$ Å and $\Delta\lambda \approx 3$Å. Both set-ups cover the blue-visible interval and extend into the far red, but the disturbance due to fringing at wavelengths longer than $\sim \lambda7500$ Å was sufficiently severe that in practice I did not use the spectrum at these longer wavelengths.

Thirty–nine spectra were observed with NOT/ALFOSC, in December 2007, using grating #16, which gives a dispersion of 0.77 Å/pix. The slit width was set to 0.45", in order to achieve a resolution of $\Delta\lambda \approx 2$ Å. The wavelength interval covers the blue spectrum, from the Balmer jump up to Hβ.

Data reduction - i.e. the standard steps of bias subtraction, flat-fielding, sky subtraction, wavelength calibration, extraction and flux calibration - was accomplished by using IRAF routines for the reduction of long slit spectra (mainly from the *twodspec, onedspec* packages).

Spectrophotometric standards were observed across all the nights, with a wider slit, to allow a relative flux calibration to be applied. Also to enable this, all target stars were observed with the slit angle set at the parallactic value. More details onto the flux calibration are given in the next section.

Negligibly reddened spectral type standards were also observed from time to time, and these provided us with some useful checks on the final flux calibration applied to our data.

On most nights, arc lamps were acquired before and after each star was observed, and were subsequently used as the basis for wavelength calibration. The wavelength precision achieved ranges between 0.10 and 0.15Å.

At least two exposures were obtained for each target in order to mitigate ill effects from unfortunately-placed cosmic rays but in many instances three or four exposures were collected to improve the signal-to-noise ratio. Individual exposure times ranged from 300 sec for the brightest targets, up to 1800 sec for the faintest. The S/N ratio, at 4500 Å, ranges from 22 up to just over 100, the median of the distribution being 45.

3.3.1 Flux calibration

Measuring reliable spectrophotometric reddenings becomes an option if there is good quality flux calibration, over a large wavelength range. To ensure this option is open, much effort has been put onto a precise flux calibration.

An unfortunate choice of standards in the first INT run prevented the construction of a validated flux calibration curve at wavelengths redder than $\lambda5000$ Å. However, at shorter

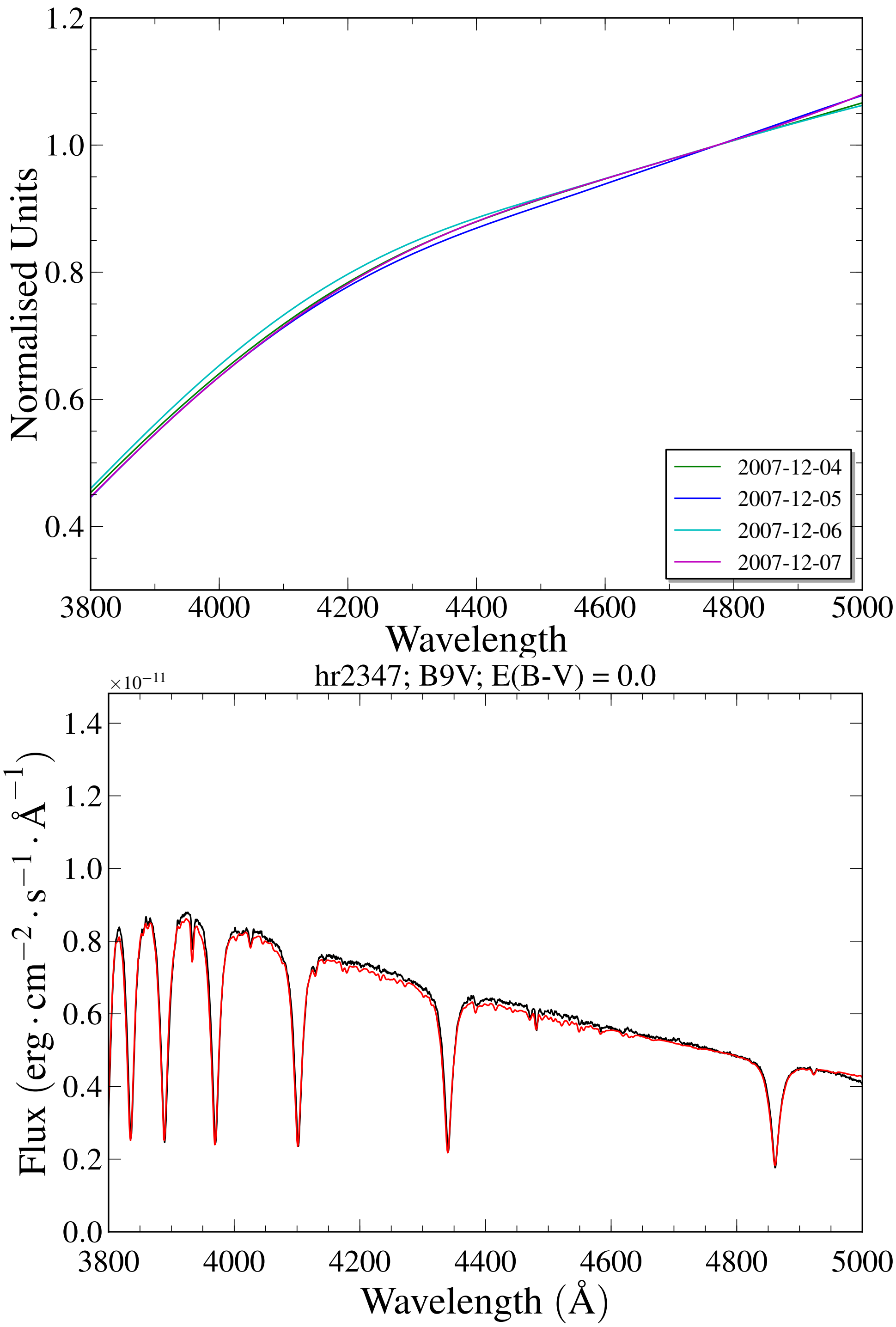

Figure 3.4: In the top panel are the average sensitivity functions for the 4 nights of observations at the NOT/ALFOSC. Bottom panel shows the spectral type standard HR2347 after flux calibration (in black) and the appropriate model atmosphere from Munari et al. (2005) superimposed (in red).

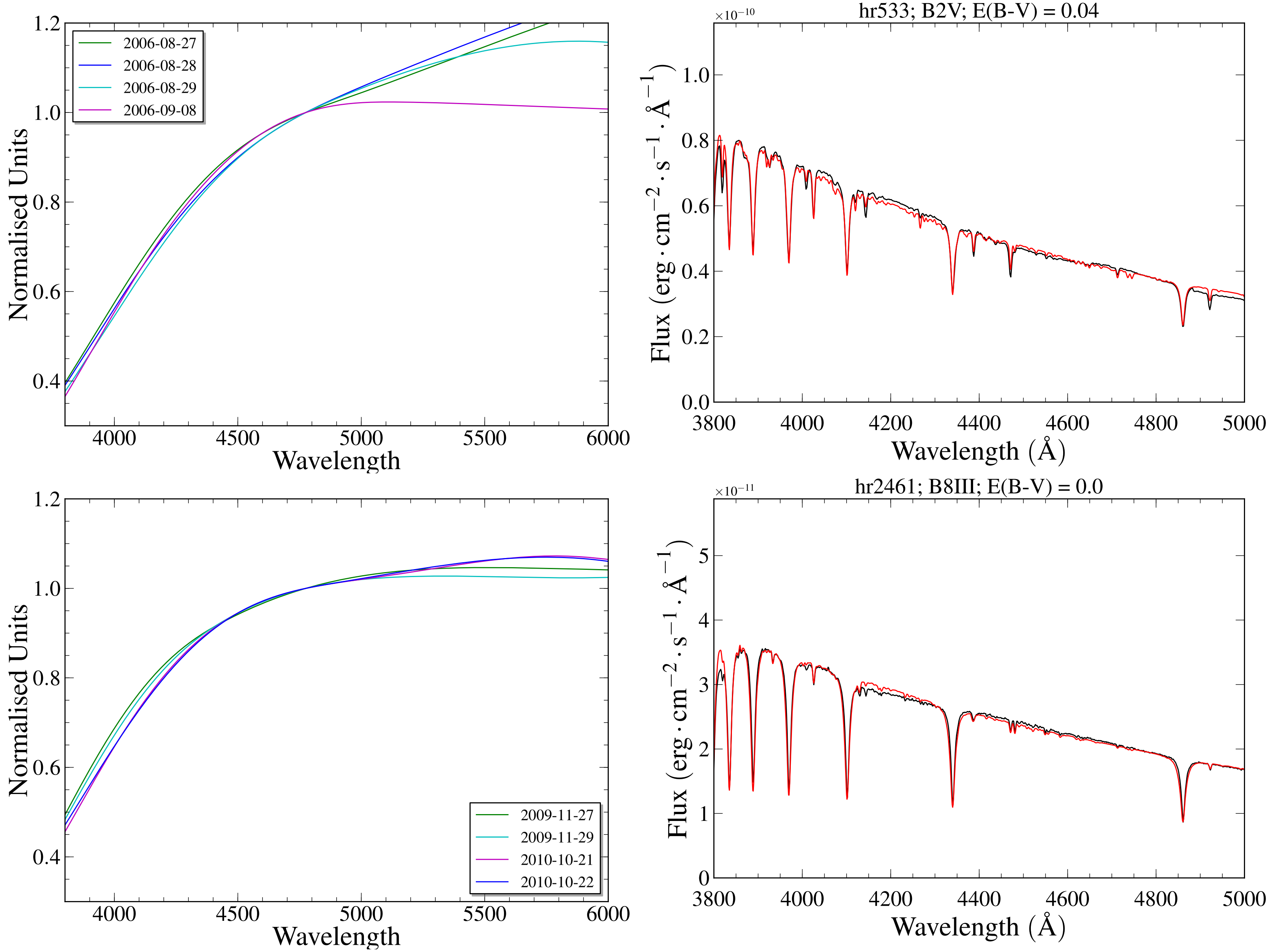

Figure 3.5: Left panels are the sensitivity functions for the INT/IDS observations: (top) the 2007 run, using the R300V grating; (bottom) the 2009/2010 runs, using the R400V grating. Right panels show two spectral type standards after flux calibration (in black) and the corresponding appropriate model atmosphere from Munari et al. (2005) superimposed (in red).

wavelengths the several standard star observations available could be combined to produce a well-validated correction curve. For this reason, and because it matches the wavelength range offered by the NOT spectra, all spectrophotometric reddening estimates (Chapter 4) are based on fits to the blue spectrum.

In Fig. 3.4 and 3.5 the normalised sensitivity functions that were determined for each night of the four runs are shown. It is evident that in the first INT/IDS run (top-left panel of Fig. 3.5) the spread in sensitivity functions reveals problems at wavelengths larger than $\lambda 5000$ Å.

The goodness of the flux calibration was investigated with help of spectral type standards that were observed across each night. These spectra were dereddened (when appropriate) and compared with appropriately chosen model atmospheres (three examples are displayed in Fig. 3.4 and 3.5). Based on the observed differences in the SED slope between the standards and the model, I concluded that the flux calibration itself will not introduce reddening errors larger than $\Delta E(B-V) = 0.05$.

3.4 Spectral classification

Some of the intermediate-resolution spectra were already observed with FLWO/FAST and, therefore, were already confirmed Hα emitters, others were observed with FLWO/FAST after the intermediate-resolution observations and four of them do not have a low-resolution spectrum. Where Hα was present in the wavelength range observed, it is always seen in emission. In the higher resolution NOT data, missing the red part of the spectrum, I generally found the Hβ line to be either in emission or partially filled in.

Spectral types were first determined by direct comparison both with spectral-type standards that were acquired during each observing run (early type stars) and also with templates taken from the INDO-US library (Valdes et al., 2004). The latter needed to be degraded in spectral resolution from the original $\sim \Delta\lambda = 1$ Å to match that of our data. Eighty-four out of 91 stars are B to early-A type stars. Among these, 4 have been observed twice with different telescope/instrument in this intermediate-resolution group. The others are later type stars.

The initial by-eye classification relied on the most evident features, as described in Section 2.4.1, with the difference that the resolution and S/N ratio of the spectra allow a more precise spectral typing of each stars generally within ± 1 sub-type. The improvement in S/N ratio at 4500 Å, can be seen from the dependence of this quantity with the r magnitude, which is measured for the 181 CBe stars with FLWO/FAST spectra and the ones with La Palma spectra (Fig. 3.6).

Based on these higher quality spectra, the 91 stars have been divided in CBe stars (68 objects) and non-CBe stars (23 objects), which are generally YSOs, applying the same principles as in Section 2.5 and 2.6.

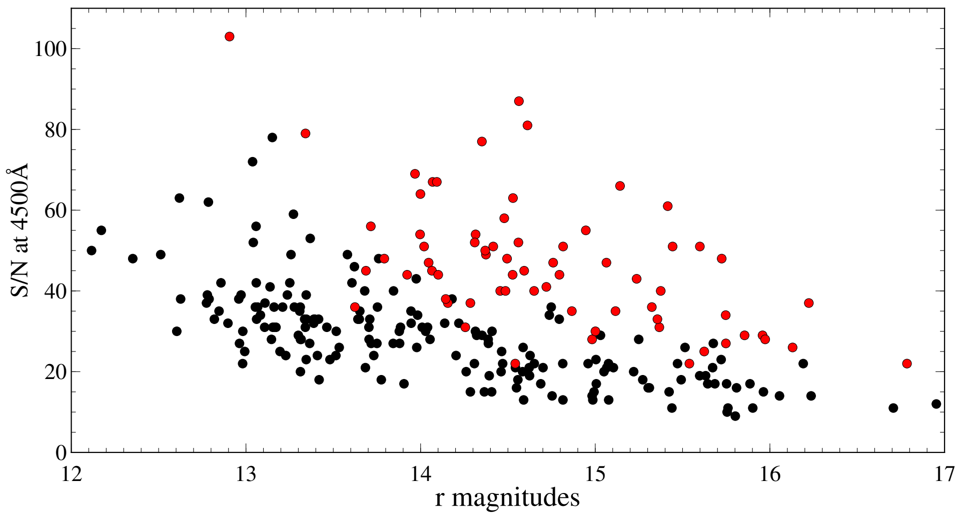

Figure 3.6: S/N ratio measured at 4500 Å is plotted against the observed *r* magnitude. Black points are used for the CBe stars identified from FLWO/FAST spectroscopy, while red dots are for the ones in the La Palma sample. The improvement in S/N ratio, in the spectral region sensible for spectral typing, is noticeable for the La Palma sample as compared to the FLWO/FAST group of CBe stars.

3.4.1 CBe stars

Nearly all stars in the sample of 68 were B stars exhibiting He I absorption, with only a couple of them crossing the boundary to A-type. No star showed He II, ruling out any as O-type. The list of reference lines for spectral type determination that I used were already given in Section 2.5. In the spectra of these stars, lines other than the Balmer series are observed sometimes in emission. Allowed strong transitions of Fe II were detectable at ($\lambda\lambda$4583, 4549, 4629 AA), ($\lambda\lambda$4923, 5018, 5169 Å) or also at ($\lambda\lambda$6248, 6318, 5384 Å), which are seen to play a role in the cooling of the circumstellar envelope (e.g. simulated disc models by Jones, Sigut & Marlborough, 2004).

How well fainter features can be detected depends on the specifics of the achieved S/N ratio and the spectral resolution – and the first of these depends in turn on how much interstellar extinction is present. Because the reddening is significant, it is generally the case that the present classification of the B stars depends heavily on the relative strengths of the He I λ4471 and Mg II λ4481 features – a good $T_{\rm eff}$ indicator, with little sensitivity to $\log g$ within classes V-III – rather than on shorter wavelength lines. As young, thin-disk objects, CBe stars are unlikely to present with distinctive blue spectra indicating significant metallicity variation, even to quite large heliocentric distances (e.g. Carraro et al., 2007, found a constant value of $[\mathrm{Fe/H}] \sim -0.35$ at $R_{\rm G} > 12$ kpc, from spectroscopy of open clusters in the outer Galaxy). So I make no attempt at this stage to treat metallicity as a detectable variable.

Furthermore, in CBe stars, the above mentioned transitions can be affected to differing extents by infilling line emission or continuum veiling due to the presence of ionised

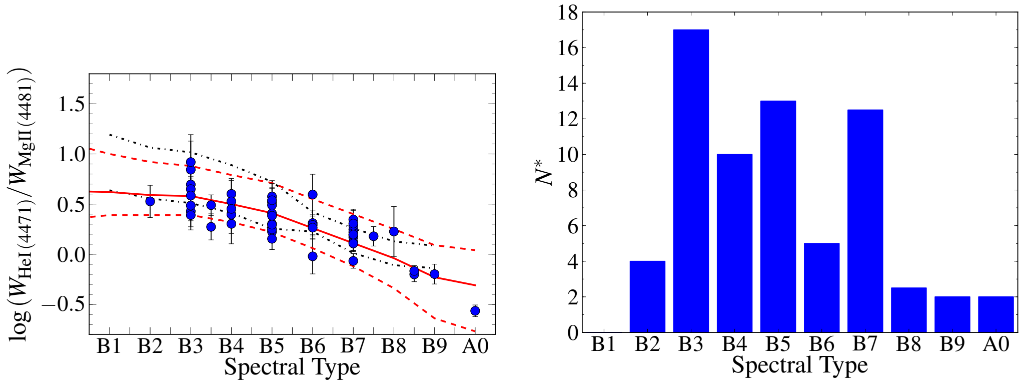

Figure 3.7: (Left): Correlation between spectral type and the logarithm of the equivalent width ratio, W(He I λ4471/Mg II λ4481. Measures are compared to with an interpolation of the high-resolution data from Chauville et al. (2001) (black dotted curves): the 68 % confidence range falls between the dashed curves. Dashed red curves represent the 1σ confidence limits obtained from repeated measures of noised model atmospheres with S/N = 40, as in Section 2.5. The blue circles are the values obtained for the observed stars. (Right): The histogram of spectral sub-types in the CBe sample.

circumstellar disks, while in faster rotators, line blending can also be an issue (Chauville et al., 2001). These factors raise challenges to a qualitative typing dependent on MS templates. To overcome these problems, line ratios rather than line strengths ought to be used, as these suffer less modification.

As a way of refining the spectral typing, where possible, I measured the absorption equivalent-width ratio $W_{\lambda 4471}/W_{\lambda 4481}$, via simple Gaussian fitting with the STARLINK/DIPSO tool, and compared it with data from Chauville et al. (2001), in Fig. 3.7. The 1σ confidence limits, determined from repeated measures from noised model atmospheres with S/N = 40, are also plotted for comparison. The precision of the typing is to ± 1 sub-type for all but the lowest quartile in S/N ratio (S/N $<$ 35) where it approaches ± 2 sub-types (these objects have generally larger uncertainties, $\Delta(\log W_{\lambda 4471}/W_{\lambda 4481}) \gtrsim 0.30$, and are not plotted in Fig. 3.7). Noisy spectra are subject to a dual bias, depending on the actual value of the line ratio. Early-B types, when the Mg II line is weaker compared to the He I line, can in principle appear earlier in type due to noise and, vice versa, a spectrum may be classified as a later type when the Mg II line is stronger than the He I line. The effect of the noise on the spectral typing, based on the $\log W_{\lambda 4471}/W_{\lambda 4481}$, is explained in Section 2.5.1.1 and it is to make the spectral typing very uncertain for $S/N \lesssim 30$. In Fig. 3.7 the distribution of spectral types in the sample is shown: most are in fact proposed to be mid B stars.

I show in Fig. 3.8 and 3.9 some examples of spectra within the 4300–4500 Å window compared with MS model atmospheres, from Munari et al. (2005), appropriate to the chosen MS spectral sub-type. The $T_{\rm eff}$ scale adopted for the mapping of spectral types onto the grid of synthetic spectra is presented in Table 1.2.

Luminosity class, for late-B and A stars, is often determined from the appearance of the

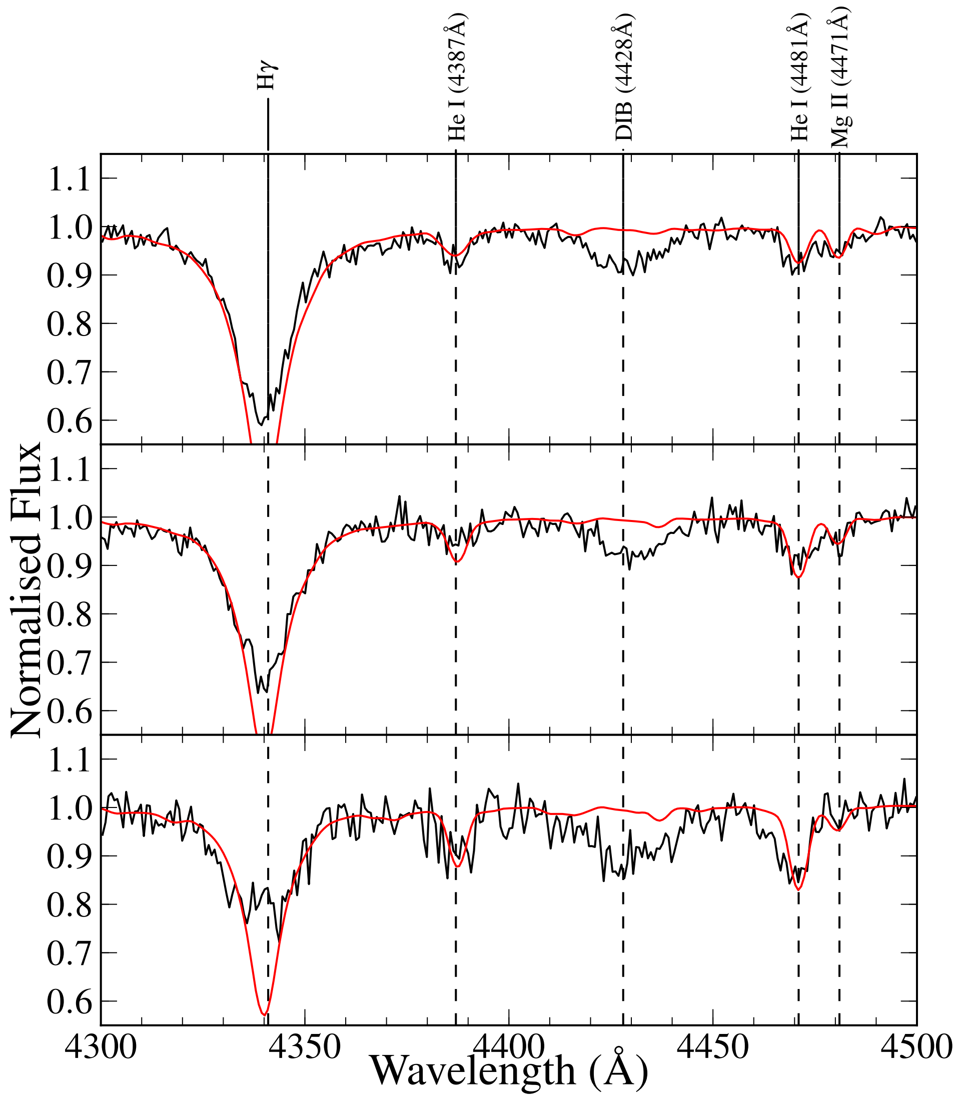

Figure 3.8: Examples of spectral type assignments based on three spectra with different S/N ratio. From top to bottom, # 41 (B7, $S/N = 64$), # 66 (B5, $S/N = 48$), # 50 (B3, $S/N = 34$). The observed spectra are in black while the preferred Munari et al. (2005) models are in red. The models have been rebinned to match that of the observations.

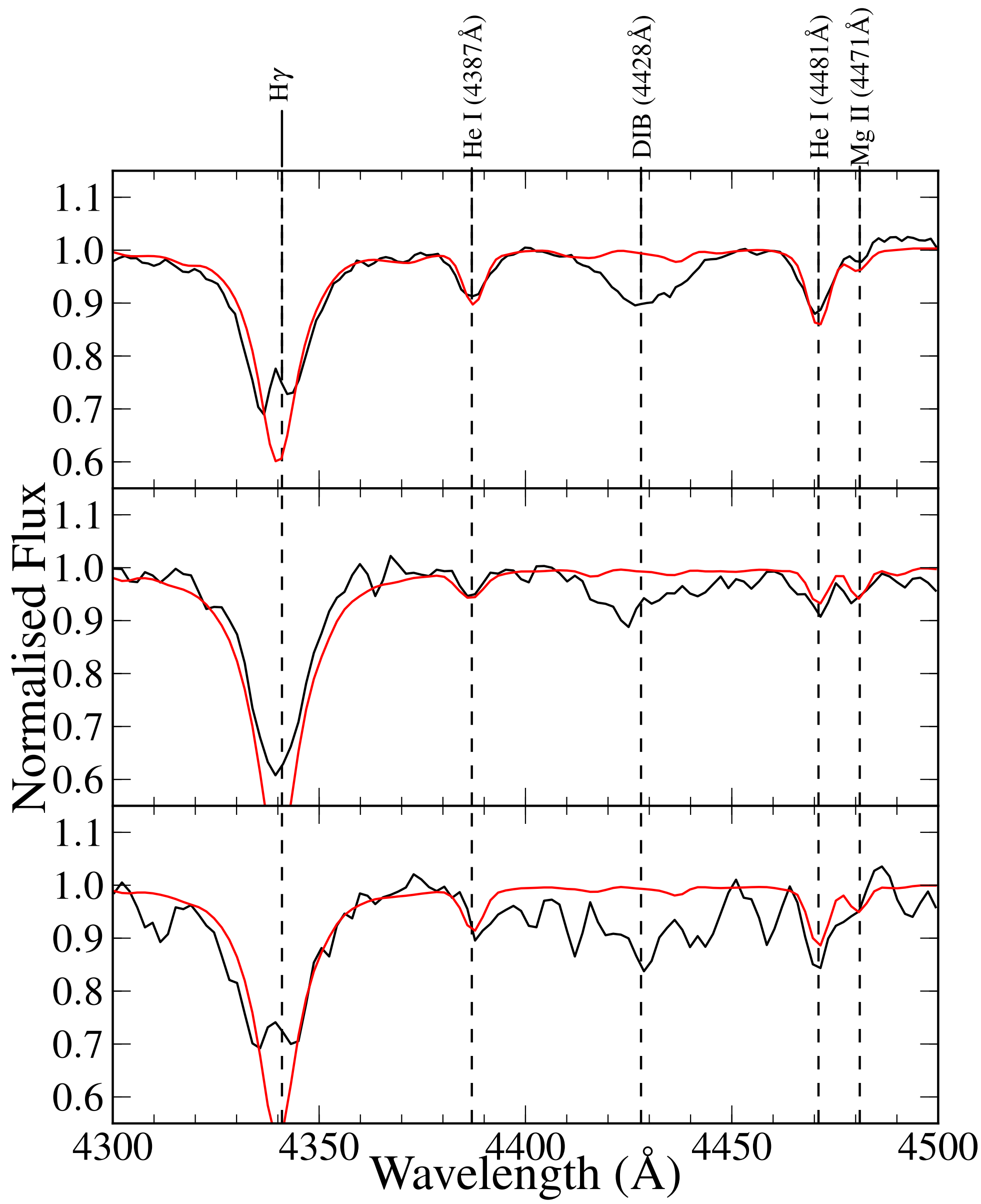

Figure 3.9: Examples of spectral type assignments based on three spectra with different S/N ratio. From top to bottom, # 45 (B3, $S/N = 103$), # 29 (B7, $S/N = 69$), # 21 (B5, $S/N = 30$). The observed spectra are in black while the preferred Munari et al. (2005) models are in red. The models have been rebinned to match that of the observations.

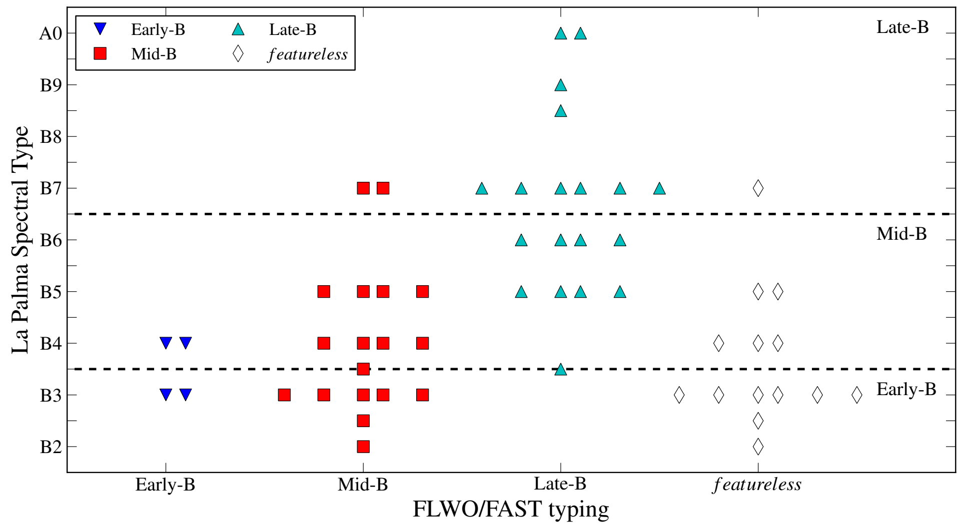

Figure 3.10: The comparison between spectral types of CBe stars, assigned both from FLWO/FAST and La Palma spectra, is shown. On the x-axis is given the spectral grouping, which has been assigned via the analysis of FLWO/FAST spectra. On the y-xais are the spectral types that I assigned from the analysis of La Palma spectra. The dahsed lines separate the spectral-type ranges, defining the grouping in early, mid, late-B types. Symbols are explained in the legend.

Balmer lines (particularly the wings). For B sub-types earlier than B4, authors cite relative strengths of O II and Si II-IV absorption lines compared with those of H I and He I ones as luminosity-sensitive also. Assigning the right luminosity class is much more difficult than assigning spectral sub-type since emission in the Balmer series interferes with the view of the Balmer line profiles for many of the objects. Furthermore the combination of S/N ratio and moderate spectral resolution hinders the classification using the Balmer-line wings and renders the weaker O and Si gravity-sensitive transitions undetectable. An evaluation of the class III-V uncertainty and its impact on the distance determination will be discussed in Section 6.

The spectral types assigned to the observed stars are set out in Table 3.2 where, for the moment, the luminosity class is left unassigned. The last two columns link to the FLWO/FAST object ID and the spectral type as it was determined from the lower resolution spectra. Spectal types assigned with an initial "guess" based on the measure of $\log(W_{\lambda\,4471}/W_{\lambda\,4481})$ from the FLWO/FAST spectra do not differ more than 2 sub-types in comparison to spectral typing based on the La Palma observations, confirming the estimated precision of the classification. Also the CBe stars having FLWO/FAST spectra with S/N ≤ 25, which were typed with a coarser classification scheme, broadly agree with the more precise typing obtained from the La Palma spectra, as it is evinced from Fig 3.10. For these CBe stars, the scatter in spectral types determined from La Palma spectra is large, as it is expected due to the fact that I grouped them in three broad groups: early, mid, and late-B. Among them, there are 4 stars that are labelled as early-B types for which the median of the La Palma spectral types is B3/B4. Eighteen CBe stars, instead, were classified in Chapter 2 as mid-B and the median of the distribution of their La Palma spectral types is B4. For the 19 stars that are classified as late-B, the median of the distribution is B7. Finally, there are other 14 stars that have only *featureless* FLWO/FAST spectra, which are mostly classified as B3 from the better spectra.

In conclusion, the spectral classification suggested in Chapter 2 is validated for the stars with FLWO/FAST spectra with S/N > 25, and satisfies the general purpose of a coarse typing for the noisier spectra.

3.4.2 Non CBe stars

Within the second group of stars there is more a variety of spectral types. I find indeed 15 candidate Herbig Ae/Be stars, 5 T-Tauri stars (G and K-types) and 3 F-type stars. All the stars showed enough photospheric absorption lines to be classified with $\pm 1 - 2$ sub-type precision, except one of the CTTSs that has a very strong veiled and emission dominated spectrum and one of the F-type stars that shows a richer spectrum of absorption lines. The spectral types assignment is presented in Table 3.2.

Consistently with the classification, both the intermediate and low-mass YSOs are clustered towards areas of higher extinction, in active SFRs. The more massive ones, are seen preferentially towards the group of molecular clouds in W3/W4/W5 that is a site of active high-mass star formation. The low-mass YSOs, are found at $\ell \approx 121^\circ$, where close-by clusters are present. The early-type stars were classified according to the scheme that is described in the previous section. Their spectra show different degrees of activity, sometimes with forbidden lines in emission (e.g. see top panel of Fig. 3.11). To classify late-type spectra, I adopted the criteria that were anticipated in Section 2.6 and I report here below with more detail (see e.g. Gray & Corbally, 2009, for reference):

- F-type: increasing strength of the Ca II K-line, in the early-F types. Fe I $\lambda\lambda$4046 Å and 4383 Å, Ca I λ4226 Å display increasing intensity at lower temperatures. Appearance of the G-Band in the mid-F spectra.

- G-type and K-types: constant increase of the Ca I λ4226 Å line, until becoming very strong at mid-K. The G-band has its maximum contrast in the G spectral types. The metal lines generally increase in strength with decreasing temperature.

As for the group of CBe stars, Balmer lines cannot be used for spectral-typing since they are seen either in emission or inverted. Particular care must be taken when using the Ca II K-line as well, since it can be filled-in or in emission.

Stars that are classified as YSOs show good examples of very strong forbidden and allowed transitions, like [O I] $\lambda\lambda$6300 Å, 6363 Å, Fe I $\lambda\lambda$4923 Å, 5018 Å, 5169 Å and He I $\lambda\lambda$5875 Å, 6678 Å. Two of the CTTSs have the whole Balmer series in emission along with the Balmer jump and the Ca I K-line in emission (mid panel of Fig. 3.11). All the late-type YSOs show Li λ6707 Å in absorption, consistent with youth.

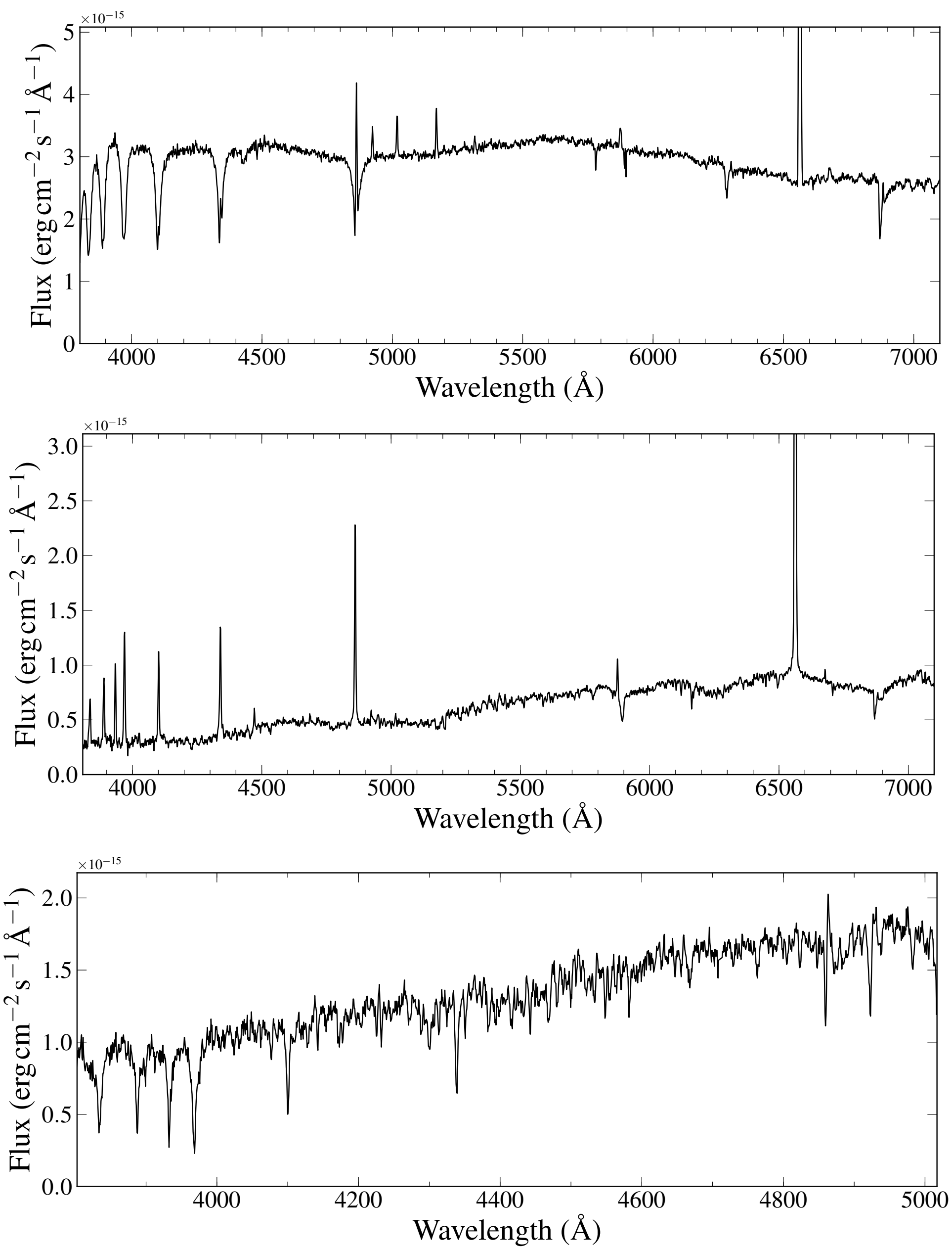

Figure 3.11: Three examples of non CBe spectra. From top to bottom: star # 85, a B9 Herbig B[e] star; star # 72 a CTTS, its FLWO/FAST spectrum (F21) was already shown in Fig. 2.10; star # 81, an F3 star.

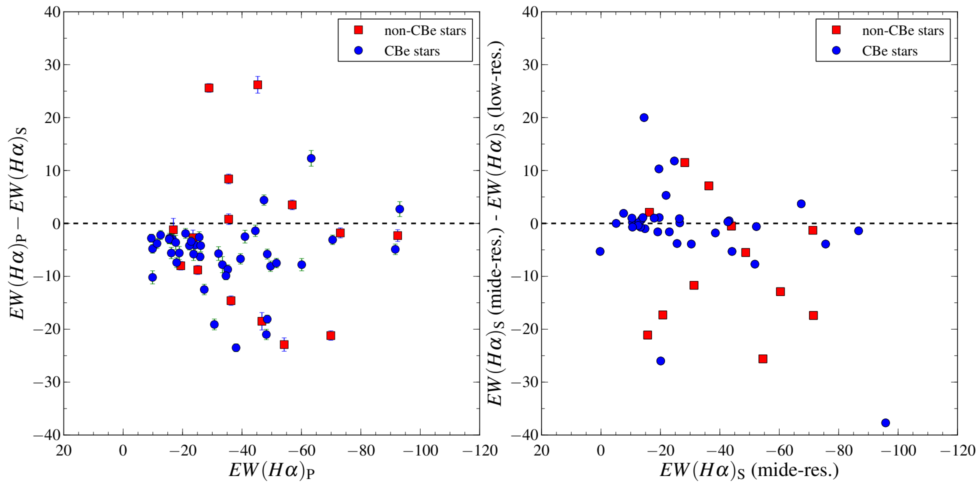

Figure 3.12: (Left): Comparison between spectroscopic measures of $EW(\mathrm{H}\alpha)_\mathrm{S}$ and photometric estimates. (Right): Hα equivalent width measures from La Palma (intermediate-resolution) and FLWO/FAST (low-resolution) spectra are compared.

The F-type stars (bottom panel of Fig. 3.11) do not show any recognisable youth signatures (all the three of them were observed with NOT/ALFOSC, therefore only the corresponding lower-resolution FLWO/FAST observations cover the red). Their $(r-i)$ colours would suggest a foreground nature, much closer than the Perseus Arm.

Finally, the left panel of Fig. 3.12 shows the comparison between photometric estimates of $EW(\mathrm{H}\alpha)_\mathrm{P}$ and spectroscopic measures $EW(\mathrm{H}\alpha)_\mathrm{S}$. CBe stars are represented in blue, while non-CBe are in red. The comparison between the two equivalent width measures appear similar to the one of Fig. 2.13. CBe stars present with $EW(\mathrm{H}\alpha)_\mathrm{P}$ generally larger than $EW(\mathrm{H}\alpha)_\mathrm{S}$. This can be either due to the fact that the photometric measure catches the star in a higher emission phase or to a systematic overestimate of the $EW(\mathrm{H}\alpha)$. On the other hand, the difference between the two measures appears more scattered around the equality line for the non-CBe stars. The right panel of Fig. 3.12, instead, shows a closer agreement between the $EW(\mathrm{H}\alpha)_\mathrm{S}$ measured from the FLWO/FAST spectrum and the La Palma spectrum, for the CBe stars, with a few scattered around. In addition, the non-CBe stars also appear to have larger scatter around the equality line.

3.5 Summary

In this chapter I presented the higher quality spectra that were acquired in four observing runs in La Palma. I divided the sample in two groups. The most numerous and homogeneous group is made of 68 CBe stars, which will be studied in the remaining chapters of the thesis. For these ones I will obtain reddening measures and distance estimates, that will be used to investigate the structure of outer Galaxy. The second one, is more heterogeneous, but it comprises a large majority of YSOs. These stars will not be followed in the remaining chapters.

Table 3.2: Photometry, $EW(\mathrm{H}\alpha)$ and spectral types of the stars with intermediate-resolution spectra Objects will be identified by their (#) number, as given in this table in the rest of the thesis. Columns are: IPHAS point-source name, which includes the J2000 RA and Dec; r magnitude, $(r-i)$ and $(r-\mathrm{H}\alpha)$ colours from IPHAS; photometric estimates of $EW(\mathrm{H}\alpha)$, from the IPHAS colour-colour diagram; J magnitudes, $(J-H)$ and $(H-K)$ colours from 2MASS; spectroscopic $EW(\mathrm{H}\alpha)$; S/N ratio at $\lambda 4500$ Å, for the CBe stars; spectral types. The last two columns are the FLWO/FAST ID number, when a match exists, and the spectral type as determined from the FLWO/FAST spectrum (see Table 2.2). The errors on the r magnitudes and the $(r-i$, $r-\mathrm{H}\alpha)$ colours are dominated by the photometric calibration and are respectively 0.02, 0.03, 0.035. $EW(\mathrm{H}\alpha)$ are not corrected for filled-in emission. CBe stars are from # 1 to # 68. The double line separates CBe stars from non-CBe stars.

#	IPHAS Jhhmmss.ss+ddmmss.s	r (mag)	$(r-i)$ (mag)	$(r-\mathrm{H}\alpha)$ (mag)	$EW(\mathrm{H}\alpha)_\mathrm{P}$ (Å)	J (mag)	$(J-H)$ (mag)	$(H-K)$ (mag)	$EW(\mathrm{H}\alpha)_\mathrm{S}$ (Å)	S/N	SpT	FAST ID	SpT
1	J002441.73+642137.5	14.76	0.86	0.61	−24	12.51 ± 0.02	0.30 ± 0.04	0.26 ± 0.04	−20.1 ± 1.1	47	B5		
2	J002926.93+630450.2	14.07	0.35	0.36	−10	13.10 ± 0.02	0.12 ± 0.04	0.18 ± 0.04	−5.1 ± 0.8	67	B7	F007	B6
3	J003248.02+664759.6	14.46	0.97	0.84	−48	12.11 ± 0.02	0.55 ± 0.03	0.36 ± 0.03	−30.4 ± 0.7	40	B3	F013	Early-B
4	J003559.30+664502.9	15.96	0.76	0.61	−27	14.11 ± 0.04	0.40 ± 0.06	0.46 ± 0.06	−14.8 ± 0.8	29	A0	F014	Late-B
5	J004014.89+651644.0	14.80	0.71	0.77	−50	12.95 ± 0.02	0.29 ± 0.04	0.26 ± 0.05	−41.5 ± 0.9	44	B2		
6	J004517.08+640124.1	15.62	0.89	0.64	−26	13.37 ± 0.02	0.41 ± 0.04	0.38 ± 0.04	−21.9 ± 1.0	25	B3	F022	Early-B
7	J004651.69+625914.3	14.87	0.51	0.45	−16	13.32 ± 0.02	0.22 ± 0.04	0.26 ± 0.05	−10.6 ± 1.0	35	B7	F025	Late-B
8	J005011.89+633525.8	15.37	0.62	0.63	−33	13.69 ± 0.02	0.28 ± 0.04	0.37 ± 0.05	−25.6 ± 1.4	31	B3	F030	Mid-B
9	J005012.69+645621.6	14.16	0.56	0.48	−18	12.65 ± 0.03	0.30 ± 0.05	0.14 ± 0.05	−10.6 ± 0.9	37	B5	F031	B5
10	J005029.25+653330.8	14.65	0.67	0.65	−35	12.97 ± 0.02	0.26 ± 0.04	0.30 ± 0.04	−26.5 ± 0.8	40	B7	F032	Mid-B
11	J005436.84+630549.9	14.95	0.62	0.76	−52	13.30 ± 0.03	0.33 ± 0.05	0.36 ± 0.05	−44.1 ± 0.8	55	B2-3	F035	Mid-B
12	J005611.62+630350.5	14.37	0.50	0.47	−19	12.95 ± 0.02	0.18 ± 0.03	0.18 ± 0.03	−13.3 ± 1.2	49	B5	F036	Late-B
13	J005619.50+625824.0	14.61	0.38	0.38	−11	13.46 ± 0.02	0.23 ± 0.03	0.20 ± 0.04	−7.6 ± 0.9	81	B5	F037	Late-B
14	J010045.58+631740.2	15.42	0.74	0.65	−32	13.53 ± 0.02	0.32 ± 0.04	0.29 ± 0.05	−26.4 ± 1.2	61	B4	F043	Featureless
15	J010707.68+625117.0	14.56	0.72	0.58	−26	12.65 ± 0.02	0.38 ± 0.03	0.24 ± 0.03	−19.6 ± 0.7	87	B5	F051	Featureless
16	J010958.80+625229.3	14.09	0.86	0.69	−35	12.44 ± 0.02	0.47 ± 0.04	0.40 ± 0.04	−24.7 ± 0.7	67	B3	F058	Featureless
17	J011543.94+660116.1	14.14	0.93	1.08	−92	11.95 ± 0.02	0.49 ± 0.04	0.40 ± 0.04	−86.7 ± 0.8	38	B3	F064	Featureless
18	J012158.74+642812.8	14.32	0.72	0.74	−44	12.74 ± 0.03	0.29 ± 0.05	0.33 ± 0.05	−43.1 ± 1.0	54	B4	F071	Mid-B
19	J012405.42+660059.9	14.98	0.63	0.54	−24	13.45 ± 0.03	0.27 ± 0.04	0.21 ± 0.04	−17.9 ± 1.1	28	B6	F078	Late-B
20	J012320.10+635830.7	14.02	0.94	0.97	−70	11.89 ± 0.02	0.47 ± 0.03	0.40 ± 0.03	−67.4 ± 0.8	51	B3	F073	Featureless
21	J012339.76+635312.9	15.00	0.85	0.74	−41	12.96 ± 0.02	0.41 ± 0.03	0.35 ± 0.03	−38.5 ± 1.1	30	B5	F076	Late-B
22	J012609.27+651617.7	14.72	0.91	0.64	−26	12.79 ± 0.03	0.45 ± 0.04	0.36 ± 0.03	−23.0 ± 0.9	41	B4	F082	Featureless
23	J012751.29+655104.0	14.50	0.74	0.77	−48	12.76 ± 0.02	0.37 ± 0.04	0.28 ± 0.04	−42.7 ± 0.9	48	B7	F086	Featureless
24	J012703.24+634333.2	14.00	0.86	0.80	−48	11.60 ± 0.02	0.37 ± 0.04	0.40 ± 0.04	−27.2 ± 0.9	54	B3	F084	Mid-B
25	J012540.54+623025.6	13.34	0.54	0.51	−22	12.06 ± 0.02	0.22 ± 0.02	0.19 ± 0.02	−18.1 ± 0.8	79	B5	F081	B5
26	J013245.66+645233.2	15.36	0.79	1.05	−93	13.31 ± 0.03	0.47 ± 0.04	0.40 ± 0.05	−95.8 ± 1.0	33	B3	F093	Featureless
27	J014218.74+624733.5	14.53	0.67	0.50	−17	12.90 ± 0.02	0.30 ± 0.04	0.23 ± 0.04	−13.6 ± 0.9	44	B5	F104	Late-B
28	J014620.44+644802.5	14.37	0.48	0.44	−16	13.25 ± 0.02	0.23 ± 0.04	0.17 ± 0.04	−12.8 ± 0.9	50	B7	F117	B5
29	J014458.14+633244.0	13.97	0.50	0.44	−16	12.89 ± 0.02	0.18 ± 0.04	0.16 ± 0.04	−12.5 ± 0.8	69	B7	F111	Late-B
30	J015037.67+644446.9	14.59	0.45	0.37	−10	13.52 ± 0.02	0.21 ± 0.04	0.22 ± 0.04	0.3 ± 1.2	45	B4	F127	Mid-B
31	J014905.18+624912.3	13.72	0.88	0.61	−23	11.49 ± 0.02	0.34 ± 0.04	0.48 ± 0.04	−19.5 ± 0.9	56	B3	F123	Mid-B
32	J015918.32+654955.8	15.14	0.53	0.50	−21	13.80 ± 0.02	0.24 ± 0.03	0.16 ± 0.04	−19.1 ± 0.8	66	B6	F156	Late-B

Table 3.2: Continued

#	IPHAS Jhhmmss.ss+ddmmss.s	r (mag)	$(r-i)$ (mag)	$(r-\mathrm{H}\alpha)$ (mag)	$EW(\mathrm{H}\alpha)_\mathrm{P}$ (Å)	J (mag)	$(J-H)$ (mag)	$(H-K)$ (mag)	$EW(\mathrm{H}\alpha)_\mathrm{S}$ (Å)	S/N	SpT	FAST ID	SpT
33	J015246.27+630315.0	14.35	0.57	0.40	−10	12.90 ± 0.02	0.25 ± 0.04	0.18 ± 0.04	-6.7 ± 0.7	77	B8-9		
34	J015613.22+635623.8	14.05	0.48	0.64	−40	12.82 ± 0.03	0.31 ± 0.04	0.33 ± 0.04	-32.8 ± 0.9	47	B3	F143	B3
35	J015922.53+635829.3	15.06	0.54	0.79	−60	13.36 ± 0.02	0.45 ± 0.02	0.36 ± 0.03	-52.3 ± 1.0	47	B2-3	F158	Featureless
36	J015427.15+612204.7	14.28	1.07	0.84	−47	11.55 ± 0.02	0.57 ± 0.03	0.51 ± 0.02	-51.8 ± 0.9	37	B4	F137	Featureless
37	J020734.24+623601.1	14.42	0.61	0.44	−13	12.98 ± 0.02	0.27 ± 0.04	0.18 ± 0.04	-10.4 ± 0.8	51	B6	F181	Late-B
38	J021121.67+624707.5	15.54	0.67	0.50	−18	13.93 ± 0.03	0.35 ± 0.05	0.25 ± 0.05	-14.1 ± 1.2	22	B5	F197	Mid-B
39	J022033.45+625717.4	15.75	0.71	0.86	−63	13.90 ± 0.02	0.40 ± 0.04	0.45 ± 0.04	-75.6 ± 1.1	27	B4	F218	Mid-B
40 [1]	J022953.82+630742.3	14.31	0.66	0.50	−18	12.85 ± 0.02	0.22 ± 0.03	0.15 ± 0.03		52	B2	F242	Mid-B
41 [1]	J022337.05+601602.8	14.00	0.57	0.50	−20	12.54 ± 0.02	0.25 ± 0.02	0.16 ± 0.03		64	B7	F227	Late-B
42 [1]	J022635.99+601401.8	14.54	0.94	0.99	−75	12.13 ± 0.02	0.56 ± 0.02	0.49 ± 0.03		22	B2	F234	Featureless
43 [1]	J024054.96+630009.7	15.72	0.43	0.53	−28	14.36 ± 0.02	0.29 ± 0.05	0.21 ± 0.07		48	B6		
44 [1]	J023642.66+614714.9	15.44	0.56	0.38	−8	13.95 ± 0.05	0.33 ± 0.07	0.14 ± 0.06		51	B5	F262	Featureless
45	J023404.70+605914.4	12.91	0.62	0.66	−38	11.30 ± 0.02	0.42 ± 0.03	0.51 ± 0.03	-14.5 ± 0.7	103	B3	F252	Mid-B
46 [1]	J023031.39+594127.1	14.49	0.57	0.43	−12	12.96 ± 0.02	0.31 ± 0.04	0.17 ± 0.04		40	B9	F244	Late-B
47 [1]	J023431.07+601616.6	13.62	1.10	0.80	−42	10.77 ± 0.02	0.55 ± 0.03	0.48 ± 0.04		36	B3	F255	Featureless
48 [1]	J023744.52+605352.8	16.78	0.73	0.47	−13	14.76 ± 0.03	0.27 ± 0.07	0.31 ± 0.09		22	B8		
49 [1]	J024405.38+621448.7	15.24	0.44	0.47	−20	13.80 ± 0.02	0.49 ± 0.03	0.49 ± 0.04		43	A0	F283	Late-B
50 [1]	J024252.57+611953.9	15.75	0.71	0.91	−72	13.95 ± 0.03	0.36 ± 0.05	0.37 ± 0.05		34	B3	F277	Featureless
51 [1]	J025016.66+624435.6	14.53	0.41	0.35	−8	13.22 ± 0.02	0.24 ± 0.04	0.11 ± 0.04		63	B8-9	F307	Late-B
52 [1]	J024504.86+612502.0	15.38	0.60	0.59	−29	13.82 ± 0.02	0.35 ± 0.04	0.21 ± 0.04		40	B7	F287	Late-B
53 [1]	J024146.74+602532.2	14.06	0.64	0.69	−42	12.31 ± 0.02	0.30 ± 0.03	0.25 ± 0.03		45	B7	F273	Late-B
54 [1]	J024618.12+613514.7	15.60	0.47	0.55	−29	14.33 ± 0.03	0.27 ± 0.04	0.13 ± 0.05		51	B3	F294	Mid-B
55 [1]	J024506.09+611409.1	15.97	0.68	0.78	−53	14.12 ± 0.02	0.35 ± 0.03	0.31 ± 0.04		28	B3-4	F288	Late-B
56 [1]	J024317.68+603205.5	13.69	0.67	0.71	−43	11.98 ± 0.03	0.32 ± 0.04	0.26 ± 0.04		45	B7	F279	Mid-B
57 [1]	J024159.21+600106.0	14.56	0.69	0.55	−23	12.80 ± 0.02	0.29 ± 0.03	0.21 ± 0.03		52	B7-8		
58 [1]	J024823.69+614107.1	13.92	0.35	0.54	−31	12.75 ± 0.02	0.29 ± 0.03	0.24 ± 0.03		44	B3	F300	B4
59 [1]	J025002.27+620135.9	15.86	0.58	1.27	−153	14.01 ± 0.03	0.42 ± 0.05	0.44 ± 0.05		29	B4	F306	Early-B
60 [1]	J025102.22+615733.8	14.10	0.44	0.72	−52	12.70 ± 0.02	0.30 ± 0.04	0.37 ± 0.04		44	B5	F309	Mid-B
61 [1]	J025059.14+615648.7	15.32	0.38	0.61	−39	14.16 ± 0.03	0.21 ± 0.04	0.22 ± 0.05		36	B3-4	F308	Mid-B
62 [1]	J025233.25+615902.2	14.82	0.43	0.36	−8	13.60 ± 0.03	0.14 ± 0.05	0.22 ± 0.06		51	B7	F316	Late-B
63 [1]	J025448.85+605832.1	16.13	0.76	0.55	−21	13.90 ± 0.03	0.41 ± 0.05	0.32 ± 0.05		26	B6	F319	Late-B
64 [1]	J025502.38+605001.9	14.48	0.52	0.45	−16	12.96 ± 0.02	0.33 ± 0.04	0.22 ± 0.04		58	B7		
65 [1]	J025704.89+584311.7	16.22	0.80	0.54	−18	14.13 ± 0.02	0.43 ± 0.03	0.21 ± 0.04		37	B5	F328	Mid-B
66 [1]	J025610.40+580629.6	13.79	0.55	0.44	−15	12.30 ± 0.02	0.20 ± 0.03	0.15 ± 0.03		48	B5	F324	Mid-B
67 [1]	J025700.49+575742.8	14.26	0.63	0.60	−30	12.60 ± 0.02	0.24 ± 0.03	0.15 ± 0.03		31	B4	F327	Mid-B
68	J031208.90+605534.3	15.12	0.80	0.65	−31	12.90 ± 0.02	0.45 ± 0.03	0.41 ± 0.03	-11.6 ± 0.9	35	B4	F368	Early-B
69	J003052.95+652859.8	14.52	0.94	0.86	−54	12.02 ± 0.02	0.76 ± 0.03	0.45 ± 0.04	-31.3 ± 1.2		G2-3	F010	early-K
70	J003856.78+630639.9	14.46	0.84	0.60	−24	12.27 ± 0.02	0.66 ± 0.03	0.17 ± 0.03	-20.8 ± 1.4		G1	F017	early-K
71	J004427.40+621046.6	14.49	0.87	0.79	−47	11.98 ± 0.02	0.88 ± 0.04	0.52 ± 0.04	-28.2 ± 1.6		K7	F020	mid-K
72	J004509.95+620426.4	15.40	1.05	0.82	−45	12.59 ± 0.02	0.87 ± 0.03	0.45 ± 0.03	-71.5 ± 1.5		G8	F021	late-G

Table 3.2: Continued

#	IPHAS Jhhmmss.ss+ddmmss.s	r (mag)	$(r-i)$ (mag)	$(r-\mathrm{H}\alpha)$ (mag)	$EW(\mathrm{H}\alpha)_\mathrm{P}$ (Å)	J (mag)	$(J-H)$ (mag)	$(H-K)$ (mag)	$EW(\mathrm{H}\alpha)_\mathrm{S}$ (Å)	S/N	SpT	FAST ID	SpT
73	J013130.51+630914.3	15.04	0.54	0.62	−36	13.64 ± 0.02	0.70 ± 0.04	0.70 ± 0.04	-36.3 ± 0.8		B7	F091	Early
	J013130.51+630914.3	15.04	0.54	0.62	−36	13.64 ± 0.02	0.70 ± 0.04	0.70 ± 0.04	-43.9 ± 0.7		B9	F091	Early
74	J013932.59+645302.3	12.93	0.54	0.57	−29	11.43 ± 0.02	1.22 ± 0.04	1.10 ± 0.04	-54.5 ± 0.8		B8	F103	Early
75	J022913.61+633224.5	13.79	0.74	0.54	−19	11.60 ± 0.02	0.64 ± 0.02	0.28 ± 0.02	-11.4 ± 0.7		B6		
76 [1]	J022333.64+610950.6	15.96	0.90	0.62	−23	13.42 ± 0.02	0.84 ± 0.03	1.00 ± 0.02			B9	F226	Featureless
77 [1]	J022618.80+615952.8	14.84	0.77	0.54	−20	12.44 ± 0.02	0.70 ± 0.03	0.81 ± 0.02			B7	F233	Featureless
78	J022423.65+604156.8	16.26	0.81	0.53	−17	13.71 ± 0.02	1.04 ± 0.03	0.93 ± 0.03	-15.7 ± 1.9		A0		
79	J022935.91+611556.8	13.78	0.83	1.06	−92	11.14 ± 0.02	1.22 ± 0.03	0.97 ± 0.02			B1	F240	Early
	J022935.91+611556.8	13.78	0.83	1.06	−92	11.14 ± 0.02	1.22 ± 0.03	0.97 ± 0.02	-90.1 ± 1.0		B1	F240	Early
80 [1]	J023250.45+612857.4	14.45	0.85	0.53	−15	12.17 ± 0.02	0.75 ± 0.02	0.51 ± 0.02			F8	F249	F-type
81 [1]	J024339.27+622328.8	14.24	0.77	0.58	−24	12.02 ± 0.02	0.55 ± 0.03	0.25 ± 0.02			F3	F282	F-type
82	J023950.93+611828.9	13.96	0.48	0.61	−36	12.08 ± 0.02	1.02 ± 0.03	0.88 ± 0.02			A0		
	J023950.93+611828.9	13.96	0.48	0.61	−36	12.08 ± 0.02	1.02 ± 0.03	0.88 ± 0.02	-21.7 ± 0.8		B9		
83 [1]	J024111.95+605125.4	15.88	0.60	0.47	−16	13.74 ± 0.03	1.13 ± 0.04	0.94 ± 0.03			A0	F272	Early
84 [1]	J025130.42+621052.1	15.85	0.47	0.76	−57	13.98 ± 0.03	0.91 ± 0.04	0.93 ± 0.04			B9		
85	J024748.61+605750.4	13.94	0.48	0.84	−70	12.04 ± 0.02	1.10 ± 0.03	0.98 ± 0.03			B9		
	J024748.61+605750.4	13.94	0.48	0.84	−70	12.04 ± 0.02	1.10 ± 0.03	0.98 ± 0.03	-48.7 ± 0.8		B9		
86 [1]	J025314.90+603845.5	15.86	0.88	0.60	−22	13.42 ± 0.02	0.86 ± 0.04	0.53 ± 0.04			G0		
87 [1]	J025625.38+610732.2	14.44	0.97	0.92	−60	11.86 ± 0.02	0.63 ± 0.03	0.49 ± 0.03			B4	F325	Featureless
88	J012751.32+655104.2	12.93	0.58	0.79	−57	10.82 ± 0.02	1.17 ± 0.03	0.98 ± 0.03	-60.4 ± 0.9		B8		
89	J030121.60+602856.6	13.89	0.66	0.57	−25	11.79 ± 0.02	0.98 ± 0.04	0.94 ± 0.03	-16.3 ± 0.8		B9		
90	J030442.30+602926.7	13.67	1.20	1.03	−73	10.75 ± 0.01	0.64 ± 0.02	0.56 ± 0.02	-71.3 ± 0.9		B2	F357	Featureless
91 [1]	J025950.85+582333.1	14.00	0.58	0.95	−84	12.09 ± 0.02	0.62 ± 0.03	0.41 ± 0.03			F0	F336	F-type

[1] NOT/ALFOSC spectra, which do not cover the Hα region.

Chapter 4

Measuring reddenings of the classical Be stars

In this chapter, I will describe the approach I adopted to measure reddenings of the CBe stars that were observed during the second follow-up, described in the previous chapter. Reddenings are obtained via SED-fitting of the flux calibrated spectra. An explanation of the method is given in Section 4.2. Alternative measures were obtained with IPHAS and UVEX photometry, when the latter was available, in order to compare with the SED-fitting results. The same approach can be applied applies to the CBe stars that were observed with FLWO/FAST, with the limitation that spectral types are usually more uncertain and therefore the reddening determination carries larger errors.

4.1 Introduction

Two methods are used to measure the reddening of each star in the sample. The first, which is the primary method that I deploy in the later parts of this study, is spectrophotometric and should be sensitive since it accesses the blue part of the spectrum (3800–5000 Å), for all the stars that were observed in the second phase of follow-up (Chapter 3). The second is essentially photometric, in that it makes use of the IPHAS $(r-i)$ colour but requires knowledge of spectral type (supplied by the spectroscopy). The second method will be employed more as a check on the results that are obtained with the first one, in order to investigate the presence of colour excess due to circumstellar discs, which are typical in CBe stars. Because of a wavelength dependence of the circumstellar excess emission, a difference between the reddening determinations in the blue part of the spectrum and in the red part is expected, in the sense that the photometric value is greater than the spectroscopic measure. Since UVEX photometry, is available for a smaller number of stars, I will also use the $(g-r)$ colours as a further comparison check on the assessed reddenings for a reduced group of CBe stars.

The shape of the reddening laws in the part of the Galactic plane under investigation, was studied by Fitzpatrick & Massa (2007). Its R_V seems to vary between 2.7 and 3.1, however this is based only on three stars that are seen on the near side of the Perseus Arm. As it will become evident later (Chapter 6), the majority of the stars in the sample are more distant than 2 kpc, there is no strong support to adopt a value of R_V lower than the standard 3.1. Furthermore, the choice of reddening law or, more specifically of the R_V, does not appear to be of extreme importance when the colour excess is to be measured at blue optical wavelengths. In Fig. 4.1, I compare three curves computed using the Fitzpatrick (1999) parameterisation (solid curves), with different values of the total-to-selective ratio (i.e. $R_V = 2.7, 2.9, 3.1$), along with the Cardelli, Clayton & Mathis (1989) (dashed curve). The smoother Fitzpatrick (1999) formulation is preferred to the Cardelli, Clayton & Mathis (1989). The three solid curves are basically the same up to ~ 7000 Å, after which they diverge slightly. It becomes evident that measures of reddenings from the blue part of the spectrum would not be affected by the choice of R_V, while IPHAS $(r-i)$ experiences a minor difference in the i band. The filter profiles are plotted in Figure 4.2, along with the transmission curve of the INT/WFC system. The choice of reddening law or, more specifically of the R_V, does not appear to be of extreme importance when the colour excess is to be measured at blue optical wavelengths.

While the measure of reddenings in the blue is independent from the particular choice of R_V, the particular choice of R_V that is made will become more important when distances are to be computed via spectroscopic parallaxes, in Chapter 6, as this choice alters A_r. A change from $R_V = 2.7$ to $R_V = 3.1$ implies shorter distances up to 8-10% less, which can be indeed relevant.

For now, the reddening law used in all cases is based on the formulation given in Fitzpatrick (1999) with a standard $R_V = 3.1$, unless it is differently specified.

4.2 Reddening estimation: spectroscopic method

Reddenings were determined with a least-squares method, finding the best-fit of reddened model atmospheres to the observed spectra. This SED fitting procedure was applied to the La Palma spectra as follows.

First, I mapped the spectral sub-types of Chapter 3.4 onto an approximate main-sequence $T_{\rm eff}$ scale, using Kenyon & Hartmann (1995) for main sequence stars (see Table 1.2). A comparison of the adopted temperature calibration with others that are available in the literature is discussed in Section 1.3.1. Furthermore, I treat all the stars as if they were dwarfs, since I did not supply a luminosity class in Chapter 3.4. Optical stellar SEDs, in the B-type range, are affected more by $T_{\rm eff}$ changes than $\log g$ variation. Therefore, an uncertain luminosity class assignment does affect the reddening determination but to a less extent. I nevertheless include the luminosity class uncertainty in the total error computation, along with the $T_{\rm eff}$ uncertainty.

Then, the basic idea of the fit is to compare each observed spectrum with the corresponding solar-abundance model for the appropriate $T_{\rm eff}$, with $\log(g) = 4.0$, taken from the Munari et al. (2005) library, as it is increasingly reddened – thereby seeking out the minimum reduced χ^2. Numerical experiments confirm that the treatment of all objects as

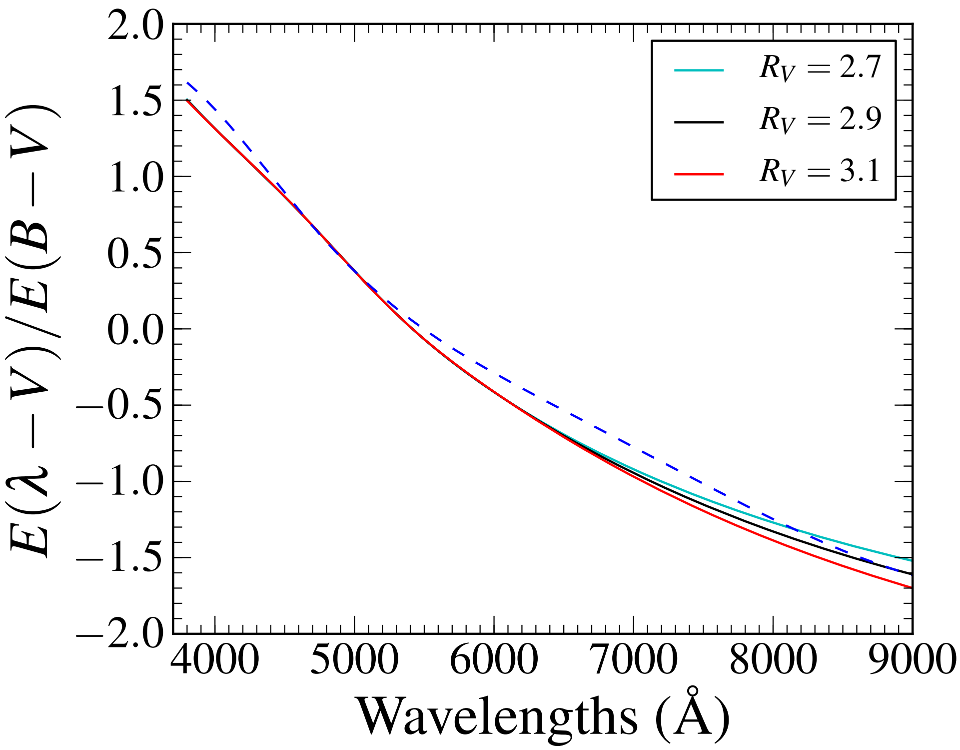

Figure 4.1: The comparison between three Fitzpatrick (1999) reddening laws, with different R_V, and the Cardelli, Clayton & Mathis (1989) (blue dashed curve) is plotted. As it appears evident, the slope of the Fitzpatrick (1999) starts changing at wavelengths redder than 7000 Å.

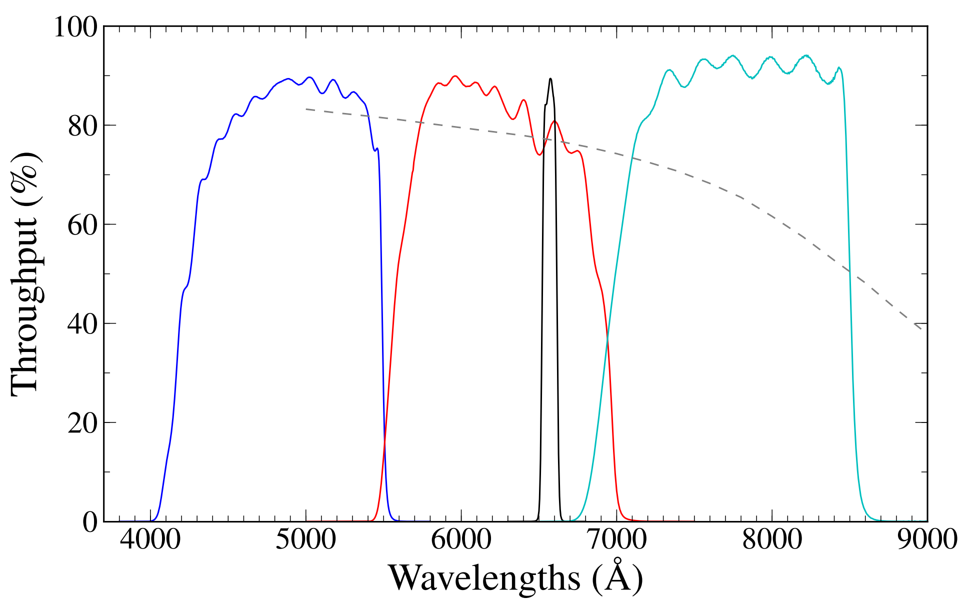

Figure 4.2: The throughput of the INT/WFC filters is shown. The g band, used in the UVEX set of filters is in blue. The IPHAS filters are in red the r band, the narrow-band Hα in black and in cyan is the i band. The dashed curve is the telescope+detector transmission curve.

main sequence stars, when they may be more luminous class IV or III stars, introduces negligible error compared to all other terms in the error budget (see below).

So that the fitting is sensitive only to the overall slope of the observed SED compared with its theoretical value and not to the details of individual lines, the fits are carried out within carefully chosen spectral intervals that are free of structure due to deep absorption lines/bands (mainly the Balmer lines and DIBs). In effect I represent both observation and model atmosphere by fluxes in a number of 'line-free' narrow bands falling in the range $\lambda\lambda 3800 - 5000$. Flux is averaged in each of these pseudo narrow bands and weighted according to the measured noise. In the fitting software, the reference model is progressively reddened, raising $E(B-V)_S$ by 0.01 mag at each step, and the quality of fit to the observed spectrum is appraised by calculating χ^2. In this approach, the number of degrees of freedom, $\nu = N - n - 1$, is the number of adopted spectral intervals (N) less the number of free parameters – here the latter number is 1 (for the reddening). In practice, fits were performed for two different normalisations at 4250 Å and 4750 Å, with the final reddening being the average of the two slightly different outcomes. Two examples of the results of this process are displayed, along with the selected wavelength intervals used in the fits, in Fig. 4.3. The corresponding minimisation of the χ^2 is shown graphically in the left panels of figure.

Errors on $E(B-V)_S$ are determined graphically, by identifying the $\Delta\chi^2 \leq 1$ range around the minimum (Fig. 4.3). I find that these are typically ± 0.05 magnitudes .

In principle a further error is introduced into the determination of $E(B-V)_S$, if the spectral type and hence the mapping onto a reference model atmosphere is incorrect. Since the Planck maximum in B and even early-A stars is in the UV, their SEDs are tending towards the Rayleigh-Jeans limit in the optical. As a consequence the spectral type uncertainty does not generate a large extra error in $E(B-V)_S$. Experiments in which the adopted model atmosphere is altered by ± 1 sub-type or uprated to luminosity class III (this corresponds to a change in temperature, according to the majority of $T_{\rm eff}$ scales available in literature; see Section 1.3.1), indicate a further error of up to ± 0.05 mag in $E(B-V)_S$. There is, in addition, a random component linked to the known SED/colour spread associated with any one spectral type: based on the *Hipparcos* dataset Houk et al. (1997) showed, for B8 – F3 stars, $\sigma(B-V) \sim 0.03$. The particular choice of reddening law does not affect the reddening determination, in this spectral range, as noted above. In the error budget, therefore, the direct fit error is in average equal or larger than the other sources of uncertainty. It is typically not more than ± 0.08 mag.

The measured spectroscopic reddenings, $E(B-V)_S$, are listed in Table 4.1.

4.3 Reddening estimation: photometric method

IPHAS photometry provides an observed $(r-i)$ colour that can be used in conjunction with the now known spectral type to give another reddening estimate. The procedure I adopted to do this has three steps:

1. The observed $(r-i)$ colour is corrected to zero Hα emission, by reference to the

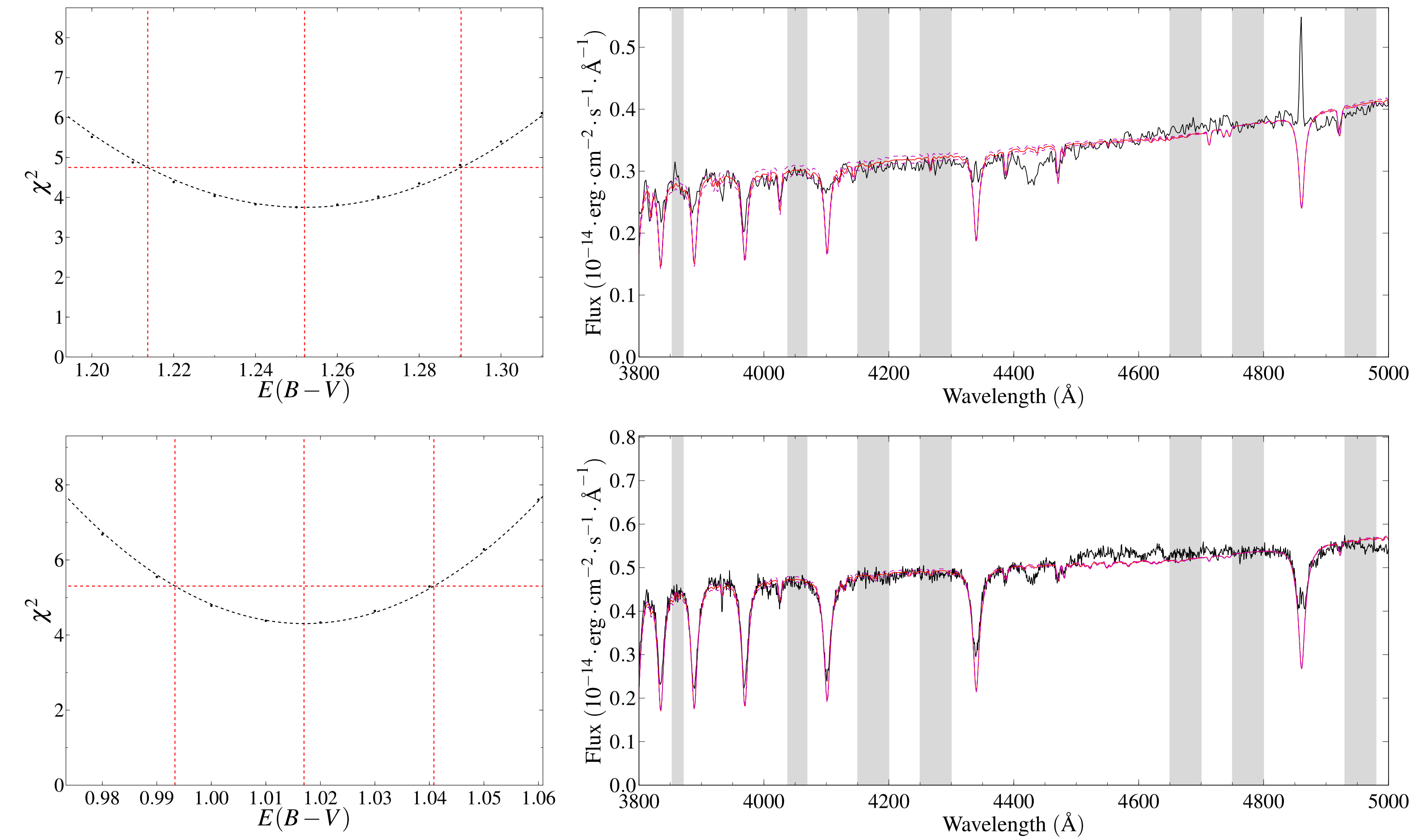

Figure 4.3: Examples of reddening measurement based on a the blue spectrum. (Top): The INT spectrum of object #16 (black line) is shown along with the model atmosphere for $T_{\rm eff} = 19000K$, reddened according to the best fitting colour excess ($E(B-V)_{\rm S} = 1.25 \pm 0.04$). The reddened model is drawn in red, with its 1-σ error bounds shown as purple dashed lines. The shaded vertical strips pick out the continuum intervals used in the fitting procedure. The normalisation applied in this instance is at λ4775Å. (Bottom): Here the NOT/ALFOSC spectrum of #41 is shown, along with the model atmosphere for $T_{\rm eff} = 13000K$. The measured reddening is $E(B-V)_{\rm S} = 1.02 \pm 0.02$. The left panels show the graphical identification of the minimum χ^2, which determines the $E(B-V)$ and the 1σ uncertainty.

synthetic tracks given in Drew et al. (Table 4, 2005). This is a small correction, in the range 0.01 – 0.05 magnitudes. Corrected colours, $(r-i)_{\rm c}$, are in Table 4.1.

2. The colour excess for each object is then:

$$E(r-i) = (r-i)_{\rm c} - (r-i)_{\rm o}, \tag{4.1}$$

where $(r-i)_{\rm o}$ is the intrinsic colour, consistent with the spectral type assigned in Section 3.4. The adopted intrinsic colours are set out in Table 1.2.

3. The $(B-V)$ colour excess is then computed as:

$$E(B-V)_{\rm P} = E(r-i)/0.69, \tag{4.2}$$

adopting the same $R_v = 3.1$ reddening curve as applied in Section 4.2.

Random photometric uncertainties in r and i for these relatively bright objects are small – not exceeding 0.01. Further uncertainties to include are:

1. The spread in intrinsic colour, as commented on above in Section 4.2.

2. The uncertainty originating from the ±1 sub-type error in the spectral-typing. Across the B class this averages to ±0.02 mag. As for the SED fitting, an uncertainty on the luminosity classes would introduce a small error, comparable to the one produced by a change in ±1 sub-type.

3. Absolute calibration error. Both the r and i photometry are subject to an uncertainty of ~ 0.02 mags in the adopted zero point. This translates to a further colour error of 0.03 magnitudes.

Photometric reddenings, $E(B-V)_{\rm P}$, are also recorded in Table 4.1.

As it was noticed at the beginning of the chapter, the choice of reddening law plays an important role, if I were to use photometric reddenings, because in the r – i range the slope of the curve is more sensitive to the R_V (Fig 4.1). This effect can be noted in Fig. 4.4, where I plot the difference $E(B-V)_{\rm S} - E(B-V)_{\rm P}$ with respect to $E(B-V)_{\rm S}$, assuming R_V takes on the values 2.7, 2.9 and 3.1. It is noticeable how the differences move by 0.1-0.2 mags, between the two extreme values of R_V. The vertical shift of the differences, introduced by the change in R_V, originates only from the relative change of slope between the reddening laws in the r and i bands. Since one would not expect the difference $E(B-V)_{\rm (S,c)} - E(B-V)_{\rm (P,c)}$ to be as extreme as seen for $R_V = 2.7, 2.9$, the adoption of the standard $R_V = 3.1$ seems to be justified.

Fig. 4.4 also confirms the result that was already discussed by Kaiser (1989), that is CBe stars possess wavelength-dependent excess emission originating from a circumstellar disc. Due to presence of excess emission in CBe stars, a measure of interstellar reddening from the blue continuum should not agree with a measure obtained in the red part of the spectrum, and indeed $E(B-V)_{\rm P}$ is in average larger than $E(B-V)_{\rm S}$. Where $E(B-$

$V)_\mathrm{P}$ is less than $E(B-V)_\mathrm{S}$ the difference is never so large to make it inconsistent with agreement within the errors. This is encouraging in the sense that this outcome would not be guaranteed if the sample contained CBe stars prone to marked variability.

Dachs, Kiehling & Engels (1988); Kaiser (1989) and more recently Carciofi & Bjorkman (2006) have studied the wavelength dependence of the excess emission. A way of dealing with it, in the *B* and *V* bands, was suggested by Dachs, Kiehling & Engels (1988). In the next chapter, I will revisit the model proposed by these authors and extend the correction for circumstellar emission in the *r* and *i* bands as well.

4.3.1 The UVEX view on reddenings

A similar comparison, as the one done between spectroscopic reddenings and photometric reddenings computed from IPHAS photometry, can be obtained using UVEX photometry. UVEX is the acronym for the UV-Excess Survey of the Northern Galactic Plane (Groot et al., 2009). It is a twin survey of IPHAS, covering the U, g and r bands. Unfortunately, the UVEX data are not yet completed or processed in this part of the Galactic plane and, furthermore, no absolute calibration is ready at the moment. However, it is worth comparing reddenings that are measured from the $(g-r)$ colours with the ones measured from $(r-i)$ and with the spectroscopic values.

UVEX photometry is available for only 72 of the CBe star candidates that have been presented in Chapter 2 and 3. As a safety measure, I only selected 44 stars having $|r_\mathrm{IPHAS} - r_\mathrm{UVEX}| < 0.1$, in order to have less chance of picking objects that underwent photometric variation or have more problematic calibration. Computing the $(g-r)$ colour for these stars, using the UVEX(r) should be safe enough to guarantee internal consistency.

The $E(g-r)$ is transformed into $E(B-V)$, by dividing it by 1.09. This number is R_V independent. The difference between reddenings measured from UVEX and IPHAS photometry is plotted in Fig. 4.5. The plot shows the expected positive trend, due to the presence of circumstellar emission. However a few points show very negative differences, more probably due to the fact that UVEX has not yet been uniformly calibrated.

4.4 Summary

In this chapter, I have presented to measure reddenings of the sample of 68 CBe stars, typed with ± 1 sub-type precision. I showed that a measure of reddenings in the blue should be preferred to a similar estimate that is computed at red wavelengths.

I compared these reddenings, which are measured from the blue-optical spectrum, to the ones that are determined from IPHAS $(r-i)$ colour. Allowing a minimal photometric variation of these stars, Fig. 4.4 confirms the expectations, revealing a systematic overestimate of $E(B-V)_\mathrm{P}$ relative to $E(B-V)_\mathrm{S}$. Assessing the amount of this overestimate would be highly subject to the dependence of the $(r-i)$ colour on the R_V choice. The same behaviour is also seen from a comparison of $E(B-V)_\mathrm{P}$ with reddenings measured from UVEX $(g-r)$ colours.

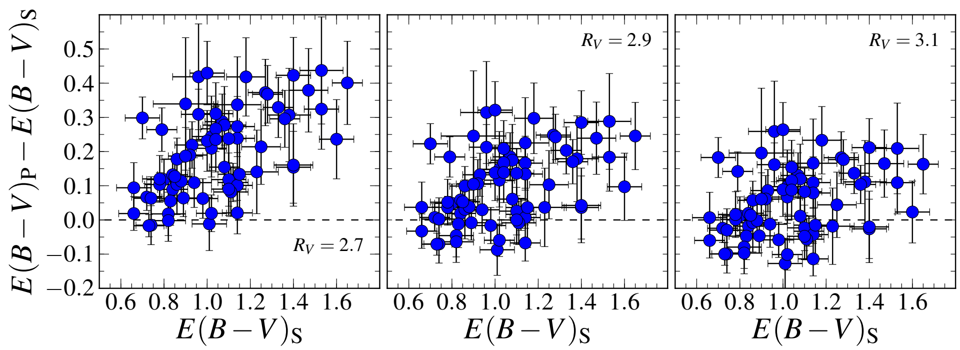

Figure 4.4: The difference between the two colour excess measurements, $E(B-V)_P - E(B-V)_S$ is plotted as a function of the spectroscopic colour excess, $E(B-V)_S$. A different value of R_V is adopted in each case. The data points are scattered with a bias to positive values, as expected, due to the reddening effect associated with the circumstellar-disc emission present in these stars.

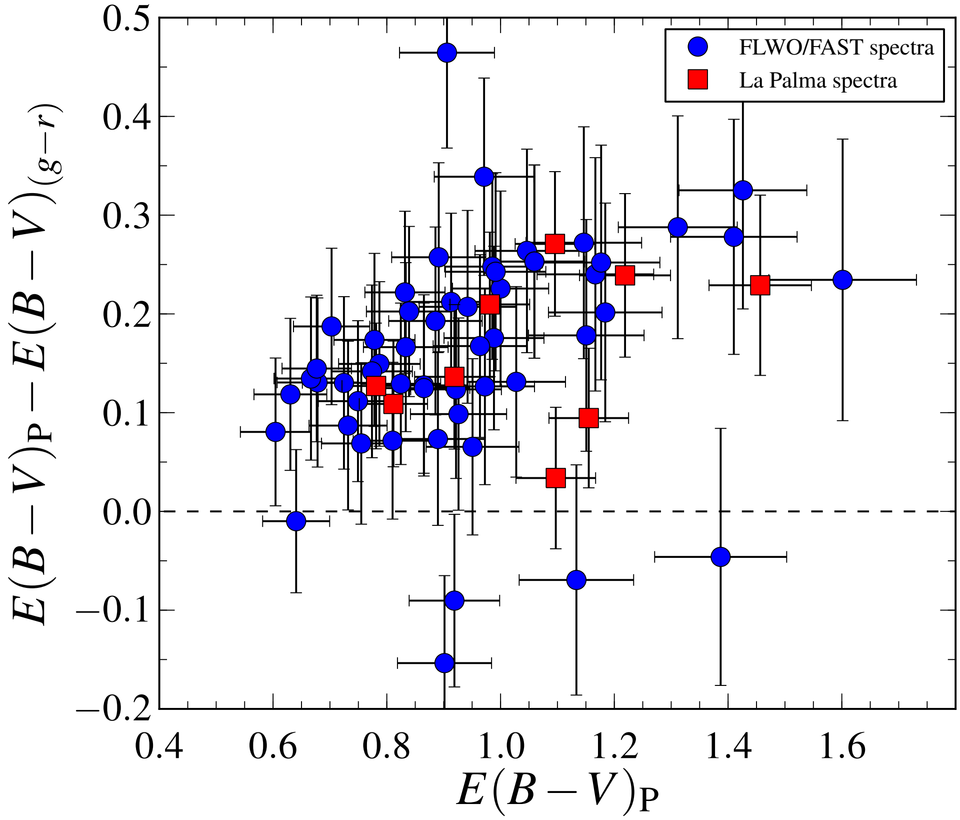

Figure 4.5: The difference between photometric reddenings that are measured using IPHAS and UVEX photometry. In figure are plotted the stars having an $|r_{\rm IPHAS} - r_{\rm UVEX}| < 0.1$. One of the stars observed in La Palma is not in the plot ranges, due to its more negative difference. The equality line is plotted. Colour excesses are converted to $E(B-V)$ using the $R_V = 3.1$ Fitzpatrick (1999) law.

Due to the relevance of getting the best possible estimate of reddenings, in order to measure distances of these CBe stars, the main issue is to asses the cause of this extra contribution to the measured colour excess.

Table 4.1: Colour excesses and spectral types of the CBe stars of chapter 3. Columns are in the following order: ID number; spectral type; measured spectroscopic colour excess; Hα emission-corrected $(r-i')_c$ colours; photometric colour excess based on the $(r-i)$ colours; $(g-r)$ colours; photometric colour excesses based on the $(g-r)$ colours. In the last column are the line-of-sight asymptotic colour excesses from SFD98.

#	SpT	$E(B-V)_S$ (mag)	$(r-i)_c$ (mag)	$E(B-V)_P$ (mag)	$(g-r)$ (mag)	$E(B-V)_{(g-r)}$ (mag)	$E(B-V)_{SFD98}$ (mag)
1	B5	1.40 ± 0.08	0.87	1.37 ± 0.09			1.51
2	B7	0.66 ± 0.07	0.35	0.60 ± 0.05			1.58
3	B3	1.60 ± 0.08	1.00	1.62 ± 0.10			1.83
4	A0	1.02 ± 0.09	0.77	1.12 ± 0.08			1.78
5	B2	1.14 ± 0.08	0.73	1.25 ± 0.08			1.55
6	B3	1.38 ± 0.10	0.91	1.49 ± 0.10			1.51
7	B7	0.84 ± 0.07	0.51	0.82 ± 0.06			1.51
8	B3	1.12 ± 0.07	0.63	1.09 ± 0.08			1.28
9	B5	0.94 ± 0.08	0.56	0.93 ± 0.07			1.60
10	B7	1.10 ± 0.08	0.68	1.08 ± 0.08			1.66
11	B2-3	0.96 ± 0.08	0.65	1.12 ± 0.07			1.07
12	B5	0.86 ± 0.09	0.51	0.85 ± 0.06			1.15
13	B5	0.66 ± 0.08	0.38	0.67 ± 0.05			1.02
14	B4	1.14 ± 0.08	0.75	1.22 ± 0.08			1.37
15	B5	1.10 ± 0.07	0.74	1.18 ± 0.08			1.66
16	B3	1.27 ± 0.08	0.88	1.45 ± 0.09			1.91
17	B3	1.53 ± 0.08	1.01	1.64 ± 0.10			1.47
18	B4	1.07 ± 0.08	0.74	1.20 ± 0.08			1.39
19	B6	1.14 ± 0.07	0.64	1.03 ± 0.07	1.41	1.29 ± 0.04	1.19
20	B3	1.40 ± 0.08	0.99	1.61 ± 0.10			1.90
21	B5	1.40 ± 0.09	0.87	1.38 ± 0.09			2.39
22	B4	1.33 ± 0.07	0.92	1.47 ± 0.10			1.40
23	B7	1.08 ± 0.09	0.77	1.20 ± 0.08			1.39
24	B3	1.36 ± 0.07	0.89	1.46 ± 0.09			1.96
25	B5	0.86 ± 0.07	0.55	0.92 ± 0.06			1.19
26	B3	1.18 ± 0.09	0.85	1.41 ± 0.09			1.37
27	B5	1.08 ± 0.07	0.67	1.09 ± 0.07			1.30
28	B7	0.83 ± 0.08	0.48	0.78 ± 0.06			1.12
29	B7	0.80 ± 0.07	0.50	0.81 ± 0.06	0.77	0.71 ± 0.05	1.42
30	B4	0.78 ± 0.07	0.45	0.78 ± 0.06	0.71	0.65 ± 0.05	0.97
31	B3	1.28 ± 0.07	0.89	1.46 ± 0.09	1.34	1.23 ± 0.04	1.74
32	B6	1.01 ± 0.08	0.54	0.88 ± 0.06			0.93

Table 4.1: Continued

#	SpT	$E(B-V)_S$ (mag)	$(r-i)_c$ (mag)	$E(B-V)_P$ (mag)	$(g-r)$ (mag)	$E(B-V)_{(g-r)}$ (mag)	$E(B-V)_{SFD98}$ (mag)
33	B8-9	0.88 ± 0.07	0.58	0.88 ± 0.07			1.02
34	B3	0.70 ± 0.08	0.49	0.88 ± 0.07			1.18
35	B2-3	0.93 ± 0.08	0.58	1.02 ± 0.07			1.09
36	B4	1.53 ± 0.10	1.11	1.74 ± 0.11			2.06
37	B6	0.92 ± 0.08	0.61	0.98 ± 0.07	0.84	0.77 ± 0.04	1.19
38	B5	0.90 ± 0.15	0.68	1.10 ± 0.07	0.90	0.83 ± 0.04	1.61
39	B4	0.96 ± 0.12	0.75	1.22 ± 0.08	1.07	0.98 ± 0.05	0.93
40	B2	1.04 ± 0.07	0.67	1.16 ± 0.08	1.16	1.06 ± 0.04	0.32
41	B7	1.02 ± 0.07	0.57	0.92 ± 0.07	0.85	0.78 ± 0.05	0.95
42	B2	1.47 ± 0.08	1.00	1.63 ± 0.10			0.94
43	B6	0.82 ± 0.07	0.44	0.74 ± 0.06			0.68
44	B5	0.79 ± 0.07	0.56	0.93 ± 0.07			0.85
45	B3	1.14 ± 0.07	0.64	1.10 ± 0.08	1.16	1.06 ± 0.04	1.51
46	B9	0.84 ± 0.07	0.57	0.86 ± 0.07			1.19
47	B3	1.65 ± 0.07	1.13	1.81 ± 0.11			1.98
48	B8	1.15 ± 0.10	0.74	1.13 ± 0.08			1.23
49	A0	0.74 ± 0.07	0.44	0.64 ± 0.06			0.72
50	B3	1.00 ± 0.08	0.75	1.26 ± 0.08			1.26
51	B8-9	0.73 ± 0.07	0.41	0.63 ± 0.06			0.78
52	B7	0.90 ± 0.08	0.60	0.96 ± 0.07			0.98
53	B7	1.11 ± 0.07	0.67	1.05 ± 0.08			1.47
54	B3	0.85 ± 0.07	0.48	0.86 ± 0.07			1.12
55	B3-4	1.04 ± 0.08	0.72	1.19 ± 0.08			1.22
56	B7	1.02 ± 0.07	0.69	1.09 ± 0.08			1.72
57	B7-8	1.00 ± 0.08	0.70	1.09 ± 0.08			1.36
58	B3	0.72 ± 0.07	0.36	0.70 ± 0.06			0.90
59	B4	1.04 ± 0.09	0.69	1.13 ± 0.08			3.16
60	B5	0.78 ± 0.08	0.47	0.80 ± 0.06			1.24
61	B3-4	0.82 ± 0.08	0.39	0.72 ± 0.06			1.24
62	B7	0.74 ± 0.08	0.43	0.71 ± 0.06			0.81
63	B6	1.23 ± 0.10	0.77	1.21 ± 0.08			1.62
64	B7	0.89 ± 0.07	0.52	0.84 ± 0.06			1.67
65	B5	1.25 ± 0.09	0.81	1.29 ± 0.09			1.32
66	B5	0.98 ± 0.07	0.56	0.92 ± 0.07			1.55
67	B4	1.10 ± 0.08	0.64	1.05 ± 0.08			1.72
68	B4	1.14 ± 0.11	0.81	1.31 ± 0.09			1.51

Chapter 5

Correcting classical Be star reddenings for circumstellar disc emission

In the present chapter, I will deal with the effect that circumstellar disc of CBe stars has on the measure of interstellar reddenings. The approach I undertake is to model the disc emission, in order to infer its contribution to the measured colour excess $E(B-V)$ and, therefore, to assess the true interstellar reddening of a star. This is done in order to better understand and update current practice in this regard. The model parameterisation is set out in Section 5.2 and its application to real data is described in Section 5.3. Section 5.4 describes a different use of the model, only tested on simulated data, which allows a simultaneous determination of interstellar reddening and circumstellar colour excess for CBe stars.

5.1 Introduction

CBe stars are known to be surrounded by circumstellar discs that are optically thin in the Paschen continuum and optically thick at wavelengths bluer than the Balmer jump and in the IR (Dachs, Kiehling & Engels, 1988). These discs are geometrically thin (Porter & Rivinius, 2003), but with very high electron density ($n_e \sim 10^{12}$ cm^{-2}), making the collisional transitions being a significant factor (Dachs, Kiehling & Engels, 1988). The disc is likely to be fully ionised, dust-free (Carciofi & Bjorkman, 2006) and can be adequately modelled at optical wavelengths as an optically-thin nebula.

The circumstellar disc emission is wavelength dependent and adds on the photospheric emission from the underlying star. The effect of this extra emission is to redden the observed optical and IR SED. As consequence of this, any measured reddening can be thought as due to two components:

$$E(B-V) = E^{is}(B-V) + E^{cs}(B-V), \tag{5.1}$$

where $E^{is}(B-V)$ is the interstellar reddening and $E^{cs}(B-V)$ is the circumstellar contribution to the total colour excess (e.g. Dachs, Kiehling & Engels, 1988; Zorec & Briot, 1991).

Previous works, aiming to study the physical properties of these circumstellar discs, demonstrated that the continuum excess accounted for by $E^{cs}(B-V)$, approximated to an optically-thin free-free and recombination free-bound continuum (see e.g. Dachs, Kiehling & Engels, 1988; Kaiser, 1989; Carciofi & Bjorkman, 2006). Specially Dachs, Kiehling & Engels (1988), investigated the correlation between $EW(\mathrm{H}\alpha)$ and $E^{cs}(B-V)$ and presented empirical evidence that the former correlates with the latter and also with the fraction of the total emission that can be attributed to the circumstellar disc (this is also as to say that the emission measure of the envelope correlates with the $EW(\mathrm{H}\alpha)$). The linear correlation that they proposed, from the analysis of B0–B3 stars mainly, is expressed in the form of:

$$E^{cs}(B-V) \approx 0.02 \cdot \frac{EW(\mathrm{H}\alpha)}{-10\text{Å}} \tag{5.2}$$

$$f_{\mathrm{D}} = \frac{F_{\mathrm{D}}}{F_{\mathrm{D}}+F^{*}} \approx 0.1 \cdot \frac{EW(\mathrm{H}\alpha)}{-30\text{Å}}, \tag{5.3}$$

where $f_{\mathrm{D}} = F_{\mathrm{D}}/(F_{\mathrm{D}}+F^{*})$ is the fraction of flux emitted by the disc compared to the total flux, at λ5550Å. In Chapter 4, I provided evidence that the measures of reddening in different wavelength ranges produce discrepant results. This outcome agrees with the predictions of previous studies, that the circumstellar contribution to the observed SED is larger at redder wavelengths.

Since the effect of circumstellar emission has been well studied in the literature and its correlation with Hα was found, in Section 5.3, I use Eq. (5.3) in order to estimate the fractional contribution of the disc emission to the total flux. However, because of the way I measured reddenings in Chapter 4, namely using the spectral range between $\lambda\lambda$ 3800-5000 Å and the $(r-i)$ colours, a straightforward application of Eq. (5.2) would not supply the appropriate reddening corrections. Therefore, I produced a grid of circumstellar recombination continua in order to estimate appropriate $E^{cs}(B-V)_{\mathrm{S}}$ and $E^{cs}(r-i)$ respectively. The description of the models and their basic application is in the following section, while in Section 5.4 I will test the possibility of retrieving interstellar reddenings and circumstellar colour excess from observed spectra simultaneously, with the use of the models.

5.2 Modelling the circumstellar emission of classical Be stars

The parameterisation of the circumstellar emission is very similar to the one adopted by Kaiser (1989), in the way that his definition of f_{D} is adopted. Normalising the spectra at λ5500 Å as in Kaiser (1989), the error I introduce by shifting by 50 Å the normalisation adopted by Dachs, Kiehling & Engels (1988) is smaller than 1%. The simulations cover the range of spectral types that are observed in the FLWO/FAST and La Palma observations (i.e. B1 to A0), and disc fractions are varied from zero to a maximum of 0.50. The significant difference with respect to earlier treatments is that the adopted scaling of

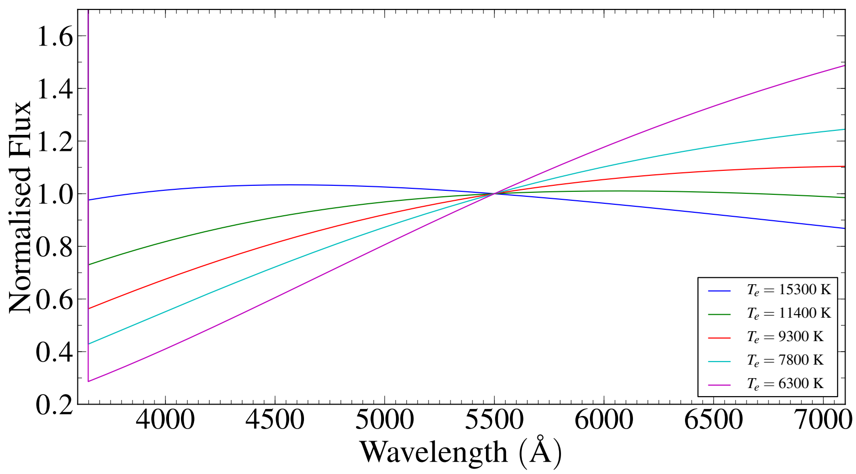

Figure 5.1: Nebular recombination continua generated at 5 different T_e are plotted. The electron temperatures correspond to $T_{\rm eff}$ of spectral types B1, B3, B5, B7, and B9.

the electron temperature in the circumstellar disk is such that $T_e = 0.6T_{\rm eff}$, as opposed to always being fixed at $T_e = 10000$ K (Dachs, Kiehling & Engels, 1988; Kaiser, 1989). This has been shown to be a good approximation by Carciofi & Bjorkman (2006) (see also Drew, 1989). The electron density is set at the suitably high, representative value, $N_e = 10^{12}\,{\rm cm}^{-3}$ (Dachs, Kiehling & Engels, 1988; Dachs, Rohe & Loose, 1990).

The disc emission models are computed with the use of the NEBCONT routine within the STARLINK/DIPSO package, which computes free-free and free-bound recombination continuum emission from a fully ionised volume of hydrogen gas. The volume is assumed to be optically thin, avoiding the need of specifying the geometry. This is in agreement with the weak dependence of the observed SED on the disc inclination, predicted at optical wavelengths by Carciofi & Bjorkman (2006). Since the scaling factor of the disc emission f_D is a free parameter of the model, the emission measure of the gas is not a parameter of interest: accordingly the NEBCONT parameter that is a proxy for it, $\log I(\beta)$, can be set to 1. On this basis the circumstellar continuum emission is generated and in Fig. 5.1, I show examples of continua for 5 different T_e, corresponding to $T_{\rm eff}$ of stars with spectral types B1, B3, B5, B7, B9. The temperature dependence is very evident.

The magnitude of the circumstellar colour excess is estimated via comparison between normal stellar SEDs and modified SEDs (star + disc). The latter are generated by adding the circumstellar emission with the appropriate T_e to the Munari et al. (2005) model atmosphere, scaling it with f_D as required at λ5500Å. In the following section I describe how the $E^{cs}(B-V)$ are measured.

5.3 Estimating the circumstellar colour excess

The most straightforward application of the models is the calculation of $E^{cs}(B-V)$ as a function of $T_{\rm eff}$ and f_D. Using the same notation of Chapter 4, the circumstellar colour ex-

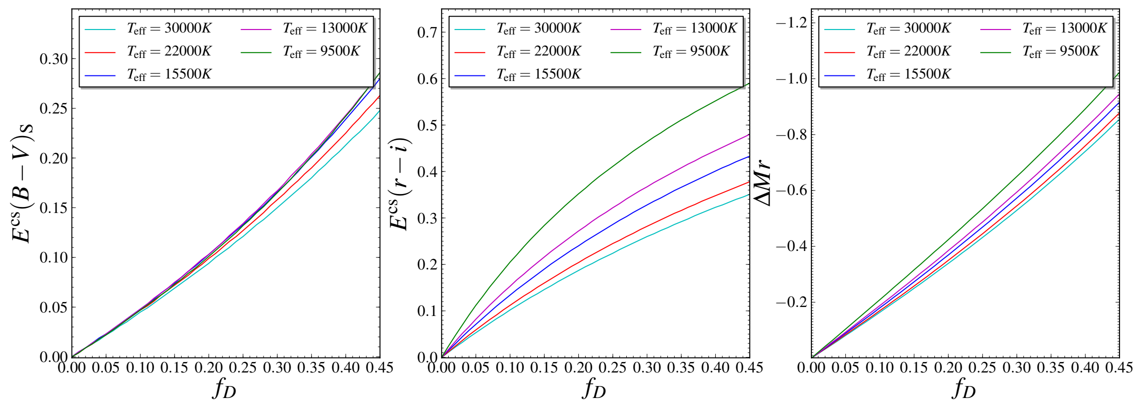

Figure 5.2: Left panel shows the blue-optical circumstellar colour excess plotted against f_D. Its dependence on the $T_{\rm eff}$ of the central star is shown by five different curves corresponding to temperatures of B1, B2, B5, B7 and A0 stars. In the middle panel, the $E^{cs}(r-i)$ is plotted against f_D, while in the right panel, also the variation in r-band magnitude is plotted as a function of f_D.

cess was computed over the wavelength range λλ 3800-5000 Å, where the spectroscopic reddenings $E(B-V)_{\rm S}$ were measured from the SED fitting. The estimate of $E^{cs}(B-V)_{\rm S}$ is carried out, following the procedure applied to the observed spectra (Section 4.2). In other words, the measure of circumstellar colour excess is obtained reddening the model atmosphere for a given spectral type onto the same model atmosphere plus the disc emission. The measured reddening corresponds to the $E^{cs}(B-V)_{\rm S}$ for the adopted spectral type and disc fraction. In Table 5.1, a grid of spectral types and $E^{cs}(B-V)_{\rm S}$, for corresponding disc contribution to the total emitted flux.

I also supply a measure of the red-optical circumstellar colour excess, $E^{cs}(r-i)$, in Table 5.2. The $E^{cs}(r-i)$ were measured as $[(r-i)_{\rm star+disc}-(r-i)_{\rm star}]$, convolving the WFC filter profiles (Fig. 4.2) respectively with the models of star plus disc and star only.

Finally, in Table 5.3 the magnitude brightening in the r-band, Δr, of a CBe as compared to a normal B-type star is listed. It is known that V magnitudes of CBe stars are indeed brighter, due to circumstellar emission, by amounts ranging from zero up to 0.5 in the most extreme cases (Zorec & Briot, 1991).

The circumstellar excesses $E^{cs}(B-V)_{\rm S}$ and $E^{cs}(r-i)$, and the magnitude brightenings Δr are plotted in Fig. 5.2 as functions of the disc fraction f_D. As anticipated in the previous section, larger circumstellar colour excesses and magnitude brightenings are seen for later spectral types. This effect is due to the steeper positive slope of the continuum emission (Fig. 5.1) at the lower T_e values expected for later spectral types. The maximum difference, found for either $E^{cs}(B-V)_{\rm S}$, $E^{cs}(r-i)$ or Δr when varying f_D at different spectral types, is in the range of 0.05 mags in $E^{cs}(B-V)_{\rm S}$, 0.3 mags in $E^{cs}(r-i)$ and reaches up to 0.2 mags in Δr. Providing that effective temperatures are available from the spectral type determination – which is true for most of the CBe stars described in Chapter 2 and all presented in Chapter 3 – and that f_D can be estimated from $EW(\mathrm{H}\alpha)$ measures via Eq. (5.3), I could correct reddening estimates that are obtained either from spectroscopy or from photometry. In practice, the $E^{cs}(B-V)_{\mathrm{S}}$ is determined for the La Palma spectra, where a well-validated flux calibration was available in the blue spectral range (λλ 3800-5000 Å), and $E^{cs}(r-i)$ is needed for the FLWO/FAST candidate CBe stars, where only photometric reddenings are available.

5.3.1 Accounting for the circumstellar colour excess with $EW(\mathrm{H}\alpha)$ measures

Circumstellar reddenings were estimated both for the CBe stars observed in La Palma and for 181 CBe stars that were observed with FLWO/FAST (Section 5.2).

The method for estimating the circumstellar reddening, begins with equation (5.3), delivering the disc fraction, f_{D}. Since CBe stars are known to be erratic variables (i.e. Zorec & Briot, 1991; Porter & Rivinius, 2003; Jones, Tycner & Smith, 2011), I took care to determine f_{D} from either observations of the Hα line that are simultaneous with the blue spectroscopy (available with all the INT/IDS and FLWO/FAST data), or from a well-validated proxy in the case of the NOT/ALFOSC spectra without coverage of the Hα region. The necessary proxy is provided by the FLWO/FAST spectra in which I found that the Hβ profile is a good match to that apparent in the NOT/ALFOSC spectrum. Fortuitously there are good matches for all but 4 objects, which do not have FLWO/FAST observations. The values of f_{D} obtained for each of the stars in the sample are in Table 5.4 and 5.5, where I also give the Hα emission equivalent width on which it is based. This quantity is corrected for the underlying absorption, according to spectral type (see tabulation in Jaschek & Jaschek, 1987). The error on f_{D} mainly reflects the scatter in the original empirical relation due to Dachs, Kiehling & Engels (1988). I estimate the average uncertainty to be ± 0.02 dex, and propagate it through into the $E^{cs}(B-V)$ error.

To obtain circumstellar colour excesses I do not simply apply Eq. (5.2) for the reason that it was constructed to provide correction to reddenings measured directly across the B to V range (roughly 4000 — 6000 Å), but I used the values that are from Table 5.1 and 5.2. This allows to choose between the most appropriate correction for each spectral type and f_D. As I said, for the La Palma observations, I used the spectroscopic estimate, where the uncertainty arising from smaller spectral typing errors affects the measured reddening less. For the FLWO/FAST spectra, the photometric measure is the only one available and the scaling of the disc emission was estimated via Eq. 5.3 using $EW(\mathrm{H}\alpha)_{\mathrm{P}}$, since the lack of a confirmed flux calibration (see Section 2.3) removes the option of measurement via SED fitting. The close agreement between the spectroscopic and photometric equivalent widths' estimates (Fig. 2.13) and the contemporaneity of the $EW(\mathrm{H}\alpha)_{\mathrm{P}}$ with $(r-i)$ supports the use of the photometric estimate in order to compute f_D. In Fig. 5.3 and Fig. 5.4, I show the histogram distribution of the spectroscopic $EW(\mathrm{H}\alpha)$ (median at about ≈ -26 Å), for the La Palma spectra and photometric $EW(\mathrm{H}\alpha)$ (median at about ≈ -28 Å) for the stars with FLWO/FAST spectra.

The final $E^{is}(B-V) \equiv E(B-V)_{(\mathrm{S,c})}$, for the stars observed in La Palma, is thus obtained by subtracting the tailored estimate of $E^{cs}(B-V)_{\mathrm{S}}$ from the measured $E(B-V)_{\mathrm{S}}$. This result is in Table 5.4. On the other hand, the interstellar reddenings estimated from

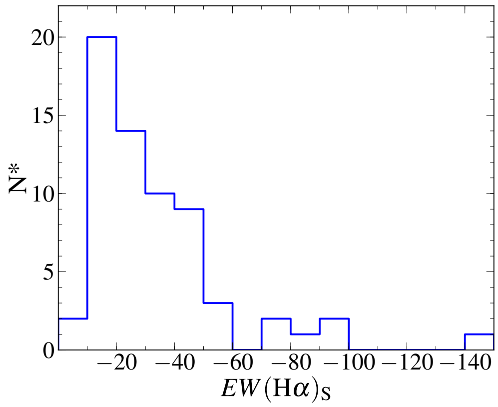

Figure 5.3: The distribution of spectroscopic Hα equivalent widths for the La Palma spectra of CBe stars. The median of the distribution falls at ≈ -26 Å and all but 6 of the 68 stars have $EW(\mathrm{H}\alpha) \leq -60$ Å. Measures are corrected for the underlying emission.

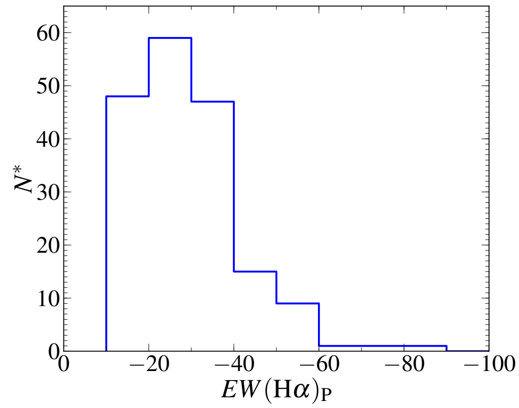

Figure 5.4: The distribution of photometric Hα equivalent widths, for the FLWO/FAST sample, corrected for underlying emission. The median of the distribution falls at ≈ -28 Å.

the IPHAS photometry for the stars with FLWO/FAST spectra are obtained from the following equations:

$$E^{is}(r-i) = E(r-i) - E^{cs}(r-i) = (r-i)_c - (r-i)_0 - E^{cs}(r-i), \tag{5.4}$$

$$E^{is}(B-V) \equiv E(B-V)_{(\mathrm{P,c})} = E^{is}(r-i)/0.69, \tag{5.5}$$

with $E(B-V)_{(\mathrm{P,c})}$ being the corrected photometric reddenings. The factor 0.69, in the second equation, comes from adopting the $R_V = 3.1$ reddening law. The quantities used in both equations and the derived reddenings are given in Table 5.5.

The validation of using corrected photometric reddenings, $E(B-V)_{(\mathrm{P,c})}$, can be tested with the comparison between the adopted $E(B-V)_{(\mathrm{S,c})}$ and the photometric estimate $E(B-V)_{(\mathrm{P,c})}$, for the stars with La Palma spectra. The expectation is that the two independent measures would agree within the errors. In Fig. 5.5, I plot the difference $E(B-V)_{(\mathrm{P,c})} - E(B-V)_{(\mathrm{S,c})}$ against $E(B-V)_{(\mathrm{S,c})}$. The mean difference is about -0.08 ± 0.09, which is consistent with the equality. However, what causes the apparent systematic difference has to be investigated. Possible options to be looked at are either the model does not provide with sensible corrections in the red spectral range or the $R_V = 3.1$ reddening law (Fitzpatrick, 1999) is not the most appropriate choice for all the sightlines.

5.3.2 Comparison with the observations

In Section 4.4, I appraised the expected evidence of a continuum excess that affects the red-optical more than the blue-optical. Fig. 4.4 compared the two reddening measurements that were obtained for all the CBe stars with La Palma spectra. In it, there is a systematic

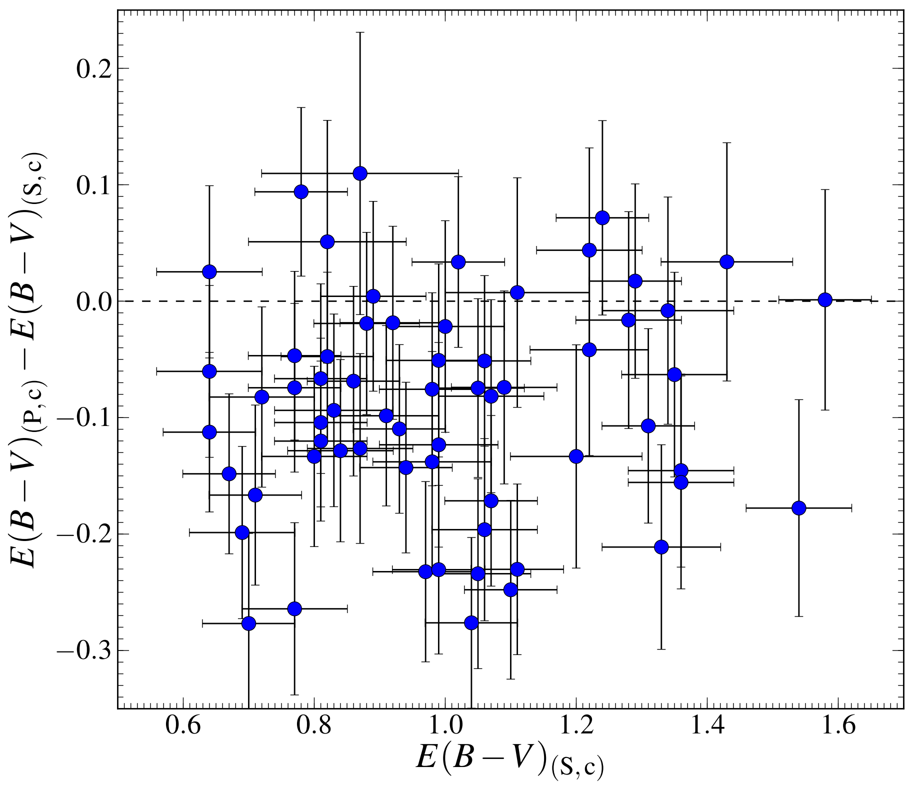

Figure 5.5: Comparison between corrected spectroscopic and photometric reddenings. The equality line is shown. The mean difference is measured at -0.05 ± 0.01.

overestimate of the red measure, $E(B-V)_\mathrm{P}$, with respect to blue one, $E(B-V)_\mathrm{S}$, which ties in with the description given by Kaiser (1989). Where the photometric reddening is less than the spectroscopic estimate, the difference is never so negative that it may not be viewed as consistent with the two measures being equal to within the errors. This is encouraging in the sense that this outcome would not be guaranteed if the sample contained CBe stars prone to marked variability.

The new feature of the higher resolution spectroscopic sample, compared to that of Dachs, Kiehling & Engels (1988), was that it includes half-a-dozen objects with $EW(\mathrm{H}\alpha) \leq -60$Å (see Fig. 5.3), that therefore lie beyond the range over which the correlations contained in equations (5.2) and (5.3) were established. In fact, the most extreme object, object 59 with $EW(\mathrm{H}\alpha) = -144$ Å, is more likely to be a young stellar object than a CBe star and it is removed from the analysis of Chapter 6.

Following the reasoning due to Dachs, Kiehling & Engels (1988) and Kaiser (1989), the expectation is that the systematic overestimate of $E(B-V)_\mathrm{P}$ with respect to $E(B-V)_\mathrm{S}$ (Fig. 4.4), should correlate with $EW(\mathrm{H}\alpha)$. If the Hα equivalent width supplies a good estimate for $E^{cs}(B-V)$, via the use of Eq. (5.2), the difference between two reddening estimates in different spectral ranges would be larger for stronger Hα emitters. This feature should also be reproduced by the disc model, providing that Eq. (5.3) enables a reliable

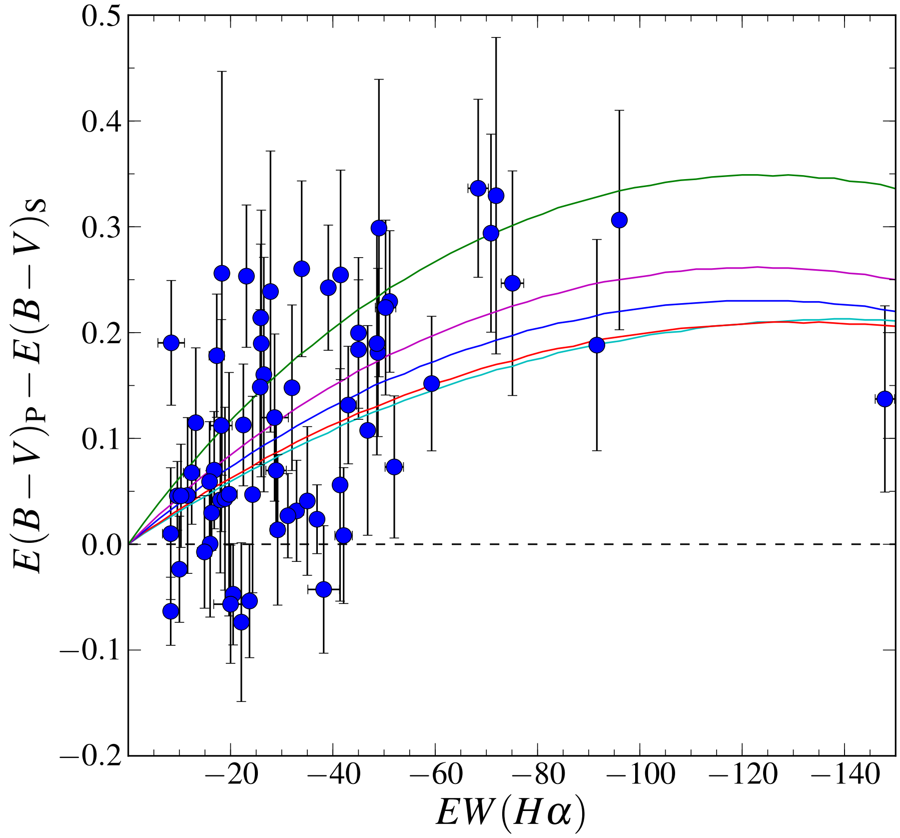

Figure 5.6: The measured difference between the red-optical and blue-optical measures of colour excess plotted against the $EW(\mathrm{H}\alpha)$, for the intermediate-resolution spectra. The solid curves are the expected differences, computed via the use of the disc model, and transforming f_D into $EW(\mathrm{H}\alpha)$ via Eq. (5.3). Different colours are used for different T_{eff}, the top curve corresponds to a A0 star, while the bottom one is for a B1 star. The dashed black curve is the equality line.

transformation between $EW(\mathrm{H}\alpha)$ and f_D.

In Fig. 5.6, where the quantity [$E(B-V)_{\mathrm{P}}$ - $E(B-V)_{\mathrm{S}}$] is plotted against $EW(\mathrm{H}\alpha)$, an evident trend is observed, albeit with substantial scatter. The same figure shows a set of curves for different spectral types, representing the difference [$E(B-V)_{\mathrm{P}}$ - $E(B-V)_{\mathrm{S}}$], as derived from the disc models. The disc fraction is converted into $EW(\mathrm{H}\alpha)$ via Eq.(5.3). The curves seem to follow loosely the same trend as the data. The observed scattering could be due to both the non-contemporaneity of the photometric and spectroscopic observations, and also to the large errors.

In principle, having either contemporaneous multiband photometry or spectroscopy over the whole optical range, it could be possible to estimate the correct $E^{cs}(B-V)$, by measuring the magnitude excess at each band/wavelength, not needing to rely on the Hα emission. This approach was indeed used by Kaiser (1989), with a single $T_e = 10000$ K model and less variety of observations. In the following section I present a different application of the model of disc emission, with simulated data, which allows a simultaneous determination of interstellar reddenings and disc fractions from the SED fitting of stellar spectra.

5.3.2.1 The corrected reddenings and r-magnitudes

While the larger uncertainty in the spectral typing of the FLWO/FAST spectra with low S/N ratio would have a strong impact on the distance determination, as I will discuss in Chapter 9, it does not produce an equally large uncertainty on the reddening measures. Because of the greater proximity of the r and i bands to the Rayleigh-Jeans part of the Planck function, their measured $E(B-V)_{\rm P}$ are typically no more uncertain than the ones measured from the blue optical SED of the La Palma spectra.

It is noticeable that plotting separately the distributions of the measured interstellar colour excesses and r-magnitudes, the la Palma and FLWO/FAST samples are differently reddened (Fig 5.7). The generally fainter stars observed in La Palma are on average more reddened (median at $r = 14.7$, and $E(B-V)_{\rm (S,c)} = 0.98$) than the FLWO/FAST objects, for which the median of the distributions are $r = 14$ and $E(B-V)_{\rm (P,c)} = 0.75$. The typical reddenings measured for open clusters in the Perseus Arm, as reported in the Dias et al. (2002) catalogue, is $E(B-V) \approx 0.8$. This suggest that a bias towards closer distances might be introduced by studying the spatial distribution resulting only from the FLWO/FAST sample. The bias is mainly the result of the observing strategy, which favoured brighter less reddened spectra. Finally, as expected, a difference between the two groups is that corrections for circumstellar colour excesses are typically larger for the FLWO/FAST stars, due to the stronger effect of the disc at red wavelengths – the histograms of uncorrected reddenings Fig 5.7 are shifted to the right on average by ~ 0.05 mag and ~ 0.15 mag for the La Palma and the FLWO/FAST samples respectively. On the other hand, the r-band corrections are comparable for the stars in the two samples, since their $EW(\mathrm{H}\alpha)$ distributions appear very similar (Fig. 5.3 and Fig. 5.4).

5.4 Disentangling the interstellar reddening from the circumstellar colour excess: the 4000 – 7000 Å range

The simulation set-up consists of a grid of Munari et al. (2005) model atmospheres (spectral types B1, B3, B5, B7, B9), to which in turn I added varying amounts of circumstellar continuum emission, scaled with $f_D = 0.05, 0.1, 0.2, 0.3$. These star-plus-disc model spectra were then noised-up to S/N = 10, 20, 30, 40, 50, 70. The stated value of S/N ratio is as measured at 4500 Å, and it changes smoothly with wavelength so as to reproduce the behaviour of the blaze function of the FLWO/FAST set-up. The wavelength dependence of the S/N was determined from observed spectra by measuring it in the continuum, in line-free bands. For each spectral-type there are 24 corresponding models with different combinations of f_D and S/N ratio. In Figure 5.8, I plot two noise curves for S/N = 20 and

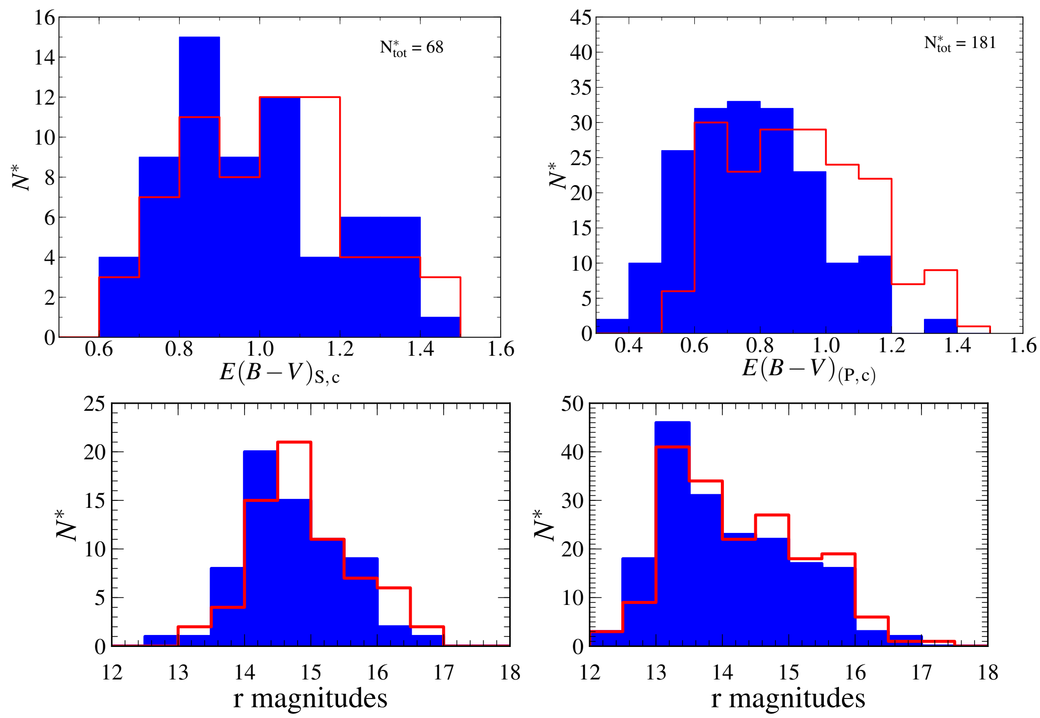

Figure 5.7: Top panels: the distribution of estimated interstellar reddenings for both the La Palma (top) and FLWO/FAST sample (top), plotted as blue histograms. The red solid curves are the measured colour excesses that include the contribution from the circumstellar disc. For the La Palma stars, the median of the distribution is found at $E(B-V)_{\rm S,c} = 0.98$, while for the FLWO/FAST ones the median of the distribution is at $E(B-V)_{\rm P,c} = 0.75$.Bottom panels: distribution of IPHAS r-magnitudes for both the La Palma (left) and FLWO/FAST sample (right), in blue. The red solid curves indicate the corrected magnitudes, corrected for circumstellar excess emission. The median measured for the corrected magnitude distributions are at $r = 14.7$ and $r = 14$, for the La Palma and FLWO/FAST samples respectively.

50. In the same figure, there are two examples that compare synthetic spectra with zero-noise and with added noise. The examples shown are for a B3V star, with $E(B-V) = 1$ and $f_D = 0.2$. The spectral resolution of the models is degraded to match $\Delta\lambda = 6$ Å, as in the FLWO/FAST spectra.

The interstellar reddening and the disc fraction were measured from the noised-up star plus disc models, in a similar way as spectroscopic reddenings were measured in Chapter 4. $E(B-V)$ and f_D are varied in order to identify the χ^2 minimum. The main difference with the simple reddening estimates is that the number of free parameters to be measured here is 2. In this respect, the search of the minimum χ^2 and its 68% confidence range become more complicated, since now it has to be found on a surface in the $(E(B-V), f_D)$ plane. A close inspection of the $(E(B-V), f_D)$ plane, showed that the χ^2 surface, around the minimum, is very shallow . However, at higher S/N, the two quantities can be measured with satisfying accuracy.

To assess the reliability of the measures, I ran 5000 Monte Carlo simulations for each

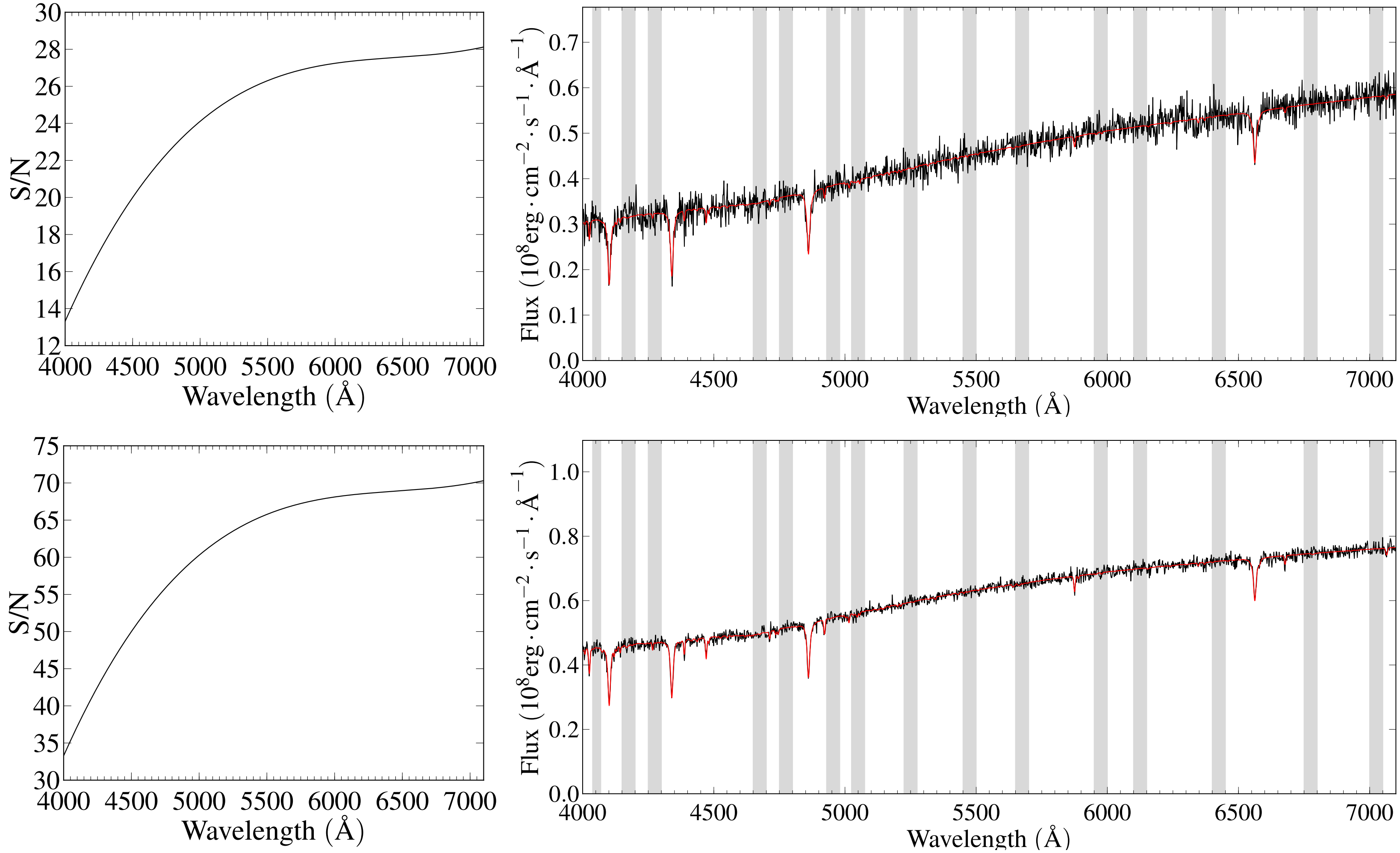

Figure 5.8: Simulations of SED fitting procedure, for two different S/N. Left panels are the S/N models, based on the average curve describing the wavelength variation of the continuum noise in the FLWO/FAST sample. S/N at 4500 Å is 20 (top panel) and 50 (bottom panel). Right panels show the comparison between the noised-up spectra of a B3V star with $E(B-V) = 1$ and $f_D = 0.2$, using the noise models of left panels. In black is the noised-up spectrum, while in red is the corresponding zero-noise model atmosphere, The shaded strips mark the bands where the χ^2 is computed, and where the model describing the S/N ratio versus wavelength curve was sampled.

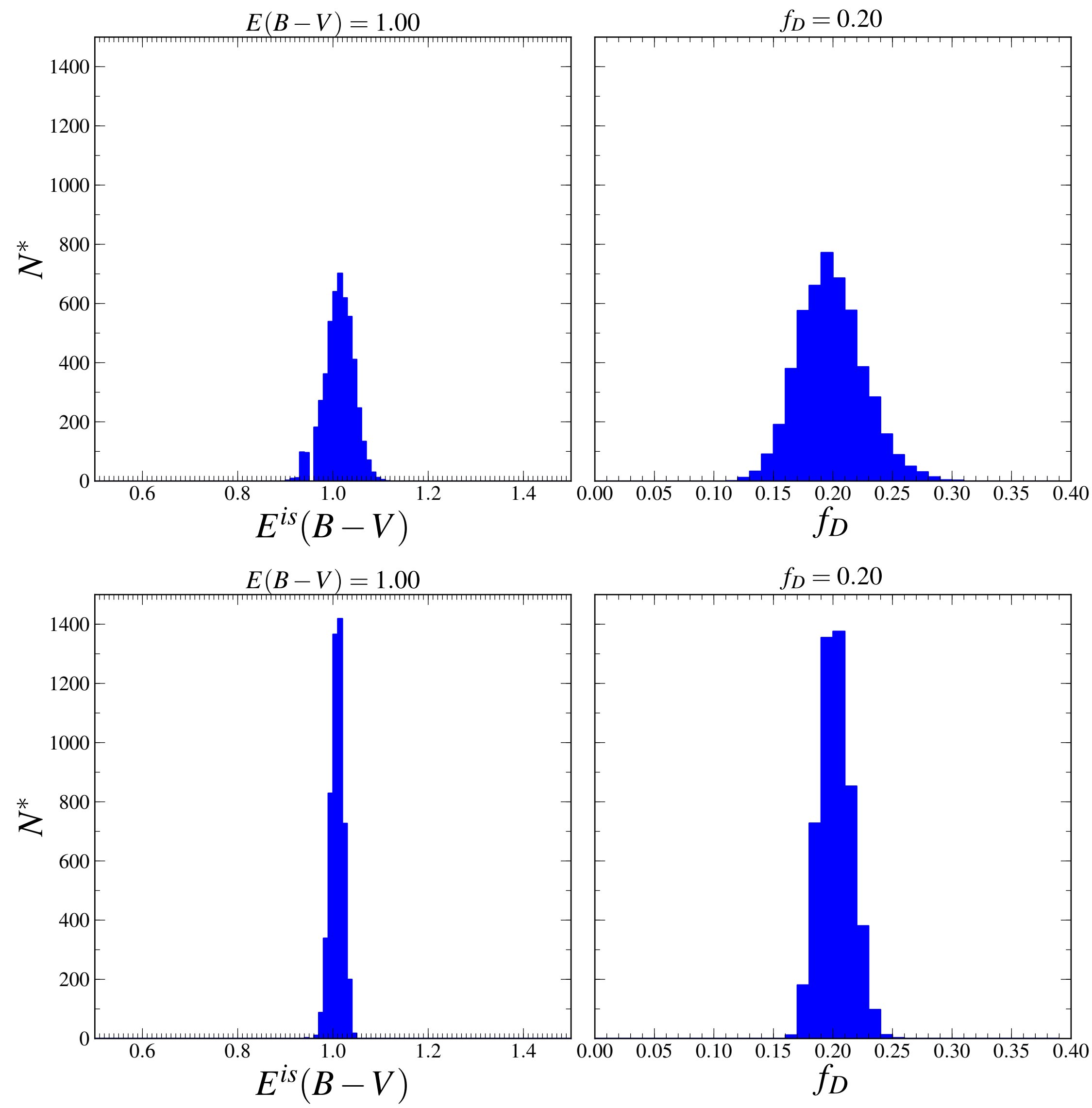

Figure 5.9: Monte Carlo simulations of simultaneous measures of $E^{is}(B-V)$ and f_D from noised-up Munari et al. (2005) model atmospheres. The chosen model atmosphere is the appropriate one for a B3 star and the input parameters to be measured are $E^{is}(B-V) = 1$ and $f_D = 0.20$ In the top panel is plotted the distribution of 1000 measures of $E^{is}(B-V)$ and f_D for a spectrum with S/N = 20. The distributions are centred at $E^{is}(B-V) = 1.01 \pm 0.03$ and $f_D = 0.20 \pm 0.03$, with $E^{is}(B-V)$ ranging between 0.90 and 1.11, and f_D between 0.11 and 0.30. Bottom panel is the same as above, but with SN = 50. Here, $E^{is}(B-V) = 1.01 \pm 0.01$ and $f_D = 0.20 \pm 0.01$, with $E^{is}(B-V)$ ranging between 0.95 and 1.04, and f_D between 0.16 and 0.25, therefore supplying more constrained values.

of the 24 models $\times$ 5 spectral types. Out of each simulation, I retrieved the $(E(B-V), f_D)$ values having the minimum value of χ^2 and binned them to produce histogram plots. In Figure 5.9, there are two examples, for the B3V star of Figure 5.8.

All the distributions of the measured parameters are close to Gaussian and centre on the input values, but their widths are very dependent on the S/N ratio. The standard deviations of the lower S/N simulations are 1/3 larger than in the second case.

To confirm the (im)possibility of measuring f_D just using the blue range between 3800 – 5000 Å, I also ran the same set of simulations within this narrower wavelength range. As expected, the weaker dependence of the disc emission on wavelength within the smaller blue range eliminated a clear minimum in the χ^2 surface.

5.5 Summary

In this chapter I revisited the standard approach to estimate circumstellar colour excesses in CBe stars. To do so, I constructed models that take into account what is known about the physics working in the circumstellar environment of CBe stars. The models are T_{eff} dependent and consist of a hydrogen recombination continuum, superimposed on a synthetic stellar spectrum. Using a well-established relation between $EW(\text{H}\alpha)$ and f_D, I estimated the fitted correction for each of the La Palma and FLWO/FAST spectra with measures of $EW(\text{H}\alpha)$.

I also tested the possibility of disentangling the interstellar colour excess from the circummstellar emission on simulated data. In future, this could be tested on observed data covering the whole optical spectral range, with accurate uniform flux calibration.

Table 5.1: Circumstellar colour excess, $E^{cs}(B-V)_{\mathrm{S}}$, in the $\lambda\lambda$3800 –5000 Å range, tabulated as function of spectral type of the central star and disc fraction.

		f_D									
SpT	T_e (K)	0.05	0.10	0.15	0.20	0.25	0.30	0.35	0.40	0.45	0.50
B0	18000	0.022	0.045	0.070	0.096	0.124	0.153	0.184	0.217	0.252	0.290
B1	15300	0.023	0.046	0.071	0.098	0.126	0.156	0.188	0.223	0.259	0.298
B2	13200	0.023	0.047	0.073	0.100	0.130	0.161	0.194	0.229	0.268	0.309
B3	11400	0.023	0.048	0.075	0.103	0.132	0.164	0.199	0.236	0.276	0.319
B4	10200	0.024	0.049	0.075	0.104	0.134	0.167	0.202	0.240	0.281	0.325
B5	9300	0.024	0.049	0.076	0.105	0.135	0.169	0.204	0.243	0.285	0.331
B6	8400	0.024	0.049	0.076	0.105	0.136	0.170	0.206	0.246	0.289	0.336
B7	7800	0.024	0.049	0.076	0.105	0.137	0.170	0.207	0.247	0.291	0.339
B8	7200	0.024	0.049	0.076	0.105	0.137	0.171	0.208	0.248	0.293	0.341
B9	6300	0.023	0.048	0.075	0.104	0.136	0.170	0.207	0.248	0.293	0.343
A0	5700	0.023	0.047	0.074	0.103	0.134	0.168	0.205	0.246	0.291	0.341

Table 5.2: Red-optical circumstellar colour excess in the $(r-i)$ range tabulated as function of spectral type of the central star and disc fraction.

		f_D									
SpT	T_e (K)	0.05	0.10	0.15	0.20	0.25	0.30	0.35	0.40	0.45	0.50
B0	18000	0.053	0.102	0.146	0.187	0.224	0.260	0.292	0.323	0.351	0.378
B1	15300	0.055	0.106	0.152	0.194	0.233	0.269	0.302	0.333	0.362	0.389
B2	13200	0.059	0.112	0.160	0.204	0.245	0.282	0.316	0.348	0.378	0.406
B3	11400	0.063	0.119	0.170	0.216	0.258	0.297	0.333	0.366	0.396	0.425
B4	10200	0.067	0.126	0.180	0.228	0.272	0.312	0.349	0.383	0.414	0.444
B5	9300	0.071	0.134	0.190	0.240	0.286	0.328	0.366	0.401	0.433	0.463
B6	8400	0.077	0.144	0.204	0.257	0.305	0.349	0.388	0.425	0.458	0.489
B7	7800	0.082	0.153	0.216	0.272	0.322	0.367	0.408	0.445	0.480	0.511
B8	7200	0.089	0.165	0.232	0.291	0.343	0.390	0.432	0.471	0.506	0.538
B9	6300	0.102	0.187	0.261	0.326	0.382	0.433	0.478	0.518	0.555	0.588
A0	5700	0.112	0.205	0.284	0.352	0.411	0.464	0.511	0.552	0.590	0.624

Table 5.3: *r*-band brightening, tabulated as function of spectral type of the central star and disc fraction.

		f_D									
SpT	T_e (K)	0.05	0.10	0.15	0.20	0.25	0.30	0.35	0.40	0.45	0.50
B0	18000	0.078	0.159	0.242	0.329	0.420	0.515	0.616	0.722	0.836	0.959
B1	15300	0.080	0.162	0.247	0.335	0.427	0.524	0.625	0.733	0.848	0.971
B2	13200	0.081	0.165	0.252	0.342	0.435	0.533	0.636	0.745	0.861	0.986
B3	11400	0.084	0.169	0.258	0.350	0.445	0.544	0.649	0.760	0.877	1.003
B4	10200	0.085	0.173	0.263	0.357	0.454	0.555	0.661	0.773	0.892	1.019
B5	9300	0.087	0.177	0.269	0.364	0.463	0.565	0.673	0.786	0.906	1.035
B6	8400	0.090	0.182	0.276	0.374	0.474	0.579	0.688	0.803	0.925	1.055
B7	7800	0.092	0.186	0.283	0.382	0.484	0.590	0.701	0.818	0.941	1.073
B8	7200	0.095	0.192	0.291	0.392	0.497	0.605	0.718	0.836	0.961	1.094
B9	6300	0.101	0.203	0.307	0.413	0.522	0.634	0.751	0.872	1.001	1.137
A0	5700	0.106	0.212	0.320	0.430	0.543	0.658	0.778	0.903	1.034	1.173

Table 5.4: Colour excesses and spectral types of the CBe stars with intermediate resolution spectra. Columns are in the following order: ID number; spectral type; measured spectroscopic colour excess; spectroscopic $EW(\mathrm{H}\alpha)$ corrected for filled-in absorption; disc fraction from the scaling relation, Eq. (5.3); spectroscopic interstellar reddening $E(B-V)_{(\mathrm{S,c})}$, after correction for circumstellar excess; $(r-i)$ colours corrected to zero Hα emission; intrinsic $(r-i)$ colours; measured $(r-i)$ colour excesses; photometric $EW(\mathrm{H}\alpha)$ corrected for filled-in absorption, with uncertainties typically in the range 1–2 Å; disc fraction from the scaling relation, Eq. (5.3); circumstellar $(r-i)$ colour excesses; interstellar $(r-i)$ colour excesses; photometric interstellar reddening $E(B-V)_{(\mathrm{P,c})}$, after correction for circumstellar excess. The final column lists the total colour excess along the sightline measured by SFD98.

#	SpT	$E(B-V)_{\mathrm{S}}$ (mag)	$EW(\mathrm{H}\alpha)_{\mathrm{S}}$ (Å)	f_D	$E(B-V)_{(\mathrm{S,c})}$ (mag)	$(r-i)_c$ (mag)	$(r-i)_0$ (mag)	$E(r-i)$ (mag)	$EW(\mathrm{H}\alpha)$ (Å)	f_D	$E^{cs}(r-i)$ (mag)	$E^{is}(r-i)$ (mag)	$E(B-V)_{(\mathrm{P,c})}$ (mag)	$E(B-V)_{\mathrm{SFD98}}$ (mag)
1	B5	1.40 ± 0.08	-25.4 ± 1.1	0.08	1.36 ± 0.08	0.87	-0.08	0.95 ± 0.06	-24	0.08	0.11	0.84 ± 0.06	1.21 ± 0.09	1.51
2	B7	0.66 ± 0.07	-12.6 ± 0.9	0.04	0.64 ± 0.07	0.35	-0.06	0.41 ± 0.03	-10	0.03	0.05	0.36 ± 0.05	0.53 ± 0.07	1.58
3	B3	1.60 ± 0.08	-34.6 ± 0.8	0.12	1.54 ± 0.08	1.00	-0.12	1.12 ± 0.07	-48	0.16	0.18	0.94 ± 0.07	1.36 ± 0.10	1.83
4	A0	1.02 ± 0.09	-22.5 ± 1.3	0.08	0.98 ± 0.09	0.77	0.00	0.77 ± 0.06	-27	0.09	0.18	0.59 ± 0.06	0.86 ± 0.09	1.78
5	B2	1.14 ± 0.08	-44.7 ± 0.9	0.15	1.07 ± 0.08	0.73	-0.13	0.86 ± 0.06	-50	0.17	0.18	0.68 ± 0.06	0.99 ± 0.08	1.55
6	B3	1.38 ± 0.10	-25.8 ± 1.1	0.09	1.34 ± 0.10	0.91	-0.12	1.03 ± 0.06	-26	0.09	0.11	0.92 ± 0.07	1.33 ± 0.09	1.51
7	B7	0.84 ± 0.07	-17.5 ± 1.2	0.06	0.81 ± 0.07	0.51	-0.06	0.57 ± 0.04	-16	0.05	0.08	0.49 ± 0.05	0.71 ± 0.07	1.51
8	B3	1.12 ± 0.07	-30.2 ± 1.4	0.10	1.07 ± 0.07	0.63	-0.12	0.75 ± 0.05	-33	0.11	0.13	0.62 ± 0.05	0.90 ± 0.08	1.28
9	B5	0.94 ± 0.08	-17.6 ± 1.0	0.06	0.91 ± 0.08	0.56	-0.08	0.64 ± 0.04	-18	0.06	0.08	0.56 ± 0.05	0.81 ± 0.07	1.60
10	B7	1.10 ± 0.08	-33.8 ± 0.8	0.11	1.05 ± 0.08	0.68	-0.06	0.74 ± 0.05	-35	0.12	0.18	0.56 ± 0.05	0.82 ± 0.08	1.66
11	B2	0.96 ± 0.08	-48.5 ± 0.9	0.16	0.88 ± 0.08	0.65	-0.12	0.77 ± 0.05	-51	0.17	0.18	0.59 ± 0.05	0.86 ± 0.07	1.07
12	B5	0.86 ± 0.09	-19.6 ± 1.2	0.07	0.83 ± 0.09	0.51	-0.08	0.59 ± 0.04	-19	0.06	0.08	0.51 ± 0.05	0.74 ± 0.07	1.15
13	B5	0.66 ± 0.08	-13.6 ± 1.0	0.05	0.64 ± 0.08	0.38	-0.08	0.46 ± 0.03	-11	0.04	0.06	0.40 ± 0.05	0.58 ± 0.07	1.02
14	B4	1.14 ± 0.08	-31.4 ± 1.3	0.10	1.09 ± 0.08	0.75	-0.09	0.84 ± 0.06	-32	0.11	0.14	0.70 ± 0.06	1.02 ± 0.09	1.37
15	B5	1.10 ± 0.07	-25.4 ± 0.8	0.08	1.06 ± 0.07	0.74	-0.08	0.82 ± 0.05	-26	0.09	0.12	0.70 ± 0.05	1.01 ± 0.08	1.66
16	B3	1.27 ± 0.08	-29.1 ± 0.8	0.10	1.22 ± 0.08	0.88	-0.12	1.00 ± 0.06	-34	0.11	0.13	0.87 ± 0.07	1.26 ± 0.09	1.91
17	B3	1.53 ± 0.08	-91.6 ± 0.9	0.31	1.36 ± 0.08	1.01	-0.12	1.13 ± 0.07	-92	0.31	0.30	0.83 ± 0.07	1.20 ± 0.10	1.47
18	B4	1.07 ± 0.08	-48.1 ± 1.0	0.16	0.99 ± 0.08	0.74	-0.09	0.83 ± 0.06	-44	0.15	0.18	0.65 ± 0.06	0.94 ± 0.09	1.39
19	B6	1.14 ± 0.07	-23.8 ± 1.2	0.08	1.10 ± 0.07	0.64	-0.07	0.71 ± 0.05	-24	0.08	0.12	0.59 ± 0.06	0.85 ± 0.08	1.19
20	B3	1.40 ± 0.08	-72.6 ± 0.8	0.24	1.28 ± 0.08	0.99	-0.12	1.11 ± 0.07	-70	0.23	0.24	0.87 ± 0.07	1.26 ± 0.10	1.90
21	B5	1.40 ± 0.09	-43.8 ± 1.3	0.15	1.33 ± 0.09	0.87	-0.08	0.95 ± 0.06	-41	0.14	0.18	0.77 ± 0.06	1.12 ± 0.09	2.39
22	B4	1.33 ± 0.07	-27.3 ± 1.0	0.09	1.29 ± 0.07	0.92	-0.09	1.01 ± 0.06	-26	0.09	0.12	0.89 ± 0.07	1.29 ± 0.09	1.40
23	B7	1.08 ± 0.09	-50.0 ± 1.0	0.17	0.99 ± 0.09	0.77	-0.06	0.83 ± 0.06	-48	0.16	0.23	0.60 ± 0.06	0.87 ± 0.09	1.39
24	B3	1.36 ± 0.07	-32.2 ± 0.8	0.11	1.31 ± 0.07	0.89	-0.12	1.01 ± 0.06	-48	0.16	0.18	0.83 ± 0.07	1.20 ± 0.09	1.96
25	B5	0.86 ± 0.07	-25.0 ± 0.8	0.08	0.82 ± 0.07	0.55	-0.08	0.63 ± 0.04	-22	0.07	0.10	0.53 ± 0.05	0.77 ± 0.07	1.19
26	B3	1.18 ± 0.09	-99.4 ± 1.1	0.33	1.00 ± 0.09	0.85	-0.12	0.97 ± 0.06	-93	0.31	0.30	0.67 ± 0.06	0.98 ± 0.09	1.37
27	B5	1.08 ± 0.07	-19.6 ± 1.0	0.07	1.05 ± 0.07	0.67	-0.08	0.75 ± 0.05	-17	0.06	0.08	0.67 ± 0.06	0.98 ± 0.08	1.30
28	B7	0.83 ± 0.08	-20.0 ± 0.9	0.07	0.80 ± 0.08	0.48	-0.06	0.54 ± 0.04	-16	0.05	0.08	0.46 ± 0.05	0.67 ± 0.07	1.12
29	B7	0.80 ± 0.07	-19.4 ± 0.9	0.06	0.77 ± 0.07	0.50	-0.06	0.56 ± 0.04	-15	0.05	0.08	0.48 ± 0.05	0.70 ± 0.07	1.42
30	B4	0.78 ± 0.07	-5.3 ± 1.2	0.02	0.77 ± 0.07	0.45	-0.09	0.54 ± 0.04	-10	0.03	0.04	0.50 ± 0.05	0.72 ± 0.07	0.97
31	B3	1.28 ± 0.07	-24.5 ± 0.9	0.08	1.24 ± 0.07	0.89	-0.12	1.00 ± 0.06	-23	0.08	0.10	0.90 ± 0.07	1.31 ± 0.09	1.74
32	B6	1.01 ± 0.08	-25.6 ± 0.9	0.09	0.97 ± 0.08	0.54	-0.07	0.61 ± 0.04	-21	0.07	0.10	0.51 ± 0.05	0.74 ± 0.07	0.93

Table 5.4: Continued

#	SpT	$E(B-V)_S$ (mag)	$EW(H\alpha)_S$ (Å)	f_D	$E(B-V)_{(S,c)}$ (mag)	$(r-i)_c$ (mag)	$(r-i)_0$ (mag)	$E(r-i)$ (mag)	$EW(H\alpha)$ (Å)	f_D	$E^{cs}(r-i)$ (mag)	$E^{is}(r-i)$ (mag)	$E(B-V)_{(P,c)}$ (mag)	$E(B-V)_{SFD98}$ (mag)
33	B8	0.88 ± 0.07	-14.4 ± 0.7	0.05	0.86 ± 0.07	0.58	-0.03	0.61 ± 0.05	-9	0.03	0.06	0.55 ± 0.06	0.79 ± 0.09	1.02
34	B3	0.70 ± 0.08	-36.9 ± 0.9	0.12	0.64 ± 0.08	0.49	-0.12	0.61 ± 0.04	-40	0.13	0.15	0.46 ± 0.05	0.67 ± 0.07	1.18
35	B2	0.93 ± 0.08	-56.5 ± 1.1	0.19	0.84 ± 0.08	0.58	-0.12	0.70 ± 0.05	-60	0.20	0.21	0.49 ± 0.05	0.71 ± 0.07	1.09
36	B4	1.53 ± 0.10	-59.0 ± 1.0	0.20	1.43 ± 0.10	1.11	-0.09	1.20 ± 0.07	-47	0.16	0.19	1.01 ± 0.07	1.46 ± 0.10	2.06
37	B6	0.92 ± 0.08	-18.5 ± 0.9	0.06	0.89 ± 0.08	0.61	-0.07	0.68 ± 0.05	-12	0.04	0.06	0.62 ± 0.06	0.89 ± 0.08	1.19
38	B5	0.90 ± 0.15	-21.0 ± 1.3	0.07	0.87 ± 0.15	0.68	-0.08	0.76 ± 0.05	-18	0.06	0.08	0.68 ± 0.06	0.98 ± 0.08	1.61
39	B4	0.96 ± 0.12	-82.4 ± 1.1	0.27	0.82 ± 0.12	0.75	-0.09	0.84 ± 0.06	-63	0.21	0.24	0.60 ± 0.06	0.87 ± 0.08	0.93
40*	B2	1.04 ± 0.07	-13.2 ± 1.5	0.04	1.02 ± 0.07	0.67	-0.13	0.80 ± 0.05	-17	0.06	0.07	0.73 ± 0.05	1.05 ± 0.08	0.32
41*	B7	1.02 ± 0.07	-19.2 ± 1.6	0.06	0.99 ± 0.07	0.57	-0.06	0.63 ± 0.04	-20	0.07	0.11	0.52 ± 0.05	0.76 ± 0.07	0.95
42*	B2	1.47 ± 0.08	-70.3 ± 2.2	0.23	1.35 ± 0.08	1.00	-0.13	1.13 ± 0.06	-75	0.25	0.25	0.88 ± 0.07	1.27 ± 0.09	0.94
43*	B6	0.82 ± 0.07			0.82 ± 0.07	0.44	-0.07	0.51 ± 0.04	-28	0.09	0.00	0.51 ± 0.04	0.74 ± 0.06	0.68
44*	B5	0.79 ± 0.07	-9.6 ± 2.6	0.03	0.78 ± 0.07	0.56	-0.08	0.64 ± 0.04	-8	0.03	0.04	0.60 ± 0.05	0.87 ± 0.07	0.85
45	B3	1.14 ± 0.07	-19.2 ± 0.8	0.06	1.11 ± 0.07	0.64	-0.12	0.76 ± 0.05	-38	0.13	0.15	0.61 ± 0.05	0.88 ± 0.08	1.51
46*	B9	0.84 ± 0.07	-16.8 ± 1.6	0.06	0.81 ± 0.07	0.57	-0.02	0.59 ± 0.05	-12	0.04	0.08	0.51 ± 0.06	0.74 ± 0.09	1.19
47*	B3	1.65 ± 0.07	-42.2 ± 1.2	0.14	1.58 ± 0.07	1.13	-0.12	1.25 ± 0.08	-42	0.14	0.16	1.09 ± 0.08	1.58 ± 0.11	1.98
48*	B8	1.15 ± 0.10			1.15 ± 0.10	0.74	-0.04	0.78 ± 0.06	-13	0.04	0.00	0.78 ± 0.06	1.13 ± 0.08	1.23
49*	A0	0.74 ± 0.07	-26.5 ± 3.3	0.09	0.70 ± 0.07	0.44	0.00	0.44 ± 0.04	-20	0.07	0.14	0.30 ± 0.06	0.44 ± 0.08	0.72
50*	B3	1.00 ± 0.08	-47.0 ± 2.0	0.16	0.92 ± 0.08	0.75	-0.12	0.87 ± 0.06	-72	0.24	0.25	0.62 ± 0.06	0.90 ± 0.09	1.26
51*	B8	0.73 ± 0.07	-12.3 ± 1.3	0.04	0.71 ± 0.07	0.41	-0.03	0.43 ± 0.04	-8	0.03	0.06	0.37 ± 0.06	0.54 ± 0.08	0.78
52*	B7	0.90 ± 0.08	-18.0 ± 2.7	0.06	0.87 ± 0.08	0.60	-0.06	0.66 ± 0.05	-29	0.10	0.15	0.51 ± 0.06	0.74 ± 0.08	0.98
53*	B7	1.11 ± 0.07	-41.6 ± 1.7	0.14	1.04 ± 0.07	0.67	-0.06	0.73 ± 0.05	-42	0.14	0.20	0.53 ± 0.05	0.76 ± 0.08	1.47
54*	B3	0.85 ± 0.07	-26.8 ± 2.0	0.09	0.81 ± 0.07	0.48	-0.12	0.60 ± 0.04	-29	0.10	0.12	0.48 ± 0.05	0.69 ± 0.07	1.12
55*	B3	1.04 ± 0.08	-37.8 ± 2.0	0.13	0.98 ± 0.08	0.72	-0.10	0.82 ± 0.06	-53	0.18	0.20	0.62 ± 0.06	0.90 ± 0.08	1.22
56*	B7	1.02 ± 0.07	-47.4 ± 1.6	0.16	0.94 ± 0.07	0.69	-0.06	0.75 ± 0.05	-43	0.14	0.20	0.55 ± 0.05	0.80 ± 0.08	1.72
57*	B7	1.00 ± 0.08			1.00 ± 0.08	0.70	-0.05	0.75 ± 0.05	-23	0.08	0.00	0.75 ± 0.05	1.09 ± 0.07	1.36
58*	B3	0.72 ± 0.07	-31.4 ± 1.2	0.10	0.67 ± 0.07	0.36	-0.12	0.48 ± 0.04	-31	0.10	0.12	0.36 ± 0.05	0.52 ± 0.07	0.90
59*	B4	1.04 ± 0.09	-144.0 ± 1.9	0.48	0.74 ± 0.09	0.69	-0.09	0.78 ± 0.06	-144	0.48	0.43	0.35 ± 0.06	0.50 ± 0.08	3.16
60*	B5	0.78 ± 0.08	-52.2 ± 1.8	0.17	0.69 ± 0.08	0.47	-0.08	0.55 ± 0.04	-52	0.17	0.21	0.34 ± 0.05	0.49 ± 0.07	1.24
61*	B3	0.82 ± 0.08	-31.2 ± 3.1	0.10	0.77 ± 0.08	0.39	-0.10	0.50 ± 0.04	-39	0.13	0.15	0.35 ± 0.05	0.51 ± 0.07	1.24
62*	B7	0.74 ± 0.08	-11.4 ± 1.6	0.04	0.72 ± 0.08	0.43	-0.06	0.49 ± 0.04	-8	0.03	0.05	0.44 ± 0.05	0.64 ± 0.07	0.81
63*	B6	1.23 ± 0.10	-16.7 ± 1.6	0.06	1.20 ± 0.10	0.77	-0.07	0.84 ± 0.06	-21	0.07	0.10	0.74 ± 0.06	1.07 ± 0.09	1.62
64*	B7	0.89 ± 0.07			0.89 ± 0.07	0.52	-0.06	0.58 ± 0.04	-16	0.05	0.00	0.58 ± 0.04	0.84 ± 0.06	1.67
65*	B5	1.25 ± 0.09	-17.0 ± 2.1	0.06	1.22 ± 0.09	0.81	-0.08	0.89 ± 0.06	-18	0.06	0.08	0.81 ± 0.06	1.18 ± 0.09	1.32
66*	B5	0.98 ± 0.07	-31.4 ± 1.4	0.10	0.93 ± 0.07	0.56	-0.08	0.64 ± 0.04	-14	0.05	0.07	0.57 ± 0.05	0.82 ± 0.07	1.55
67*	B4	1.10 ± 0.08	-25.5 ± 1.4	0.08	1.06 ± 0.08	0.64	-0.09	0.73 ± 0.05	-30	0.10	0.13	0.60 ± 0.05	0.86 ± 0.08	1.72
68	B4	1.14 ± 0.11	-18.2 ± 0.9	0.06	1.11 ± 0.11	0.81	-0.09	0.90 ± 0.06	-31	0.10	0.13	0.77 ± 0.06	1.12 ± 0.09	1.51

[1] NOT/ALFOSC observations, for which $EW(H\alpha)_S$ were measured from FLWO/FAST spectra when available.

Table 5.5: Colour excesses and spectral types of the 181 candidate CBe stars with FLWO/FAST spectra. Columns are in the following order: ID number; spectral type; Hα emission-corrected $(r-i)_c$ colours; intrinsic $(r-i)$ colours; measured $(r-i)$ colour excesses; photometric $EW(\mathrm{H}\alpha)$ corrected for filled-in absorption, with uncertainties typically in the range 1–2 Å; disc fraction from the scaling relation, Eq. (5.3); circumstellar $(r-i)$ colour excesses; interstellar $(r-i)$ colour excesses; interstellar reddening $E(B-V)_{(\mathrm{P,c})}$, after correction for circumstellar excess.

#	SpT	$(r-i)_c$ (mag)	$(r-i)_0$ (mag)	$E(r-i)$ (mag)	$EW(\mathrm{H}\alpha)$ (Å)	f_D	$E^{cs}(r-i)$ (mag)	$E^{is}(r-i)$ (mag)	$E(B-V)_{(\mathrm{P,c})}$ (mag)	$E(B-V)_{\mathrm{SFD98}}$ (mag)
F003	Mid-B	0.64	-0.08	0.71 ± 0.06	-14	0.05	0.08	0.64 ± 0.06	0.93 ± 0.09	1.59
F004	Late-B	0.49	-0.04	0.53 ± 0.05	-11	0.04	0.07	0.46 ± 0.06	0.67 ± 0.09	0.94
F012	B6	0.50	-0.07	0.57 ± 0.03	-26	0.09	0.13	0.44 ± 0.04	0.64 ± 0.06	1.89
F018	Early-B	0.76	-0.13	0.89 ± 0.06	-37	0.12	0.14	0.75 ± 0.06	1.09 ± 0.08	1.54
F024	Mid-B	0.62	-0.08	0.70 ± 0.06	-24	0.08	0.11	0.59 ± 0.06	0.85 ± 0.09	1.51
F026	B7	0.41	-0.06	0.47 ± 0.04	-17	0.06	0.10	0.37 ± 0.05	0.55 ± 0.07	1.39
F027	B6	0.58	-0.07	0.65 ± 0.04	-11	0.04	0.06	0.59 ± 0.05	0.86 ± 0.07	1.85
F028	Late-B	0.82	-0.04	0.86 ± 0.05	-21	0.07	0.12	0.74 ± 0.06	1.07 ± 0.09	1.66
F029	B5	0.40	-0.08	0.48 ± 0.04	-25	0.08	0.11	0.37 ± 0.04	0.54 ± 0.06	1.31
F033	Late-B	0.57	-0.04	0.61 ± 0.05	-19	0.06	0.10	0.51 ± 0.06	0.74 ± 0.09	1.24
F039	B5	0.40	-0.08	0.48 ± 0.04	-13	0.04	0.06	0.42 ± 0.04	0.62 ± 0.06	1.51
F040	Late-B	0.48	-0.04	0.52 ± 0.05	-31	0.10	0.17	0.35 ± 0.06	0.51 ± 0.09	1.06
F041	B3	0.31	-0.12	0.43 ± 0.04	-43	0.14	0.16	0.27 ± 0.04	0.40 ± 0.06	1.28
F042	B8	0.46	-0.04	0.49 ± 0.04	-24	0.08	0.14	0.36 ± 0.05	0.52 ± 0.07	1.69
F044	Late-B	0.49	-0.04	0.53 ± 0.05	-11	0.04	0.07	0.46 ± 0.06	0.67 ± 0.09	1.92
F045	Late-B	0.57	-0.04	0.61 ± 0.05	-24	0.08	0.14	0.47 ± 0.06	0.69 ± 0.09	1.93
F046	Late-B	0.53	-0.04	0.57 ± 0.05	-17	0.06	0.10	0.47 ± 0.06	0.68 ± 0.09	1.40
F047	Late-B	0.59	-0.04	0.63 ± 0.05	-41	0.14	0.22	0.41 ± 0.06	0.60 ± 0.09	1.92
F054	B6	0.37	-0.07	0.44 ± 0.04	-13	0.04	0.06	0.38 ± 0.04	0.54 ± 0.06	0.84
F059	Late-B	0.34	-0.04	0.38 ± 0.05	-2	0.01	0.02	0.36 ± 0.06	0.52 ± 0.09	1.15
F060	B9	0.72	-0.02	0.73 ± 0.04	-27	0.09	0.17	0.57 ± 0.05	0.82 ± 0.08	1.95
F061	B1	0.67	-0.15	0.82 ± 0.04	-23	0.08	0.09	0.73 ± 0.04	1.06 ± 0.07	1.75
F066	Late-B	0.78	-0.04	0.82 ± 0.05	-18	0.06	0.10	0.72 ± 0.06	1.04 ± 0.09	1.87

Table 5.5: Continued

#	SpT	$(r-i)_c$ (mag)	$(r-i)_0$ (mag)	$E(r-i)$ (mag)	$EW(\mathrm{H}\alpha)$ (Å)	f_D	$E^{cs}(r-i)$ (mag)	$E^{is}(r-i)$ (mag)	$E(B-V)_{(\mathrm{P,c})}$ (mag)	$E(B-V)_{\mathrm{SFD98}}$ (mag)
F069	Mid-B	0.62	-0.08	0.70 ± 0.06	-43	0.14	0.18	0.52 ± 0.06	0.75 ± 0.08	1.43
F074	Late-B	0.72	-0.04	0.76 ± 0.06	-20	0.07	0.12	0.64 ± 0.06	0.93 ± 0.09	1.49
F075	Late-B	0.88	-0.04	0.92 ± 0.05	-20	0.07	0.12	0.80 ± 0.06	1.17 ± 0.09	1.97
F077	B7	0.50	-0.06	0.56 ± 0.04	-18	0.06	0.10	0.46 ± 0.05	0.67 ± 0.07	1.40
F079	B3	0.74	-0.12	0.86 ± 0.04	-13	0.04	0.05	0.81 ± 0.05	1.18 ± 0.07	1.86
F083	B3	0.71	-0.12	0.83 ± 0.04	-24	0.08	0.10	0.73 ± 0.04	1.07 ± 0.07	1.40
F085	B3	0.51	-0.12	0.63 ± 0.04	-31	0.10	0.12	0.51 ± 0.04	0.75 ± 0.07	1.19
F089	Early-B	1.04	-0.13	1.17 ± 0.06	-74	0.25	0.26	0.91 ± 0.06	1.32 ± 0.08	1.59
F092	B4	0.62	-0.09	0.71 ± 0.04	-11	0.04	0.06	0.65 ± 0.05	0.95 ± 0.07	1.39
F095	B6	0.43	-0.07	0.50 ± 0.03	-37	0.12	0.17	0.33 ± 0.04	0.49 ± 0.06	1.33
F097	Late-B	0.68	-0.04	0.72 ± 0.05	-17	0.06	0.10	0.62 ± 0.06	0.89 ± 0.09	1.42
F098	B3	0.69	-0.12	0.81 ± 0.04	-74	0.25	0.26	0.55 ± 0.04	0.80 ± 0.06	1.12
F099	Mid-B	0.55	-0.08	0.63 ± 0.06	-16	0.05	0.08	0.55 ± 0.06	0.81 ± 0.09	1.12
F100	Mid-B	0.67	-0.08	0.75 ± 0.06	-24	0.08	0.11	0.64 ± 0.06	0.93 ± 0.10	1.13
F102	B6	0.63	-0.07	0.70 ± 0.03	-14	0.05	0.08	0.62 ± 0.04	0.91 ± 0.06	1.22
F106	Late-B	0.50	-0.04	0.54 ± 0.05	-10	0.03	0.06	0.48 ± 0.06	0.70 ± 0.09	1.44
F107	B6	0.37	-0.07	0.44 ± 0.03	-10	0.03	0.05	0.39 ± 0.04	0.57 ± 0.06	1.62
F108	B7	0.48	-0.06	0.54 ± 0.04	-22	0.07	0.11	0.43 ± 0.05	0.63 ± 0.07	1.19
F110	Late-B	0.64	-0.04	0.68 ± 0.05	-25	0.08	0.14	0.54 ± 0.06	0.78 ± 0.09	1.19
F112	Early-B	0.68	-0.13	0.81 ± 0.06	-30	0.10	0.12	0.69 ± 0.06	1.00 ± 0.09	1.59
F113	Mid-B	0.47	-0.08	0.55 ± 0.06	-29	0.10	0.14	0.41 ± 0.06	0.60 ± 0.09	1.36
F114	B2	0.57	-0.13	0.70 ± 0.04	-28	0.09	0.10	0.60 ± 0.04	0.86 ± 0.07	2.09
F116	B4	0.59	-0.09	0.68 ± 0.04	-47	0.16	0.19	0.49 ± 0.04	0.70 ± 0.07	2.29
F118	B3	0.50	-0.12	0.61 ± 0.04	-6	0.02	0.03	0.59 ± 0.05	0.85 ± 0.07	2.27
F121	Mid-B	0.70	-0.08	0.77 ± 0.06	-40	0.13	0.17	0.61 ± 0.06	0.87 ± 0.09	1.13
F122	Late-B	0.45	-0.04	0.49 ± 0.05	-23	0.08	0.14	0.35 ± 0.06	0.51 ± 0.09	1.28

Table 5.5: Continued

#	SpT	$(r-i)_c$ (mag)	$(r-i)_0$ (mag)	$E(r-i)$ (mag)	$EW(\mathrm{H\alpha})$ (Å)	f_D	$E^{cs}(r-i)$ (mag)	$E^{is}(r-i)$ (mag)	$E(B-V)_{(\mathrm{P,c})}$ (mag)	$E(B-V)_{\mathrm{SFD98}}$ (mag)
F124	Late-B	0.63	-0.04	0.67 ± 0.05	-11	0.04	0.07	0.60 ± 0.06	0.88 ± 0.09	1.34
F125	B6	0.50	-0.07	0.57 ± 0.04	-13	0.04	0.06	0.51 ± 0.05	0.74 ± 0.07	1.02
F126	B9	0.71	-0.02	0.73 ± 0.04	-16	0.05	0.10	0.63 ± 0.05	0.91 ± 0.07	1.71
F129	B7	0.48	-0.06	0.53 ± 0.04	-8	0.03	0.05	0.49 ± 0.05	0.71 ± 0.08	1.69
F130	Mid-B	0.58	-0.08	0.66 ± 0.06	-17	0.06	0.08	0.58 ± 0.06	0.84 ± 0.10	1.30
F131	B7	0.40	-0.06	0.46 ± 0.04	-7	0.02	0.03	0.43 ± 0.05	0.62 ± 0.08	1.24
F132	Mid-B	0.64	-0.08	0.72 ± 0.06	-31	0.10	0.14	0.58 ± 0.06	0.84 ± 0.09	1.23
F134	B5	0.42	-0.08	0.50 ± 0.04	-10	0.03	0.04	0.46 ± 0.05	0.66 ± 0.07	0.96
F135	B6	0.40	-0.07	0.47 ± 0.03	-4	0.01	0.01	0.46 ± 0.04	0.66 ± 0.06	1.08
F136	B7	0.36	-0.06	0.42 ± 0.04	-2	0.01	0.02	0.40 ± 0.05	0.57 ± 0.07	0.91
F138	Late-B	0.54	-0.04	0.58 ± 0.06	-10	0.03	0.06	0.52 ± 0.06	0.75 ± 0.09	1.29
F139	B3	0.48	-0.12	0.60 ± 0.04	-15	0.05	0.06	0.54 ± 0.04	0.78 ± 0.07	1.66
F141	B3	0.58	-0.12	0.70 ± 0.04	-34	0.11	0.13	0.57 ± 0.04	0.82 ± 0.07	1.06
F142	Late-B	0.60	-0.04	0.64 ± 0.05	-20	0.07	0.12	0.52 ± 0.06	0.76 ± 0.09	1.58
F144	B1	0.44	-0.15	0.58 ± 0.04	-23	0.08	0.09	0.50 ± 0.04	0.72 ± 0.07	1.38
F145	B4	0.27	-0.08	0.36 ± 0.04	-29	0.10	0.13	0.22 ± 0.04	0.33 ± 0.07	0.96
F146	Mid-B	0.53	-0.08	0.61 ± 0.06	-7	0.02	0.03	0.58 ± 0.06	0.84 ± 0.10	1.08
F147	B3	0.59	-0.12	0.71 ± 0.04	-24	0.08	0.10	0.61 ± 0.04	0.89 ± 0.07	1.63
F151	Late-B	0.73	-0.04	0.77 ± 0.05	-16	0.05	0.09	0.68 ± 0.06	0.99 ± 0.09	2.44
F152	B4	0.37	-0.09	0.46 ± 0.04	-6	0.02	0.03	0.43 ± 0.05	0.63 ± 0.07	0.87
F154	Mid-B	0.71	-0.08	0.79 ± 0.06	-25	0.08	0.11	0.68 ± 0.06	0.99 ± 0.09	1.30
F157	B4	0.37	-0.09	0.46 ± 0.04	-22	0.07	0.09	0.37 ± 0.04	0.54 ± 0.07	0.91
F159	B5	0.44	-0.08	0.52 ± 0.03	-26	0.09	0.12	0.40 ± 0.04	0.58 ± 0.06	0.95
F160	Late-B	0.53	-0.04	0.57 ± 0.05	-9	0.03	0.06	0.51 ± 0.06	0.75 ± 0.09	1.30
F161	Mid-B	0.37	-0.08	0.45 ± 0.06	-2	0.01	0.01	0.44 ± 0.06	0.63 ± 0.09	0.82
F162	B3	0.67	-0.12	0.79 ± 0.04	-34	0.11	0.13	0.66 ± 0.04	0.95 ± 0.07	1.05

Table 5.5: Continued

#	SpT	$(r-i)_c$ (mag)	$(r-i)_0$ (mag)	$E(r-i)$ (mag)	$EW(\mathrm{H}\alpha)$ (Å)	f_D	$E^{cs}(r-i)$ (mag)	$E^{is}(r-i)$ (mag)	$E(B-V)_{(\mathrm{P,c})}$ (mag)	$E(B-V)_{\mathrm{SFD98}}$ (mag)
F163	Mid-B	0.68	-0.08	0.76 ± 0.06	−39	0.13	0.17	0.59 ± 0.06	0.85 ± 0.09	1.27
F166	Mid-B	0.44	-0.08	0.52 ± 0.06	−7	0.02	0.03	0.49 ± 0.06	0.71 ± 0.09	1.18
F167	B7	0.46	-0.06	0.52 ± 0.04	−11	0.04	0.07	0.45 ± 0.05	0.65 ± 0.08	1.31
F169	Early-B	0.79	-0.13	0.92 ± 0.06	−43	0.14	0.16	0.76 ± 0.06	1.11 ± 0.08	1.20
F170	Mid-B	0.62	-0.08	0.70 ± 0.06	−27	0.09	0.12	0.58 ± 0.06	0.83 ± 0.10	1.27
F171	Mid-B	0.57	-0.08	0.65 ± 0.06	−19	0.06	0.08	0.57 ± 0.06	0.82 ± 0.09	1.06
F172	B7	0.46	-0.06	0.52 ± 0.04	−13	0.04	0.07	0.45 ± 0.05	0.65 ± 0.08	0.92
F173	B5	0.37	-0.08	0.45 ± 0.04	−13	0.04	0.06	0.39 ± 0.05	0.57 ± 0.07	0.90
F174	Late-B	0.60	-0.04	0.64 ± 0.05	−13	0.04	0.07	0.57 ± 0.06	0.83 ± 0.09	1.14
F175	B1	0.38	-0.15	0.53 ± 0.04	−12	0.04	0.05	0.48 ± 0.04	0.69 ± 0.07	1.03
F176	Mid-B	0.40	-0.08	0.48 ± 0.06	−29	0.10	0.14	0.34 ± 0.06	0.49 ± 0.09	0.91
F178	Mid-B	0.40	-0.08	0.49 ± 0.06	−5	0.02	0.03	0.45 ± 0.06	0.66 ± 0.09	1.32
F179	B3	0.35	-0.12	0.47 ± 0.04	−26	0.09	0.11	0.36 ± 0.04	0.52 ± 0.07	0.89
F180	Late-B	0.72	-0.04	0.76 ± 0.05	−11	0.04	0.07	0.69 ± 0.06	1.00 ± 0.09	1.02
F182	Late-B	0.36	-0.04	0.39 ± 0.06	−7	0.02	0.03	0.37 ± 0.07	0.52 ± 0.09	0.85
F183	B3	0.57	-0.12	0.69 ± 0.04	−27	0.09	0.11	0.58 ± 0.04	0.83 ± 0.07	1.43
F184	A0	0.69	0.00	0.69 ± 0.04	−20	0.07	0.14	0.55 ± 0.05	0.79 ± 0.07	1.26
F185	Late-B	0.57	-0.04	0.61 ± 0.05	−23	0.08	0.14	0.47 ± 0.06	0.68 ± 0.09	1.01
F187	B3	0.35	-0.12	0.47 ± 0.04	−12	0.04	0.05	0.42 ± 0.05	0.61 ± 0.07	1.12
F188	Late-B	0.53	-0.04	0.57 ± 0.05	−8	0.03	0.06	0.51 ± 0.06	0.74 ± 0.09	0.92
F189	B9	0.83	-0.02	0.85 ± 0.04	−17	0.06	0.12	0.73 ± 0.05	1.07 ± 0.08	1.56
F190	B8	0.37	-0.04	0.41 ± 0.04	−9	0.03	0.06	0.35 ± 0.05	0.52 ± 0.08	0.94
F192	Late-B	0.58	-0.04	0.62 ± 0.06	−8	0.02	0.03	0.59 ± 0.07	0.84 ± 0.09	1.17
F194	Mid-B	0.61	-0.08	0.69 ± 0.06	−22	0.07	0.10	0.59 ± 0.06	0.86 ± 0.09	1.23
F195	B8	0.56	-0.04	0.60 ± 0.04	−11	0.04	0.08	0.52 ± 0.05	0.77 ± 0.08	1.43
F196	B6	0.50	-0.07	0.57 ± 0.04	−5	0.02	0.03	0.54 ± 0.05	0.78 ± 0.07	1.79

Table 5.5: Continued

#	SpT	$(r-i)_c$ (mag)	$(r-i)_0$ (mag)	$E(r-i)$ (mag)	$EW(\mathrm{H}\alpha)$ (Å)	f_D	$E^{cs}(r-i)$ (mag)	$E^{is}(r-i)$ (mag)	$E(B-V)_{(\mathrm{P,c})}$ (mag)	$E(B-V)_{\mathrm{SFD98}}$ (mag)
F198	B6	0.56	-0.07	0.63 ± 0.04	-10	0.03	0.05	0.58 ± 0.05	0.84 ± 0.07	1.01
F199	Late-B	0.91	-0.04	0.95 ± 0.05	-31	0.10	0.17	0.78 ± 0.06	1.14 ± 0.09	1.49
F200	Mid-B	0.91	-0.08	0.99 ± 0.06	-20	0.06	0.08	0.91 ± 0.06	1.32 ± 0.10	1.48
F201	B5	0.37	-0.08	0.45 ± 0.03	-19	0.06	0.08	0.37 ± 0.04	0.54 ± 0.06	1.02
F202	Mid-B	0.62	-0.08	0.70 ± 0.06	-27	0.09	0.12	0.58 ± 0.06	0.84 ± 0.09	1.50
F203	Early-B	0.78	-0.13	0.91 ± 0.06	-25	0.08	0.10	0.81 ± 0.06	1.18 ± 0.09	1.29
F204	Late-B	0.61	-0.04	0.65 ± 0.05	-6	0.02	0.03	0.62 ± 0.06	0.89 ± 0.09	2.11
F205	B7	0.48	-0.06	0.54 ± 0.04	-11	0.04	0.07	0.47 ± 0.05	0.68 ± 0.08	1.00
F209	Early-B	0.64	-0.13	0.78 ± 0.06	-31	0.10	0.12	0.65 ± 0.06	0.95 ± 0.09	1.02
F211	Late-B	0.50	-0.04	0.54 ± 0.05	-18	0.06	0.10	0.44 ± 0.06	0.64 ± 0.09	1.06
F212	B4	0.59	-0.09	0.68 ± 0.04	-36	0.12	0.14	0.54 ± 0.04	0.77 ± 0.06	1.13
F213	Mid-B	0.58	-0.08	0.66 ± 0.06	-34	0.11	0.14	0.52 ± 0.06	0.75 ± 0.09	1.06
F216	Late-B	0.57	-0.04	0.61 ± 0.05	-13	0.04	0.07	0.54 ± 0.06	0.79 ± 0.09	0.96
F219	Late-B	0.50	-0.04	0.54 ± 0.05	-19	0.06	0.10	0.44 ± 0.06	0.64 ± 0.09	0.64
F220	Late-B	0.52	-0.04	0.56 ± 0.06	-26	0.09	0.15	0.41 ± 0.06	0.59 ± 0.09	1.02
F221	Late-B	0.42	-0.04	0.46 ± 0.05	-10	0.03	0.06	0.40 ± 0.06	0.58 ± 0.09	0.92
F222	Mid-B	0.69	-0.08	0.77 ± 0.06	-26	0.09	0.12	0.65 ± 0.06	0.94 ± 0.10	1.13
F223	Late-B	0.65	-0.04	0.69 ± 0.05	-11	0.04	0.07	0.62 ± 0.06	0.90 ± 0.09	0.81
F224	B8	0.48	-0.04	0.52 ± 0.04	-50	0.17	0.26	0.26 ± 0.04	0.38 ± 0.07	0.82
F228	B7	0.70	-0.06	0.76 ± 0.04	-14	0.05	0.08	0.68 ± 0.04	0.98 ± 0.07	0.72
F229	Late-B	0.66	-0.04	0.70 ± 0.05	-19	0.06	0.10	0.60 ± 0.06	0.86 ± 0.09	0.69
F232	B5	0.59	-0.08	0.67 ± 0.03	-15	0.05	0.07	0.60 ± 0.04	0.87 ± 0.06	1.10
F237	Late-B	0.59	-0.04	0.63 ± 0.06	-18	0.06	0.10	0.53 ± 0.06	0.76 ± 0.09	1.01
F238	B3	0.56	-0.12	0.68 ± 0.04	-38	0.13	0.15	0.53 ± 0.04	0.77 ± 0.07	0.44
F243	Late-B	0.56	-0.04	0.60 ± 0.05	-24	0.08	0.14	0.46 ± 0.06	0.66 ± 0.09	1.01
F245	Early-B	0.66	-0.13	0.79 ± 0.06	-14	0.05	0.06	0.73 ± 0.06	1.05 ± 0.08	0.96

Table 5.5: Continued

#	SpT	$(r-i)_c$ (mag)	$(r-i)_0$ (mag)	$E(r-i)$ (mag)	$EW(\mathrm{H}\alpha)$ (Å)	f_D	$E^{cs}(r-i)$ (mag)	$E^{is}(r-i)$ (mag)	$E(B-V)_{(\mathrm{P,c})}$ (mag)	$E(B-V)_{\mathrm{SFD98}}$ (mag)
F246	B4	0.44	-0.09	0.53 ± 0.04	−5	0.02	0.03	0.50 ± 0.05	0.72 ± 0.07	0.61
F247	Late-B	0.63	-0.04	0.67 ± 0.06	−10	0.03	0.06	0.61 ± 0.07	0.90 ± 0.09	0.95
F248	Mid-B	0.73	-0.08	0.81 ± 0.06	−48	0.16	0.21	0.60 ± 0.06	0.87 ± 0.09	0.99
F254	B3	0.61	-0.12	0.73 ± 0.04	−27	0.09	0.11	0.62 ± 0.04	0.90 ± 0.07	1.06
F256	Mid-B	0.71	-0.08	0.79 ± 0.06	−17	0.06	0.08	0.71 ± 0.07	1.03 ± 0.11	1.11
F259	Late-B	0.57	-0.04	0.61 ± 0.06	−15	0.05	0.09	0.52 ± 0.07	0.76 ± 0.10	0.62
F261	Mid-B	0.61	-0.08	0.69 ± 0.06	−33	0.11	0.14	0.55 ± 0.06	0.79 ± 0.09	0.95
F263	Early-B	0.52	-0.13	0.65 ± 0.06	−8	0.03	0.03	0.62 ± 0.06	0.90 ± 0.09	0.54
F264	B7	0.30	-0.06	0.36 ± 0.04	−9	0.03	0.05	0.31 ± 0.05	0.45 ± 0.08	0.79
F265	B4	0.56	-0.09	0.65 ± 0.04	−15	0.05	0.07	0.58 ± 0.04	0.85 ± 0.07	0.57
F266	Late-B	0.59	-0.04	0.63 ± 0.05	−17	0.06	0.10	0.53 ± 0.06	0.76 ± 0.09	1.01
F269	Late-B	0.39	-0.04	0.43 ± 0.05	−16	0.05	0.09	0.34 ± 0.06	0.49 ± 0.09	0.85
F276	Late-B	0.61	-0.04	0.65 ± 0.05	−16	0.05	0.09	0.56 ± 0.06	0.82 ± 0.09	2.23
F278	Early-B	0.47	-0.13	0.60 ± 0.06	−38	0.13	0.14	0.46 ± 0.06	0.66 ± 0.09	0.76
F281	B3	0.37	-0.12	0.49 ± 0.04	−22	0.07	0.08	0.41 ± 0.04	0.59 ± 0.07	0.78
F286	Mid-B	0.52	-0.08	0.60 ± 0.06	−33	0.11	0.14	0.46 ± 0.06	0.67 ± 0.09	0.96
F289	Early-B	0.57	-0.13	0.70 ± 0.06	−58	0.19	0.20	0.50 ± 0.06	0.72 ± 0.09	0.98
F290	Early-B	0.48	-0.13	0.61 ± 0.06	−46	0.15	0.17	0.44 ± 0.06	0.65 ± 0.08	0.91
F291	Mid-B	0.38	-0.08	0.46 ± 0.06	−19	0.06	0.08	0.38 ± 0.06	0.54 ± 0.09	0.93
F292	B3	0.44	-0.12	0.56 ± 0.04	−30	0.10	0.12	0.44 ± 0.04	0.64 ± 0.07	0.94
F293	Mid-B	0.61	-0.08	0.69 ± 0.06	−28	0.09	0.12	0.57 ± 0.06	0.82 ± 0.09	0.97
F295	B5	0.36	-0.08	0.44 ± 0.04	−11	0.04	0.06	0.38 ± 0.05	0.56 ± 0.07	2.47
F297	B3	0.65	-0.12	0.77 ± 0.04	−33	0.11	0.13	0.64 ± 0.04	0.92 ± 0.07	1.01
F298	Early-B	0.55	-0.13	0.68 ± 0.06	−49	0.16	0.17	0.51 ± 0.06	0.73 ± 0.09	1.45
F299	B5	0.38	-0.08	0.46 ± 0.03	−23	0.08	0.11	0.35 ± 0.04	0.51 ± 0.06	1.01
F301	Mid-B	0.43	-0.08	0.51 ± 0.06	−44	0.15	0.19	0.32 ± 0.06	0.46 ± 0.09	1.15

Table 5.5: Continued

#	SpT	$(r-i)_c$ (mag)	$(r-i)_0$ (mag)	$E(r-i)$ (mag)	$EW(\mathrm{H\alpha})$ (Å)	f_D	$E^{cs}(r-i)$ (mag)	$E^{is}(r-i)$ (mag)	$E(B-V)_{(\mathrm{P,c})}$ (mag)	$E(B-V)_{\mathrm{SFD98}}$ (mag)
F302	Mid-B	0.34	-0.08	0.42 ± 0.06	-30	0.10	0.14	0.28 ± 0.06	0.41 ± 0.09	0.97
F303	Early-B	0.82	-0.13	0.95 ± 0.06	-41	0.14	0.16	0.79 ± 0.06	1.14 ± 0.08	1.87
F304	B5	0.29	-0.08	0.37 ± 0.03	-15	0.05	0.07	0.30 ± 0.04	0.44 ± 0.06	0.87
F312	Late-B	0.42	-0.04	0.46 ± 0.06	-20	0.07	0.12	0.34 ± 0.06	0.50 ± 0.09	1.46
F314	B6	0.38	-0.07	0.45 ± 0.04	-22	0.07	0.10	0.35 ± 0.05	0.51 ± 0.07	1.90
F315	B7	0.35	-0.06	0.41 ± 0.04	-21	0.07	0.11	0.30 ± 0.05	0.43 ± 0.07	1.26
F317	Mid-B	0.55	-0.08	0.63 ± 0.06	-32	0.11	0.14	0.49 ± 0.06	0.71 ± 0.09	0.70
F326	Mid-B	0.75	-0.08	0.83 ± 0.06	-45	0.15	0.19	0.64 ± 0.06	0.92 ± 0.09	0.75
F329	Late-B	0.46	-0.04	0.50 ± 0.05	-3	0.01	0.02	0.48 ± 0.06	0.70 ± 0.09	0.90
F332	Late-B	0.40	-0.04	0.44 ± 0.05	-8	0.03	0.06	0.38 ± 0.06	0.55 ± 0.09	0.75
F334	Late-B	0.43	-0.04	0.47 ± 0.05	-27	0.09	0.15	0.32 ± 0.06	0.46 ± 0.09	1.61
F337	Late-B	0.57	-0.04	0.61 ± 0.05	-18	0.06	0.10	0.51 ± 0.06	0.74 ± 0.09	1.50
F340	Early-B	0.52	-0.13	0.65 ± 0.06	-15	0.05	0.06	0.59 ± 0.06	0.85 ± 0.08	0.63
F343	Mid-B	0.35	-0.08	0.43 ± 0.06	-6	0.02	0.03	0.40 ± 0.06	0.58 ± 0.09	0.72
F346	Mid-B	0.56	-0.08	0.64 ± 0.06	-20	0.07	0.10	0.54 ± 0.06	0.79 ± 0.09	3.19
F349	Mid-B	0.70	-0.08	0.78 ± 0.06	-34	0.11	0.14	0.64 ± 0.06	0.92 ± 0.09	1.13
F350	B3	0.73	-0.12	0.85 ± 0.04	-45	0.15	0.17	0.68 ± 0.04	0.98 ± 0.06	1.00
F352	Late-B	0.75	-0.04	0.79 ± 0.05	-22	0.07	0.12	0.67 ± 0.06	0.97 ± 0.09	1.33
F353	Mid-B	0.77	-0.08	0.85 ± 0.06	-17	0.06	0.08	0.77 ± 0.06	1.11 ± 0.09	1.53
F354	Late-B	0.57	-0.04	0.61 ± 0.05	-12	0.04	0.07	0.54 ± 0.06	0.78 ± 0.09	1.05
F355	Late-B	0.63	-0.04	0.67 ± 0.05	-26	0.09	0.15	0.52 ± 0.06	0.75 ± 0.09	1.26
F356	Mid-B	0.67	-0.08	0.75 ± 0.06	-28	0.09	0.12	0.63 ± 0.06	0.91 ± 0.09	1.06
F359	Early-B	0.83	-0.13	0.96 ± 0.06	-54	0.18	0.19	0.77 ± 0.06	1.11 ± 0.09	1.33
F360	Mid-B	0.83	-0.08	0.91 ± 0.06	-25	0.08	0.11	0.80 ± 0.06	1.15 ± 0.09	1.37
F362	Mid-B	0.87	-0.08	0.95 ± 0.06	-40	0.13	0.17	0.78 ± 0.06	1.13 ± 0.09	1.08
F363	Late-B	0.75	-0.04	0.79 ± 0.05	-26	0.09	0.15	0.64 ± 0.06	0.92 ± 0.09	0.94

Table 5.5: Continued

#	SpT	$(r-i)_c$ (mag)	$(r-i)_0$ (mag)	$E(r-i)$ (mag)	$EW(\mathrm{H\alpha})$ (Å)	f_D	$E^{cs}(r-i)$ (mag)	$E^{is}(r-i)$ (mag)	$E(B-V)_{(\mathrm{P,c})}$ (mag)	$E(B-V)_{\mathrm{SFD98}}$ (mag)
F367	Late-B	0.55	-0.04	0.59 ± 0.05	-8	0.03	0.06	0.53 ± 0.06	0.78 ± 0.09	0.98
F369	Late-B	0.88	-0.04	0.92 ± 0.05	-20	0.07	0.12	0.80 ± 0.06	1.16 ± 0.09	1.57

Chapter 6

Distance determinations of the La Palma spectroscopic sample of classical Be stars

In this chapter I will assess the distances of the CBe stars with La Palma spectra, for which I measured interstellar colour excesses. Distances will be estimated via spectroscopic parallax. The description of the method will focus on the stars with intermediate-resolution spectra, although spectroscopic parallaxes will be determined also for the FLWO/FAST candidate CBe stars in Chapter 9. In this chapter, I will also propose a more likely luminosity class for the studied CBe stars.

6.1 Introduction

Classical Be stars are observed to span over three luminosity classes, namely V, IV and III (Zorec & Briot, 1997). Due to the intrinsic properties of the sample (average $E(B-V) \sim 1$ and mean $r \sim 14.7$), the intermediate-resolution spectra of CBe stars, which were observed in La Palma, did not provide the required quality of data in the blue that is necessary to assess the luminosity class (the same is even more true of the lower-resolution FLWO/FAST CBe stars). A simple measure of spectroscopic parallax would thus offer a three-fold choice, using absolute magnitudes for B-type stars from dwarf to giant luminosity class.

Without a constraint on luminosity class the best that could be done would be to set a minimum distance corresponding to that obtained for the lowest luminosity class V. The present chapter will deal with the estimate of distances, through the method of spectroscopic parallax, and I will offer a method to constrain the luminosity class of 63 CBe stars for which I computed reddenings corrected for circumstellar emission, out of the 68 CBe stars in total that were observed in La Palma.

After the data have been presented, the obtained distances and luminosity classes will be compared with two other methods. A discussion on the spatial distribution of the sample will begin in Section 6.5.

6.2 Distances from spectroscopic parallax

Spectroscopic parallax distances, D_{SP}, are computed in the standard way, via the use of spectral types and reddenings that were determined in Chapter 3 and 4 and 5, and the absolute magnitudes listed in Table 1.2. The magnitude scale is taken from Zorec & Briot (1991) from which I also obtain error estimates. If compared to others available in the literature (e.g Straizys & Kuriliene, 1981; Aller et al., 1982; Wegner, 2000) the Zorec & Briot scale furnishes slightly fainter magnitudes although they agree within the errors. Their V-band absolute magnitudes are transformed into r absolute magnitudes, using the intrinsic $(V - R_C)$ colours for dwarfs supplied by Kenyon & Hartmann (1995), whilst noting that R_C and r magnitudes of B stars in the Vega system are close enough to identical for present purposes. Furthermore, the differences between dwarf and giant colours are small compared to all errors, permitting the use of MS colours in obtaining M_r for B giants.

The observed r magnitude needs to be corrected for the added flux due to circumstellar emission that makes the star look brighter (and redder) than it would otherwise be (example values for the correction, Δr, appear in Table 5.3). The extinction in the r band is given by $A_r = 2.53 \cdot E(B-V)_{(\mathrm{S,c})}$, applying the same $R = 3.1$ extinction law adopted in Chapter 4. The photometric contributions to the uncertainty in D_{SP} are the error in $E(B-V)_{(\mathrm{S,c})}$ ($\sigma \sim 0.1$) and in M_r (as specified in Table 1.2). A further source of error in the measure of spectroscopic parallax arises from the uncertain determination of the spectral type, which is within ± 1 subtype.

In Table 6.2 I give the input corrected magnitudes $r + \Delta r$ and D_{SP}, computed for each of the likely luminosity classes V, IV and III. The errors supplied with D_{SP} include the contribution from the errors on $E(B-V)_{(\mathrm{S,c})}$, Δr, and M_r, for each luminosity class. The error contribution given by the spectral type uncertainty is given separately in Table 6.2, so that the final error on D_{SP} must be obtained by summing the independent contributions in quadrature. .

6.3 Constraining the luminosity class

In Chapter 3, it was noted that the spectra used for typing are not of the quality needed to pin down luminosity class. I now attempt to establish some constraints on this by exploiting a very general property of the IPHAS colour-colour plane, which permits disentangling of intrinsic colours and reddenings of ordinary MS stars. Here I do not go as far as computing complete extinction-distance curves for individual sightlines (applying the methods of e.g. Sale et al., 2009). Instead, I will use this approach more as a validation tool for a part of the 63 stars in the sample in Section 6.6

Essentially, for each CBe star, I pick out from IPHAS photometry fainter nearby non-emission line objects of similar reddening to see if, collectively, these putative lower main sequence companion objects favour a particular if uncertain distance modulus. This finding in turn implies a particular luminosity class for the CBe stars. By this means I choose between the class V, class IV and class III distance options listed in Table 6.2.

The method consists of the following steps and is illustrated by the two examples shown in Fig. 6.1:

1. The photometry of all the stellar and probably-stellar point sources (morphology classification codes -1 and -2) with $r \leq 20$ is collected (cyan empty circles), within an on-sky box of 10×10 arcmin^2 centred on each CBe star (black star in Fig. 6.1).

2. The MS colour-colour track, reddened by the amount corresponding to $E(B-V)_{S,c}$, is set (plotted as the red solid curve in the left-hand panels of Fig. 6.1). This was produced by computing synthetic (r, i, Hα) photometry from a grid of Munari et al. (2005) MS models, that were scaled to the Calspec Vega model spectrum[1] (Bohlin, 2007).

3. All the point sources that fall within the reddening range, $E(B-V)_{S,c} \pm 0.5\sigma$ (dashed red curves), and have the colours appropriate to early-A to late-F stars, are selected. The working assumption is that these stars, in sharing essentially the same reddening, are likely to be as far away as the CBe star.

4. I estimate the distance to the group of stars selected from the IPHAS colour-magnitude diagram by finding the MS track that fits them best (dashed black curve in each of the right-hand panels). In the fitting procedure, the selected stars are weighted according to their photometric errors and with a sigmoid function computed as described by (Sale et al., 2009). The latter limits the bias to too short a distance that is otherwise induced by stars just brighter than the magnitude limit. Furthermore, since the IPHAS colours roughly signal spectral type, and early-A candidates are the least ambiguous, extra weight was awarded to them (5 times that of other later-type stars). I also applied a 3-σ cut to bright (redder) outliers and recomputed the fit, in order to inhibit shortening of the distance due to interloping giant stars. The MS absolute magnitude scale applied to the selected A and F stars is taken from Sale et al. (2009) The distances estimated this way are reported in Table 6.2. In view of the modest sample sizes involved, these distances are indicative only and certainly approximate. They are used here solely as a guide to likely luminosity class.

5. A luminosity class (either V, IV or III, given in the final column of Table 6.2) is then assigned to each CBe star according to the option falling closest to the rough distance estimate from MS-fitting. In Fig. 6.1, the MS loci consistent with class V, IV and III luminosity-class assignments for the CBe star are plotted in the colour-magnitude diagrams. It is noticeable in a large minority of cases, that the distance estimate obtained from the candidate normal A–F stars distinctly undershoots the class V spectroscopic parallax, $D_{S,V}$. When this happens, the default action is to adopt the (longer) distance compatible with class V.

[1]Obtained from http://www.stsci.edu/hst/observatory/cdbs/calspec.html.

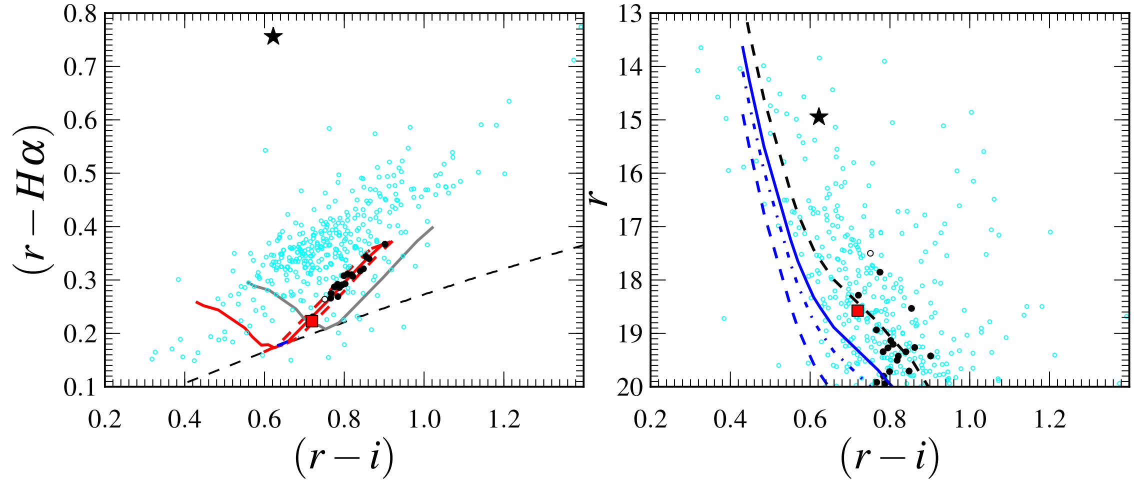

(a) # 11

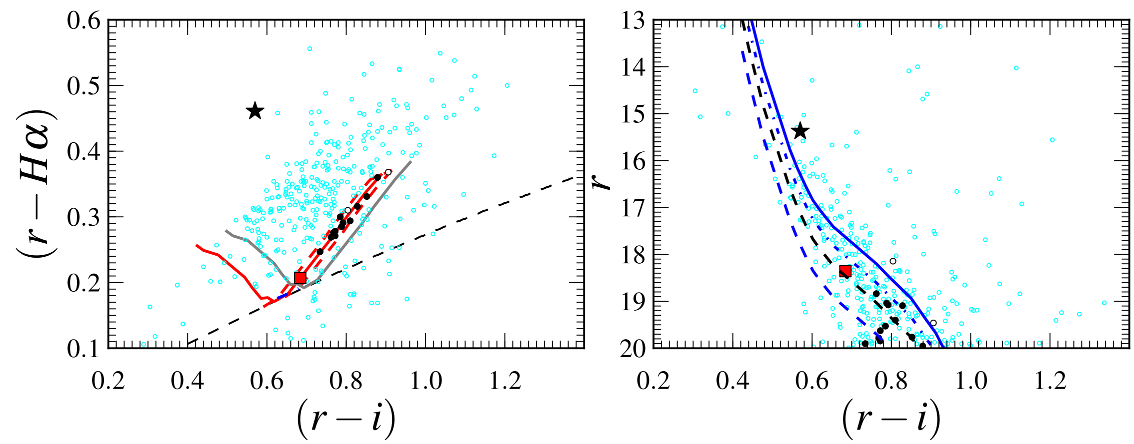

(b) # 52

Figure 6.1: Two examples of luminosity class assignment based on the IPHAS photometry of stars selected within a box of 10×10 arcmin^2 centred on the CBe star. The top panel shows the data relevant to star # 11, while the bottom one pertains to star # 52. To the left, sightline colour-colour diagrams for stars with $r \leq 20$ are presented. The solid red curve in each case is the MS track, reddened by same amount as the CBe star. The red-dashed lines are the tracks for $E(B-V)_{\mathrm{S,c}} \pm 0.5\sigma$: stars falling between them are selected as stars of similar reddening – only those with $(r-H\alpha)$ colour consistent with their being A–F stars are retained (these are picked out in black). The CBe star itself is marked by the star symbol. The grey MS track also drawn is reddened at the line-of-sight SFD98 asymptotic colour excess. The dashed black curve is the early-A reddening line. The right hand panels present the colour-magnitude diagrams for the 10×10 arcmin^2 selections. The reddened MS loci, computed for the distance moduli consistent with the CBe star as (i) class V, (ii) class IV, or (iii) class III are plotted respectively as solid, dash-dotted and dashed blue curves. The formal best-fit MS locus (reddened by the same amount as the CBe star) is plotted as a dashed black curve. Stars contributing to the fit are the black filled dots and the red squares (early A stars), while the unfilled black circles are stars excluded from the fit.

For the 63 CBe stars in the La Palma sample, the pattern emerging from the luminosity class assignments is similar to that among the sample of Be stars presented by Zorec & Briot (1997): 43 are assigned to class V (cf 36 on scaling to this older work), while 12 and 8 are placed into classes IV and III respectively (cf expectations of 14–15, and 13). That there are more dwarfs may just be a consequence of the much fainter apparent magnitude range the sample is drawn from, as compared to previous works. It may also indicate a bias in the spectral typing towards earlier spectral type.

6.4 Testing the spectral typing and luminosity classification with the BCD method

To appraise the reliability of the spectral typing of Chapter 3 and the proposed luminosity classes determined in the present chapter, I compared my results with those obtained on the sample of La Palma spectra with the BCD method by J. Fabregat (priv. comm.).

The BCD method uses the temperature and gravity dependence of the Balmer jump appearance in order to identify at the same time spectral types and luminosity classes of stars with spectral types ranging from O to F. The BCD classification is based on the measure of only two parameters (λ_1, D). λ_1 is a measure of the effect of pressure broadening and, by implications, of gravity on the Balmer jump, while D is a measure of the magnitude of the Balmer jump itself, which is more $T_{\rm eff}$ dependent. The λ_1 parameter is the midpoint of the curvature of the Balmer jump. D is measured as the difference between the continuum fluxes before and after λ3700 Å, against a logarithmic scale. A graphic representation of the measure of (λ_1, D) is given in Figure 6.2.

In contrast to normal B-type stars, Be stars show a "discrepancy" d (see Figure 6.3) at λ3700 Å, with the appearance of an absorption feature. This discrepancy originates from the continuum emission in the disc that raises the Balmer continuum by an amount d a little to the blue of the main discontinuity. Kaiser (1989) found that d correlates with Hα emission. A direct measure of D, for a CBe star, would give rise to a wrong typing. The jump actually measured, in CBe stars, is $D^* = D + d + 0.03$ (Kaiser, 1989).

The BCD classification was defined for spectra with resolution of $\Delta\lambda = 8$ Å (Zorec et al., 2009). Furthermore, it is very effective when standard MK stars are observed with the same instrument set-up, in order to be used as calibrators for the system. Therefore, the intermediate-resolution spectra were degraded to meet the required spectral resolution as long as the spectral type standards that were observed in the corresponding nights (J. Fabregat priv. comm.).

J. Fabregat tested the INT/IDS observations, for which more spectral type standards observed with the same set-up were available. In Table 6.1, I report the physical parameters and the MK spectral types that J. Fabregat estimated from (λ_1, D), along with the spectral types and suggested luminosity classes from Chapter 4 and Section 6.3. Fourteen out of 13 stars had a sufficient S/N ratio at the Balmer jump wavelengths. The other 8 have spectral types and luminosity classes that are more uncertain. The (λ_1, D) parameters were transformed by J.Fabregat into spectral types and luminosity classes via interpolation with

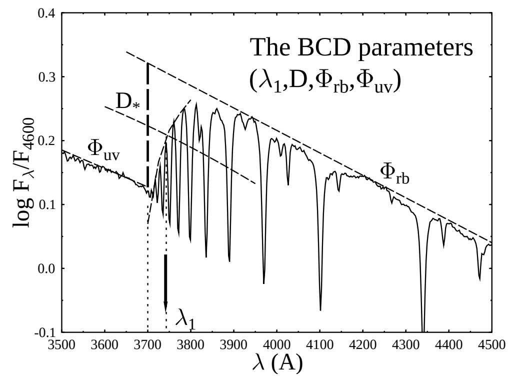

Figure 6.2: Example of measure of BCD parameters, from Figure A.1 in Zorec et al. (2009). The fit to the Balmer continuum and Paschen continuum are Φ_{rb} and Φ_{uv} respectively. D and λ_1 are also shown. The flux is in logarithmic units.

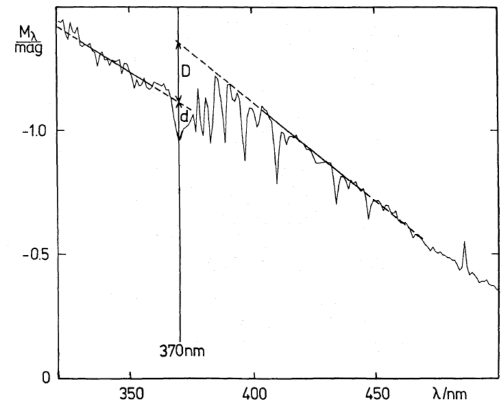

Figure 6.3: Figure 1 from Kaiser (1989), showing the Balmer discontinuity at λ3700 Åin a Be star.

data from Table 6 in Zorec et al. (2009). $T_{\rm eff}$ is also interpolated from the same table, while the $\log g$ is estimated from unpublished data (Zorec priv. comm.).

Interestingly, the mean of the differences between the two classifications is zero. Spectral types are in average not more different than 2 sub-types and luminosity classes not more different than one. The largest difference between the adopted classification and the BCD one is measured for object # 23 (i.e. 4 sub-types). However, this star appears to be noisier at λ3700 Å, so that its BCD typing is more uncertain.

6.5 Spatial distribution of the CBe sample

In Fig. 6.4, I plot all the stars at the distance corresponding to their assigned luminosity class against Galactic longitude, marking on the diagram the expected locations of the Perseus and Outer Arms. The four stars for which I do not have spectroscopic Hα observations are not included in this plot. I also left out of the plot star # 59 that, due to its very strong emission (EW(Hα) ~ -140), is more likely a YSO (see Section 8.3 for some further comment on this object). The emergent picture presented by these 63 stars is certainly not one of pronounced clustering picking out the spiral arms in the distance-longitude plot. Closest to this possible reality is seen at longitude $\sim$135° where there is a group of six stars near the star-forming complexes W3/W4/W5, well in front of another group of stars, sitting closer to the OH maser in the Outer Arm. Elsewhere there is no sign of such orderly behaviour. The casual impression is of a scattered, more or less random, distribution of emission line stars.

In the sample, no CBe star is closer than 2.2 ± 0.3 kpc (# 56) or more distant than 11.6 ± 2.0 kpc (# 39). This is mainly a reflection of the magnitude limits ($13 \lesssim r \lesssim 16$)

Table 6.1: BCD parameters of the intermediate-resolution spectra. Column list: ID number; magnitude of the Balmer jump; shift of the mid-point of the Balmer jump; inferred $T_{\rm eff}$ and $\log g$; corresponding spectral type; MK spectral type, as determined in Chapter 3 and luminosity class of Section 6.3.

#	D (mag)	$\lambda_1 - 3700$ (Å)	$T_{\rm eff}$ (K)	$\log g$	SpT (BCD)	SpT (This work)
1	0.300	44	14500	3.50	B6IV [2]	B5III
2	0.350	61	12500	4.10	B8V	B7V
5	0.200	60	19500	4.10	B3V	B2V
7	0.300	63	14000	4.15	B6V [2]	B7V
10	0.280	50	15000	3.80	B5IV	B7IV
11	0.202	63	19000	4.15	B3V	B2-3V
12	0.346	52	12500	3.85	B7V [2]	B5V
13	0.300	66	14000	4.20	B6V [2]	B5V
15	0.310	59	13750	4.05	B6V	B5V
17	0.121	45	23500	3.55	B2III [2]	B3IV
18	0.155	60	22500	4.08	B2V	B4V
20	0.110	66	28000	4.15	B1V	B3V
23	0.205	61	19000	4.10	B3V [2]	B7V
28	0.350	49	12500	3.70	B7IV	B7V
29	0.360	57	12500	4.00	B8V	B7IV
30	0.235	50	17000	3.80	B4IV [2]	B4V
31	0.117	44	22500	3.45	B2III	B3IV
32	0.350	57	12500	4.00	B7V	B6IV
33	0.430	50	11000	3.75	B9IV	B8-9III
34	0.157	65	22500	4.20	B2V [2]	B3V
35	0.243	47	17000	3.65	B4IV	B2-3V
45	0.220	63	18500	4.20	B4V	B3IV

[2] BCD uncertain; low S/N at λ3700 Å.

placed on the sample of CBe stars. At the bright end ($r = 13$), a main sequence dwarf with a median spectral type (B5), and a median reddening of $A_r = 2.5$, just falls within the sample at the minimum distance of ~ 2.0 kpc. For B3V this estimate of the minimum rises to 2.9 kpc, consistent with the brightest object (# 45) in the sample, that happens to be a B3 star, being assigned a distance of 2.8 kpc (its reddening is a little above the median value). For the latest spectral types present in the sample, the near distance limit drops as low as 1 to 1.5 kpc. That I do not find any in the allowed range between 1 and 2 kpc is perhaps because the reddening only rises up to and through the median for the distribution once the Perseus Arm is well and truly entered at $\sim$2 kpc (i.e. late-B stars at these shorter distances are "too bright").

The upper distance limit can in principle be expected to be more variable, following to an extent the variation of the integrated Galactic reddening with sightline (SFD98):

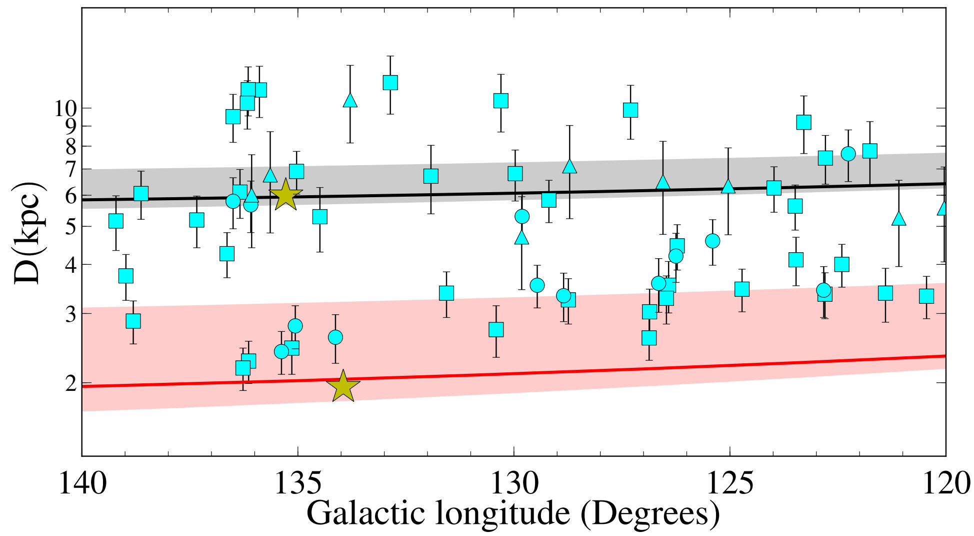

Figure 6.4: The spatial distribution of the 63 CBe stars with intermediate-resolution spectra on the Galactic Plane is shown. Different symbols are used for the luminosity class: dwarf (squares), circles (sub-giants), triangles (giants). The spiral arms are plotted following the prescriptions given in Vallée (2008) – solid red curve for the Perseus Arm, black solid curve for the Outer Arm. Instead, the two bands of width 1.4 kpc (Russeil, Adami & Georgelin, 2007), represent the range of distances that are covered by the two spiral arms in (Russeil, Adami & Georgelin, 2007). The Perseus Arm is in pink, the Outer Arm is in grey. The two yellow stars mark the trigonometric parallaxes of masers as specified by Reid et al. (2009a), which are sitting on the near edge of the spiral arms where the star formation is active.

for most of the CBe sample the maximum possible A_r varies from $\sim$2 up to $\sim$5. But our selection has, for practical observational reasons, avoided the most heavily reddened objects and sightlines (the maximum A_r in the sample is 4). On deploying the median spectral type and reddening for the sample, again – but this time combining them with the absolute magnitude appropriate to luminosity class III — we would expect a faint magnitude limit of $r \sim 16$ to translate to a maximum heliocentric distance of $\sim$16 kpc (dropping to 10–12 kpc for the latest B sub-types). The actual outcome is that the most distant/faintest objects in the sample are B3-4Ve objects inferred to be 10–12 kpc away. The objects assigned to luminosity class III are, in contrast, mostly relatively bright and/or relatively heavily reddened, bringing all but one of them in to distances closer than 10 kpc. So whilst there is not a simple upper limiting distance to the observed window, there is reason to assume that the range from 3 to 8 kpc is well captured by the sample at all sub-types – so if CBe stars are preferentially located in the Outer Arm at 5 to 6 kpc, it would be likely to be evident, if the combination of sample size and typical error provides sufficient definition. I return to this below in the discussion of Section 6.7.2.

The most distant early-type dwarf stars at heliocentric distances of 10–11 kpc are 16–17 kpc away from the Galactic Centre. This places them significantly outside the disc 'truncation' radius estimated by Ruphy et al. (1996), and since re-examined by Sale et al.

(2010). Although dependent in detail on how the stellar density profile steepens at these large Galactocentric radii, I would not expect a selection of CBe stars fainter than $r = 16$ to yield too many more-distant objects – instead, it would more likely add in stars that are later in spectral type, more reddened, or both. Indeed the number of early-type stars that are already known at such a large Galactocentric radii is very small. In Rolleston et al. (2000), just 14 out of the 80 studied B-type stars, between $6 \leq R_G \leq 18$ kpc, are found at distances larger than $R_G \sim 13$ kpc.

6.6 Measuring extinction distances: an H-MEAD test

A useful comparison for the distances measured in Section 6.2 comes from the use of extinction-distance curves computed from IPHAS photometry. These have the advantage of extending the same basic ideas noted in Chapter 6.3 to much larger number of stars, improving the sensitivity of the distance measure. The algorithm applied is H-MEAD (Sale, 2012). H-MEAD is a hierarchical Bayesian algorithm that estimates distances, reddenings and luminosity classes from observed data, based on a careful choice of a priori probabilities. It replaces the simpler non-Bayesian approach of MEAD (Sale et al., 2009). The priors defining the Galactic model that is implemented in H-MEAD fix constraints on the IMF, star formation history, scale length and height of the Galactic disc primarily. With the chosen priors, given the set of input $(r, i, \mathrm{H}\alpha)$ photometry from IPHAS, it is possible to estimate the distance and extinction of all A to mid-K stars along the line-of-sight of interest, and combine them to produce a statistically robust curve.

To ensure there are enough stars with IPHAS photometry ($r \lesssim 20$) for H-MEAD to convert into a credible line-of-sight extinction curve, stellar sources within a $10' \times 10'$ area, centred on each CBe star, are analysed. A larger selection area would improve the statistics, but too large areas smooth over small scale structures in the ISM degrading the resolution and validity of the mapping. The choice of $10' \times 10'$ area, as in Section 6.3, is the adopted compromise between resolution and number of stars to be used (Sale et al., 2009).

The H-MEAD output I use is the line-of-sight monochromatic extinction A_{6250} that is a close proxy of A_r, binned to a depth resolution of 50 pc, and its $\pm\sigma$ range. Having determined the interstellar extinction affecting the CBe stars, it is straightforward to go on to estimate their distances by comparison with the computed extinction curves.

The extinction distance, D_{E}, of each object is at the intersection point between the object's measured monochromatic extinction, A_{6250} and the H-MEAD extinction curve for its sightline. Uncertainties in D_{E} are measured from the intersections of the error bounds on the object reddening with the upper/lower boundaries of the extinction curve. Some examples of how reddening distances estimates are constructed are shown in Fig. 6.5. For comparison, the range of the luminosity class V and class III spectroscopic parallaxes, determined previously in Section 6.2, are plotted as well, as two vertical shaded areas. The measured extinction distances are in Table 6.2.

With the use of the extinction-distance curves, the sample appears to splits into three

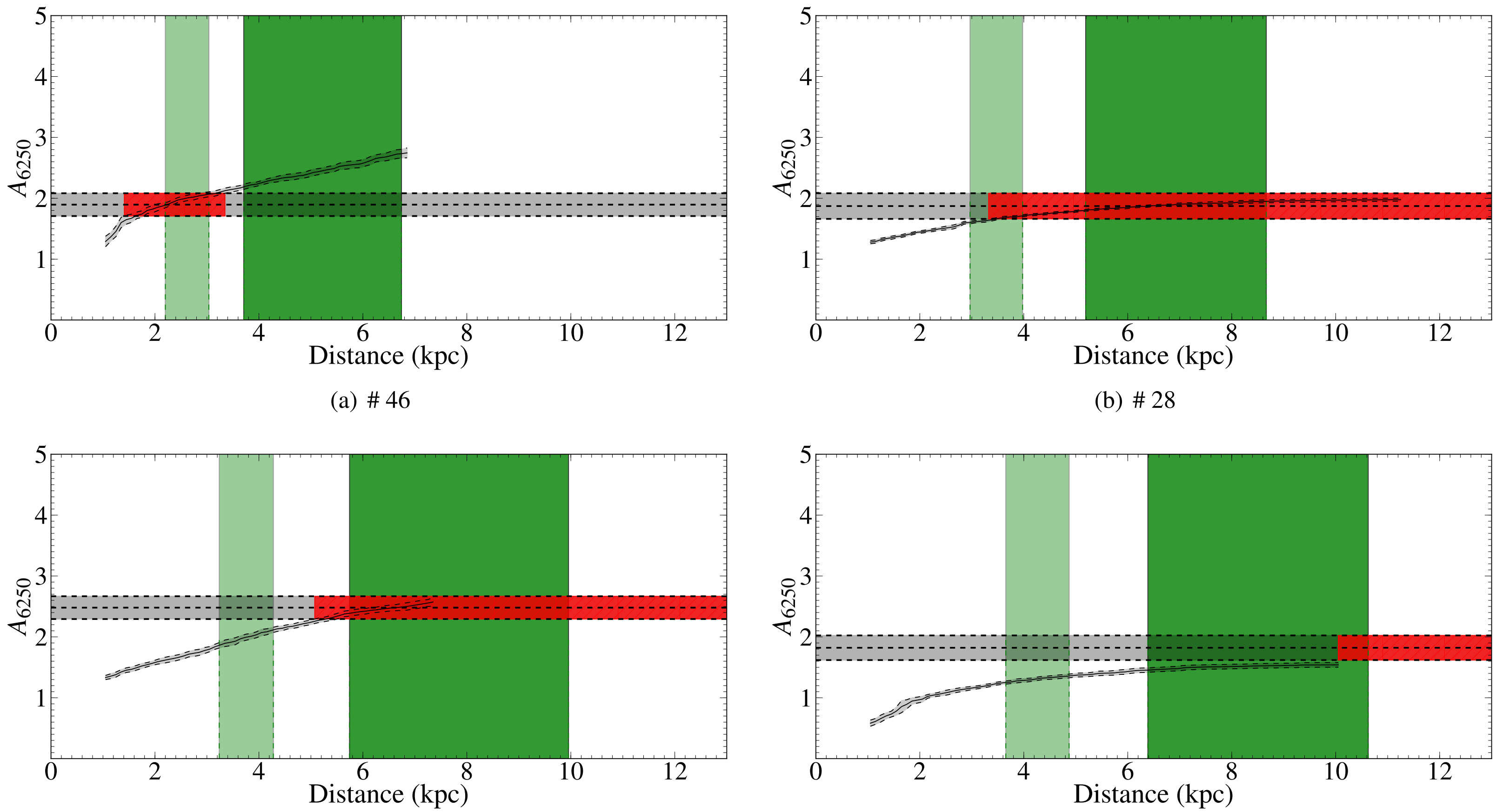

(a) # 46
(b) # 28
(c) # 15
(d) # 62

Figure 6.5: Four examples of distance estimates via use of H-MEAD extinction curves. In each figure, the monotonically rising extinction curves represent the distance dependence of monochromatic extinction at λ6250 Å averaged over a sky area of 10×10 arcmin^2 centred on the named object. The mean fit along with its 68% confidence range is shown. The horizontal grey shaded area is the measured A_{6250} for the star. The extinction distance is at the intercept between the extinction-distance curve and the A_{6250} line. The two vertical shaded areas are the spectrophotometric-photometric distance estimates for luminosity class V (light green) and class III (dark green), respectively. (a) Is a likely class V star in the Perseus Arm. The other examples have lower-limit extinction distances: in (b) the extinction curve asymptotes at about the reddening of the CBe star; in (c), the extinction distance curve ends before it flattens, but in this example it is likely the CBe star is a class III object; in (d), I show the result for one of the stars with a particularly high minimum distance.

groups, according to how the measured reddening of the CBe compares with the inferred total Galactic extinction for the sight-line and the H-MEAD result. Specifically:

1. Where the value of A_{6250} for the emission line object crosses the extinction-distance curve below its reddening maximum, a bounded distance estimate is obtained (see e.g. Fig. 6.5(a)). 22 CBe stars out of the original sample of 63 with measured and corrected reddenings belong in this group.

2. For the remaining 41 stars, a lower limit on the extinction distance is the best that can be obtained. These are the cases when the A_{6250} measurement and/or its uncertainty crosses the extinction curve either as the latter flattens out (Figure 6.5(b)) or when it simply terminates at a maximum value (Figure 6.5(c)). Where the extinction-distance curve clearly flattens, it should never be the case that the CBe-star reddening exceeds the asymptotic field reddening – in principle this should be impossible (to within the errors).

3. Acceptable lower limits on D_{E} are obtained for 35 stars, leaving 6 reddenings that are too high to be compatible with the highest extinction-curve reddening. Not all the computed extinction-distance curves extend into the asymptotic domain. In such cases it may be concluded provisionally that the statistical information derived by H-MEAD from the photometry happens to be insufficient to capture the entire sight-line dust column density.

I now split the sample into two groups, based on the D_{E} outcome. I first investigate the agreement between D_{E} and the spectroscopic parallaxes for the stars with bounded extinction measures. Then, I consider what can be learnt from the objects with only lower limits on D_{E}.

6.6.1 Spatial distribution for the CBe stars with bounded extinction distances

Twenty-two of the 63 tested CBe stars have a bounded extinction distance D_{E}. Given that the original selection of candidate CBe stars is magnitude-limited, it comes as no surprise, that this group is dominated by later B sub-types (15 are B5 or later, including one A0 star). By appraising the agreement between the two different types of distance estimate (both given in Table 6.2, I find that there are large discrepancies for three stars (i.e. # 34, 50, 53) in the way that D_{E} falls significantly shorter than $D_{\mathrm{SP,V}}$. In two cases, also the A/F fit (Section 4.3.1) suffered from the same problem, although the D_{E} measured for object 53 is improbably short, placing it well in front of the Perseus Arm. For objects # 2, 10 and 18, extinction distance favours a higher luminosity class (IV or III instead of V). In general, the bounded extinction distances give a closer agreement with the spectroscopic parallaxes, although the large uncertainties arising from the intercept with the $\sigma E(B-V)$ boundaries do not always supply a more definite assessment of the luminosity class. The

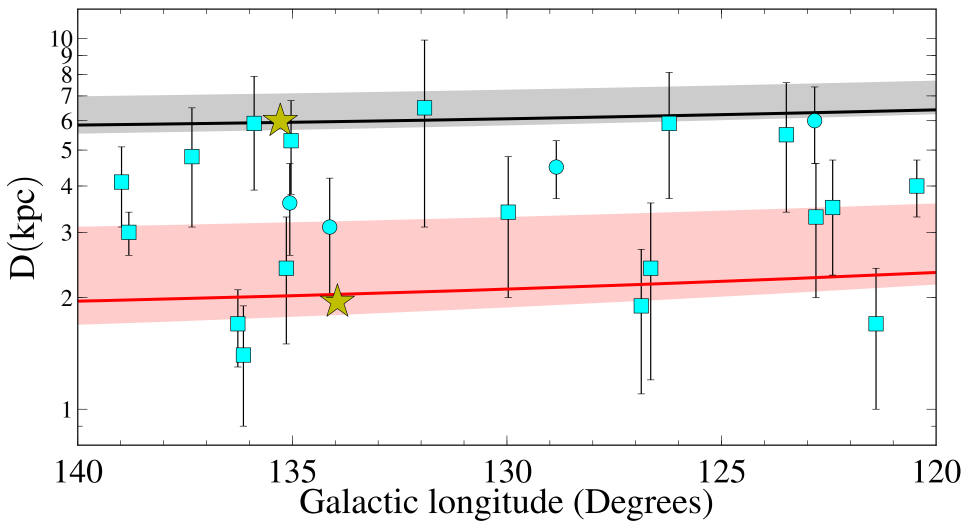

Figure 6.6: The spatial distribution of the 22 CBe stars with intermediate-resolution spectra on the Galactic Plane is shown, with bounded extinction distances. Symbols and spiral arms location as in Figure 6.4

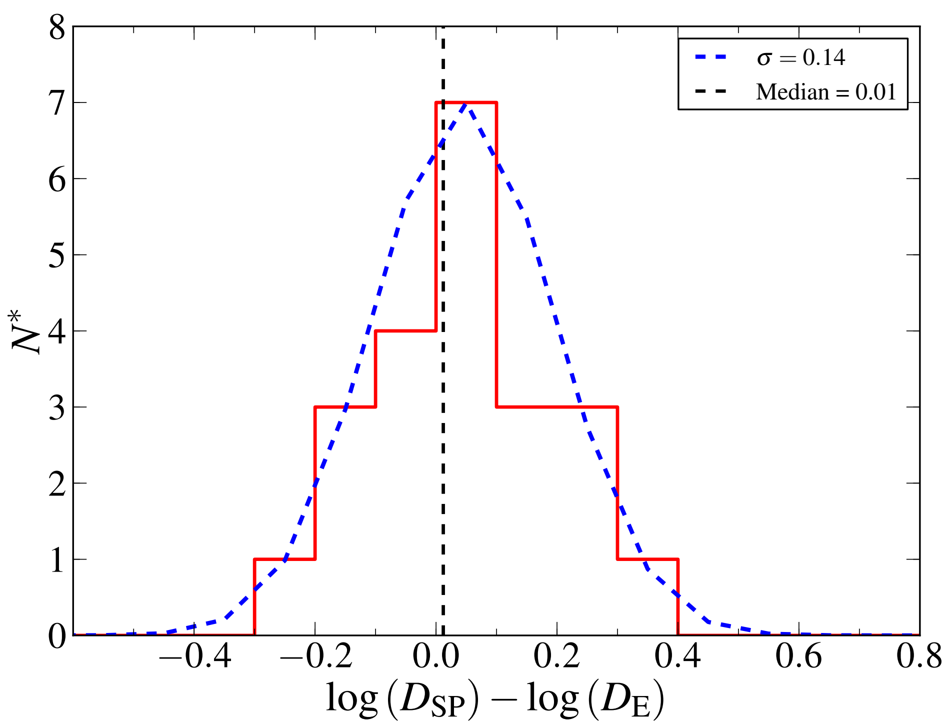

Figure 6.7: The histogram of the difference $\log D_E - \log D_{SP}$ is given for the 22 stars with bounded extinction distances. The blue dashed curve is the Gaussian fitting this distribution. The median is picked out by the vertical dashed line.

agreement found is not surprising, since the method used in Section 6.3 draws on the same photometry (if in a much more limited way).

The spatial distribution of the 22 with bounded extinction distances is shown in Figure 6.6, where each star is plotted at its extinction distance. As the sample of stars is much smaller than that shown in Fig. 6.4, and the error bars are also quite large, it comes as no surprise that there is less sign of association with spiral arms.

The histogram distribution of the differences, $\log D_{\mathrm{E}} - \log D_{\mathrm{SP}}$, is plotted in (Fig. 6.7). It centres at 0.01, with a $\sigma = 0.16$. The sigma of the distribution is comparable to the average combined error in the $\log D_{\mathrm{E}} - \log D_{\mathrm{SP}}$ quantity, which is ~ 0.17. This suggests that the observed distribution of the differences, in the limited sample, is due to the measurement errors.

6.6.2 Lower limiting extinction distances

For the remaining two thirds of the sample (41 out of 63 stars), a bounded extinction distance measurement is not returned. As I already said previously, I cannot measure a bounded distance either if (i) the measured A_{6250} hits the extinction-distance curve as it rolls over to a maximum (e.g. Fig. 6.5(b) and 6.5(d)) or (ii) the curve ends abruptly at some maximum value, and the measured A_{6250} (e.g. Fig. 6.5(c)). Furthermore, in a few instances, I also have that (iii) a star has a reddening exceeding the distance-extinction curve maximum.

To obtain useful results from the extinction curves, case (i) is the most favourable one. In this instance, the lower limiting reddening distance is decided more by the unavoidable asymptoting behaviour of the curve, when the total column of dust along the line-of-sight has been reached, than being an actual problem. If the error bars on A_{6250} had been smaller, the number of stars belonging to this set would have been lower and more stars would have belonged to the bounded-distance group.

In case (ii), the lower limit estimate is due to the magnitude limit of the photometry. Generally, extinction-distance curves are expected to reach an asymptote when all the dust, along a given sight-line, has accumulated - this can happen well before the expected Galactic disc truncation between 14 –16 kpc (see e.g. the lower surface density of molecular gas in the outer Galaxy Heyer & Terebey, 1998; Snell, Carpenter & Heyer, 2002). If the extinction-distance curve ends abruptly, it usually signals a more obscured line-of-sight in which the IPHAS $\sim 20^{\mathrm{th}}$ magnitude photometric cutoff prevents the detection of stars behind the entire dust column. In a very few instances there is evidence that the curve is still rising, in that the SFD98 total reddening (also listed in Table 5.4) exceeds the highest H-MEAD reddening by 0.5 mags or more.

Finally, 6 stars are problem cases of type (iii), where I cannot measure a lower limit on D_{E}. One could ascribe the cause of no possible D_{E} measure to systematic effects in the estimate of reddenings. However distances and luminosity classes were successfully estimated with the method of Section 6.3. This disagreement is under investigation. In Fig 6.8, I show one of these problem cases, for the sightline corresponding to star # 51. Furthermore, the SFD98 asymptotic colour excess does match the redder edge of the stellar

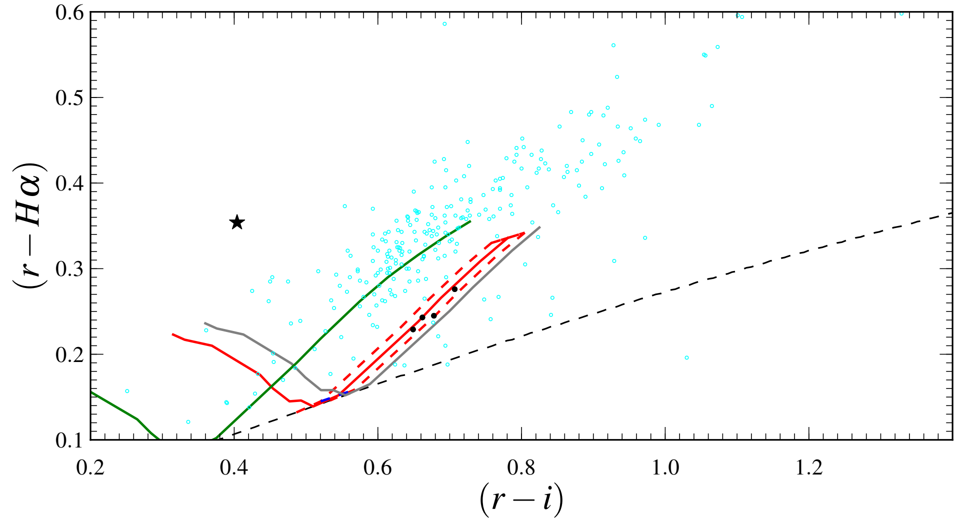

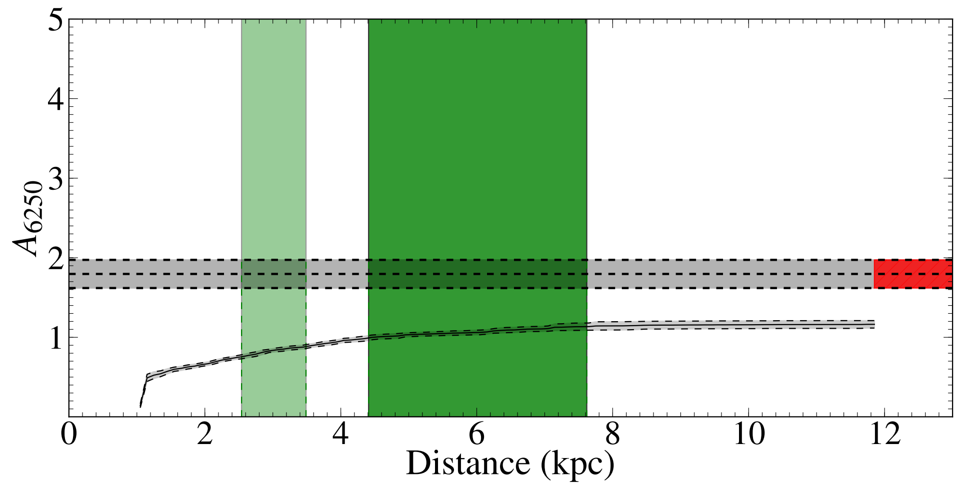

Figure 6.8: The top panels shows the colour-colour and colour-magnitude diagrams for # 11, a B8-9III star at 6 kpc. The luminosity class is assigned with the help of 4 neighbouring MS stars (top right panel). Star # 51 presents with a $E(B-V) = 0.71$ that is consistent with the SFD98 value (red and grey MS tracks respectively, in the top left panel), signifying the star is at the edge of the total column of dust. The maximum reddening measured by H-MEAD, for this sightline, is associated to the green MS track. The bottom panel shows indeed a problematic H-MEAD extinction curve. The curve flattens very soon, and its maximum reddening does not reach up to 0.45 mags.

locus in the colour-colour magnitude, implying that the H-MEAD should reach up to an $E(B-V) \sim 0.79$. In the bottom panel of Fig 6.8, instead, the H-MEAD curve does not go higher than 0.45 mags in $E(B-V)$, making the extinction distance impossible to be measured.

In Chapter 8, I will return to the comparison between the maximum extinction along the line-of-sight that is obtained with H-MEAD and the reddenings I measure for these 63 CBe stars.

6.7 Discussion

In this section, I identify the main insights provided by the sample of 63 CBe stars, identifying robust outcomes and possible biases. Regarding the latter, I analyse the impact that choices of reddening law and absolute magnitude scale, and the method of correction for circumstellar disc fraction, may have had on the distance estimates. I will also discuss how the presence of unresolved binaries and gravitational darkening effects would influence distance estimates. Finally, I compare the inferred cumulative distribution of object distances with two models considering an equally number of stars, which simulate: (i) a population of stars, which is distributed following the regularly declining disc stellar density profile, but randomly scattered with the measured error-distance dependence in order to reproduce the error measurements; (ii) a population of stars, equally distributed within the spiral arms, with distances scattered as in the model (i).

6.7.1 Possible measurement biases

6.7.1.1 The absolute magnitude scale and luminosity classification

In Section 6.2, I pointed out that the chosen absolute magnitude scale is the faintest among those to be found in current literature. For example the class V magnitudes I have adopted are, on average, 0.4-0.6 mag fainter than others reported in literature (see e.g. Straizys & Kuriliene, 1981; Aller et al., 1982; Wegner, 2000, and Figure 1.13) for the early and late-B types, whilst they are better aligned for mid-B stars. Had I favoured a brighter absolute magnitude scale, I should expect to obtain distances up to 25% larger than those tabulated. However it is worth noting that I found that the great majority of the class V spectroscopic parallaxes gave larger values than those crudely inferred from nearby candidate A/F stars (section 6.3 and Table 6.2). This may turn out to be part of the explanation for the attribution of a somewhat higher proportion of the sample to class V, based on the existing absolute magnitude scale, relative to the earlier sample of Zorec & Briot (1997). Indeed, on balance, I would doubt that there is a bias to too low a distance, and speculate if instead the absolute magnitude scale may still be a bit too bright. But it is also true that this is a fainter selection than in earlier works, so I might expect to find more dwarfs.

The deduced distance to each CBe star is necessarily strongly dependent on adopted luminosity class. Here, a rough constraint on luminosity class has come from estimating the distances to probable main-sequence A and F stars of comparable reddening within a few arcminutes angular separation (section 6.3) Where the luminosity assignment is wrong by one class, the distance will be over or under-estimated by 30 % – a large uncertainty. It is reassuring that the spread of the smaller sample of intermediate-resolution spectra across luminosity class is not radically different from that found by Zorec & Briot (1997), and that the BCD method of Section 6.3, confirmed the spectral typing and luminosity classification to the expected level.

6.7.1.2 Disc fraction estimates

The disc fraction and circumstellar excess estimates were obtained using the commonly adopted method proposed by Dachs, Kiehling & Engels (1988), in which the measured $E(B-V)_{\rm S}$ is corrected downwards using a scaling to the Hα emission equivalent width. As I already noticed in Sec.8.3.1.1, six stars of the La Palma sample have $EW(\mathrm{H}\alpha) \leq -60$ Å, that lie outside the range in which Eq.5.2 and 5.3 were defined. This makes their $E^{cs}(B-V)$ determination more uncertain. Furthermore, both of (Dachs, Kiehling & Engels, 1988) equations are based on quite scattered data.

For the most extreme emitter in the sample that is # 26 (excluding # 59, which is dealt with in Chapter 8), a variation of f_D twice as large as the 0.02 uncertainty that I considered in the error propagation, with its $EW(\mathrm{H}\alpha) \approx -100$ Å would move the star by $\pm 5\%$ around its measured distance, on taking into account the corresponding $E^{cs}(B-V)$ and Δr changes. The estimate of $E^{cs}(B-V)$ also has an effect on the identification of the preferred luminosity class, in that a different $E(B-V)_{(\mathrm{S,c})}$ value slightly changes the selection of stars in the colour-colour diagrams of Sec.4.3.1 and, hence, the A/F star fits. In short, the role of the disc fraction and the uncertainties in its estimation is complex, but it is fortunate that for most of the sample its impact is not very large

6.7.1.3 Choice of reddening law

As I mentioned in Section 4.1 a different choice of R_V would affect the distance estimates, although the measured colour excesses would not change too much since the shape of the Fitzpatrick (1999) curve at blue wavelengths does not change significantly if R_V is altered by a few tenths. A smaller/larger R_V produces lower/higher reddening for a given colour excess, and hence a larger/smaller inferred spectroscopic parallax. A study of the shape of reddening laws across much of the Galactic Plane was undertaken by Fitzpatrick & Massa (2007). Taken at face value, this work would seem to imply a lower R_V of 2.9 ± 0.2 within the region delimited by $\ell = (120^\circ, 140^\circ)$ and $b = (-5^\circ, +5^\circ)$. However this is based only on three bright B stars, that apparently lie on the near side of the Perseus Arm. Since the majority of the stars are appreciably more distant than 2 kpc, there is no strong incentive yet to stray from the widely accepted mean law ($R_V = 3.1$). If I had preferred $R_V = 2.9$, the derived spectroscopic parallaxes would be about $8-10\%$ larger than specified here. Conversely, raising R_V above the typical Galactic value would shorten the distance scale. If a change in either sense turns out to be necessary, it is more likely that R_V should be increased.

6.7.1.4 Unresolved binaries

Studies of binarity in normal B-type stars as well as in Be stars have given sometimes contrasting results. Abt & Cardona (1984) quote similar binary fractions for long period B and Be stars ($\sim$ 38% and $\sim$ 35% respectively). They also measured a smaller binary fraction in field stars ($\sim$ 25%). Oudmaijer & Parr (2010) found similar results with use of AO, finding $29 \pm 8\%$ for normal B stars and $30 \pm 8\%$ for Be stars. An extensive search in the Sco OB2 association, by Kouwenhoven et al. (2005), has shown a very high binary fraction for early-B ($\sim$ 80%) and late-B stars ($\sim$ 50%), investigating the primordial binary fraction. Given the non negligible fraction of B and also Be stars with companions, it is very likely that a good portion of CBe stars in the sample here considered are in binary systems. Due to the fact that the mass ratio distribution seem to be fairly uniform or at least not extremely peaked towards companions with much lower mass (Oudmaijer & Parr, 2010), up to 20% of the stars in the sample could have as a companion another B star. The contribution to the observed magnitude of the binary system depends on the spectral type of the two stars. If for instance the primary is a B1V star and the secondary is a B3V the flux ratio in the r-band is about $F_{\rm B1}/F_{\rm B3} \sim 0.31$, that corresponds to an overall brightening of ~ 0.29 mags with respect to the B1V star alone. Larger differences in spectral type induce more negligible contributions. Considering a fainter primary, as for instance a B5V: if again the companion is two sub-types later, the contribution to the flux due to the secondary will be $\sim 0.63 F_{\rm B5}$. This implies that the binary system has an intrinsic magnitude ~ 0.53 brighter.

In conclusion, the presence of binaries would affect more the late type stars, where the contribution to the total flux, due to the secondary, is larger. The measured distances, in the case of a binary system will then need to be pushed further away, of about 15% in the first example and up to 28% in the second one, for the later spectral types.

6.7.1.5 Gravitational darkening effects

Be stars are known to be fast rotators. Observational studies find their equatorial velocities to be sub-critical (e.g. $v_e/v_c \sim 0.8$ in Chauville et al., 2001). Other studies go further in claiming bias in determining $V \sin i$ due to gravitational darkening effect, and suggest that the ratio v_e/v_c would be much closer to ~ 0.95 (Townsend, Owocki & Howarth, 2004; Frémat et al., 2005). Townsend, Owocki & Howarth (2004, and references therein), note that the gravitational darkening may combine with the circumstellar emission, in explaining the anomalous position occupied by CBe stars in the colour-magnitude diagram. The effect of the gravitational darkening, on the observed magnitude and colours of CBe stars, is inclination dependent. Townsend, Owocki & Howarth (2004) showed that in a star with $v_e/v_c = 0.95$ seen pole-on, the hotter atmosphere would appear up to $\Delta V \sim 1$ mag brighter but with negligible colour change. On the other hand, a star that is seen edge-on, will experience a change in colour of about $(B-V) \sim 0.04$. This edge-on effect happens to be stronger for later than early B-types. For a typical inclination $i \sim 50^\circ$, the star will have both a magnitude and a colour change, in the range of $\Delta V \sim -0.5$ and $(B-V) \sim 0.02$.

In conclusion, gravitational darkening affects the spectroscopic parallaxes in a way

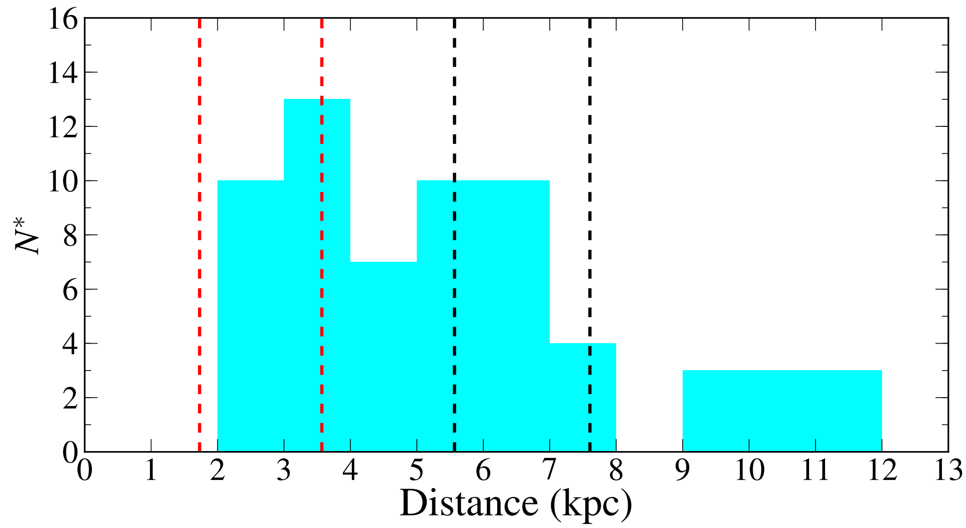

Figure 6.9: Histogram distribution of stars with luminosity class being assigned accordingly to Table 6.2. The vertical dashed lines define the distance ranges thought to be occupied by the spiral arms: red is used for the Perseus Arm, black for the Outer Arm.

that is inclination dependent. If the star is seen pole-on, it is actually fainter than assumed and as a result is inferred to be up to 24% further away. On the other hand, an edge-on star will have an intrinsically redder colour than assumed, which in turn implies a smaller reddening than inferred. This means that the edge-on star is over-corrected for reddening and placed to a shorted distance (5% less in the most extreme case). On balance, gravitational darkening biases towards distance over-estimation.

Due to the faster rotation of Be stars, gravitational darkening related effects may influence the spectral typing and luminosity class assignment (Fabregat & Gutierrez-Soto, 2005), in a way that pole-on stars look like earlier-type dwarfs and edge-on appear as later-type giants. This interpretation is used to explain the lack of correlation between position in the HR diagram and luminosity class that is found at the turn-off of the main sequence in open clusters. Such an effect on the spectral typing brings back to the initial considerations of this section.

6.7.2 The cumulative distribution of CBe-star distances

In Fig. 6.4 I plotted the distances to 63 of the 68 objects observed in La Palma as a function of Galactic longitude, leaving out four objects for which I do not have the $EW(\mathrm{H}\alpha)_S$ data needed to correct the measured reddenings for circumstellar emission, and one further star that is more likely to be a YSO. Similarly to Fig. 6.4, the binned histogram distribution, which is shown in Fig. 6.9, does not display a pronounced clustering within the expected spiral arm locations. It must be noted that, collapsing the spatial distribution in the one-dimensional histogram plot, the spiral arms might occupy a larger range of distances due to the projection effect, if their width is constant over the considered range of Galactic longitudes (cf. ~ 1.4 kpc, as suggested by Russeil, Adami & Georgelin, 2007). This "stretching" of the spiral arms, in combination with the errors on the distance determination ($\delta D_{SP}/D_{SP} \sim 0.2 - 0.3$), makes the identification of the spiral arms difficult. To underpin this point, I compared the observed distribution of stars with two simple models:

1. The stars are assumed to be distributed along the sightline in the same way normal A stars are. The length scales and disc 'truncation radius' are derived by Sale et al. (2010): essentially the exponential length scale out to $R_G = 13 \pm 0.5$ kpc is (3.0 ± 0.12) kpc, and thereafter it shortens to (1.2 ± 0.3) kpc.

2. The stars are only found within the spiral arms, which are defined as two identical boxcar functions within the limits identified by Russeil, Adami & Georgelin (2007) in the range $\ell = (120°, 140°)$. The relative weight of the spiral arms is regulated by the disc A-star density profile of above (see Fig. 6.10(a)).

Both stellar distributions are weighted with a D^2 term, to reproduce the conical volume sample function. Furthermore, to take into account the effect of random errors, distances of stars are scattered with 10k MC simulations, varying the distances randomly with Gaussian noise, which is modelled as function of the distance, and based on the real data (Fig. 6.10(b)). The starting distance of the two models should be important, to crudely emulate the observational selection, although choosing it between 1–2 kpc does not affect the median distribution of a large number of random MC simulations. Because of the steep decline in stellar density outside the truncation radius, the end point does not greatly effect the outcome.

The median distributions, resulting from the MC simulations of the two models, are shown in Fig. 6.11(a) overplotted onto the observed histogram distribution of the 63 CBe stars. It is difficult to distinguish which model gives a better description of the data, as expected, due to the blurring effect of the errors. Both models predict a few stars in the range 1–2 kpc, where none of the CBe stars was identified, as an effect of the random scattering of points in the simulations.

In this part of the Galactic Plane ($120° \leq \ell \leq 140°$ and $-1° \leq b \leq 4°$), Galactic models (Russeil, 2003; Vallée, 2008) place the Perseus Arm at ~ 2 kpc and the Outer Arm at ~ 6 kpc, consistent with measured maser parallaxes (Reid et al., 2009a). By means of OB-star spectroscopic parallaxes derived from a brighter sample ($8 < V < 13$) of stars than here, Negueruela & Marco (2003), identified a number of OB stars at $d \approx 5.3$ kpc for $115° < \ell < 120°$ and $d = 5 - 6$ kpc for $\ell = 175° - 215°$. Thanks to the high quality of their spectroscopic data, the authors claim the spectral types to be determined with precision better than ± 1 subtype, and distances less uncertain than 10%. They surmised that these objects could belong to the Outer Arm, but did not claim detection of a spiral arm, as such. Within the same Galactic longitude range as considered here, they had very few stars at their disposal. Here I have filled in this gap – but I would not claim that either Fig. 6.11(a) or the preferred cyan curve in Fig. 6.11(b) that accounts for the spread of luminosity classes present in the sample, picks out an Outer Arm at 5–6 kpc.

I reconsider the distribution collapsed into a cumulative form that permits an analysis free of binning effects (Fig. 6.11(b)). The blue curve shown is the cumulative distribution

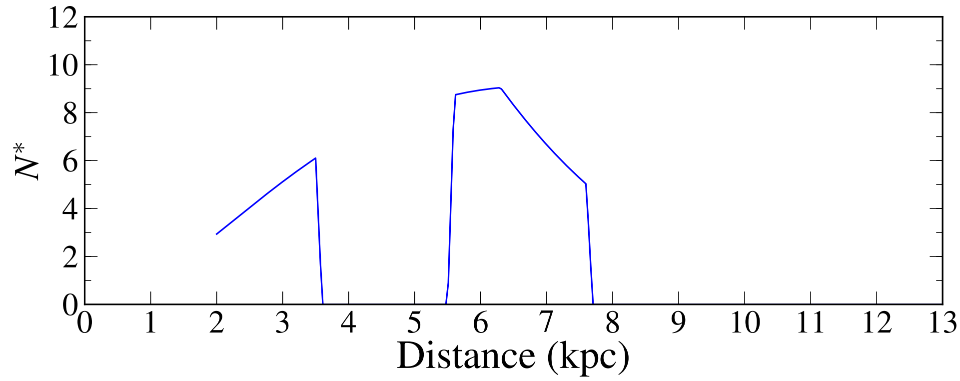

(a)

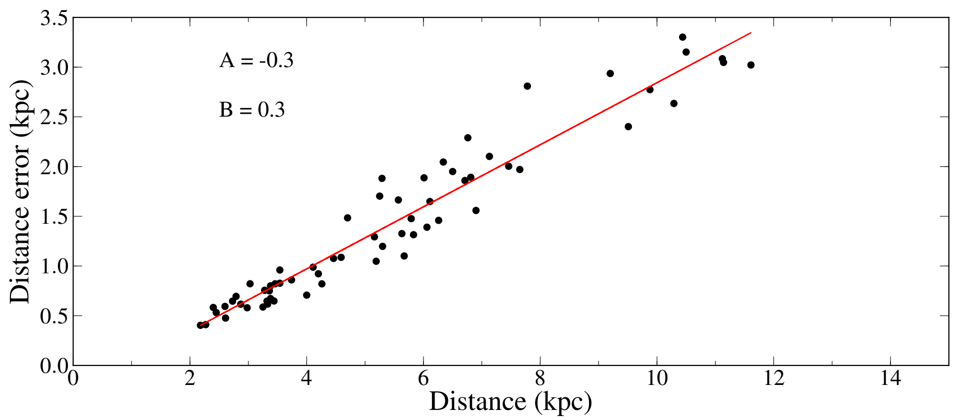

(b)

Figure 6.10: Figure (a) shows the input function, describing the spiral arm density profile. In Figure (b) is the distribution of the distance errors, plotted against the measured distances (black dots), for the 63 CBe stars. A linear regression fit is also plotted. The coefficients of the fit, A and B in figure, are used to model the error-distance dependence in the MC simulations of the spiral arms distribution.

as a function of distance obtained when all CBe stars are classified as dwarfs, while the cyan curve is the result obtained on assigning luminosity classes as given in Table 6.2. If the CBe stars were preferentially located in the Perseus and Outer Arms and the precision sufficient, I would expect to see steepenings of the cumulative distribution curve (CDC) in the distance ranges associated with the Arms (picked out in the figure).

The CDCs are overplotted onto the contours defining the 1σ, 2σ, and 3σ confidence limits derived from the family of CDCs produced with the MC simulations: coloured contours are for the model (1), simulating a population of 63 CBe stars that are distributed as the disc A-star density profile from Sale et al. (2010); black contours are for model (2), assuming the stars being found only within the spiral arms. A direct visual comparison between the CDC of the 63 CBe stars (cyan curve) and the contours generated with the simulations, does not allow distinction between the best of the two models. The spiral arm

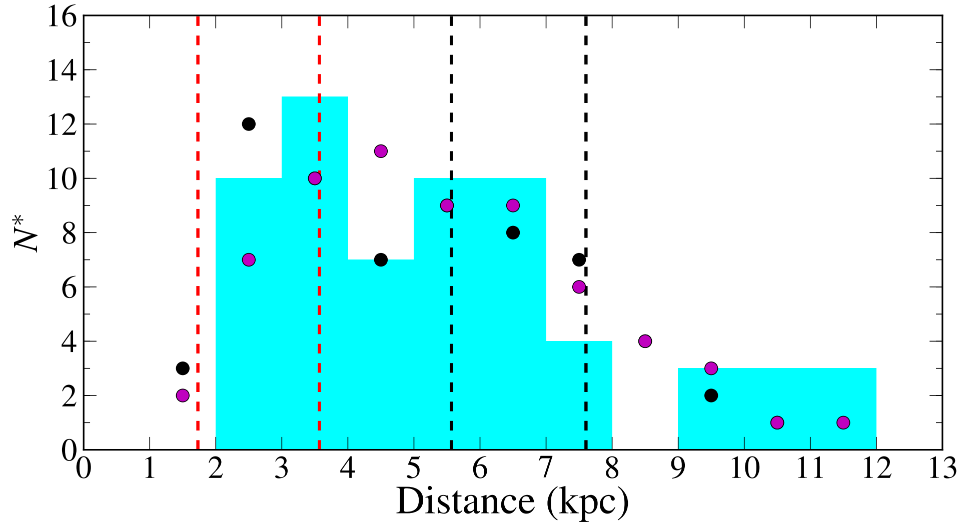

(a)

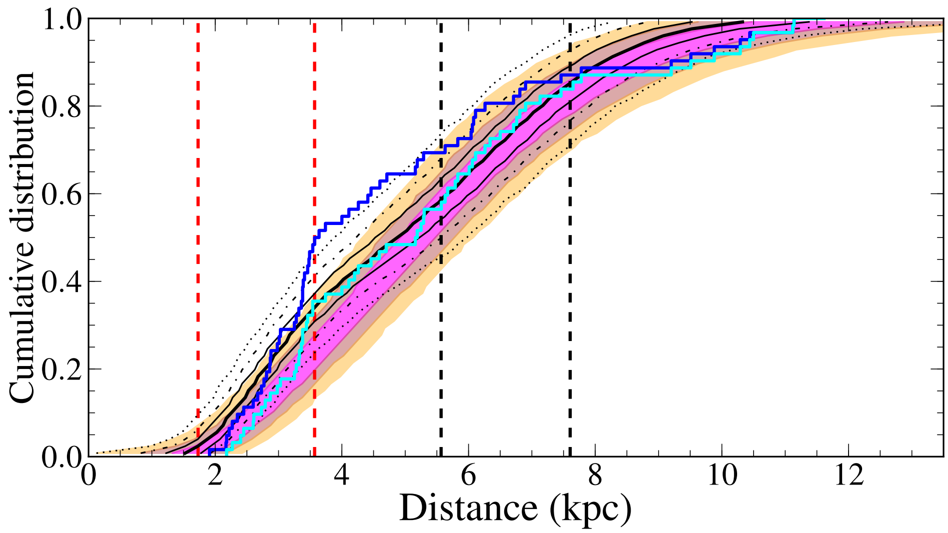

(b)

Figure 6.11: (a) Histogram distribution of the 63 CBe stars as in Fig. 6.9. The magenta dots mark the expected distribution of stars obtained, from the median of the MC simulations, for the stars distributed according to the smooth exponentially decreasing A-star density. The black dots, instead, are for the expected distribution of stars obtained, from the median of the MC simulations, for the the stars distributed according to the spiral arms' model. The vertical dashed lines define the distance ranges as in Fig. 6.9. (b) The cumulative distribution of stars is plotted against the CBe-star distances derived from spectroscopic parallax. The cyan curve expresses the distribution of stars that takes note of the preferred luminosity class assignment in Table 6.2. The dark blue curve is the result obtained if all the CBe stars are assumed to be class V. The comparison CDCs are plotted as contours providing the 1σ, 2σ, and 3σ confidence limits, determined from the envelope of CDCs of the family of 10k MC simulations, for stars distributed according to: (i) the smooth disc A-star density profile (coloured contours); (ii) the spiral arms' model (black contours). Vertical dashed lines define the range of distances associated to the spiral arms, as in panel (a).

option cannot be ruled out, although it is not the only option either, as shown later. On the other hand, the CDC obtained with all the stars classified as dwarfs (blue curve) is exposed as implausible, since a too many stars are assigned to the Perseus region. In conclusion, the magnitude of the errors does not permit confirmation of the presence of the Outer Arm.

K-S tests were performed comparing the observed cumulative functions with the median of the simulated distributions. For the blue curve (all stars being dwarfs), I obtain $D_{\mathrm{no-arms}} = 0.25$ and $p_{\mathrm{no-arms}} = 0$, $D_{\mathrm{arms}} = 0.16$ and $p_{\mathrm{arms}} = 0.32$. Due to the generally large values of D, which is a measure of the separation between the blue curve and the simulated data, both options can be rejected. This confirms the impression that one has from the inspection of Fig. 6.11(b), that the blue curve does not give a sensible description of the spatial distribution of stars.

On the other hand, for the cyan curve, I measure $D = 0.11$ and $p = 0.8$, in both cases. This means that no distinction can be made between the two models, so that the observed data are consistent with both models or in other words, that the observed distribution of CBe stars is equally consistent with the stars being within the spiral arms or being distributed as the disc A-star density profile.

6.7.2.1 What would be needed to improve the present results

The present absence of evidence for preferential clustering, within the Outer Arm in particular, is an indication that both the combination of the reduced sample size and precision does not deliver sharp results.

The second point is straightforward, since previous claims on the presence of an Outer Arm have been made from authors presenting data of higher precision, either using single bright stars or clusters, whose distances were determined to better than 10% (cf. Negueruela & Marco, 2003; Pandey, Sharma & Ogura, 2006). To help the visualisation of the problem, I replotted the cumulative distribution plot in Fig. 6.12, but tracing instead the contours for simulated data in the case that the errors are halved. The contours traced from the simulated data show that an observed distribution would resemble more closely a step-like CDC, in the case of spiral arm objects. At the reduced error level, the CDC of the observed CBe would appear to be more consistent with all the CBe stars contained within spiral arms than being distributed smoothly like the A stars.

I also tested the improvement that could be achieved by using a sample four times larger than the present one – this possibility represents the case of bringing into consideration the sample CBe stars identified in Chapters 2, although the noise characteristics of more than half of those 181 CBe stars does not allow reliable distance determinations, as it will be discussed in Chapter 9. The simulation resulting from the use of a larger sample is plotted in Fig. 6.13(b) and can be visually compared the contours resulting from the simulation that makes use of 63 stars, in Fig. 6.13(a). The black curves in figure represent, as in the previous plots, the confidence limits resulting from 10k MC simulations of a CDC for stars distributed according to the spiral arms' model and distances varying with random Gaussian noise. The coloured contours are for stars that are distributed according to a smooth disc A-star density profile. It appears evident, that the use of a larger sam-

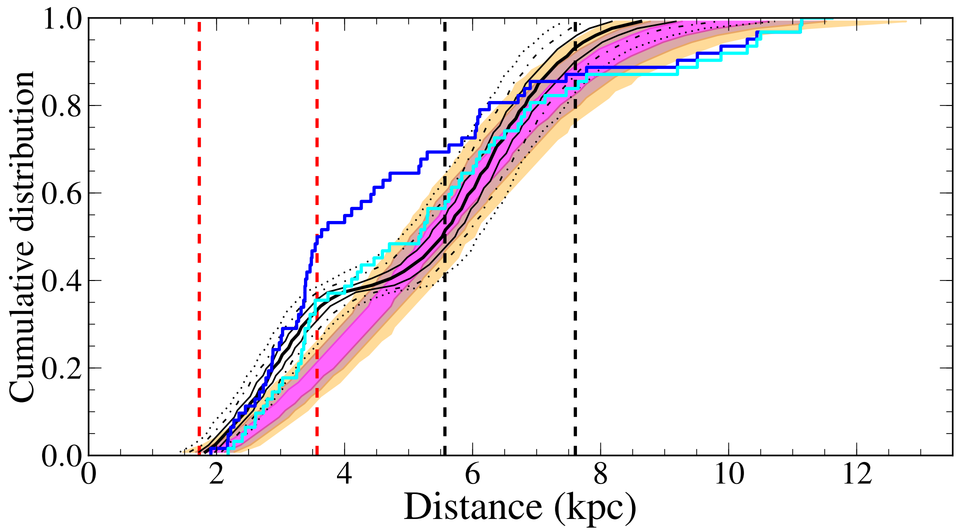

Figure 6.12: The same plot as in Fig. 6.11(b), but with contours representing the confidence limits that are computed considering only an half of the distance uncertainty and using the same linear dependence of the error-distance relationship, as plotted in Fig. 6.10(b).

ple, i.e. 252 stars, reduces the width of the contours, lessening the confusion effect due to random noise. However, at this level of uncertainty, it would probably still be difficult to distinguish between the two distributions. In Fig. 6.13(c) I plot the larger number of simulated stars but with errors halved. In this case, there would be prospect of being able to chose empirically between the two cases.

6.8 Summary

In this chapter I presented the measure of spectroscopic parallaxes for 63 CBe stars with intermediate-resolution spectra. Their interstellar reddenings have been estimated via the spectroscopic method of Chapter 4. I proposed a luminosity classification, via MS fitting to A/F stars, in the IPHAS $(r, r-i)$ plane, that are seen near each CBe star and share similar reddenings. The distances associated with this luminosity classification were compared with extinction distances obtained from extinction-distances curves computed using H-MEAD. An independent assessment of spectral types and luminosity classes, determined with the BCD method, is also presented. To conclude, I also investigated possible sources of bias in the spectroscopic parallaxes. The sample of 63 CBe stars neither confirms the existence of an Outer Arm nor excludes it, while simple simulations show this is to be expected given the present sample size and error budget.

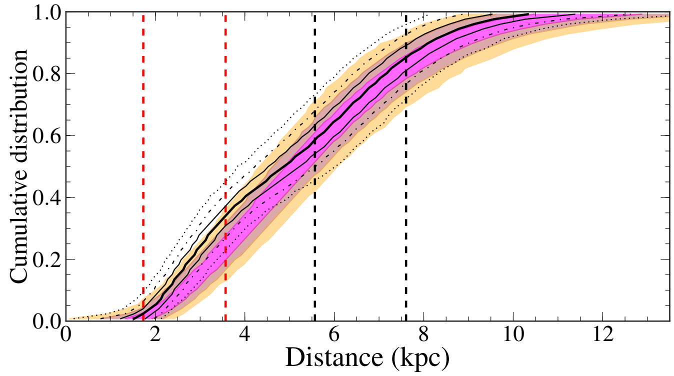

(a)

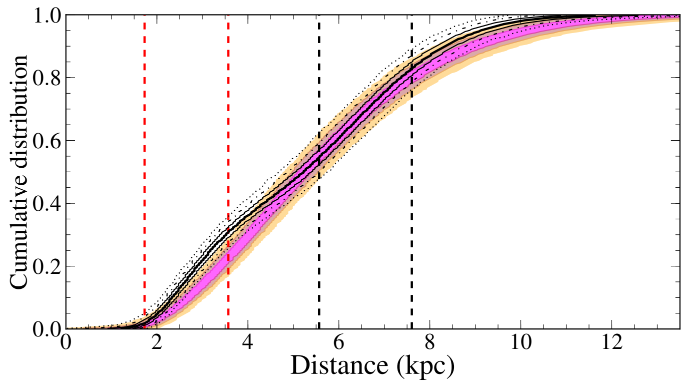

(b)

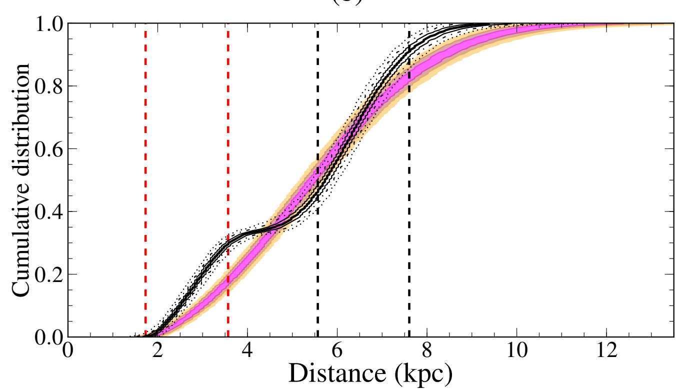

(b)

Figure 6.13: The three panels show the contours representing the confidence limits of the family of 10k simulated CDCs, which are generated with the models: (i) for the stars distributed according to the smooth disc A-star density profile (coloured contours); (ii) the stars distributed according to the spiral arm's model (black contours). In panel (a), is plotted the contours generated with the model that uses 63 stars, as in Fig. 6.11(b). Panel (b) and (c), instead, show narrower contours, since they are computed both using 252 stars. However, in panel (c) the error contribution is halved.

Table 6.2: Table of spectroscopic parallaxes of the 68 CBe stars. Columns list: ID number; spectral type; Galactic coordinates; the observed r magnitude corrected for circumstellar disc emission; A_r, computed from $E(B-V)_{(S,c)}$; A/F fit approximate distances; spectro-photometric distances for luminosity classes V, IV and and III: in bold-face are distances that are associated to the preferred luminosity class; preferred luminosity class; extinction distances. The three last columns give the distance errors arising from the spectral type uncertainty.

#	SpT	ℓ (deg)	b (deg)	$r+\Delta r$ (mag)	A_r (mag)	A/F fit (kpc)	Distances $D_{SP,V}$ (kpc)	$D_{SP,IV}$ (kpc)	$D_{SP,III}$ (kpc)	Likely Class	Error on distances due to SpT $\sigma D_{SP,V}$ (kpc)	$\sigma D_{SP,IV}$ (kpc)	$\sigma D_{SP,III}$ (kpc)	D_E (kpc)
1	B5	120.04	1.64	14.90 ± 0.04	3.44	5.1	2.7 ± 0.3	3.4 ± 0.5	$\mathbf{5.6 \pm 1.5}$	III	0.5	0.7	0.7	≥ 9.9
2	B7	120.45	0.32	14.14 ± 0.04	1.62	2.9	$\mathbf{3.3 \pm 0.4}$	4.0 ± 0.6	6.6 ± 1.6	V	0.5	0.5	0.9	4.0 ± 0.7
3	B3	121.09	3.99	14.66 ± 0.03	3.90	4.7	2.9 ± 0.4	3.6 ± 0.5	$\mathbf{5.2 \pm 1.3}$	III	0.7	0.7	1.1	≥ 8.2
4	A0	121.40	3.92	16.12 ± 0.04	2.48	3.7	$\mathbf{3.4 \pm 0.5}$	4.2 ± 0.7	6.7 ± 2.0	V	0.6	0.8	1.2	1.7 ± 0.7
5	B2	121.76	2.43	15.05 ± 0.03	2.71	3.4	$\mathbf{7.8 \pm 1.5}$	9.4 ± 1.6	13.5 ± 3.1	V	2.4	2.4	2.7	≥ 5.1
6	B3	122.26	1.16	15.78 ± 0.04	3.39	7.0	6.1 ± 1.0	$\mathbf{7.7 \pm 1.1}$	11.1 ± 2.9	IV	1.4	1.6	2.3	≥ 11.3
7	B7	122.41	0.12	14.98 ± 0.04	2.05	3.0	$\mathbf{4.0 \pm 0.5}$	4.8 ± 0.7	8.0 ± 1.9	V	0.5	0.6	1.1	3.5 ± 1.2
8	B3	122.79	0.72	15.54 ± 0.04	2.71	5.5	$\mathbf{7.5 \pm 1.1}$	9.4 ± 1.2	13.6 ± 3.3	V	1.7	1.9	2.8	≥ 9.0
9	B5	122.80	2.07	14.26 ± 0.04	2.30	3.1	$\mathbf{3.4 \pm 0.5}$	4.2 ± 0.6	7.0 ± 1.9	V	0.6	0.9	0.9	3.3 ± 1.3
10	B7	122.83	2.69	14.86 ± 0.04	2.66	4.4	2.9 ± 0.4	$\mathbf{3.4 \pm 0.5}$	5.7 ± 1.4	IV	0.4	0.4	0.8	6.0 ± 1.4
11	B2-3	123.29	0.23	15.22 ± 0.04	2.23	6.1	$\mathbf{9.2 \pm 1.5}$	11.3 ± 1.7	16.4 ± 3.9	V	2.5	2.6	3.3	≥ 7.4
12	B5	123.47	0.20	14.50 ± 0.04	2.10	3.4	$\mathbf{4.1 \pm 0.6}$	5.2 ± 0.8	8.6 ± 2.4	V	0.8	1.1	1.1	≥ 5.1
13	B5	123.49	0.11	14.70 ± 0.03	1.62	6.0	$\mathbf{5.6 \pm 0.7}$	7.1 ± 1.1	11.8 ± 3.2	V	1.1	1.5	1.5	5.5 ± 2.1
14	B4	123.98	0.44	15.59 ± 0.04	2.76	4.9	$\mathbf{6.3 \pm 0.8}$	7.9 ± 1.0	11.4 ± 3.1	V	1.2	1.5	1.5	≥ 6.2
15	B5	124.72	0.04	14.71 ± 0.04	2.68	3.8	$\mathbf{3.5 \pm 0.4}$	4.3 ± 0.6	7.2 ± 1.9	V	0.7	0.9	0.9	≥ 5.3
16	B3	125.04	0.08	14.27 ± 0.04	3.09	7.2	3.5 ± 0.5	4.4 ± 0.6	$\mathbf{6.3 \pm 1.6}$	III	0.8	0.9	1.3	≥ 7.0
17	B3	125.40	3.27	14.72 ± 0.04	3.44	4.7	3.6 ± 0.6	$\mathbf{4.6 \pm 0.6}$	6.6 ± 1.6	IV	0.9	0.9	1.4	≥ 6.5
18	B4	126.22	1.79	14.60 ± 0.04	2.50	2.5	$\mathbf{4.5 \pm 0.6}$	5.6 ± 0.7	8.1 ± 2.2	V	0.9	1.1	1.1	5.9 ± 2.2
19	B6	126.25	3.36	15.13 ± 0.04	2.78	4.1	3.5 ± 0.4	$\mathbf{4.2 \pm 0.6}$	7.0 ± 1.9	IV	0.5	0.7	1.1	
20	B3	126.42	1.32	14.45 ± 0.04	3.24	2.1	$\mathbf{3.5 \pm 0.5}$	4.5 ± 0.6	6.5 ± 1.6	V	0.8	0.9	1.3	≥ 5.5
21	B5	126.47	1.24	15.27 ± 0.03	3.37	3.2	$\mathbf{3.3 \pm 0.5}$	4.1 ± 0.7	6.8 ± 1.9	V	0.6	0.9	0.9	≥ 7.9
22[3]	B4	126.55	2.64	14.88 ± 0.04	3.26	9.2	3.6 ± 0.4	4.5 ± 0.6	$\mathbf{6.5 \pm 1.7}$	III	0.7	0.9	0.9	
23	B7	126.65	3.24	14.82 ± 0.03	2.53	3.0	$\mathbf{3.0 \pm 0.4}$	3.6 ± 0.6	5.9 ± 1.5	V	0.4	0.4	0.8	2.4 ± 1.2
24	B3	126.86	1.13	14.19 ± 0.04	3.31	3.0	$\mathbf{3.0 \pm 0.4}$	3.8 ± 0.5	5.5 ± 1.4	V	0.7	0.8	1.1	≥ 6.5
25	B5	126.87	-0.10	13.48 ± 0.04	2.08	2.1	$\mathbf{2.6 \pm 0.3}$	3.3 ± 0.5	5.4 ± 1.4	V	0.5	0.7	0.7	1.9 ± 0.8
26	B3	127.30	2.36	15.97 ± 0.04	2.53	5.7	$\mathbf{9.9 \pm 1.6}$	12.4 ± 1.8	18.0 ± 4.6	V	2.3	2.5	3.7	≥ 9.9
27	B5	128.71	0.49	14.65 ± 0.04	2.66	6.5	3.4 ± 0.4	4.3 ± 0.6	$\mathbf{7.1 \pm 1.9}$	III	0.6	0.9	0.9	≥ 10.9

Table 6.2: Continued

#	SpT	ℓ	b	$r+\Delta r$	A_r	A/F fit	Distances			$\sigma D_{\rm SP,V}$	Error on distances due to SpT			$D_{\rm E}$
							$D_{\rm SP,V}$	$D_{\rm SP,IV}$	$D_{\rm SP,III}$		$\sigma D_{\rm SP,IV}$	$\sigma D_{\rm SP,III}$	Likely	
		(deg)	(deg)	(mag)	(mag)	(kpc)	(kpc)	(kpc)	(kpc)	Class	(kpc)	(kpc)	(kpc)	(kpc)
28	B7	128.74	2.55	14.50 ± 0.04	2.02	3.5	**3.2 ± 0.4**	3.9 ± 0.6	6.5 ± 1.6	V	0.4	0.5	0.9	$\geq$ 3.5
29	B7	128.85	1.29	14.08 ± 0.04	1.95	3.2	2.8 ± 0.3	**3.3 ± 0.5**	5.5 ± 1.4	IV	0.4	0.4	0.8	4.5 ± 0.8
30	B4	129.19	2.60	14.63 ± 0.04	1.95	4.9	**5.8 ± 0.7**	7.3 ± 0.9	10.6 ± 2.8	V	1.1	1.4	1.4	$\geq$ 5.8
31	B3	129.46	0.68	13.85 ± 0.04	3.14	3.9	2.8 ± 0.4	**3.5 ± 0.4**	5.1 ± 1.2	IV	0.7	0.7	1.0	$\geq$ 7.1
32	B6	129.81	3.87	15.31 ± 0.04	2.45	5.2	4.4 ± 0.6	**5.3 ± 0.8**	8.8 ± 2.4	IV	0.6	0.9	1.4	
33	B8-9	129.82	1.00	14.45 ± 0.03	2.18	4.9	2.4 ± 0.3	3.0 ± 0.5	**4.7 ± 1.2**	III	0.4	0.5	0.8	$\geq$ 7.7
34	B3	129.97	1.96	14.26 ± 0.03	1.62	3.5	**6.8 ± 1.0**	8.6 ± 1.1	12.4 ± 3.1	V	1.6	1.7	2.5	3.4 ± 1.4
35	B2-3	130.30	2.08	15.40 ± 0.04	2.12	5.2	**10.4 ± 1.8**	12.8 ± 1.9	18.6 ± 4.4	V	2.8	2.9	3.7	$\geq$ 7.2
36	B4	130.41	-0.59	14.65 ± 0.03	3.62	2.9	**2.7 ± 0.4**	3.4 ± 0.5	5.0 ± 1.4	V	0.5	0.7	0.7	$\geq$ 8.1
37	B6	131.56	1.01	14.53 ± 0.04	2.25	3.2	**3.4 ± 0.5**	4.1 ± 0.6	6.7 ± 1.8	V	0.5	0.7	1.1	$\geq$ 4.0
38	B5	131.92	1.32	15.66 ± 0.04	2.20	3.7	**6.7 ± 1.3**	8.4 ± 1.8	14.0 ± 4.3	V	1.3	1.8	1.8	6.5 ± 3.4
39	B4	132.86	1.81	16.25 ± 0.04	2.08	4.5	**11.6 ± 2.0**	14.6 ± 2.5	21.1 ± 6.1	V	2.3	2.8	2.9	$\geq$ 5.0
40[3]	B2	133.79	2.35	14.38 ± 0.03	2.58	11.9	6.0 ± 1.1	7.3 ± 1.2	**10.5 ± 2.4**	III	1.8	1.9	2.1	
41	B7	134.13	-0.59	14.11 ± 0.04	2.50	2.5	2.2 ± 0.3	**2.6 ± 0.4**	4.3 ± 1.1	IV	0.3	0.3	0.6	3.1 ± 1.1
42	B2	134.49	-0.49	14.95 ± 0.03	3.44	3.4	**5.3 ± 1.0**	6.4 ± 1.1	9.2 ± 2.1	V	1.6	1.6	1.8	$\geq$ 7.7
44	B5	135.03	1.41	15.50 ± 0.04	1.97	3.2	**6.9 ± 0.9**	8.7 ± 1.2	14.4 ± 3.8	V	1.3	1.8	1.8	5.3 ± 1.5
45	B3	135.06	0.55	13.01 ± 0.04	2.81	2.6	2.2 ± 0.3	**2.8 ± 0.3**	4.0 ± 1.0	IV	0.5	0.6	0.8	3.6 ± 1.0
46	B9	135.14	-0.81	14.61 ± 0.04	2.05	2.4	**2.5 ± 0.3**	3.1 ± 0.5	4.9 ± 1.4	V	0.4	0.6	0.9	2.4 ± 0.9
47	B3	135.38	-0.08	13.87 ± 0.03	4.00	2.6	1.9 ± 0.3	**2.4 ± 0.3**	3.5 ± 0.8	IV	0.4	0.5	0.7	$\geq$ 4.8
49	A0	135.64	2.19	15.42 ± 0.04	1.77	6.1	3.4 ± 0.5	4.3 ± 0.7	**6.8 ± 1.9**	III	0.6	0.8	1.2	$\geq$ 6.1
50	B3	135.89	1.30	16.03 ± 0.04	2.33	5.5	**11.1 ± 1.7**	14.0 ± 1.9	20.2 ± 5.0	V	2.6	2.9	4.1	5.9 ± 2.0
51	B8-9	136.07	2.94	14.61 ± 0.04	1.80	8.7	3.0 ± 0.4	3.8 ± 0.6	**6.0 ± 1.6**	III	0.5	0.6	1.0	
52	B7	136.09	1.48	15.49 ± 0.04	2.20	6.9	4.7 ± 0.6	**5.7 ± 0.8**	9.4 ± 2.3	IV	0.6	0.7	1.3	$\geq$ 6.1
53	B7	136.14	0.42	14.33 ± 0.03	2.63	2.1	**2.3 ± 0.3**	2.7 ± 0.4	4.5 ± 1.1	V	0.3	0.3	0.6	1.4 ± 0.5
54	B3	136.15	1.70	15.75 ± 0.04	2.05	5.2	**11.1 ± 1.6**	14.0 ± 1.7	20.3 ± 5.0	V	2.6	2.9	4.1	$\geq$ 5.3
55	B3-4	136.17	1.32	16.20 ± 0.04	2.48	6.8	**10.3 ± 1.4**	13.0 ± 1.7	18.7 ± 4.9	V	2.2	2.6	3.2	$\geq$ 7.1
56	B7	136.27	0.59	13.99 ± 0.04	2.38	2.4	**2.2 ± 0.3**	2.6 ± 0.4	4.3 ± 1.1	V	0.3	0.3	0.6	1.7 ± 0.4
58	B3	136.34	1.90	14.10 ± 0.04	1.70	5.2	**6.1 ± 0.9**	7.7 ± 1.0	11.1 ± 2.7	V	1.4	1.6	2.3	$\geq$ 6.5
59	B4	136.36	2.29	16.84 ± 0.05	1.87	5.1	**16.7 ± 2.4**	21.0 ± 3.0	30.4 ± 8.4	V	3.3	4.1	4.1	$\geq$ 6.2
60	B5	136.50	2.28	14.41 ± 0.03	1.77	5.8	4.6 ± 0.6	**5.8 ± 0.9**	9.6 ± 2.6	IV	0.9	1.2	1.2	$\geq$ 7.0
61	B3-4	136.50	2.26	15.50 ± 0.04	1.95	6.3	**9.5 ± 1.3**	12.0 ± 1.6	17.3 ± 4.5	V	2.0	2.4	2.9	

Table 6.2: Continued

#	SpT	ℓ (deg)	b (deg)	$r+\Delta r$ (mag)	A_r (mag)	A/F fit (kpc)	Distances $D_{SP,V}$ (kpc)	$D_{SP,IV}$ (kpc)	$D_{SP,III}$ (kpc)	$\sigma D_{SP,V}$ Class	Error on distances due to SpT $\sigma D_{SP,IV}$ (kpc)	$\sigma D_{SP,III}$ (kpc)	Likely (kpc)	D_E (kpc)
62	B7	136.64	2.38	14.89 ± 0.04	1.82	4.3	**4.3 ± 0.6**	5.1 ± 0.8	8.5 ± 2.1	V	0.6	0.6	1.2	≥ 6.7
63	B6	137.34	1.60	16.24 ± 0.04	3.04	2.7	**5.2 ± 0.8**	6.2 ± 1.0	10.3 ± 2.9	V	0.7	1.0	1.7	4.8 ± 1.7
65	B5	138.63	-0.27	16.33 ± 0.04	3.09	3.1	**6.1 ± 0.8**	7.6 ± 1.2	12.7 ± 3.5	V	1.1	1.6	1.6	≥ 7.7
66	B5	138.81	-0.87	13.97 ± 0.04	2.35	1.8	**2.9 ± 0.4**	3.6 ± 0.5	6.0 ± 1.6	V	0.5	0.8	0.8	3.0 ± 0.4
67	B4	138.98	-0.94	14.40 ± 0.04	2.68	2.8	**3.7 ± 0.5**	4.7 ± 0.6	6.8 ± 1.8	V	0.7	0.9	0.9	4.1 ± 1.0
68	B4	139.21	2.58	15.22 ± 0.04	2.81	3.6	**5.2 ± 0.8**	6.5 ± 1.0	9.4 ± 2.7	V	1.0	1.3	1.3	≥ 3.0

[3]For these sightlines the A/F fit distance estimate is based on 2 or 3 nearby early-A stars alone.

Chapter 7

Measures of radial velocities

In this chapter, I describe the measurement of radial velocities for a sub-sample of CBe stars. These were selected among the ones having better quality intermediate-resolution spectra. Their relatively small uncertainties in the Doppler shifts of spectral lines allow a more testing comparison with the spectroscopic parallaxes of Chapter 6.

7.1 Introduction

In Chapter 1, it was pointed out that measures of radial velocities in the Perseus Arm, both of gas and young stars, are known to deviate from the velocity field due to the Galactic rotation. This discrepancy has arguably produced an obvious offset between the distances obtained via kinematic measures and those from spectroscopic parallaxes (Heyer & Terebey, 1998; Massey, Johnson & Degioia-Eastwood, 1995). Typically, the observed difference amounts to -20 km s^{-1} that, in terms of distance, moves the Perseus Arm out to 3 and 5 kpc. The difference between observed and predicted radial velocities was explained by several authors (see e.g. Roberts, 1972; Humphreys, 1976; Brand & Blitz, 1993; Heyer & Terebey, 1998; Vallée, 2008) as a disturbance arising from non circular motions of molecular clouds when passing through the spiral arm - this is also observed in young stars observed in SFRs. The conclusion is that kinematic distances, based on a flat Galactic rotation curve, would give wrong estimates of the distance if used to study the spiral arm structure.

Recently, the measure of trigonometric parallaxes, for masers in SFRs of the Perseus and Outer Arms, has reduced the distances to the spiral arms placing W3(OH) at 1.95 kpc in the Perseus arm and WB89-437 at 6 kpc (Reid et al., 2009a) in the Outer Arm, with radial velocities of -45 and -72 km s^{-1} respectively. With the standard IAU values for R_0 and Θ_0, the observed radial velocities place the two masers at the much larger distances of 4.3 and 7.8 kpc instead. By adopting the circular rotation speed that the authors propose in the paper, which is $\Theta_0 = 254 \pm 16$ km s^{-1}, shorter kinematic distances are obtained ($\sim$ 3.4 and 6.9 kpc respectively).

Here I measure radial velocities for a limited number of stars with spectra of better S/N ratio, among those that were observed with intermediate-resolution spectra. The outcome can be used as a further check on distances that have been determined from spectroscopic parallaxes in Section 6, under the assumption that the rotation law is reliable

7.2 Kinematic distances of the CBe stars

Doppler shifts were measured for 7 lines, whose equivalent widths are strong enough to allow a more precise fitting in B-type stars. Some care has to be used when Doppler shifts are measured from emission lines, especially double-peaked ones, due to the fact that velocity components associated to gas motion in the circumstellar disc could affect the line shifts. Typically, CBe stars with double-peaked lines might show cyclical variation of the height of the peaks (V/R variation), which is due probably to the presence of spiral waves within the circumstellar disc (e.g. Porter & Rivinius, 2003). The lines I have chosen to measure are the Hα, Hβ, He I (λ4771 Å) and Mg II (λ4481 Å), He I ($\lambda\lambda$4009 – 4026 Å) and He I (λ4388 Å). For some stars not all of these transitions give good results and a fewer ones must be used. The fitting procedure is very simple and is described by the following steps:

1. The spectral window where the lines are located is normalised and continuum subtracted, by fitting the continuum in two 5 Å bands on both sides of the line with a linear function.

2. The line profile is fitted with the ELF package in STARLINK/DIPSO. The fitted profile is Gaussian in every case.

The two sets of neighbouring lines are fitted together, requiring that the Gaussian centres have the same separation as the rest wavelengths of the two lines. The fitting procedure for the Hα and Hβ lines uses always two components, one in emission and the other in absorption. Keeping their mutual separation equal to zero, but leaving the amplitude and width as free parameters, allows the fitting of symmetrical double-peaked line profiles. The rest wavelengths are taken from Didelon (1982). Examples of the fitting are given in Figure 7.1. I measured Doppler shifts for 39 out 68 stars in the group of intermediate-resolution spectra. The He I/Mg II pair of lines gives the best results, among the absorption lines, since the spectra are generally noisier at bluer wavelengths. On the other hand the Hα and Hβ, despite being visible in all the spectra when observed within the covered spectral range, could not always be used to determine the radial velocities due to asymmetries in the profiles or poorer fitting in partly filled-in profiles. I only retain measurements with fit errors smaller than 15 km s^{-1}.

Measured shifts and heliocentric radial velocities can be found in Table 7.1. I also include velocities transformed to the local standard of rest (LSR). When the radial velocity measured from the single line or pair of neighbouring lines had an uncertainty too large, a blank space is left. The listed velocities are the error-weighted mean of the available measurements for each star.

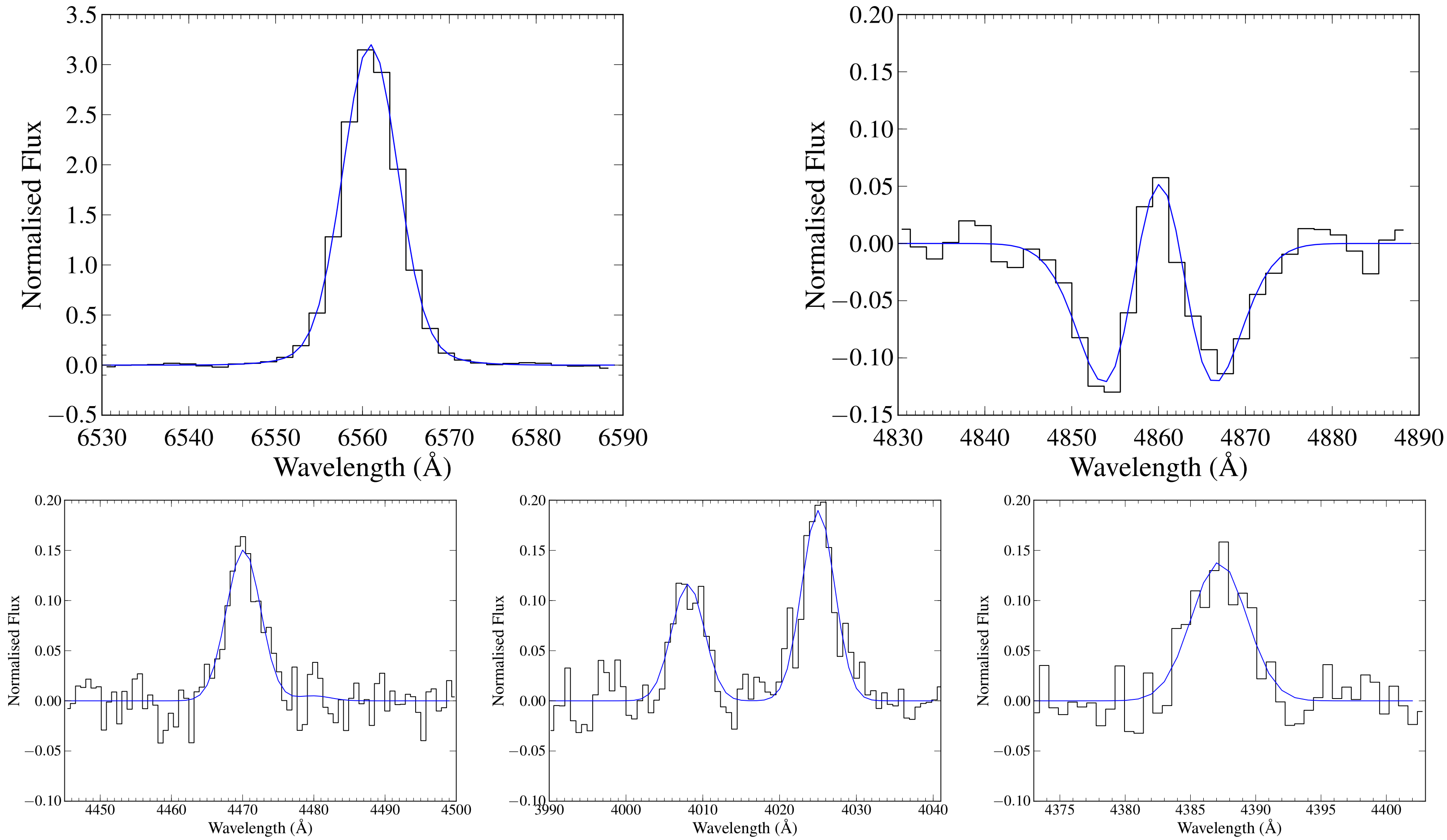

Figure 7.1: Six examples of line fitting for the determination of Doppler shifts. Top panels are for object # 10, while bottom ones are for object # 40. From top left to right bottom, the line fitted are: Hα, Hβ, He I (λ4771 Å) and Mg II (λ4481 Å), He I (λλ4009 – 4026 Å), He I (λ4388 Å). The lines are normalised and continuum subtracted. The flux is inverted, in the case of the absorption lines. The normalisation is done by fitting the continuum in two 5 Å bands on both sides of each line.

Table 7.1: Table reporting the kinematic distances of 39 CBe stars with intermediate-resolution spectra. Columns are: ID number; date of observation; measured wavelength shift; measured radial velocity; LSR radial velocity; kinematic distance; spectroscopic parallaxes; velocity residuals. The V_{lsr} uncertainty includes the Aumer & Binney (2009) and the wavelength calibration factors.

#	He I 4471, Mg II 4481 Δλ (Å)	He I 4009, 4026 Δλ (Å)	He I 4388 Δλ (Å)	Hα Δλ (Å)	Hβ Δλ(Å)	V_r (km s^{-1})	V_{lsr} (km s^{-1})	D_K (kpc)	D_{SP} (kpc)	ΔV (km s^{-1})
1	-1.73 ± 0.26			-2.18 ± 0.01	-1.50 ± 0.13	-102	-78 ± 18	$8.2^{+3.1}_{-2.4}$	5.6 ± 1.7	-25 ± 21
2				-2.01 ± 0.02		-92	-67 ± 15	$6.7^{+2.2}_{-1.8}$	3.3 ± 0.6	-33 ± 15
3	-1.60 ± 0.26			-2.35 ± 0.01	-1.55 ± 0.10	-103	-79 ± 17	$8.3^{+3.2}_{-2.4}$	5.2 ± 1.7	-28 ± 20
4				-1.41 ± 0.02		-64	-41 ± 16	$3.7^{+1.7}_{-1.5}$	3.4 ± 0.8	-6 ± 16
5				-1.87 ± 0.01		-85	-60 ± 14	$5.9^{+1.9}_{-1.6}$	7.8 ± 2.8	7 ± 15
6				-2.71 ± 0.01	-1.55 ± 0.26	-109	-86 ± 16	$9.6^{+3.5}_{-2.6}$	7.7 ± 2.0	-18 ± 18
9				-0.98 ± 0.05	-0.54 ± 0.34	-39	-25 ± 18	$2.2^{+1.8}_{-1.6}$	3.4 ± 0.8	8 ± 18
10				-1.90 ± 0.01	-1.21 ± 0.19	-80	-56 ± 16	$5.3^{+2.2}_{-1.8}$	3.4 ± 0.6	-20 ± 17
11				-2.40 ± 0.03		-109	-84 ± 14	$9.4^{+3.0}_{-2.3}$	9.2 ± 2.9	-8 ± 15
12				-1.75 ± 0.02	-1.12 ± 0.13	-74	-49 ± 15	$4.6^{+1.9}_{-1.6}$	4.1 ± 1.0	-8 ± 15
13				-1.85 ± 0.08		-84	-59 ± 15	$5.7^{+2.1}_{-1.7}$	5.6 ± 1.3	-6 ± 15
14				-2.34 ± 0.02	-1.67 ± 0.16	-104	-81 ± 15	$8.9^{+3.1}_{-2.4}$	6.3 ± 1.5	-23 ± 15
15				-1.65 ± 0.02		-75	-50 ± 15	$4.6^{+1.8}_{-1.6}$	3.5 ± 0.8	-14 ± 15
16				-2.48 ± 0.01		-113	-88 ± 14	$10.3^{+3.4}_{-2.5}$	6.3 ± 2.0	-29 ± 18
17				-2.79 ± 0.01		-127	-102 ± 14	$13.8^{+4.9}_{-3.4}$	4.6 ± 1.1	-57 ± 15
18				-2.10 ± 0.01		-95	-70 ± 14	$7.4^{+2.6}_{-2.0}$	4.5 ± 1.1	-26 ± 14
20				-2.46 ± 0.01		-112	-87 ± 14	$10.3^{+3.5}_{-2.6}$	3.5 ± 1.0	-51 ± 14
23				-2.79 ± 0.04		-127	-102 ± 15	$14.2^{+5.7}_{-3.8}$	3.0 ± 0.6	-71 ± 15
25	-1.36 ± 0.16			-0.88 ± 0.01	-0.76 ± 0.12	-59	-46 ± 16	$4.2^{+2.1}_{-1.7}$	2.6 ± 0.6	-18 ± 16
26				-2.19 ± 0.01		-99	-76 ± 14	$8.3^{+2.9}_{-2.2}$	9.9 ± 2.8	0 ± 15
28				-1.81 ± 0.02		-82	-57 ± 15	$5.7^{+2.3}_{-1.9}$	3.2 ± 0.6	-24 ± 15
29				-1.56 ± 0.01	-1.17 ± 0.18	-71	-46 ± 16	$4.3^{+2.1}_{-1.7}$	3.3 ± 0.6	-12 ± 17
31	-1.10 ± 0.13	-0.98 ± 0.13	-0.83 ± 0.17	-1.32 ± 0.11		-65	-65 ± 20	$6.8^{+3.7}_{-2.6}$	3.5 ± 0.8	-29 ± 20
32				-1.66 ± 0.06	-1.21 ± 0.00	-75	-50 ± 15	$4.8^{+2.1}_{-1.7}$	5.3 ± 1.2	0 ± 16
33				-2.23 ± 0.03		-102	-77 ± 16	$8.7^{+3.6}_{-2.6}$	4.7 ± 1.5	-31 ± 18
34	-1.18 ± 0.30			-2.44 ± 0.07		-95	-70 ± 18	$7.6^{+3.8}_{-2.7}$	6.8 ± 1.9	-11 ± 19
35				-2.54 ± 0.06		-115	-90 ± 14	$11.9^{+4.6}_{-3.2}$	10.4 ± 3.3	-13 ± 15
36				-1.47 ± 0.05	-0.97 ± 0.04	-63	-50 ± 15	$4.8^{+2.1}_{-1.7}$	2.7 ± 0.6	-21 ± 15
37	-1.35 ± 0.31			-1.48 ± 0.01		-79	-65 ± 18	$7.0^{+3.6}_{-2.6}$	3.4 ± 0.7	-31 ± 18
38				-1.67 ± 0.05		-76	-62 ± 15	$6.5^{+2.7}_{-2.1}$	6.7 ± 1.9	-4 ± 15
39				-2.03 ± 0.02		-92	-78 ± 14	$9.5^{+3.9}_{-2.8}$	11.6 ± 3.0	0 ± 15
40	-1.35 ± 0.17	-1.17 ± 0.13	-0.73 ± 0.20			-75	-76 ± 21	$9.4^{+6.2}_{-3.8}$	10.5 ± 3.2	-2 ± 23
41	-1.09 ± 0.30	-1.18 ± 0.25			-0.80 ± 0.15	-70	-72 ± 25	$8.6^{+6.9}_{-4.0}$	2.6 ± 0.5	-45 ± 25
45			-0.80 ± 0.12	-0.78 ± 0.02	-0.66 ± 0.14	-43	-43 ± 16	$4.1^{+2.4}_{-1.8}$	2.8 ± 0.7	-14 ± 17
47	-0.98 ± 0.22	-1.05 ± 0.15				-72	-74 ± 19	$9.3^{+5.6}_{-3.5}$	2.4 ± 0.6	-49 ± 19
54	-0.47 ± 0.18	-0.64 ± 0.18			-0.80 ± 0.05	-42	-45 ± 18	$4.4^{+2.9}_{-2.1}$	11.1 ± 3.0	29 ± 19
56	-0.26 ± 0.23	-0.93 ± 0.28			-0.14 ± 0.03	-32	-34 ± 22	$3.1^{+2.9}_{-2.2}$	2.2 ± 0.4	-11 ± 22
58	-1.38 ± 0.21	-0.65 ± 0.22				-70	-72 ± 21	$9.1^{+6.3}_{-3.8}$	6.1 ± 1.6	-20 ± 21
68				-1.20 ± 0.03	-0.68 ± 0.24	-48	-33 ± 17	$3.1^{+2.3}_{-1.8}$	5.2 ± 1.3	11 ± 17

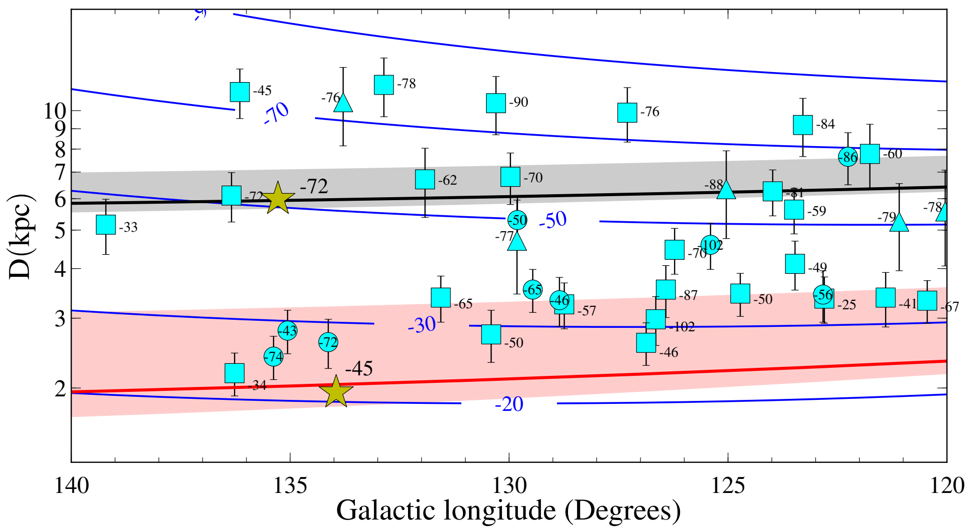

Figure 7.2: The radial velocity field of the Galaxy between $120° \leq \ell \leq 140°$ is plotted. The iso-velocity curves (in blue) are plotted in accordance to the Brand & Blitz (1993) radial relation. The numbers are in units of km s^{-1}.The spiral arms are plotted as in Fig. 6.4. The measured radial velocities are annotated nearby each target on the left hand side. Luminosity classes are flagged by different symbols, i.e. squares for class V, circles for class IV and triangles for class III. I also report the radial velocities of the two methanol masers (star symbols) as they were given by Reid et al. (2009a).

Studies based on the kinematics of stars in the solar neighbourhood show that space velocities of stars are dispersed around the pure rotation value in a manner that is spectral type dependent (Aumer & Binney, 2009). The dispersion of velocities is due to the multiple interactions with the ISM and other stars in the disc, in a way that it grows with the average age of the star. For this reason, the uncertainty on the velocity should also include a spectral type dependent term. The components of the velocity dispersion tensor, which are significantly non-zero for Galactic plane stars, are σ_u and σ_v. These are combined into a radial dispersion $\sigma_r^2 = |\sigma_u \cos(\ell)|^2 + |\sigma_v \cos(\ell - 90°)|^2$, which I summed in quadrature with the measurement error. The two components vary between $\sim$ 8.5-15 km s^{-1} and $\sim$ 8.5-10 km s^{-1} respectively, for B0 to A0 stars. The combined velocity dispersion σ_r, in the considered Galactic longitude range, varies in the range 9 –13 km s^{-1}.

Another small contribution to the velocity error is the uncertainty arising from the wavelength calibration. This was in the range of 0.10-0.15 Å, as estimated from the residuals of the fit to the dispersion relation, and corresponds to a further 7-15 km s^{-1}.

A way of comparing the measured V_{lsr} with the theoretical predictions is to plot the stars in a radial velocity field as in Figure 7.2. Each star is plotted at its own spectroscopic parallax and the number close to it is the measured radial velocity (LSR frame). The iso-velocity curves shown give the changing projection of the Brand & Blitz (1993) rotation curve onto the line-of-sight. By looking at the measured V_{lsr} and the iso-velocity curves, the majority of stars have radial velocities that are more negative by several km s^{-1}, with

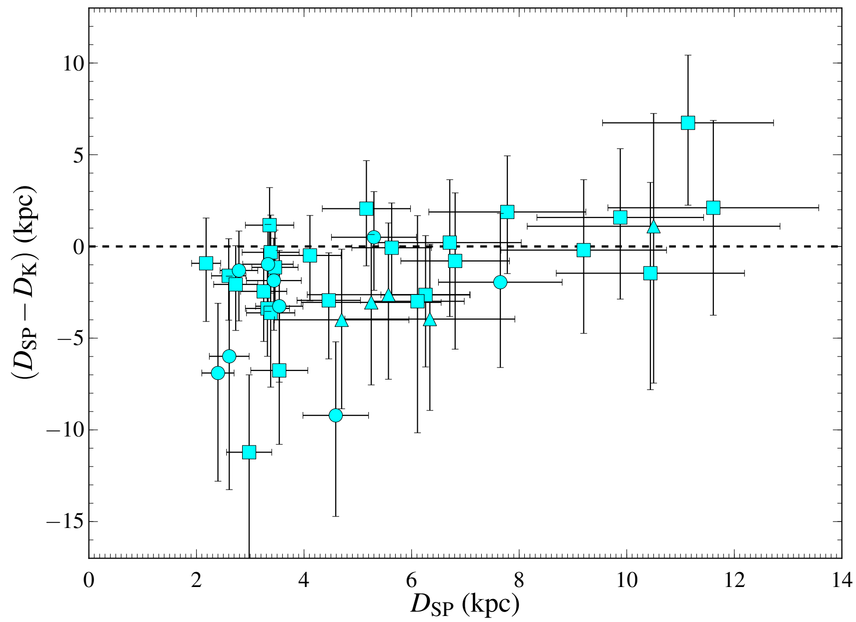

Figure 7.3: The comparison between measured spectroscopic parallaxes and kinematic distances for the 39 CBe stars of Table 7.1 is displayed, plotting their difference $D_{SP} - D_K$ against D_{SP}. Symbols, as before, are used to distinguish between luminosity classes. Squares are used for class V, circles for class IV, and triangles for class III.

respect to the predicted velocity. A finer cross match is done by comparing instead the kinematic distances, which I list in Table 7.1, with the spectroscopic parallaxes as depicted in Fig. 7.3. Most of the stars have their distances agreeing within the errors, although for five of them I measure large negative values of the quantity $D_{SP} - D_K < -5$ kpc. These stars are: # 17, 20, 23, 41, and 47, while for object # 54 the difference is also large but positive. In the case of objects # 17, 20, and 23, only the Hα line was used to estimate D_K, and the measured radial velocity might be more unreliable. For the other three stars, more than one line was used for the measure of D_K, so that the discrepancy is unexplained. The general trend is that the kinematic distances are larger than the spectroscopic parallaxes, specially at distances shorter than 8 kpc. On the other hand, for stars observed at distances larger than 8 kpc, I find a better agreement, with only # 54 having $D_{SP} > D_K$. Nevertheless, uncertainties on the distance estimates are too large to allow more than a qualitative analysis.

If this result is consistent with the current view of non-circular motions induced by the density-wave perturbation (Lin & Shu, 1964; Roberts, 1972), for which the rotational velocity of stars located in the spiral arms deviates from the circular rotation motion, the radial velocity residuals $\Delta V = V_{lsr} - V_{model}$, where V_{model} is the expected radial velocity for the measured D_{SP}, should be consistent with measures from the literature. Non circular motions are expected to have different sign (-/+) on the nearer and more distant sides of the spiral arms respectively – Humphreys (1976) measured an average $\Delta V = -10.7 \pm 5.4$ km s^{-1} for stars on the inner side of the Perseus arm, while $\Delta V = +7.0 \pm 3.8$ km s^{-1} on the far side. This is explained as the manifestation of two components of the velocity perturbation, which arises from the shock front in spiral arms (Mel'Nik, Dambis & Rastorguev, 1999, and references therein): (i) the radial component (directed towards the Galactic centre) and an azimuthal component (opposite to the Galactic rotation) have opposite signs inside or outside the corotation radius; (ii) on the far side of spiral arms the first becomes zero, while the latter is oriented in the Galactic rotation direction; (iii) small streaming motions are present also in the interarm regions.

The negative radial velocity residuals that are measured for stars in the Perseus Arm want it to be inside the corotation radius. Some debate, instead, regards the sign of radial velocity residuals in the Outer Arm. Russeil, Adami & Georgelin (2007) found that radial velocity residuals are in average negative in the Perseus Arm (~ -15 km s^{-1}) and positive in the Outer Arm (~ 8 km s^{-1}), from which they infer a Galactocentric distance for the corotation radius of 12.7 kpc: the Outer Arm crosses the corotation radius at anticentre longitudes. On the other hand, measures of radial velocities of the masers given by Reid et al. (2009a) imply that radial velocity residuals for W3(OH) and WB 89-437, assuming a standard rotation speed, are in the range of ~ -30 km s^{-1}, as if both spiral arms were within the corotation radius. The Outer Arm being within the corotation radius is also confirmed by measures of 3D-velocity residuals of the maser G75.30+1.32, in the first Galactic quadrant (Sanna et al., 2012)

Within the sample of 39 stars considered, 17 have D_{SP} that are consistent with the Perseus Arm (i.e. # 2, 4, 9, 10, 15, 20, 23, 25, 28, 29, 31, 36, 37, 41, 45, 47 and 56). All of them have negative ΔV, apart from # 9. I do not observe the expected trend, as observed by Humphreys (1976), i.e. that stars on the close side of the arm possess residuals with opposite sign (-) in comparison to the ones on the far side of the arm (+), although this is probably due to the magnitude of the errors. However, the fact that the median of the measured residuals is around $\Delta V \approx -21$ km s^{-1} is reassuring. Typical velocity residuals in the Perseus Arm, lie between -10 and -30km s^{-1} (Humphreys, 1976; Russeil, Adami & Georgelin, 2007) and measures from Reid et al. (2009a).

A comparison for the stars that are closer to the predicted Outer Arm's location appear to be more difficult. Heyer & Terebey (1998) made the remark that little molecular gas is seen further away than the Perseus Arm, but later papers that are analysed in Vallée (2008), identified structures that could be associated to the Outer Arm. Vallée (2008), in the discussion, makes the point that many publications misidentified the Outer Arm with the Perseus Arm, due to possible blending of measures of LSR velocities. The bottom line is that if similar velocity residuals are present in the Outer Arm, the measured radial velocity would have a two-fold solution. Five CBe stars that seem to be associated with the Outer Arm in Fig. 7.2 are giants (# 1, 3, 16, 40, and 58) following the luminosity class assignment from the previous chapter. These stars, therefore, are unlikely to be more distant than the distance given. Interestingly, the most distant one, # 40, that is on the far side of the arm location, has $\Delta V \sim 0$ within the errors, while the others that are at closer distances display more negative velocity residuals. This would be in agreement with the usual interpretation of velocity residuals. The largest positive residual is measured for object # 54 that is placed at the further side of the Outer Arm by its spectroscopic parallax.

7.3 Summary

In this chapter, I presented measures of Doppler shifts for a sub-sample of 39 spectra, from the intermediate-resolution observations. The inferred kinematic distances are in agreement within the errors for all but 7 of the 39 CBe stars considered. Velocity residuals seem consistent with predicted ones for the Perseus Arm. The large discrepancies that are observed between measures of kinematic and spectroscopic parallaxes might be reconciled with a larger value of the rotation speed (at least for some of the stars in consideration). There are hints that it is might be indeed larger than the widely used $\Theta_0 = 220$ km s^{-1} (Reid et al., 2009a; Brunthaler et al., 2011). A $\Theta_0 = 250$ km s^{-1} (Reid et al., 2009a), for instance, would reduce $D_{\rm K}$ up to 20%.

Chapter 8

Exploring the properties of the interstellar medium with the classical Be stars

Here I discuss the properties of the ISM that are highlighted by the CBe stars. The discussion focuses on the DIBs in Section 8.2. In Section 8.3 I will examine how the reddenings of CBe stars compare with the total column of dust measured along the line-of-sight.

8.1 Introduction

Among the current sample of 248 CBe stars, there are several examples of CBe stars at distances large enough that they almost certainly lie beyond even the putative Outer Arm. The reddening of such objects ought to closely match the integrated Galactic value since nearly all the interstellar dust would lie between them and the Sun. This comes along with two interesting prospects for the study of the properties of the ISM in this part of the Milky Way.

First, the large spectral coverage, which for most of the spectra extends from ~ 3500 to 7400 Å , with the exclusion of the NOT/ALFOSC spectra, allows the study of a number of DIBs, in particular three of the deepest and more studied ones at optical wavelengths (i.e. $\lambda\,4428$ Å, $\lambda\lambda\,5580.5 - 5797$ Å Herbig, 1995; Snow, Zukowski & Massey, 2002; Friedman et al., 2011). This allows to re-open the question of correlations between DIBs strength and measures of reddenings, over a large area of the Galactic plane.

Second, the interstellar colour excesses that are measured for these stars can be compared with the most widely used source of integrated reddenings, which is the work of SFD98. Furthermore, no star in the sample should be significantly reddened beyond, the values returned by the database due to SFD98. The impression that is found in the literature (Cambrésy, Jarrett & Beichman, 2005, RF09) of a systematic overestimate of asymptotic reddenings, by SFD98, can also be tested.

8.2 Measures of diffuse interstellar bands equivalent widths

The DIBs, as the name indicates, are spectral features that are observed in stellar spectra as the corresponding sightline passes through diffuse clouds in the ISM. The most recent review about them is the one by Herbig (1995), which I follow to describe their general properties. The first identification of their interstellar nature dates back to Merrill (1934). Even if the carriers originating the DIBs are still unidentified, there is rising evidence suggesting their association to polycyclic aromatic hydrocarbons (PAH) or fullerenes (Herbig, 1995; Garcia-Hernandez & Diaz-Luis, 2013).

Since the first observations (Merrill, 1934; Merrill & Wilson, 1938), the line strength of certain DIBs was noted to show a positive correlation with distance, or better with the $E(B-V)$ measured for the star, in which spectrum the DIBs are identified. With the advance of technology, it appeared evident that the observed scatter of data is real, and a tight linear correlation between DIBs strength and interstellar reddening might not be existent, although the two quantities are largely proportional (Herbig, 1995). In studies that focused on the correlation between EW(DIBs) and $E(B-V)$, several reasons are invoked by Herbig (1995) as causes of the observed scatter, which are in turn: (i) the difficulty of determining the stellar continuum with precision even in B-type spectra and inaccuracy in the photospheric-lines removal; (ii) environmental effects. The importance of the environment on the line strength of DIBs, in general, has been acknowledged since Wampler (1963) and it is known that very obscured sightlines may show in average weaker DIBs (Herbig, 1975). The fact that DIBs form mostly in the external layers of molecular clouds, and in less extent in their interiors, is called skin effect. As Herbig (1995) reported, the line strength of DIBs is known to correlate with the column density of neutral hydrogen, $N(\mathrm{H\,I})$, and not with the molecular hydrogen, $N(\mathrm{H_2})$. In fact, the latter increases towards the core of molecular clouds, in opposition to $N(\mathrm{H\,I})$ that is larger at the surface.

A standard test, which has been adopted in the quest for the identification of the DIBs carriers, is the study of DIB-DIB correlations. As a result of this somewhat speculative approach, several families of DIBs have been identified, which are thought to be produced by the same carriers. Herbig (1995) reported contrasting results, although it seems possible that the DIB(5780.5) and DIB(5797) correlate with each other and with $E(B-V)$, as also confirmed by Friedman et al. (2011) with high resolution and high S/N ratio observations. In particular, these authors focused on the study of DIB(5780.5), which they propose as calibrator for estimating $N(\mathrm{H\,I})$, although to be used with care. Finally, Friedman et al. (2011) also mention an effect called $\sigma-\zeta$ that, acting similarly to the skin effect, generates scatter in the observed data. Since Krełowski & Sneden (1995), it has been observed that along σ sightlines the DIB(5780.5) is deeper than DIB(5797), while along ζ lines-of-sight the depths of both DIBs are comparable and $N(\mathrm{H_2})$ are larger, where σ and ζ sightlines are named after the two proptotype stars σ Sco and ζ Oph that first were discovered to show this effect.

One of the most studied DIBs is the one at $\lambda 4428$ Å, which profile is quite shallow and broad. This DIB correlates well with $E(B-V)$, although it presents with a strong skin effect along dense sightlines, where the $EW(4428)$ vs $E(B-V)$ distribution seems to

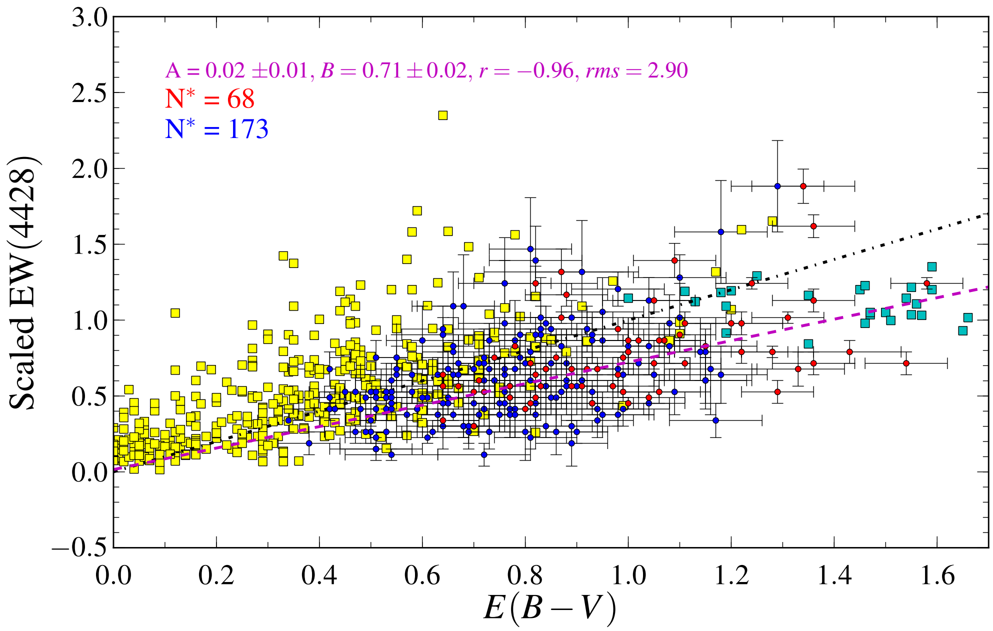

Figure 8.1: Comparison between equivalent widths of the DIB at $\lambda 4428$ Å with interstellar colour excess. Data are scaled to the ratio $E(B-V)/EW(\lambda\mathrm{DIB})$ for HD 183143 (Herbig, 1995), which are $E(B-V) = 1.28$ and $EW(4428) = 3.4$ Å. Blue circles are used for the CBe stars with FLWO/FAST spectra, while red circles are for the stars with La Palma spectra. Yellow symbols are data from Guarinos (1988) and cyan symbols are for data by Snow, Zukowski & Massey (2002). The black line is the equality line. The number of points plotted is colour coded matching to the symbols colour. The coefficients of the best-fit line, in purple, are given figure.

flatten out at around a limiting reddening (e.g. $E(B-V) \gtrsim 1$, Herbig, 1995; Snow, York & Welty, 1977; Snow, Zukowski & Massey, 2002). The DIB(4428) is suggested to be formed by a large number of unresolved narrow lines, which blend together forming the observed shallow profile. The saturation of these lines has been rejected by (Snow, Zukowski & Massey, 2002), who tend to prefer the skin effect as dominating phenomenon.

Due to the limiting spectral resolution and S/N ratio of the sample, I have chosen to measure these three DIBs that are well documented in the literature, which are DIB(4428), DIB(5580.5), and DIB(5797). The last couple of DIBs are only available for the spectra covering wavelengths redder than $\lambda 5000$ Å, i.e. the NOT/ALFOSC spectra are excluded. Fits to the line profiles were run similarly to the other line fits of Chapter 2, for instance, using the STARLINK/DIPSO line fitting package. I fitted the lines with Gaussian profiles centred on the rest wavelengths given by Herbig (1995). The measured equivalent widths are listed in Tables 8.1 and 8.2.

In Fig. 8.1, $EW(4428)$ are plotted against $E(B-V)$ for the CBe stars in the sample. For the CBe stars with La Palma spectra, I used $E(B-V)_{(\mathrm{S,c})}$, while for the others with FLWO/FAST spectra I used $E(B-V)_{(\mathrm{P,c})}$. These are compared with data from Guarinos (1988), which is an update of the catalogue by Snow, York & Welty (1977), and Snow, Zukowski & Massey (2002). The equivalent widths are scaled to the ra-

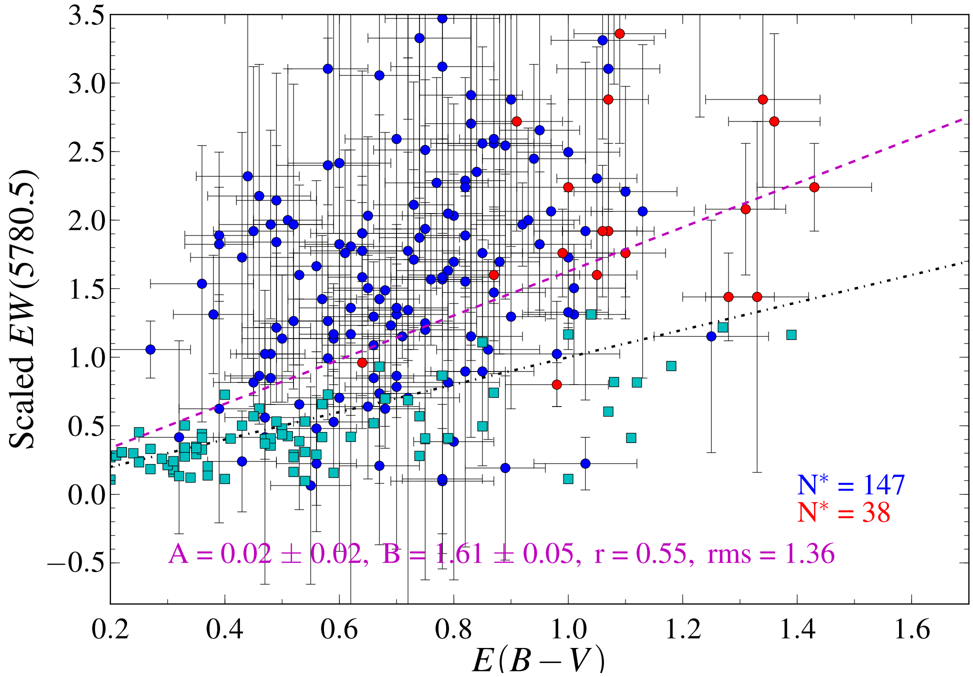

Figure 8.2: Comparison between equivalent widths of DIB(5780.5) with interstellar colour excess. Data are scaled to the ratio $E(B-V)/EW(\lambda\text{DIB})$ for HD 183143 (Herbig, 1995), which are $E(B-V) = 1.28$ and $EW(5780.5) = 0.80$ Å. Blue circles are used for the CBe stars with FLWO/FAST spectra, while red circles are for the stars with La Palma spectra. Cyan symbols are for data by Friedman et al. (2011). The black line is the equality line. The number of points plotted is colour coded matching to the symbols colour. The coefficients of the best-fit lines, in purple, are given in figure.

tio $E(B-V)/EW(\text{DIB})$ of HD 183143, with values taken from Herbig (1995), where $E(B-V) = 1.28$ and $EW(4428) = 3.4$ Å.

The sightlines to the stars considered within Guarinos (1988) go across the Galactic plane, but also cover high Galactic latitudes, while the ones in Snow, Zukowski & Massey (2002) are mainly in the direction of the Cyg OB2 Association. The data from the literature show the expected positive trend of $EW(4428)$ vs $E(B-V)$, which follows the equality line. The data from Snow, Zukowski & Massey (2002), i.e. the cyan squares, display the saturation effect, which happens for $E(B-V) \gtrsim 1$ along the lines-of-sight crossing the Cyg OB2 Association. Also the $EW(4428)$, which I measure from the sample, present a positive trend with reddenings, although the magnitude of errors is quite large, specially for the FLWO/FAST data, due to the noise characteristics of the spectra. The datapoints are largely scattered around the equality line and to quantify the correlation of data, I computed a linear regression fit to the points. Coefficients for the fits are plotted in Fig. 8.1. The coefficient of linear correlation, $r = 0.95$, along with the relatively small *rms* measured confirm the positive linear correlation. However, due to the fact that many sightlines pass through areas of larger extinction, the slope of the best-fit line is influenced by the

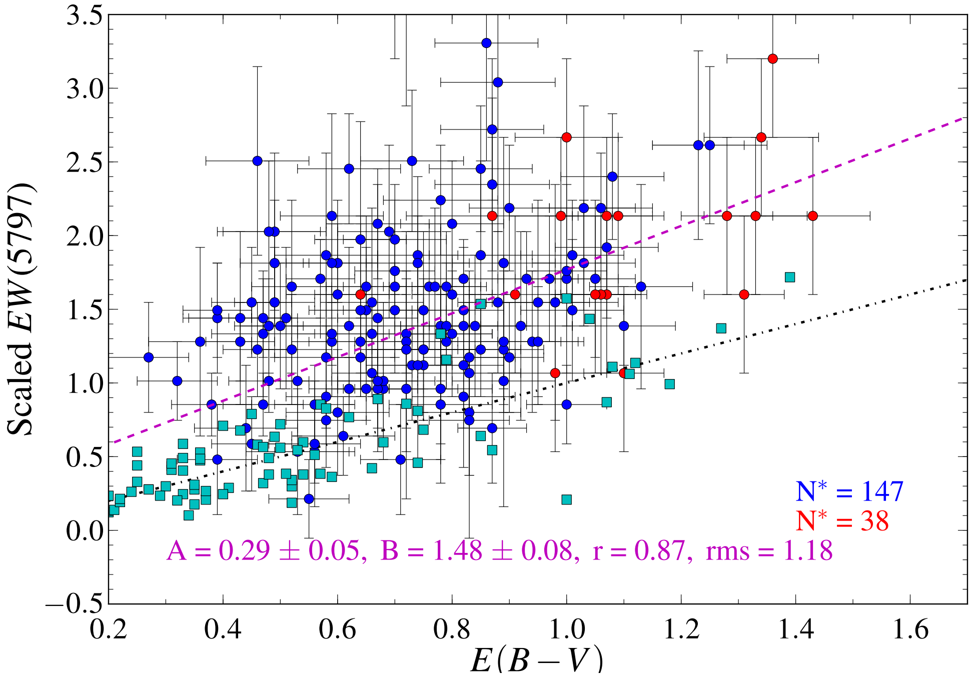

Figure 8.3: Comparison between equivalent widths of DIB(5797) with interstellar colour excess. Similarly to Fig. 8.2, data are scaled to the ratio $E(B-V)/EW(\lambda\text{DIB})$ for HD 183143 (Herbig, 1995), which are $E(B-V) = 1.28$ and $EW(5797) = 0.24$ Å. Colours and symbols are plotted as in Fig. 8.2. The coefficients of the best-fit lines, in purple, are given in figure.

saturation effect observed in (Snow, Zukowski & Massey, 2002), so that $B < 1$. From the look of the data, it appears very difficult to quantify it due to the scatter of points. For this reason and because the sightlines to the studied CBe stars sample very different environments, saturation effects might either appear reduced or stronger than they are, depending on how the dust is distributed in the Galactic plane.

For the DIB(5780.5) and DIB(5797), I did not attempt a DIB-DIB comparison plot, since their equivalent widths are weaker than the ones measured for DIB(4428) and errors introduce too much scatter in the plot. The $EW(5780.5)$ and $EW(5797)$, plotted against $E(B-V)$ in Fig. 8.2 and Fig. 8.3, are compared to data from (Friedman et al., 2011). The plotted $EW(\text{DIB})$ are scaled again with the quantity $E(B-V)/EW(\text{DIB})$, with $EW(5780.5) = 0.80$ Å and $EW(5797) = 0.24$ Å.

The linear regressions computed for these other two DIBs produce the following $r = 0.55, 0.87$, against the values measured by (Friedman et al., 2011) of $r = 0.90, 0.72$ for DIB(5780.5) and DIB(5797) respectively. The measured *rms* are pretty small although, in both cases, I notice quite a large offset of the points with respect to the Friedman et al. (2011) data, which possibly is due to systematic overestimates of the equivalent widths of this fainter DIBs. In the case of DIB(5780.5), there is a known shallower broad feature centred at λ5778, which is difficult to be removed. The quality of the data at hand does not allow a more useful comparison with the literature.

8.3 Comparison between colour excesses of CBe stars and total Galactic reddenings

8.3.1 Classical Be stars with La Palma observations

I have plotted the measured interstellar colour-excess for each CBe star against the SFD98, $E(B-V)_{\rm SFD98}$, and RF09 integrated line-of-sight colour excess, $E(B-V)_{\rm RF09}$, for the objects with La Palma spectra, in the left panel of Fig. 8.4. In the right panel of Fig. 8.4, instead, the interstellar colour excess is also plotted against the reddening that is obtained from the most distant bin of the H-MEAD extinction curve, for each sightline corresponding to the stars in the sample. The plotted quantities are given in Tables 5.4 and 8.1.

The measured interstellar colour excess is a spot value pertaining to a single line of sight, while $E(B-V)_{\rm SFD98}$ apply to a spatial resolution element about 6 arcmins across. $E(B-V)_{\rm RF09}$, instead, is determined from the median near-IR colours of the 49 nearest stars to a given sightline, so that it has variable spatial resolution between $\sim$ 1–10 arcmin, depending on the sightline, with the highest resolution measured towards molecular clouds. Hence it should be kept in mind that small variations in the ISM may occur that slightly falsify the colour excess due to SFD98 or RF09. Similarly, the extinction-curves that are build with H-MEAD are computed from the IPHAS photometry of stars found within a 10×10 arcmin^2 box, centred on each CBe sightlines.

Now, I will discuss first the left diagram of Fig. 8.4. A general property of the figure is that for all but two objects, $E(B-V)_{\rm SFD98} > E(B-V)_{\rm (S,c)}$, to within the errors. This accords with expectation. On the other hand, $E(B-V)_{\rm RF09} < E(B-V)_{\rm (S,c)}$ always. According to RF09, along sightlines going thorough molecular clouds, where most of the stars are foreground objects, $E(B-V)_{\rm RF09}$ measures the foreground reddenings. Hence, if I measure reddenings that exceed $E(B-V)_{\rm RF09}$, it would be reasonable to think that the CBe star is in the background of the distances for which $E(B-V)_{\rm RF09}$ holds. Since none of the stars in this sample of CBe stars is detected at distances closer than 2 kpc, it is a legitimate assumption that the reddenings measured by RF09 generally correspond at most to Perseus Arm distances.

The stars shown in blue or grey, in the left panel of Fig. 8.4, are the most distant, at more than 8 kpc away (specifically, objects # 11, 26, 35, 39, 40, 50, 54, 55, and 61). All but one (# 40) are dwarfs. These stars are, as noted in Section 3.4, mainly early-B stars and I also notice that they are average to strong Hα emitters (implying $E^{cs}(B-V)$ =0.04-0.18). All of them seem to have reddenings, after correction, that would be linked to tracks falling close to the red edge of the main stellar concentration in the IPHAS colour-colour diagram (see e.g. Fig. 6.1(a)), consistent with their being at large Galactocentric radii beyond much of the dust column. But, excepting the case of # 40, I find that the measured colour excesses are distinctly less than those from the SFD98 reddening map. The discrepancy is of order 0.2-0.3 magnitudes. This is more than the amount by which I have had to lower the measured colour excesses to correct for circumstellar emission. So whilst these corrections can be seen as uncertain, this is not the explanation. There are further options. One is that the dust temperatures adopted by SFD98 along these lines of sight are too low,

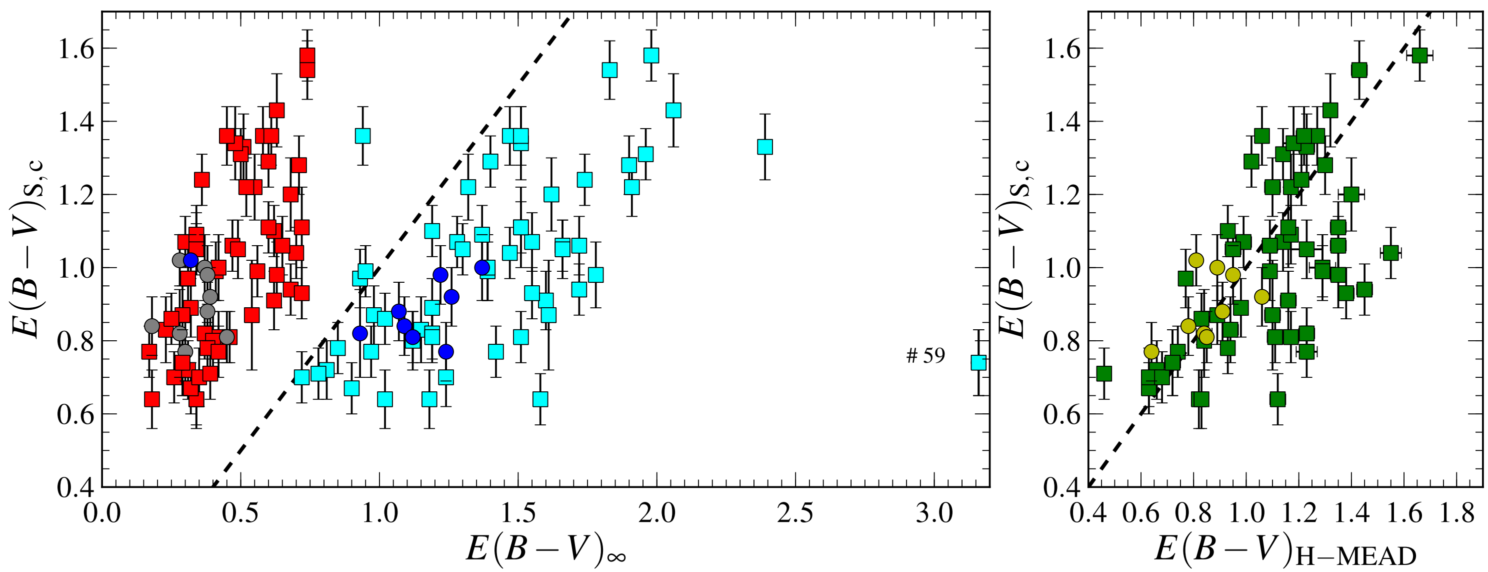

Figure 8.4: Left panel: the corrected colour excesses for the CBe star sample with La Palma spectra is plotted against the corresponding integrated Galactic colour excesses from SFD98 (cyan and blue symbols) and RF09 (red and grey symbols), for each sightline. Blue and grey symbols are used for the stars with a measured distance larger than 8 kpc, well beyond the expected location of the Outer Arm. The dashed black line is the equality line. Right panel: corrected colour excesses for the CBe star sample with La Palma spectra plotted against the reddening measured by the last bin of the extinction-distance curves built with H-MEAD. Yellow symbols are for the stars with $D \leq 8$ kpc.

yielding over-estimates of the total dust columns. But the following might be the better solution: perhaps imposing the mean reddening law on these particularly long sightlines has led us to under-estimate these stars' extinctions, A_r – and hence over-estimate the distances to them. For example, increasing A_r by a few tenths would lower the heliocentric distances by a similar proportion. Also by enforcing the selection of redder nearby A/F stars, the effect of choosing higher A_r would push that distance estimate up, bringing the two estimates closer together than they are presently (see data in Table 6.2).

For object # 40 the situation is quite different, since the datum from SFD98 indicates a very much lower total dust column than obtained. I notice indeed in their temperature map (that is much less well-resolved spatially than the emissivity map) a large hot spot roughly corresponding to the upper part of the galactic chimney linked to W4: it seems plausible therefore that the cause of the problem is the adoption of too high a dust temperature for this particular sightline predicting too low a dust column. A similar but not so extreme discrepancy arises in the case of object # 42.

Another group of stars can be picked out in Fig. 8.4, whose colour excesses agree to within the errors with the values from SFD98 (these authors quote a 0.04 uncertainty on their estimates). They are objects # 17, 19, 22, 32, 39, 41, 44, 49, 51, 52, 62, 65. Yet it is noticeable that the residuals favour the SFD98 colour excess as the higher value – thus hinting that here too there may be over-estimation of the total integrated extinction. This tendency was already noted by Cambrésy, Jarrett & Beichman (2005), using the 2MASS colours of galaxies to compare with the line-of-sight colour excess measured by SFD98 in the anti-centre direction. However, for five of these objects (# 32, 41, 44, 49, 52), the IPHAS colour-colour diagram indicates that $E(B-V)_{\mathrm{SFD98}}$ may in fact be *too small* compared to the red extent of the main stellar locus. All the other stars in this group seem to have reddenings that both agree with those of SFD98 and are compatible with the maximum reddening indicated by the IPHAS colour-colour diagram for their localities – i.e. both measures agree these objects are behind $\sim$all Galactic dust. Their distances either exceed ~ 6 kpc, or their sightlines are at latitudes higher than $b = 2^{\circ}$. Object # 39 was already mentioned above, as belonging to the most distant group – its reddening is the least discrepant relative to SFD98 of that group.

The comparison with reddenings obtained from the last bin of the extinction-curves built with H-MEAD, $E(B-V)_{\mathrm{H-MEAD}}$, should offer an alternative comparison with a quantity measuring a proxy to the total colour excess along each sightline. This comparison is plotted for for the 63 CBe stars in the left panel of Fig. 8.4. Here one would expect two possible outputs, depending on how the measured reddenings compare with the extinction-curve: (i) $E(B-V)_{\mathrm{H-MEAD}} > E(B-V)_{(\mathrm{S,c})}$, when the CBe star has a bounded extinction-distance measure; (ii) $E(B-V)_{\mathrm{H-MEAD}} \lesssim E(B-V)_{(\mathrm{S,c})}$ for stars with lower limiting extinction-distances. Expectation of point (i), is respected for the 22 stars with bounded extinction-distances. Also point (ii) satisfy the expectations for the stars with lower limiting distances. The 6 stars of Table 6.2, for which I did not measure D_{E}, show indeed the largest separation from the equality line.

The most interesting comparison is obtained for the 9 stars with distances larger than 8 kpc, plotted in yellow. If these stars are actually very distant and supposedly behind most of the interstellar dust, their $E(B-V)_{(\mathrm{S,c})}$ should be consistent with $E(B-V)_{\mathrm{H-MEAD}}$ within the errors: this is verified for 5 of them (# 11, 35, 39, 54, and 55). Object # 50, has a $E(B-V)_{\mathrm{H-MEAD}} > E(B-V)_{(\mathrm{S,c})}$: the star has indeed a bounded extinction-distance. This might be an indication of a somehow shorter distance for the CBe star than what measured. On the other hand, the remaining 3 stars (# 26, 40, and 61) have $E(B-V)_{\mathrm{H-MEAD}} < E(B-V)_{(\mathrm{S,c})}$. Objects # 40 and 61 have extinction-distance curves that asymptote very early, in contrast to what would be expected from the look of the colour-colour diagrams of the stars used by H-MEAD to construct the curve – this was already indicated as a problem in Section 6.6.2. On the other hand, the measured $E(B-V)_{(\mathrm{S,c})}$ for the object # 26 is just about 1σ larger than $E(B-V)_{\mathrm{H-MEAD}}$, so that they can be considered as consistent.

8.3.1.1 Star # 59, a special case

Different considerations apply to star # 59, whose measured $EW(\mathrm{H}\alpha) \approx -144$ Å could be taken to imply a very large disc fraction. If it is truly a CBe star, so bright an Hα emission line would yield a very large downwards correction to the measured interstellar reddening that, in turn, leads to an extreme, but quite implausible, distance estimate (Table 6.2). Fig. 8.4 provides a further strong hint that a CBe classification is not viable, since the corrected extinction turns out to be very far below the maximum Galactic reddening (# 59 is on its own far to the right in the figure). Given also the sky location of this star, sitting on an extinction peak in the (SFD98) dust maps not far from an embedded cluster in the Perseus Arm (Carpenter, Heyer & Snell, 2000), as well as its unusually strong Hα for a CBe star, it seems much more likely that # 59 is actually a young stellar object. If so, its optical spectral energy distribution may include an optically thick accretion component that I do not take into account for. Accordingly, I have excluded it from the various distance plots. The stars # 60 and 61, not far from # 59 on the sky, do not seem to be affected by similar problems and are more likely genuine CBe stars.

8.3.2 Classical Be stars with FLWO/FAST observations

In Fig. 8.5, I plot the measured reddenings of the CBe stars with FLWO/FAST spectra, $E(B-V)_{(\mathrm{P,c})}$, against asymptotic reddenings from SFD98 and RF09. The plotted reddenings are given in Tables 5.5 and 8.2. For these stars the discussion parallels the one on the La Palma sample.

One star is deduced to be at distances larger than 8 kpc (i.e. F281) with $E(B-V)_{\mathrm{SFD98}} > E(B-V)_{(\mathrm{P,c})}$. The MS tracks in the IPHAS colour-colour diagram of Fig. 8.6, which are reddened to the value measured for F281, seem to suggest there are still a few tens of magnitudes of extinction that can be found at distances larger than 8 kpc – several stars are indeed found between these tracks and the one reddened to the corresponding line-of-sight $E(B-V)_{\mathrm{SFD98}}$.

Nine stars happen to have $E(B-V)_{\mathrm{SFD98}} < E(B-V)_{(\mathrm{P,c})}$ (i.e. F228, F229, F238, F246, F259, F263, F265, F326, F340). They seem to suffer with the same problem of objects # 40 and 42, since they are seen in parts of the plane where the temperature map

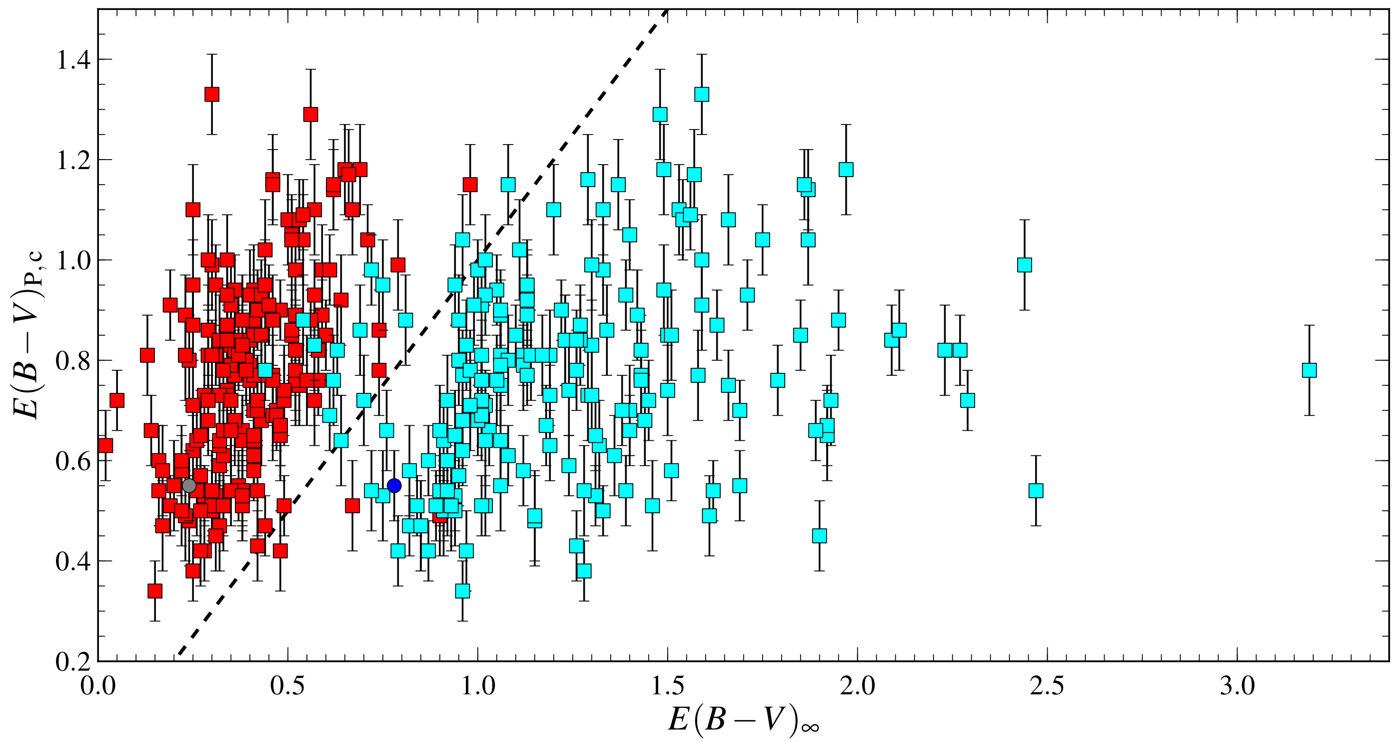

Figure 8.5: Corrected colour excesses for the CBe star with FLWO/FAST spectra, plotted against the corresponding integrated Galactic colour excesses from SFD98 (cyan and blue symbols) and RF09 (red and grey symbols). Blue and grey symbols are used for the star F281 with a measured distance of 8 kpc. The dashed black line is the equality line.

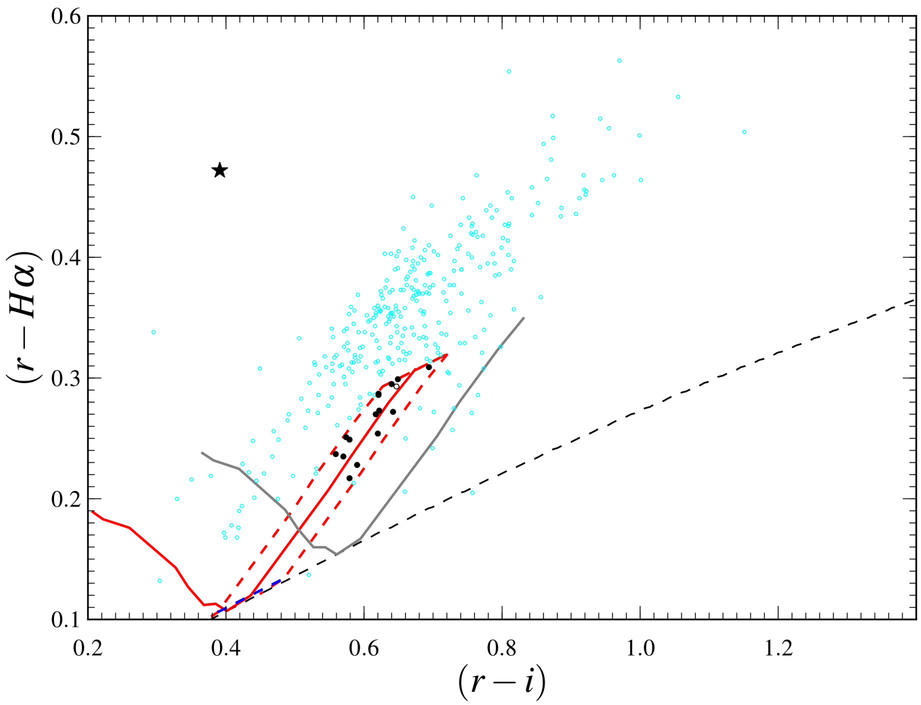

Figure 8.6: The IPHAS colour-colour diagram of stars nearby the CBe star F281. The MS tracks reddened (red curves) at $E(B-V) = 0.55 \pm 0.07$ closely follow the edge of the stellar locus, as the grey MS does (reddened at the $E(B-V)_{\mathrm{SFD98}} = 0.78$. Some stars are still found with $(r-i)$ colours, which imply larger extinction than the value measured for the CBe star.

by SFD98 presents with large hot spots, near the H II regions linked to W3/W4/W5.

Furthermore, I found several stars with $E(B-V)_{\mathrm{SFD98}} > 2$, which are F114, F116, F118, F151, F204, F276, F295, and F346. The ones for which I measure distances (Chapter 9), i.e. F114, F116, F118, and F295, are at closer than ~ 4.6 kpc. The first three are probable members of a cluster, as it will also be discussed in Chapter 9. These stars are seen towards denser parts of the ISM even if their direct sightline is more free of dust.

In the same figure, is the comparison with the asymptotic reddenings that are measured by RF09. These, as discussed for the CBe stars with La Palma sample, are smaller than the measured $E(B-V)_{(\mathrm{P,c})}$ for most of the sightlines and probably describe reddenings typical of Perseus Arm distances. Object F344, for instance, has $E(B-V)_{\mathrm{RF09}}$ that is larger than the reddening measured by SFD98 and the $E(B-V)_{(\mathrm{P,c})}$: the star is projected over W5. In this figure, symbols are generally closer to the equality line, since the reddenings that are measured for the CBe stars with FLWO/FAST spectra are in average smaller (see Chapter 5), suggesting that the stars should be in average found at closer distances than the ones with La Palma spectra.

In conclusion, and not surprisingly, I uncover complexity in the pattern of the sightline reddenings measured from the CBe stars. I note that I never measure a reddening that places the CBe star not sensibly beyond the maximum reddening apparent from the IPHAS colour-colour diagram for its locality. If there is a tendency for data from SFD98 to over-estimate the total sightline extinction, there are also some instances of under-estimation. As SFD98 remarked, the spatial resolution of the temperature map, at low Galactic latitudes, does not resolve the complexity of the Galactic plane. Furthermore their maps were not tested for $|b| < 5°$, so they advised not to entirely trust the reddenings. In the mean, I find that the map of SFD98 provides a viable, if imperfect, description of total extinction in this part of the Galactic Plane.

On the other hand, the impression that one deduce from the RF09 maps is that these are probably a valuable measure for Perseus Arm reddenings, but they cannot be used as an useful comparison for more distant stars, which could be at the extremity of the Galactic stellar disc.

Table 8.1: Measures of DIBs equivalent widths (La Palma sample) and asymptotic reddenings from RF09 and from the last bin of the extinction-distance curves built with H-MEAD. Columns are: star ID number; equivalent widths of DIBs at λ4428 Å, $\lambda\lambda$5580.5 – 5797 Å; RF09 asymptotic reddenings; H-MEAD asymptotic reddenings.

#	$EW(4428)$ Å	$EW(5780.5)$ Å	$EW(5797)$ Å	$E(B-V)_{\rm RF09}$ (mag)	$E(B-V)_{\rm H-MEAD}$ (mag)
1	4.3 ± 0.2	1.7 ± 0.4	0.6 ± 0.1	0.45	1.22
2	0.9 ± 0.1	0.5 ± 0.1	0.3 ± 0.0	0.34	1.12
3	1.9 ± 0.2	0.5 ± 0.2	0.4 ± 0.0	0.74	1.43
4	1.7 ± 0.3	0.5 ± 0.1	0.2 ± 0.1	0.63	1.35
5	2.3 ± 0.2	1.2 ± 0.4	0.4 ± 0.1	0.34	1.14
6	5.0 ± 0.3	1.8 ± 0.4	0.5 ± 0.1	0.48	1.18
7	1.2 ± 0.2	1.0 ± 0.2	0.3 ± 0.0	0.42	1.11
8	2.3 ± 0.3	1.8 ± 0.5	0.3 ± 0.1	0.30	0.99
9	1.5 ± 0.2	1.7 ± 0.5	0.3 ± 0.1	0.62	1.16
10	3.0 ± 0.2	1.2 ± 0.3	0.3 ± 0.0	0.49	1.23
11	3.1 ± 0.2		0.3 ± 0.1	0.38	0.91
12	1.5 ± 0.2	1.1 ± 0.2	0.4 ± 0.0	0.23	0.94
13	1.5 ± 0.2	0.6 ± 0.3	0.3 ± 0.1	0.18	0.82
14	3.7 ± 0.3	2.1 ± 0.5	0.4 ± 0.1	0.34	1.17
15	2.3 ± 0.1	1.2 ± 0.3	0.3 ± 0.1	0.47	1.09
16	2.6 ± 0.2	1.0 ± 0.2	0.3 ± 0.0	0.52	1.10
17	1.9 ± 0.2	1.2 ± 0.2	0.3 ± 0.0	0.61	1.06
18	2.0 ± 0.1	0.8 ± 0.1	0.3 ± 0.0	0.41	1.09
19	2.4 ± 0.3	1.1 ± 0.3	0.2 ± 0.1	0.62	0.93
20	2.1 ± 0.1	0.9 ± 0.2	0.4 ± 0.1	0.71	1.30
21	1.8 ± 0.3	0.9 ± 0.8	0.4 ± 0.1	0.51	1.23
22	1.4 ± 0.2	1.4 ± 0.3	0.4 ± 0.0	0.60	1.02
23	2.1 ± 0.2	1.1 ± 0.2	0.4 ± 0.1	0.42	1.29
24	2.7 ± 0.1	1.3 ± 0.3	0.3 ± 0.1	0.50	1.14
25	1.3 ± 0.1	1.1 ± 0.4	0.1 ± 0.0	0.37	1.23

Table 8.1: Continued

#	$EW(4428)$ Å	$EW(5780.5)$ Å	$EW(5797)$ Å	$E(B-V)_{\mathrm{RF09}}$ (mag)	$E(B-V)_{\mathrm{H-MEAD}}$ (mag)
26	2.3 ± 0.4	1.4 ± 0.3	0.5 ± 0.1	0.37	0.89
27	1.9 ± 0.1	1.0 ± 0.2	0.3 ± 0.1	0.34	0.95
28	1.1 ± 0.2	0.5 ± 0.3	0.2 ± 0.0	0.40	0.84
29	1.5 ± 0.1	0.0 ± 0.3	0.2 ± 0.0	0.42	1.23
30	1.3 ± 0.2	0.5 ± 0.2	0.2 ± 0.0	0.17	0.74
31	3.3 ± 0.1	1.3 ± 0.3	0.5 ± 0.0	0.36	1.21
32	1.5 ± 0.2	0.6 ± 0.1	0.2 ± 0.0	0.31	0.77
33	2.0 ± 0.1	0.8 ± 0.2	0.2 ± 0.0	0.25	0.83
34	1.7 ± 0.2	0.8 ± 0.2	0.2 ± 0.0	0.34	0.83
35	1.8 ± 0.2	1.3 ± 0.2	0.5 ± 0.0	0.18	0.78
36	2.1 ± 0.2	1.4 ± 0.2	0.4 ± 0.1	0.63	1.32
37	1.8 ± 0.1	1.4 ± 0.3	0.3 ± 0.0	0.32	0.98
38	3.5 ± 0.4	1.0 ± 0.3	0.4 ± 0.1	0.54	1.10
39	3.3 ± 0.3		0.3 ± 0.1	0.28	0.84
40	2.3 ± 0.1			0.28	0.81
41	1.4 ± 0.1			0.56	1.29
42	3.0 ± 0.2			0.58	1.27
43	1.7 ± 0.1			0.30	0.62
44	2.2 ± 0.1			0.38	0.93
45	1.9 ± 0.1	0.9 ± 0.1	0.4 ± 0.0	0.60	1.35
46	1.9 ± 0.1			0.46	1.17
47	3.3 ± 0.1			0.74	1.66
48	2.2 ± 0.2			0.41	1.18
49	0.8 ± 0.1			0.26	0.68
50	1.8 ± 0.2			0.39	1.06
51	1.6 ± 0.1			0.39	0.46
52	2.7 ± 0.1			0.29	0.89
53	1.3 ± 0.1			0.70	1.55
54	1.9 ± 0.1			0.45	0.85
55	2.5 ± 0.2			0.38	0.95
56	1.8 ± 0.1			0.68	1.45
57	1.2 ± 0.1			0.51	1.45
58	1.5 ± 0.1			0.32	0.63
59	2.0 ± 0.2			0.29	0.72
60	1.4 ± 0.1			0.35	0.63
61	1.5 ± 0.1			0.30	0.64
62	1.4 ± 0.1			0.31	0.66
63	2.6 ± 0.2			0.68	1.40
64	1.5 ± 0.1			0.48	1.13

Table 8.1: Continued

#	$EW(4428)$ Å	$EW(5780.5)$ Å	$EW(5797)$ Å	$E(B-V)_{\rm RF09}$ (mag)	$E(B-V)_{\rm H-MEAD}$ (mag)
65	2.1 ± 0.2			0.55	1.17
66	1.2 ± 0.1			0.72	1.38
67	1.4 ± 0.2			0.65	1.35
68	2.6 ± 0.2	1.1 ± 0.2	0.3 ± 0.0	0.72	1.16

Table 8.2: Measures of DIBs equivalent widths (FLWO/FAST sample) and asymptotic reddenings from RF09. Columns are: star ID name; equivalent widths of DIBs at λ4428 Å, $\lambda\lambda$5580.5 – 5797 Å; RF09 asymptotic reddenings.

#	$EW(4428)$ Å	$EW(5780.5)$ Å	$EW(5797)$ Å	$E(B-V)_{\rm RF09}$ (mag)
F003	3.5 ± 0.9	1.6 ± 0.3	0.4 ± 0.1	0.3
F004	1.8 ± 0.4	0.8 ± 0.5	0.3 ± 0.1	0.3
F012	2.1 ± 0.1	1.1 ± 0.3	0.3 ± 0.1	0.3
F018	2.6 ± 0.4	0.8 ± 0.3	0.3 ± 0.1	0.5
F024	1.3 ± 0.2		0.3 ± 0.1	0.4
F026	1.4 ± 0.2	0.8 ± 0.3	0.2 ± 0.1	0.4
F027	2.5 ± 0.2	1.4 ± 0.4	0.3 ± 0.0	0.6
F028	2.6 ± 0.5	1.2 ± 0.8	0.3 ± 0.1	0.5
F029	1.1 ± 0.2	0.8 ± 0.3	0.3 ± 0.1	0.3
F033	1.6 ± 0.4	0.5 ± 0.7	0.8 ± 0.1	0.3
F039	1.7 ± 0.2	0.9 ± 0.3	0.3 ± 0.1	0.4
F040	2.0 ± 0.4	1.1 ± 0.4	0.4 ± 0.1	0.2
F041		0.3 ± 0.4	0.2 ± 0.1	0.2
F042	1.7 ± 0.2	1.3 ± 0.6	0.3 ± 0.1	0.4
F044	1.2 ± 0.2	1.1 ± 0.4	0.5 ± 0.1	0.5
F045	1.1 ± 0.3	0.8 ± 0.2	0.2 ± 0.1	0.6
F046	1.8 ± 0.2	1.1 ± 0.3	0.2 ± 0.1	0.4
F047	1.9 ± 0.3	0.7 ± 0.1	0.3 ± 0.1	0.5
F054	0.6 ± 0.1	0.6 ± 0.1	0.3 ± 0.1	0.2
F059	1.1 ± 0.3		0.2 ± 0.1	0.2
F060	1.6 ± 0.3	1.2 ± 0.2	0.3 ± 0.0	0.6
F061	1.2 ± 0.2	1.1 ± 0.3	0.2 ± 0.1	0.7
F066	2.2 ± 0.5	1.6 ± 0.8	0.3 ± 0.1	0.5
F069	1.5 ± 0.2	0.8 ± 0.2	0.3 ± 0.1	0.4
F074	1.1 ± 0.3	2.8 ± 1.3	0.3 ± 0.2	0.4
F075	4.2 ± 0.9	1.3 ± 0.8	0.3 ± 0.1	0.7
F077	1.7 ± 0.2		0.4 ± 0.1	0.4
F079	1.7 ± 0.5		0.4 ± 0.1	0.5

Table 8.2: Continued

#	$EW(4428)$ Å	$EW(5780.5)$ Å	$EW(5797)$ Å	$E(B-V)_{\mathrm{RF09}}$ (mag)
F083	1.7 ± 0.2	0.8 ± 0.2	0.3 ± 0.1	0.5
F085	2.3 ± 0.3	0.9 ± 0.8	0.3 ± 0.2	0.3
F089		3.1 ± 1.4	0.5 ± 0.1	0.3
F092	1.8 ± 0.4	1.8 ± 0.7	0.4 ± 0.1	0.6
F095	0.9 ± 0.1	0.1 ± 0.2	0.2 ± 0.1	0.3
F097	0.8 ± 0.2	3.1 ± 1.5		0.5
F098	1.9 ± 0.2	0.5 ± 0.2	0.3 ± 0.1	0.3
F099	2.4 ± 0.3	1.6 ± 0.7	0.3 ± 0.1	0.4
F100	1.4 ± 0.1	2.4 ± 1.4	0.6 ± 0.2	0.4
F102	0.7 ± 0.2	1.6 ± 0.8	0.1 ± 0.1	0.5
F106	0.8 ± 0.2	0.4 ± 0.3	0.3 ± 0.1	0.4
F107	1.2 ± 0.2	1.2 ± 0.7	0.3 ± 0.1	0.4
F108	1.7 ± 0.3	1.9 ± 0.6	0.2 ± 0.1	0.0
F110	2.1 ± 0.4		0.4 ± 0.1	0.3
F112	2.2 ± 0.4	1.5 ± 0.4	0.2 ± 0.1	0.3
F113	0.6 ± 0.1		0.3 ± 0.1	0.4
F114	1.5 ± 0.2	1.0 ± 0.2	0.3 ± 0.1	0.4
F116	1.6 ± 0.2	1.0 ± 0.3	0.2 ± 0.1	0.1
F118	1.0 ± 0.2	1.1 ± 0.4	0.3 ± 0.1	
F121	2.7 ± 0.3	1.4 ± 0.5	0.2 ± 0.1	0.2
F122	1.4 ± 0.2	1.2 ± 0.4	0.4 ± 0.1	0.4
F124	1.3 ± 0.6	1.8 ± 1.0	0.2 ± 0.1	0.3
F125	1.0 ± 0.2	0.4 ± 0.1	0.2 ± 0.1	0.4
F126	2.4 ± 0.4	0.1 ± 0.4	0.2 ± 0.1	0.4
F129	1.2 ± 0.1	0.1 ± 0.4	0.2 ± 0.1	0.4
F130	2.7 ± 0.7		0.3 ± 0.1	0.3
F131	1.1 ± 0.2	0.1 ± 0.3	0.1 ± 0.0	0.3
F132	1.5 ± 0.5		0.3 ± 0.1	0.4
F134	0.7 ± 0.1	0.3 ± 0.2	0.2 ± 0.1	0.2
F135	1.3 ± 0.3	0.7 ± 0.2	0.2 ± 0.0	0.3
F136	0.7 ± 0.2		0.0 ± 0.0	0.3
F138	1.8 ± 0.5		0.1 ± 0.1	0.3
F139	1.0 ± 0.2	0.8 ± 0.2	0.2 ± 0.1	0.5
F141	1.6 ± 0.3	0.8 ± 1.1	0.2 ± 0.1	0.3
F142	1.1 ± 0.5	0.4 ± 1.6	0.2 ± 0.1	0.4
F144	0.8 ± 0.1	0.5 ± 0.1	0.2 ± 0.0	0.5
F145	1.1 ± 0.2	0.7 ± 0.1	0.2 ± 0.1	0.1
F146	1.9 ± 0.5			0.2
F147	1.5 ± 0.4	0.6 ± 0.8	0.2 ± 0.1	0.2

Table 8.2: Continued

#	$EW(4428)$ Å	$EW(5780.5)$ Å	$EW(5797)$ Å	$E(B-V)_{\mathrm{RF09}}$ (mag)
F151	1.1 ± 0.3	1.1 ± 0.3	0.3 ± 0.1	0.8
F152	1.3 ± 0.1	0.8 ± 0.2	0.1 ± 0.0	0.2
F154	1.7 ± 0.4	1.2 ± 0.2	0.3 ± 0.1	0.3
F157	1.3 ± 0.1	0.5 ± 0.1	0.2 ± 0.0	0.3
F159	1.5 ± 0.4	0.4 ± 0.5	0.2 ± 0.1	0.3
F160	0.7 ± 0.3	1.6 ± 0.7	0.3 ± 0.1	0.3
F161		0.6 ± 0.3	0.3 ± 0.1	0.2
F162	1.7 ± 0.4	1.1 ± 0.4	0.3 ± 0.1	0.4
F163	2.2 ± 0.3	1.3 ± 0.5	0.4 ± 0.1	0.3
F166	1.7 ± 0.2		0.1 ± 0.1	0.5
F167	1.3 ± 0.1	0.7 ± 1.5	0.2 ± 0.0	0.4
F169		0.1 ± 0.1	0.4 ± 0.1	0.2
F170	2.6 ± 0.3	2.2 ± 0.6	0.4 ± 0.1	0.3
F171	1.6 ± 0.4	1.2 ± 0.5	0.2 ± 0.1	0.3
F172	1.6 ± 0.6		0.2 ± 0.1	0.2
F173	1.0 ± 0.3	0.7 ± 0.3	0.3 ± 0.1	0.2
F174	2.2 ± 0.7	1.9 ± 0.8	0.2 ± 0.1	0.2
F175	1.0 ± 0.1	1.3 ± 0.4	0.2 ± 0.0	0.1
F176	0.7 ± 0.2	1.4 ± 0.8	0.1 ± 0.1	0.3
F178	1.0 ± 0.1	1.1 ± 0.5	0.1 ± 0.1	0.3
F179	0.4 ± 0.1	0.5 ± 0.1	0.1 ± 0.1	0.4
F180	2.1 ± 0.4	1.3 ± 0.5	0.3 ± 0.1	0.3
F182		1.4 ± 0.6	0.5 ± 0.1	0.2
F183	1.2 ± 0.3	1.0 ± 0.3	0.3 ± 0.1	0.6
F184	1.8 ± 0.4	1.3 ± 0.5	0.3 ± 0.1	0.3
F185		0.5 ± 0.2	0.4 ± 0.1	0.5
F187	1.4 ± 0.2	0.0 ± 0.5	0.0 ± 0.1	0.2
F188	1.9 ± 0.6	0.8 ± 0.3	0.4 ± 0.1	0.3
F189	1.4 ± 0.6	1.4 ± 0.6	0.3 ± 0.1	0.5
F190	1.4 ± 0.2	0.3 ± 0.2	0.2 ± 0.0	0.2
F192	3.9 ± 0.9	0.1 ± 0.2	0.2 ± 0.1	0.1
F194	0.8 ± 0.2	0.5 ± 0.3	0.3 ± 0.1	0.4
F195	1.2 ± 0.2	1.3 ± 0.6	0.2 ± 0.1	0.6
F196	1.8 ± 0.3	1.2 ± 0.1	0.3 ± 0.1	0.4
F198	0.6 ± 0.2	0.1 ± 0.3	0.2 ± 0.1	0.4
F199	1.7 ± 0.5	1.2 ± 0.1	0.3 ± 0.1	0.7
F200	5.0 ± 0.8	0.7 ± 0.5	0.5 ± 0.1	0.6
F201	1.4 ± 0.1	0.6 ± 0.1	0.3 ± 0.1	0.3
F202	1.9 ± 0.3	1.0 ± 0.4	0.2 ± 0.1	0.5

Table 8.2: Continued

#	$EW(4428)$ Å	$EW(5780.5)$ Å	$EW(5797)$ Å	$E(B-V)_{\rm RF09}$ (mag)
F203	2.1 ± 0.9		0.5 ± 0.2	0.5
F204		0.7 ± 0.1	0.1 ± 0.1	0.7
F205	0.8 ± 0.2	0.9 ± 0.1	0.3 ± 0.1	0.3
F209	1.3 ± 0.4		0.3 ± 0.1	0.3
F211	1.2 ± 0.4	1.5 ± 0.8	0.1 ± 0.1	0.4
F212	1.3 ± 0.6		0.2 ± 0.1	0.5
F213	1.2 ± 0.4	0.9 ± 0.7	0.2 ± 0.1	0.5
F216	1.0 ± 0.7	2.1 ± 1.0	0.3 ± 0.1	0.4
F219	2.5 ± 0.4	0.4 ± 0.7	0.3 ± 0.1	0.3
F220	0.8 ± 0.4	1.5 ± 0.6	0.2 ± 0.1	0.4
F221	0.3 ± 0.1	1.0 ± 0.4	0.1 ± 0.1	0.3
F222	1.0 ± 0.3	1.6 ± 0.7	0.2 ± 0.1	0.2
F223			0.1 ± 0.1	0.4
F224	1.4 ± 0.3	1.2 ± 0.4	0.3 ± 0.1	0.4
F228	1.0 ± 0.2	1.7 ± 0.8	0.2 ± 0.1	0.6
F229	0.8 ± 0.6		0.1 ± 0.1	0.5
F232		1.0 ± 0.4	0.3 ± 0.1	0.4
F237	3.3 ± 0.8	2.9 ± 1.2	0.2 ± 0.1	0.6
F238	1.1 ± 0.2	0.7 ± 0.1	0.1 ± 0.1	0.4
F243	0.7 ± 0.3		0.3 ± 0.1	0.5
F245	3.0 ± 0.4	0.9 ± 0.1	0.3 ± 0.1	0.5
F246	0.8 ± 0.3	1.9 ± 0.7	0.2 ± 0.1	0.5
F247	1.5 ± 0.3	1.6 ± 0.4	0.5 ± 0.1	0.5
F248	1.2 ± 0.6	1.7 ± 1.0	0.2 ± 0.1	0.5
F254	1.1 ± 0.5	5.5 ± 5.2	0.1 ± 0.1	0.6
F256	1.9 ± 0.8	0.6 ± 0.2	0.3 ± 0.1	0.4
F259	2.6 ± 1.1	3.5 ± 1.5	0.8 ± 0.2	0.5
F261	0.7 ± 0.5		0.3 ± 0.1	0.4
F263	1.9 ± 0.6	0.7 ± 0.4	0.6 ± 0.1	0.4
F264	1.1 ± 0.3	0.4 ± 0.5	0.1 ± 0.1	0.3
F265	2.1 ± 0.4	0.2 ± 0.6	0.2 ± 0.1	0.4
F266	2.0 ± 0.6	1.1 ± 0.5	0.2 ± 0.1	0.6
F269	0.7 ± 0.2		0.3 ± 0.1	0.3
F276	1.5 ± 0.7	1.0 ± 1.3	0.2 ± 0.1	0.5
F278	0.9 ± 0.6	2.3 ± 1.1	0.4 ± 0.1	0.3
F281	1.2 ± 0.7	1.2 ± 0.6	0.3 ± 0.1	0.2
F286	2.9 ± 0.9			0.4
F289	1.9 ± 0.5		0.1 ± 0.1	0.2
F290	1.9 ± 0.4	1.0 ± 0.4	0.1 ± 0.1	0.3

Table 8.2: Continued

#	$EW(4428)$ Å	$EW(5780.5)$ Å	$EW(5797)$ Å	$E(B-V)_{\rm RF09}$ (mag)
F291	2.0 ± 0.3	0.3 ± 0.7	0.2 ± 0.1	0.3
F292	1.2 ± 0.3	0.3 ± 0.3	0.2 ± 0.1	0.4
F293	2.5 ± 0.4	1.4 ± 0.5	0.3 ± 0.1	0.6
F295	1.7 ± 0.4		0.5 ± 0.1	0.3
F297	1.6 ± 0.2	1.1 ± 0.4	0.2 ± 0.1	0.2
F298	1.7 ± 0.5	1.2 ± 0.7	0.4 ± 0.1	0.3
F299	1.1 ± 0.2	0.5 ± 0.2	0.2 ± 0.1	0.5
F301	1.6 ± 0.5			0.2
F302	1.8 ± 0.3	1.0 ± 0.6	0.2 ± 0.1	0.5
F303	1.6 ± 0.7	1.9 ± 0.7	0.4 ± 0.1	0.6
F304	1.3 ± 0.1	1.1 ± 0.3	0.3 ± 0.1	0.3
F312	0.4 ± 0.2		0.2 ± 0.2	0.7
F314	1.3 ± 0.4	1.2 ± 0.8	0.3 ± 0.1	0.3
F315	1.1 ± 0.1	0.8 ± 0.3	0.2 ± 0.0	0.4
F317	0.8 ± 0.5	0.7 ± 0.2	0.3 ± 0.1	0.4
F326	2.3 ± 0.5	0.9 ± 0.4	0.5 ± 0.1	0.4
F329	2.0 ± 0.9	1.2 ± 0.2	0.3 ± 0.1	0.3
F332	1.4 ± 0.5	0.1 ± 0.1		0.4
F334	0.6 ± 0.3	1.1 ± 0.6	0.3 ± 0.1	0.9
F337	1.6 ± 0.3	0.8 ± 0.4	0.4 ± 0.1	0.5
F340	1.6 ± 0.3		0.2 ± 0.1	0.4
F343	1.1 ± 0.3		0.1 ± 0.1	0.3
F346	2.3 ± 0.7	2.6 ± 1.2	0.2 ± 0.1	0.7
F349	2.4 ± 0.5	0.6 ± 0.4	0.3 ± 0.1	0.6
F350	1.8 ± 0.2	0.8 ± 0.4	0.2 ± 0.1	0.5
F352	3.2 ± 0.3	1.2 ± 0.4	0.3 ± 0.1	0.6
F353	3.4 ± 0.4	2.1 ± 0.5	0.4 ± 0.1	0.7
F354	1.2 ± 0.4	1.1 ± 0.4	0.5 ± 0.1	0.5
F355	2.0 ± 0.4		0.4 ± 0.1	0.5
F356	1.9 ± 0.4	1.5 ± 0.8	0.3 ± 0.1	0.4
F359	2.7 ± 0.6		0.2 ± 0.1	0.6
F360	1.6 ± 0.4	1.4 ± 0.5	0.3 ± 0.1	0.6
F362	1.6 ± 0.6	2.5 ± 0.6	0.5 ± 0.1	1.0
F363	2.6 ± 1.0	2.4 ± 1.4	0.2 ± 0.2	0.3
F367	1.9 ± 0.6	0.8 ± 0.6	0.2 ± 0.1	0.3
F369	1.2 ± 0.9			0.7

Chapter 9

Discussion and conclusions

9.1 Constraints on widening the CBe sample for mapping the space distance

In Chapter 6, an IPHAS photometric method was applied to the higher quality spectroscopic data, obtained in La Palma, in order to place constraints on the luminosity classes of 63 CBe stars and to select the most appropriate spectroscopic parallax estimates. The procedure of Section 6.3 can be extended to the larger sample of CBe stars of Chapter 2, and include the 4 CBe stars that were excluded from the discussion in Chapter 6, because they only possess NOT/ALFOSC spectra not covering the Hα region. Setting aside the stars that also have better quality La Palma spectra, the number of FLWO/FAST CBe stars is 181.

It must be noted that 60% of the CBe stars within the sample of FLWO/FAST spectra have more approximate spectral type determinations (due to lower S/N ratio on average), when compared to the La Palma sample. It was shown in Section 2.5, that down to a S/N of ~ 25, the spectral type can be determined with a typical accuracy of $\pm$1-2 subtypes, at the 6 Å resolution of the FLWO/FAST spectra. The spectral type becomes very uncertain for the poorer quality spectra, which I classify only as early, mid, and late-B types. The quality of the estimated spectral type generally anti-correlates with the r magnitude and is strongly controlled by the slope of the stellar continuum, or in other words by the amount of reddening (interstellar plus circumstellar colour excess). The number of spectra with poorer spectral typing amounts to $\sim 45\%$ of the total number of CBe stars identified in this thesis (109 out of 248 objects).

Spectroscopic parallaxes of the 4 La Palma CBe stars with only NOT/ALFOSC spectra and of the 72 objects with FLWO/FAST spectra with S/N ratio $\gtrsim 25$ are given in Table 9.4 and Table 9.5. The errors I report along with the distance are derived from the photometric, reddening and absolute magnitude uncertainties only and do not include the contribution coming from the spectral-type uncertainty. These are reported separately in the last three columns of Table 9.5, as I did for the 63 CBe stars studied in Chapter 6.

The luminosity class of these 72 FLWO/FAST CBe stars is inferred from the compari-

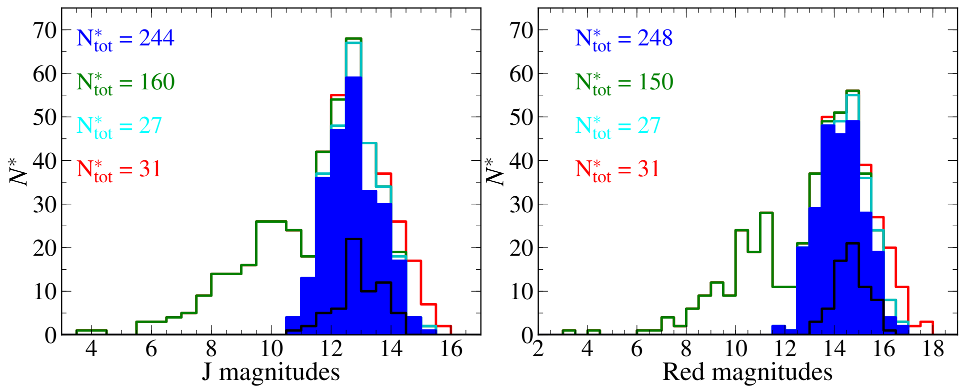

Figure 9.1: Distribution of the 2MASS *J*-magnitudes, on the left, and red magnitudes (IPHAS and USNO-B1.0, Monet et al., 2003, as a proxy, when available), on the right, for: i) the CBe stars studied in this thesis (blue filled histograms); ii) FLWO/FAST spectra, which have a *featureless* continuum but are likely candidate CBe stars (cyan step-histograms); iii) Witham et al. (2008) candidate CBe stars (red step-histograms); candidate CBe in Kohoutek & Wehmeyer (1999) and the CBe stars in the BeSS database by Neiner et al. (2011) (green step-histograms). Each histogram bar represents the total number of CBe stars and candidate CBe stars in the corresponding magnitude bin. Finally, the black step histogram shows the distribution of the 63 CBe stars observed in La Palma.

son with the A/F star MS fit, in the IPHAS colour-magnitude diagram, following the same procedure used in Section 6.3 for the La Palma CBe stars. Considering all the 139 CBe stars (i.e. 63 with La Palma spectra and 72 with FLWO/FAST spectra), the luminosity class assignment favours dwarfs (71%) against sub-giants (18%) and giants (11%). This stronger bias towards class V contrasts with the Zorec & Briot (1997) view of field CBe stars as being more equally distributed within luminosity classes (57%, 24%, and 19% respectively). This may in part be due to the faint range of magnitudes covered by this work, relative to those that so far have been discussed in the literature. Or, conversely, it may reflect the rather brighter magnitudes of the objects with higher quality FLWO/FAST observations that may preferentially be located in the Perseus Arm.

I will not repeat the examination of the combined samples, as it was done for the 63 La Palma CBe stars in Chapter 6, because of the bias to brighter stars it could introduce, and also because of somewhat larger typical errors.

9.2 Comparison with previously known CBe stars

To place the 248 CBe stars studied in this work in relation to previously known ones, brighter examples in the area of sky I have studied, it is instructive to compare their combined magnitude distribution.

In left panel of Fig. 9.1, I show the histogram distribution of 2MASS J-magnitudes of the observed CBe stars, along with confirmed and candidate CBe stars from other cata-

Table 9.1: Table summarising the cross-match between different catalogues. Each number represents the overlaps between: the CBe stars studied in this work; the candidate CBe stars with *featureless* FLWO/FAST spectra; candidate CBe stars in Witham et al. (2008), W08; candidate and confirmed CBe stars in Kohoutek & Wehmeyer (1999), KW99; and the CBe stars in the BeSS database.

	This Work	Featureless	W08	KW99	BeSS
This Work	248				
Featureless	14	81			
W08	205	42	261		
KW99	6	1	5	148	
BeSS	2	0	2	45	64

logues (Kohoutek & Wehmeyer, 1999; Neiner et al., 2011) and the candidate CBe stars that can be identified among the unobserved point-source emitters in the Witham et al. (2008) catalogue. As a reminder, I consider here candidate CBe stars only the objects presenting with $(J-H) \leq 0.6$ and their $(H-K)$ colours within the boxes defined in the IR colour-colour diagram (see Fig.9.2(b)). In this figure, I also include some of the *featureless* objects of Section 2.4, for which I could not assess the spectral type but that have near-IR colours typical of candidate CBe stars. The total number of known CBe stars in this part of the Galactic plane amounts to 469 although, in Fig. 9.1, I did not plot 3 stars from the BeSS database (Neiner et al., 2011) for which I could not find 2MASS photometry, they probably are too bright. Each histogram bar of Fig. 9.1 represents the total number of stars in the corresponding magnitude bin, so that the deficit of stars seen for $J \approx 11$ is a real feature of the sample. This apparent lack of stars might be due to the combined incompleteness of the Witham et al. (2008) and Kohoutek & Wehmeyer (1999), whose bright and faint limits meet in this proximity. Another option is that the magnitude distribution picks out an over-density of CBe stars, which might be associated to the Perseus Arm. However, this hypothesis cannot yet be examined due to the fact that the completeness of the sample is presently unknown.

Since a certain number of matches is found between the considered catalogues, I summarise them in Table 9.1. The choice of plotting a star as belonging to one or the other catalogue, in Fig. 9.1, relies on whether the object is a confirmed CBe star or only a candidate CBe star. Priority is given to the stars with better typing, i.e. the ones in this work, than to the stars with spectral types given in the BeSS database and in the Kohoutek & Wehmeyer (1999) catalogue, followed by stars with *featureless* spectra and by the candidate CBe stars identified among the Kohoutek & Wehmeyer (1999) and Witham et al. (2008) catalogues. Interestingly, the 2 CBe stars within the BeSS catalogue that match with the ones studied in this work have not been allocated subtypes before.

The vast majority of previously known CBe stars in the area are found at brighter magnitudes with respect to the sample of CBe stars studied here. The typical V magnitudes of these stars are in the range of 10–11 mags, and their 2MASS colours suggest lower reddenings, with an $A_V \lesssim 2$ (see e.g. filled and empty green circles in Fig. 9.2(b)). Considering the median observed magnitude, these CBe stars must be at distances closer than or at most at the distant edge of the Perseus Arm – a B3V star, with $r = 10.5$, would be seen a distance of 1.3 kpc for $A_V = 2$, while a B3III star would be further away, at almost 3 kpc. In contrast, a B8V or B8III star would be seen in the range of distances between 0.5 – 1 kpc away.

In conclusion, the majority of new CBe stars studied here extend the range of distances of such a class objects and doubles their number in this part of the Galaxy. The observed red magnitudes (R $\sim$ 16 – 18) and colours of the remaining candidate CBe stars, mainly from the Witham et al. (2008) catalogue, suggest that some more stars would mainly be at larger distances, in the region of around 6 kpc. At least five of them have fainter red magnitudes than the studied stars and many are picked in the range of $r \approx 16$ (right panel Fig. 9.1).

However, the adopted near-IR criterion, which reduces contamination of the sample from other classes of objects, limits it in a way that more reddened CBe stars might be excluded.

9.3 Association with known clusters

Having such a large number of candidate CBe stars, it would seem opportune to search for possible members of known young open clusters. Forty-eight clusters from the Dias et al. (2002) fall within the surveyed area, although just 25 of them are younger than 100 Myr – in which CBe stars are likely to reside Fabregat & Torrejón (2000). However, cross matching the 248 CBe stars here considered with the clusters gives only 8 matches within 2 cluster radii. The matching clusters are listed in the left hand side of Table 9.2, while the matched stars are listed in the right hand side of Table 9.2. The clusters are:

- **NGC 637:** Object F108 matches both the cluster's reddening and distance.
- **NGC 663:** Three stars are found within the cluster's radius. Object F114, F116, and F118 have also been observed by Mathew & Subramaniam (2011), with a spectral resolution of 10 Å at the Hβ, typing them as B2V, B5V, and B5-7V respectively. The spectral types given by the authors agree only with the one I determine for F114, for which I find agreement also between the measured reddening and distance with cluster's values. The spectral types I measure for F116 and F118 are B4V and B3V respectively, which put their spectroscopic parallaxes in excess of $\sim 1 - 2.5$ kpc with respect to the cluster distance. Adopting the spectral types from Mathew & Subramaniam (2011), only F118 would be reconciled with the cluster distance, while F116 would still be found at $\sim$ 3.5 kpc. This star has a lower reddening, but still compatible with the one measured for NGC 663. This remaining discrepancy may indicate both a problem with the assigned spectral type (too early) and reddening (too low) in this case.
- **Teutsch 162:** Object F295 presents with an interstellar reddening in agreement with the cluster value, although its distance is larger. The distance I determine from the

Table 9.2: On the left side, is the list of clusters from Dias et al. (2002) within the surveyed area, matching the CBe stars presented here. Columns are: cluster ID name; Galactic coordinates; distance; reddening; cluster diameter in arcmin (from Dias et al., 2002); age; references from which distances, reddenings and ages are taken. On the right side, are the cross-matched stars. Columns are: Object ID name; Galactic coordinates, spectroscopic distance; interstellar reddening; angular separation from the cluster centre in arcmin. The double line separates clusters with sensible matches among the 248 CBe stars, from the clusters whose matching CBe stars seem to be background objects.

Clusters' parameters								Stars						
Cluster	ℓ (deg)	b (deg)	D (kpc)	$E(B-V)$ (mag)	θ'	$\log t$ (Myr)	Ref.	Obj.	ℓ (deg)	b (deg)	A/F fit (kpc)	D (kpc)	$E(B-V)$ (mag)	s'
NGC637	128.55	1.73	2.5 ± 0.2	0.64 ± 0.05	3	7.0	(2)	F108	128.58	1.72	2.0	2.5 ± 0.3	0.63 ± 0.07	2
NGC 663	129.47	-0.94	2.4 ± 0.1	0.80 ± 0.15	14	7.4	(3)	F114	129.41	-0.97	2.5	2.6 ± 1.0	0.86 ± 0.07	4
								F116	129.45	-0.93	2.0	5.1 ± 1.0	0.70 ± 0.07	1
								F118	129.51	-0.99	3.0	3.5 ± 1.0	0.85 ± 0.07	4
Teutsch 162	136.13	2.12	2.0 ± 0.5	0.51 ± 0.16	9	7.0	(6)	F295	136.15	2.07	3.7	3.7 ± 0.9	0.56 ± 0.07	3
King 16	122.09	1.33	1.9 ± 0.8	0.89 ± 0.10	17	7.0	(1)	6	122.26	1.16	7.0	7.7 ± 1.9	1.34 ± 0.10	14
Stock 5	130.71	2.67	1.1 ± 0.1	0.40 ± 0.03	24	7.7	(4)	F173	130.65	2.75	4.5	4.6 ± 1.3	0.57 ± 0.07	6
								F175	130.92	2.47	3.7	5.8 ± 1.9	0.69 ± 0.07	17

References:
(1) Maciejewski & Niedzielski (2007); (2) Yadav et al. (2008); (3) Pandey et al. (2005);
(4) Kharchenko et al. (2005); (5) Camargo, Bonatto & Bica (2009); (6) Bonatto & Bica (2010).

A/F fit, gives a larger distance for the neighbouring MS stars. No other observations are available in the literature that point to a different spectral typing and the data presented by Bonatto & Bica (2010), for this cluster, are tagged as lower quality data by the authors. Therefore, the discrepancy between the measured distance for F295 and the one available in the literature for this cluster suggests more investigation is needed.

- **King 16:** Object # 6 exhibits a noticeably larger interstellar reddening than the one measured for the cluster and it is seen quite far away from the cluster centre. It is therefore likely to be a background star.

- **Stock 5:** Objects F173 and F175 present with reddenings that are also larger than that measured for the cluster, and their distances are larger. Due also to the large angular separation from the cluster centre and the larger A/F fit distances, they too can be background stars.

The interesting result, coming from these cross-matches, is the comparison between the cluster distance and the distances obtained via the A/F fit. For NGC 637 and NGC 663, where I find CBe stars belonging to the cluster, the measured A/F fit distances are closely comparable with the cluster distance. This validate the use of the fits to constrain the luminosity class of CBe stars, when enough neighbouring MS stars are found. In the case of Teutsch 162, where the A/F fit does not coincide with the cluster distance, the proposition is that latter could be subject to revision also taking into account the fact that Bonatto & Bica (2010) consider the data in their possession to be of poorer quality.

A research line that has not been explored in the present thesis, is the discovery and study of previously unknown or not well defined clusters (as for instance Teutsch 162), which may host several of the CBe stars studied here.

9.4 Most distant CBe stars in the Milky Way

The majority of the 248 CBe stars, studied in this work, are observed between 2 and 8 kpc. Previously known Galactic CBe stars are found mainly at nearby distances (only 35 CBe stars out of ~ 700 listed in the whole BeSS catalogue, with known distances, are more distant than 2.5 kpc). Otherwise, the most distant known CBe are indeed observed in the Magellanic Clouds (e.g. Martayan et al., 2007), since the corresponding Galactic sightlines are much less obscured.

I found 10 stars ($\sim 4\%$ of the studied sample) at distances larger than 8 kpc (see Table 9.3). Their distance is measured with an accuracy better than 30%, which still places them at distances larger or at least within the putative Outer Arm at ~ 6 kpc (Negueruela & Marco, 2003; Russeil, Adami & Georgelin, 2007; Reid et al., 2009a). Their sightlines are emptier of dust, with $E(B-V)_{\mathrm{SFD98}} \lesssim 1.4$, allowing a deeper exploration of the Galactic disc. Six of these stars are seen at Galactic locations near but higher in Galactic latitude than the W4/W5 H II regions ($134^{\circ} \lesssim \ell \lesssim 136^{\circ}$ and $b \sim 1^{\circ}$). All the 10 stars stars are

Table 9.3: Properties of the 10 CBe stars more distant than 8 kpc. Columns are: object's ID;, Galactic coordinates; observed r magnitude corrected for circumstellar disc emission; interstellar extinction in the r-band; distance and relative distance error; SFD98 asymptotic colour excess.

#	SpT	ℓ (deg)	b (deg)	$r+\Delta r$ (mag)	A_r (mag)	D (kpc)	$E(B-V)_{\mathrm{SFD98}}$ (mag)
11	B2-3	123.29	0.23	14.95	2.23	9.2 ± 3.0	1.07
26	B3	127.30	2.36	15.36	2.53	9.9 ± 2.8	1.37
35	B2-3	130.30	2.08	15.06	2.12	10.4 ± 3.3	1.09
39	B4	132.86	1.81	15.75	2.08	11.6 ± 3.0	0.93
40	B2	133.79	2.35	14.31	2.58	10.5 ± 3.2	0.32
F281	B3	135.11	3.17	14.22	1.39	8.0 ± 2.2	0.78
50	B3	135.89	1.30	15.75	2.33	11.1 ± 3.1	1.26
54	B3	136.15	1.70	15.60	2.05	11.1 ± 3.0	1.12
55	B3-4	136.17	1.32	15.97	2.48	10.3 ± 2.6	1.22
61	B3-4	136.50	2.26	15.32	1.95	9.5 ± 2.4	1.24

seen above the Galactic equator, more precisely all for $b > 1°$, but one (# 11) is found at $b \approx 0.2°$.

Since in this part of the sky, the warp of the stellar disc, as seen from the red giant branch stars in 2MASS (Momany et al., 2006), is comprised between $b \sim 1°$, at heliocentric distance of ~ 7.3 kpc, and $b \sim 1.6°$ at ~ 16 kpc, one would naturally expect that these stars are seen in densest parts of the Galactic plane, and their Galactic latitudes must be consistent with the warp. I estimated the approximate distances from the warped midplane, which are in the range of $|z| \approx 0.2 – 0.4$ kpc. These correspond to several scale heights of the young disc (e.g. 50 pc, in Sale et al., 2010).

The question, whether these stars formed at those latitudes or not, should be investigated.

9.5 Final remarks

In this work, I have tested the possibility of using the CBe stars as tracers of the Milky Way structure. Considering that the idea has never been put into practice before, this study represents a worked-example of a new usage for this particular class of objects. Because I concluded that, at the present level of noise affecting the data, it is hard to disentangle the signature of spiral arms from the Galactic background, I analysed what is needed for improving the results. It became evident, in Section 6.7.2, that if one wants to reduce the level of ambiguity resulting from the comparison between a distribution of (i) stars located within the spiral arms or (ii) following the density profile of A-stars in the Galactic disc, there are two possible solutions. These are either to increase the sample size or to reduce dramatically the distance uncertainties. In the ideal case, both improvements should be achieved. The inclusion of the CBe stars that were identified in Chapter 2 would quadruple the sample size, relative to the La Palma sample of 63. Unfortunately, as noted in Section 9.1, the enlarged sample would be accompanied by larger errors and a bias to brighter magnitudes.

To build a more compelling sample, one option is to try a selection of stars based on sensible colour or other cuts in order to achieve a clearly volume limited selection. For instance, the obscuring effect of the column of dust along a given line-of-sight can affect the sample selection, by limiting the exploration of the volume of space. Hence, a cut based on the line-of-sight asymptotic reddening would exclude most reddened sightlines, giving only a shorter view. It was shown in the previous section, that the most distant CBe stars are seen along sightlines with $E(B-V)_{\mathrm{SFD98}} \leq 1.4$, which means that those sightlines can be explored up to the edges of the Galactic disc. Supposing the cut is applied to the larger sample, 168 among the observed stars present with $E(B-V)_{\mathrm{SFD98}} \leq 1.4$.

In alternative to this, if one wanted to build up a photometric sample, targeting an averagely younger population of early B-type CBe stars, an $(r-\mathrm{H}\alpha)$ cut (see e.g. the $EW(\mathrm{H}\alpha) \leq -15$ Å line in Fig. 9.2(a)) could be expected to favour selection of early-B types on the basis of larger discs surrounding these spectral types (cf. Tycner et al., 2005). Such a choice would look more favourable for studies of the spiral structure of the Galaxy. However, in the present sample this is not confirmed, since very numerous mid and late-B type stars are found with $EW(\mathrm{H}\alpha) \leq -15$ Å (Fig. 9.3). This rules out a clean spectral-type selection from just IPHAS photometric data.

The adoption of one or the other selection cuts could be tested on the larger sample made of 248 CBe stars but, even if applied to the reduced sample of 139 CBe stars with more precise spectral typing, the size of the resulting sample is comparable to the existing La Palma CBe sample.

Samples created from the above mentioned cuts, could be designed just from photometric data. Yet the role of follow-up spectroscopy cannot be minimised, due to the need of precise typing of the targeted stars. It can be redefined, if larger spectral coverage is reached with the available optical broad-band photometry offered by UVEX or VPHAS+ (Drew et al, in prep) in the north and south respectively, in combination with similarly designed surveys in the near-IR, as for instance UKIDS GPS in the north (Lucas et al., 2008), which unfortunately does not cover the entire area surveyed in this thesis, or VVV (Minniti et al., 2010) in the south. Interstellar reddenings can be assessed from the photometry only, while follow-up spectroscopy with higher resolution and S/N ratio could be obtained for a more accurate typing. Also the selection of targets can be improved, with use of the more precise near-IR photometry.

However, as a legacy of the present work a very large number of new CBe stars have been identified, which doubles the sample of previously known CBe stars in the area and that are found at larger distances. The consequences of a rapid low-resolution and low S/N ratio follow-up are highlighted by the resulting larger errors in the measure of spectroscopic parallaxes, but it is now the case that there is a sample of 248 stars over 100 deg^2 that can be built on through further spectroscopy. Finally, the identification of these stars also comes with an added value, in the form of reliable determination of interstellar reddenings. Good measures of extinctions are indeed necessary to estimate absolute magnitudes,

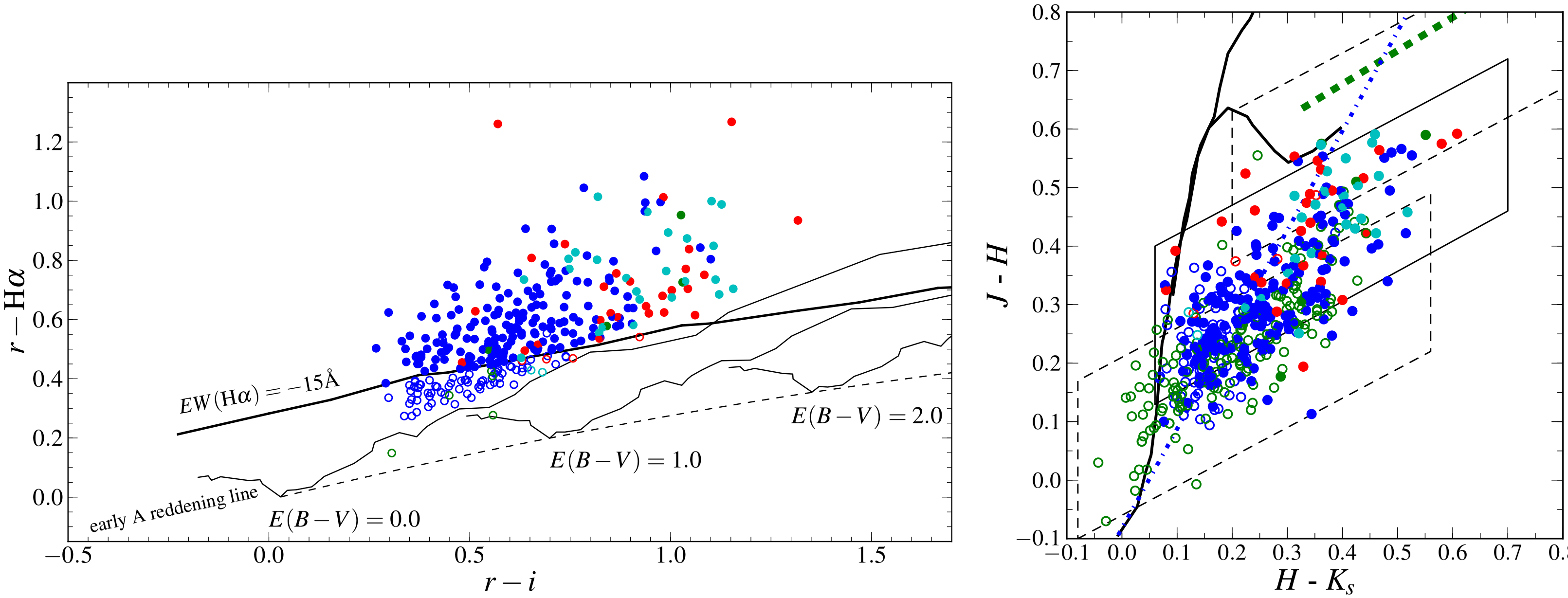

(a) (b)

Figure 9.2: Figure (a) shows the IPHAS colour-colour diagram, for 315 out of the 469 CBe stars and candidate CBe stars in the surveyed area. Main sequence colours, reddened at $E(B-V)=0$, 1, 2 are plotted. The solid black line marks the limiting colours for $EW(\mathrm{H}\alpha)=-15$. Filled circles are used for stars with $EW(\mathrm{H}\alpha)\leq-15$ and $E(B-V)_{\mathrm{SFD98}}\leq1.5$. Colours code: (black) (i) the 139 CBe stars studied here; (blue) the other 109 CBe stars with noisier FLWO/FAST spectra; (green) the stars Kohoutek & Wehmeyer (1999) and Neiner et al. (2011) catalogues; (cyan) candidate CBe stars with *featureless* FLWO/FAST spectra; (red) Witham et al. (2008) candidate CBe stars. Figure (b) shows the 2MASS colour-colour diagram. The colour scheme is the same as in figure (a). Out of the 469 CBe stars in the area, only 3 Neiner et al. (2011) CBe stars do not have 2MASS colours. The three boxes are the regions where CBe stars with $A_V=2$, 4, 6 are found (cf. Corradi et al., 2008)

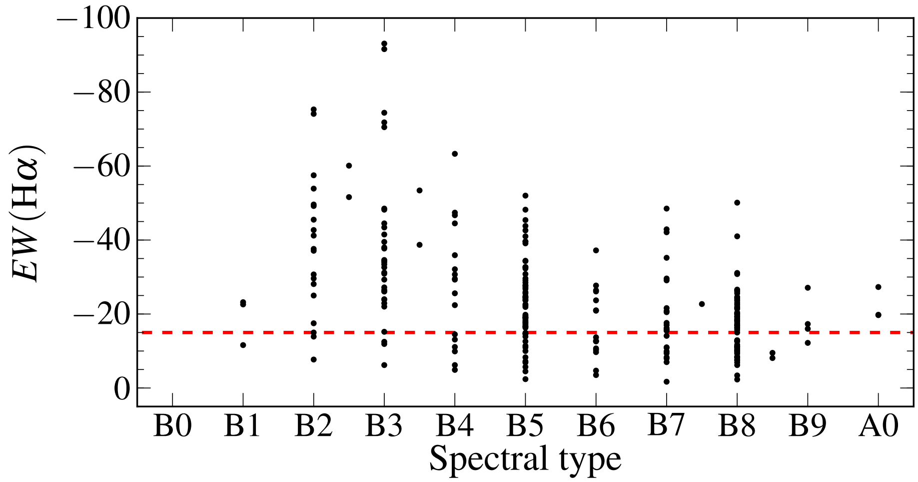

Figure 9.3: The distribution of measured $EW(\mathrm{H}\alpha)$ is plotted against spectral types, for the 248 CBe stars in the sample. The dashed red line cuts at $EW(\mathrm{H}\alpha) = -15$ Å. 175 stars in the sample have $EW(\mathrm{H}\alpha) \leq -15$.

once trigonometric parallaxes will be available from GAIA. In the meanwhile, such a large database prepares the ground for other studies regarding CBe stars in more general Galactic structure studies, due to their valuable use as probes of the Galactic disc over many kiloparsecs. A straightforward use of the reddenings will comes from a more intensive use of extinction-distance curves determined with H-MEAD. This is possible, since the larger spectral-type uncertainty of the CBe stars with FLWO/FAST spectra with S/N ratio < 25 does not influence distance measurement via comparison with the extinction-distance curves.

Finally, there are two open problems regarding CBe stars that could be addressed to, in future:

- Testing the validity of the scaling relation, $f_D \propto EW(\mathrm{H}\alpha)$, on samples including later-B type stars. Its application to correct reddenings measured at wavelengths different than the canonical *B–V* range remains to be gauged also, with the use of wider wavelength coverage up to the Paschen Jump, possibly.

- The spectral type distribution continues to be debated. The inclusion of fainter CBe stars, spread over a larger fraction of the Galactic plane, will offer a fuller view of the subject.

The follow-up search of unidentified distant open clusters will take advantage from the discovery of these new CBe stars too. And, finally, the reduction of the distance uncertainties is probably the most important goal, if the spatial distribution is to be clarified. In future, with GAIA, it will be possible to reach a precision as high as 5% on the measure of distances for stars within the explored range of magnitudes ($13 \leq r \leq 17$), although only with the end-mission data-releases ($\sim$ 10 yr time, de Bruijne, 2012).

Table 9.4: Spectroscopic parallaxes of the 4 CBe stars with NOT/ALFOSC spectra, for which the scaling of the circumstellar disc emission was computed from the measure of $EW(\mathrm{H}\alpha)_{\mathrm{P}}$. Columns list: ID number; spectral type; Galactic coordinates; the observed r magnitude corrected for circumstellar disc emission; A_r, computed from $E(B-V)_{(\mathrm{P,c})}$; A/F fit approximate distances; spectro-photometric distances for luminosity classes V, IV and and III: in bold-face are distances that are associated to the preferred luminosity class; preferred luminosity class; extinction distances; the three last columns give the distance errors arising from the spectral type uncertainty.

#	SpT	ℓ (deg)	b (deg)	$r+\delta r$ (mag)	A_r (mag)	A/F fit (kpc)	Distances $D_{\mathrm{SP,V}}$ (kpc)	$D_{\mathrm{SP,IV}}$ (kpc)	$D_{\mathrm{SP,III}}$ (kpc)	Likely Class	Error on distances due to SpT $\sigma D_{\mathrm{SP,V}}$ (kpc)	$\sigma D_{\mathrm{SP,IV}}$ (kpc)	$\sigma D_{\mathrm{SP,III}}$ (kpc)
43	B6	134.99	2.72	15.89 ± 0.04	1.87	7.3	$\mathbf{7.5\pm0.9}$	9.1 ± 1.2	15.0 ± 4.0	V	1.0	1.5	2.5
48	B8	135.50	0.65	16.86 ± 0.04	2.86	3.7	$\mathbf{5.7\pm0.8}$	7.2 ± 1.1	11.4 ± 2.8	V	0.9	0.9	1.8
57	B7-8	136.34	0.06	14.71 ± 0.04	2.76	1.8	$\mathbf{2.4\pm0.3}$	2.9 ± 0.4	4.8 ± 1.2	V	0.3	0.4	0.7
64	B7	137.43	1.49	14.57 ± 0.03	2.12	3.2	$\mathbf{3.2\pm0.4}$	3.9 ± 0.5	6.4 ± 1.5	V	0.4	0.4	0.9

Table 9.5: Spectroscopic parallaxes of the 72 CBe stars with FLWO/FAST spectra. Columns list: ID number; spectral type; Galactic coordinates; the observed r magnitude corrected for circumstellar disc emission; A_r, computed from $E(B-V)_{(\mathrm{P,c})}$; A/F fit approximate distances; spectro-photometric distances for luminosity classes V, IV and and III: in bold-face are distances that are associated to the preferred luminosity class; preferred luminosity class; extinction distances; the three last columns give the distance errors arising from the spectral type uncertainty.

#	SpT	ℓ (deg)	b (deg)	$r+\delta r$ (mag)	A_r (mag)	A/F fit (kpc)	Distances $D_{\mathrm{SP,V}}$ (kpc)	$D_{\mathrm{SP,IV}}$ (kpc)	$D_{\mathrm{SP,III}}$ (kpc)	Likely Class	Error on distances due to SpT $\sigma D_{\mathrm{SP,V}}$ (kpc)	$\sigma D_{\mathrm{SP,IV}}$ (kpc)	$\sigma D_{\mathrm{SP,III}}$ (kpc)
F012	B6	120.72	-0.13	13.58 ± 0.04	1.54	3.1	$\mathbf{3.0\pm0.4}$	3.6 ± 0.5	6.0 ± 1.6	V	0.4	0.6	1.0
F026	B7	122.50	-0.17	14.25 ± 0.04	1.37	2.8	$\mathbf{3.9\pm0.5}$	4.7 ± 0.7	7.8 ± 1.9	V	0.5	0.5	1.1
F027	B6	122.64	1.87	14.82 ± 0.04	2.15	2.3	$\mathbf{4.0\pm0.5}$	4.9 ± 0.7	8.1 ± 2.2	V	0.6	0.8	1.3
F029	B5	122.80	0.99	13.90 ± 0.04	1.26	2.4	$\mathbf{4.6\pm0.5}$	5.8 ± 0.8	9.6 ± 2.5	V	0.9	1.2	1.2
F039	B5	123.62	1.18	14.25 ± 0.04	1.52	2.8	$\mathbf{4.8\pm0.6}$	6.0 ± 0.9	10.0 ± 2.7	V	0.9	1.3	1.3
F041	B3	123.78	0.57	13.38 ± 0.03	0.78	1.9	$\mathbf{6.7\pm0.9}$	8.4 ± 1.0	12.2 ± 3.0	V	1.6	1.7	2.5
F042	B8	123.77	2.34	13.50 ± 0.04	1.32	1.2	$\mathbf{2.5\pm0.3}$	3.1 ± 0.4	4.9 ± 1.2	V	0.4	0.4	0.8
F054	B6	124.96	-0.88	13.69 ± 0.04	1.34	2.8	$\mathbf{3.5\pm0.4}$	4.2 ± 0.6	7.0 ± 1.9	V	0.5	0.7	1.1
F060	B9	125.32	0.30	12.78 ± 0.04	2.15	1.9	1.0 ± 0.1	1.3 ± 0.2	$\mathbf{2.0\pm0.6}$	III	0.2	0.2	0.4
F061	B1	125.50	0.20	12.91 ± 0.03	2.50	2.2	$\mathbf{4.4\pm0.7}$	5.0 ± 0.6	6.6 ± 1.2	V	1.3	1.4	1.4
F077	B7	126.31	2.78	13.76 ± 0.04	1.67	3.0	2.7 ± 0.4	$\mathbf{3.3\pm0.5}$	5.4 ± 1.4	IV	0.4	0.4	0.7
F079	B3	126.59	0.86	13.13 ± 0.03	2.91	2.8	2.2 ± 0.3	$\mathbf{2.8\pm0.4}$	4.1 ± 1.0	IV	0.5	0.6	0.8

Table 9.5: Continued

#	SpT	ℓ (deg)	b (deg)	$r+\delta r$ (mag)	A_r (mag)	A/F fit (kpc)	Distances $D_{SP,V}$ (kpc)	$D_{SP,IV}$ (kpc)	$D_{SP,III}$ (kpc)	Likely Class	Error on distances due to SpT $\sigma D_{SP,V}$ (kpc)	$\sigma D_{SP,IV}$ (kpc)	$\sigma D_{SP,III}$ (kpc)
F083	B3	126.73	1.70	12.92 ± 0.04	2.56	2.5	**2.4 ± 0.3**	3.0 ± 0.4	4.3 ± 1.1	V	0.6	0.6	0.9
F085	B3	127.06	0.28	13.51 ± 0.04	1.72	2.2	**4.6 ± 0.7**	5.8 ± 0.7	8.4 ± 2.1	V	1.1	1.2	1.7
F092	B4	127.60	0.12	13.42 ± 0.04	2.35	2.4	**2.8 ± 0.4**	3.5 ± 0.5	5.0 ± 1.4	V	0.5	0.7	0.7
F095	B6	127.82	0.29	13.12 ± 0.03	1.14	0.0	**3.0 ± 0.3**	3.5 ± 0.5	5.9 ± 1.6	V	0.4	0.6	1.0
F098	B3	128.06	1.48	13.42 ± 0.04	1.70	3.9	**4.5 ± 0.6**	5.6 ± 0.7	8.1 ± 2.0	V	1.0	1.1	1.7
F102	B6	127.83	3.31	13.73 ± 0.03	2.25	1.5	**2.3 ± 0.3**	2.8 ± 0.4	4.7 ± 1.2	V	0.3	0.5	0.8
F107	B6	128.81	0.23	13.20 ± 0.04	1.42	1.9	**2.7 ± 0.3**	3.2 ± 0.5	5.4 ± 1.4	V	0.4	0.5	0.9
F108	B7	128.58	1.72	13.44 ± 0.04	1.57	2.0	**2.5 ± 0.3**	3.0 ± 0.4	4.9 ± 1.2	V	0.3	0.3	0.7
F114	B2	129.41	-0.97	12.27 ± 0.04	2.00	2.6	**3.0 ± 0.5**	3.6 ± 0.6	5.2 ± 1.2	V	0.9	0.9	1.0
F116	B4	129.45	-0.93	13.97 ± 0.04	1.59	2.0	**5.1 ± 0.6**	6.4 ± 0.8	9.2 ± 2.5	V	1.0	1.2	1.2
F118	B3	129.51	-0.99	13.34 ± 0.03	2.12	3.0	**3.5 ± 0.5**	4.5 ± 0.6	6.5 ± 1.6	V	0.8	0.9	1.3
F125	B6	129.01	3.29	13.82 ± 0.04	1.85	3.2	**3.0 ± 0.4**	3.5 ± 0.5	5.9 ± 1.6	V	0.4	0.6	1.0
F126	B9	129.42	1.57	15.78 ± 0.03	2.35	3.6	**3.6 ± 0.6**	4.6 ± 0.8	7.3 ± 2.1	V	0.7	0.8	1.3
F129	B7	130.04	-0.78	13.64 ± 0.04	1.77	2.1	**2.5 ± 0.3**	3.0 ± 0.4	4.9 ± 1.2	V	0.3	0.3	0.7
F131	B7	129.81	0.75	13.08 ± 0.04	1.57	2.5	2.1 ± 0.3	**2.5 ± 0.4**	4.1 ± 1.0	IV	0.3	0.3	0.6
F134	B5	129.39	2.92	14.04 ± 0.04	1.62	4.2	**4.1 ± 0.6**	5.2 ± 0.8	8.7 ± 2.3	V	0.8	1.1	1.1
F135	B6	130.11	0.04	12.86 ± 0.03	1.64	2.4	2.1 ± 0.3	**2.5 ± 0.4**	4.2 ± 1.1	IV	0.3	0.4	0.7
F136	B7	129.54	2.45	14.00 ± 0.03	1.44	3.6	**3.4 ± 0.5**	4.0 ± 0.6	6.7 ± 1.7	V	0.5	0.5	0.9
F139	B3	130.53	-0.63	13.45 ± 0.03	1.87	2.4	**4.2 ± 0.6**	5.3 ± 0.7	7.6 ± 1.9	V	1.0	1.1	1.6
F141	B3	130.16	0.88	14.50 ± 0.04	1.90	4.3	**6.7 ± 1.0**	8.5 ± 1.1	12.2 ± 3.0	V	1.6	1.7	2.5
F144	B1	130.61	-0.40	12.75 ± 0.03	1.64	2.4	**6.0 ± 1.0**	6.9 ± 0.9	9.1 ± 1.7	V	1.8	1.9	1.9
F145	B4	130.23	1.11	13.45 ± 0.04	0.71	1.3	**5.4 ± 0.7**	6.8 ± 0.9	10.5 ± 2.8	V	1.0	1.4	1.4
F147	B3	130.05	1.92	13.25 ± 0.04	2.10	5.2	3.4 ± 0.5	**4.3 ± 0.5**	6.2 ± 1.5	IV	0.8	0.9	1.3
F152	B4	129.77	3.52	13.09 ± 0.04	1.57	3.7	**3.4 ± 0.5**	4.3 ± 0.6	6.2 ± 1.7	V	0.7	0.8	0.8
F157	B4	130.07	2.92	12.91 ± 0.04	1.26	4.1	3.6 ± 0.5	**4.6 ± 0.6**	6.6 ± 1.8	IV	0.7	0.9	0.9
F159	B5	130.17	2.69	13.40 ± 0.04	1.37	2.5	**3.5 ± 0.4**	4.4 ± 0.6	7.2 ± 1.9	V	0.7	0.9	0.9
F162	B3	130.45	2.14	14.20 ± 0.04	2.23	6.6	5.0 ± 0.7	**6.3 ± 0.8**	9.1 ± 2.2	IV	1.2	1.3	1.9
F167	B7	131.19	-0.21	13.22 ± 0.04	1.64	2.2	**2.1 ± 0.3**	2.6 ± 0.4	4.3 ± 1.1	V	0.3	0.3	0.6
F172	B7	131.08	1.00	13.83 ± 0.04	1.64	5.0	2.8 ± 0.4	3.4 ± 0.5	**5.7 ± 1.4**	III	0.4	0.4	0.8
F173	B5	130.65	2.75	14.02 ± 0.04	1.39	4.5	**4.6 ± 0.6**	5.7 ± 0.9	9.5 ± 2.6	V	0.9	1.2	1.2
F175	B1	130.92	2.47	12.69 ± 0.03	1.67	3.7	**5.8 ± 1.0**	6.7 ± 0.9	8.8 ± 1.6	V	1.7	1.8	1.8

Table 9.5: Continued

#	SpT	ℓ (deg)	b (deg)	$r+\delta r$ (mag)	A_r (mag)	A/F fit (kpc)	Distances $D_{\rm SP,V}$ (kpc)	$D_{\rm SP,IV}$ (kpc)	$D_{\rm SP,III}$ (kpc)	Likely Class	Error on distances due to SpT $\sigma D_{\rm SP,V}$ (kpc)	$\sigma D_{\rm SP,IV}$ (kpc)	$\sigma D_{\rm SP,III}$ (kpc)
F179	B3	130.88	3.15	12.67 ± 0.04	1.16	3.6	$\mathbf{4.0\pm0.6}$	5.1 ± 0.6	7.4 ± 1.8	V	0.9	1.0	1.5
F183	B3	131.91	0.18	13.54 ± 0.04	1.95	2.5	$\mathbf{4.2\pm0.6}$	5.3 ± 0.7	7.7 ± 1.9	V	1.0	1.1	1.6
F184	A0	131.55	1.39	14.53 ± 0.04	2.10	3.6	1.9 ± 0.3	2.4 ± 0.4	$\mathbf{3.9\pm1.1}$	III	0.3	0.4	0.7
F187	B3	131.52	1.68	12.42 ± 0.03	1.47	3.5	$\mathbf{3.1\pm0.5}$	4.0 ± 0.5	5.7 ± 1.4	V	0.7	0.8	1.2
F189	B9	132.08	0.03	13.96 ± 0.04	2.76	2.4	1.3 ± 0.2	1.7 ± 0.3	$\mathbf{2.6\pm0.8}$	III	0.2	0.3	0.5
F190	B8	131.37	2.57	12.85 ± 0.04	1.32	2.5	1.8 ± 0.3	$\mathbf{2.3\pm0.3}$	3.6 ± 0.9	IV	0.3	0.3	0.6
F195	B8	132.31	-0.18	13.14 ± 0.04	1.97	2.1	1.6 ± 0.2	$\mathbf{1.9\pm0.3}$	3.1 ± 0.8	IV	0.2	0.3	0.5
F196	B6	131.88	1.30	14.01 ± 0.04	1.97	2.7	$\mathbf{3.0\pm0.4}$	3.6 ± 0.5	6.0 ± 1.6	V	0.4	0.6	1.0
F198	B6	131.64	2.26	14.00 ± 0.04	2.10	4.3	2.8 ± 0.4	$\mathbf{3.4\pm0.5}$	5.7 ± 1.5	IV	0.4	0.6	0.9
F201	B5	132.09	1.12	12.28 ± 0.04	1.29	1.9	$\mathbf{2.1\pm0.3}$	2.7 ± 0.4	4.5 ± 1.2	V	0.4	0.6	0.6
F205	B7	131.68	2.96	15.10 ± 0.04	1.72	4.1	$\mathbf{4.9\pm0.7}$	5.9 ± 0.9	9.8 ± 2.5	V	0.7	0.7	1.3
F212	B4	131.98	3.38	13.92 ± 0.03	1.77	3.7	$\mathbf{4.6\pm0.6}$	5.8 ± 0.7	8.3 ± 2.2	V	0.9	1.1	1.1
F224	B8	133.19	1.55	14.72 ± 0.03	0.99	0.0	$\mathbf{5.0\pm0.7}$	6.3 ± 0.9	10.1 ± 2.5	V	0.8	0.8	1.6
F228	B7	134.02	-0.27	13.08 ± 0.03	2.45	2.7	1.4 ± 0.2	1.7 ± 0.2	$\mathbf{2.8\pm0.7}$	III	0.2	0.2	0.4
F232	B5	132.68	3.74	13.40 ± 0.03	2.12	4.2	2.5 ± 0.3	3.1 ± 0.4	$\mathbf{5.1\pm1.4}$	III	0.5	0.6	0.7
F238	B3	133.57	2.46	13.05 ± 0.04	1.75	5.8	3.7 ± 0.5	4.6 ± 0.6	$\mathbf{6.7\pm1.6}$	III	0.9	0.9	1.4
F246	B4	134.86	0.31	13.92 ± 0.04	1.80	3.0	$\mathbf{4.5\pm0.6}$	5.7 ± 0.8	8.2 ± 2.2	V	0.9	1.1	1.1
F254	B3	135.47	-0.40	13.33 ± 0.04	2.12	2.6	$\mathbf{3.5\pm0.5}$	4.4 ± 0.6	6.4 ± 1.6	V	0.8	0.9	1.3
F264	B7	134.38	3.30	13.33 ± 0.04	1.11	3.9	2.9 ± 0.4	$\mathbf{3.5\pm0.5}$	5.8 ± 1.4	IV	0.4	0.4	0.8
F265	B4	135.09	1.71	13.25 ± 0.03	2.08	5.0	2.9 ± 0.4	3.7 ± 0.5	$\mathbf{5.3\pm1.4}$	III	0.6	0.7	0.7
F281	B3	135.11	3.17	14.34 ± 0.04	1.37	7.5	$\mathbf{8.0\pm1.1}$	10.0 ± 1.2	14.5 ± 3.5	V	1.9	2.0	3.0
F292	B3	137.03	-0.34	13.43 ± 0.04	1.44	2.3	$\mathbf{5.1\pm0.7}$	6.4 ± 0.8	9.2 ± 2.2	V	1.2	1.3	1.9
F295	B5	136.15	2.07	13.53 ± 0.04	1.37	4.0	$\mathbf{3.7\pm0.5}$	4.7 ± 0.7	7.7 ± 2.1	V	0.7	1.0	1.0
F297	B3	136.33	1.76	14.54 ± 0.04	2.15	4.7	$\mathbf{6.1\pm0.9}$	7.7 ± 0.9	11.1 ± 2.7	V	1.4	1.6	2.3
F299	B5	136.29	1.99	13.00 ± 0.04	1.19	4.8	3.1 ± 0.4	$\mathbf{4.0\pm0.5}$	6.5 ± 1.7	IV	0.6	0.8	0.8
F304	B5	136.23	2.46	13.15 ± 0.03	1.04	3.7	$\mathbf{3.6\pm0.5}$	4.5 ± 0.6	7.5 ± 2.0	V	0.7	0.9	1.0
F314	B6	136.49	2.54	14.01 ± 0.04	1.24	4.0	$\mathbf{4.2\pm0.5}$	5.1 ± 0.7	8.5 ± 2.2	V	0.6	0.8	1.4
F315	B7	138.12	-0.70	13.09 ± 0.04	1.06	1.8	$\mathbf{2.6\pm0.3}$	3.2 ± 0.5	5.3 ± 1.3	V	0.4	0.4	0.7
F350	B3	138.73	0.77	14.32 ± 0.03	2.25	3.1	$\mathbf{5.2\pm0.7}$	6.6 ± 0.8	9.5 ± 2.3	V	1.2	1.3	1.9

Acknowledgements

Writing thelast words is always the most difficult tasks. One doesn't want to forget people and it generally doesn't happen. If you are here, it's because your contribution was important. Most of you didn't help in writing this thesis, but you're in the acknowledgements because we met and I did enjoyed your company as well as you enjoyed mine (hopefully!). Without you all, these could have been four very boring years.

First of all, of course, I must thank Janet. Working with her has always stimulated my curiosity and desire for improvement. Second, I would like to thank Mark, who's been there when I needed him. A few other people gave their contribution to my research: Juan, Stuart, Danny, Nick. All of them are top researchers and nice people to drink a pint with.

Now, I must thank a person, who I have more than one reason to be obliged to. Kieran has been a very good friend, one of those without an equal. He's a computer genius, the best drinking buddy, and always fun to talk to. I cannot forget my flatmates, with whom it's been a pleasure to share the house: Federico, Hugo, Hywel, and at last, but not the least, Zeng Hua. He's been my very first friend in the UK, my personal interpreter during our trip in China and a very wise man. Manuel is a person that probably would need a chapter on his own, yet this thesis is already too long.

Of course, now, it's Hanifa turn. She's one of the most beautiful women I know and I am very proud to say we're friend. Between us, I'm not sure who's the most stubborn and crazy about silly things. A special place in my hearth is also occupied by Iolanda. I'd never expected to meet a person like her in Hatfield. She's been a good friend in difficult times. Here we're with Joana. Before meeting her I'd never thought that Portuguese women could be as special as she is. I also cannot forget Silvia: I'm very glad I met her, even if I didn't when she was in Napoli.

I also need to thank James for his sarcasm. He's a cool dude, although he's also a smart ass despite Maria's nice efforts in trying to make him act better. Carlos and Noemí also need a particular mention; I always appreciate the affection they have for me. Many other people could be mentioned but, above all, Lisette who's always one of the nicest, John for is patience and help with my computer problems, and James for the interesting conversations on history, art, music and more.

At the very end, I would like to thank H.R.M. the Queen Elizabeth II, who probably doesn't know me. However, I thank Her for being the monarch of this wonderful land, which I very much appreciated during these four years.

Bibliography

Abadi M. G., Navarro J. F., Steinmetz M., Eke V. R., 2003, ApJ, 591, 499

Abt H. A., Cardona O., 1984, ApJ, 285, 190

Alcala J. M., Krautter J., Schmitt J. H. M. M., Covino E., Wichmann R., Mundt R., 1995, A&AS, 114, 109

Aller L. H., Appenzeller I., Baschek B., Duerbeck H. W., Herczeg T., Lamla E., Meyer-Hofmeister E., Schmidt-Kaler T., Scholz M., Seggewiss W., Seitter W. C., Weidemann V., eds., 1982, Landolt-Börnstein: Numerical Data and Functional Relationships in Science and Technology - New Series " Group 6 Astronomy and Astrophysics " Volume 2: Astronomy and Astrophysics " Stars and Star Clusters

Aumer M., Binney J. J., 2009, MNRAS, 397, 1286

Balick B., Frank A., 2002, ARA&A, 40, 439

Barentsen G. et al., 2011, MNRAS, 415, 103

Battaglia G. et al., 2005, MNRAS, 364, 433

Bensby T., Feltzing S., Lundström I., Ilyin I., 2005, A&A, 433, 185

Bertout C., 1989, ARA&A, 27, 351

Bessell M. S., Brett J. M., 1988, PASP, 100, 1134

Binney J., Merrifield M., 1998, Galactic Astronomy

Bohlin R. C., 2007, in Astronomical Society of the Pacific Conference Series, Vol. 364, The Future of Photometric, Spectrophotometric and Polarimetric Standardization, Sterken C., ed., p. 315

Bonatto C., Bica E., 2010, A&A, 521, A74

Bovy J., Rix H.-W., Hogg D. W., 2012, ApJ, 751, 131

Brand J., Blitz L., 1993, A&A, 275, 67

Brunthaler A. et al., 2011, Astronomische Nachrichten, 332, 461

Calvet N., Gullbring E., 1998, ApJ, 509, 802

Camargo D., Bonatto C., Bica E., 2009, A&A, 508, 211

Cambrésy L., Jarrett T. H., Beichman C. A., 2005, A&A, 435, 131

Camenzind M., 1990, in Reviews in Modern Astronomy, Vol. 3, Reviews in Modern Astronomy, Klare G., ed., p. 234

Carciofi A. C., Bjorkman J. E., 2006, ApJ, 639, 1081

Carciofi A. C., Bjorkman J. E., Otero S. A., Okazaki A. T., Štefl S., Rivinius T., Baade D., Haubois X., 2012, ApJ, 744, L15

Cardelli J. A., Clayton G. C., Mathis J. S., 1989, ApJ, 345, 245

Carpenter J. M., 2001, AJ, 121, 2851

Carpenter J. M., Heyer M. H., Snell R. L., 2000, ApJS, 130, 381

Carraro G., Geisler D., Villanova S., Frinchaboy P. M., Majewski S. R., 2007, A&A, 476, 217

Carraro G., Vázquez R. A., Moitinho A., Baume G., 2005, ApJ, 630, L153

Cazzolato F., Pineault S., 2003, AJ, 125, 2050

Chauhan N., Pandey A. K., Ogura K., Jose J., Ojha D. K., Samal M. R., Mito H., 2011, MNRAS, 415, 1202

Chauville J., Zorec J., Ballereau D., Morrell N., Cidale L., Garcia A., 2001, A&A, 378, 861

Chen L., Hou J. L., Wang J. J., 2003, AJ, 125, 1397

Chiappini C., Matteucci F., Romano D., 2001, ApJ, 554, 1044

Corradi R. L. M. et al., 2008, A&A, 480, 409

Corradi R. L. M., Sabin L., Munari U., Cetrulo G., Englaro A., Angeloni R., Greimel R., Mampaso A., 2011, A&A, 529, A56

Curtis H. D., 1921, Bull. Nat. Res. Coun., 2, 194

Dachs J., Hanuschik R., Kaiser D., Rohe D., 1986, A&A, 159, 276

Dachs J., Kiehling R., Engels D., 1988, A&A, 194, 167

Dachs J., Rohe D., Loose A. S., 1990, A&A, 238, 227

Dame T. M., Hartmann D., Thaddeus P., 2001, ApJ, 547, 792

Dame T. M., Thaddeus P., 2011, ApJ, 734, L24

de Bruijne J. H. J., 2012, APSS, 341, 31

de la Fuente Marcos R., de la Fuente Marcos C., 2008, ApJ, 672, 342

de La Fuente Marcos R., de La Fuente Marcos C., 2009, New Astronomy, 14, 180

de Vaucouleurs G., 1964, in IAU Symposium, Vol. 20, The Galaxy and the Magellanic Clouds, Kerr F. J., ed., p. 195

de Vaucouleurs G., Pence W. D., 1978, AJ, 83, 1163

Dennison B., Topasna G. A., Simonetti J. H., 1997, ApJ, 474, L31

Dias W. S., Alessi B. S., Moitinho A., Lépine J. R. D., 2002, A&A, 389, 871

Didelon P., 1982, A&AS, 50, 199

Digel S., de Geus E., Thaddeus P., 1994, ApJ, 422, 92

Digel S. W., Lyder D. A., Philbrick A. J., Puche D., Thaddeus P., 1996, ApJ, 458, 561

Dobbs C. L., Pringle J. E., 2010, MNRAS, 409, 396

Dougherty S. M., Taylor A. R., 1992, Nature, 359, 808

Dougherty S. M., Waters L. B. F. M., Burki G., Cote J., Cramer N., van Kerkwijk M. H., Taylor A. R., 1994, A&A, 290, 609

Drew J. E., 1989, ApJS, 71, 267

Drew J. E. et al., 2005, MNRAS, 362, 753

Drimmel R., 2000, A&A, 358, L13

Drimmel R., Spergel D. N., 2001, ApJ, 556, 181

Elmegreen B. G., 2007, ApJ, 668, 1064

Elmegreen B. G., Seiden P. E., Elmegreen D. M., 1989, ApJ, 343, 602

Fabregat J., Gutierrez-Soto J., 2005, Publications of the Astronomical Institute of the Czechoslovak Academy of Sciences, 93, 9

Fabregat J., Torrejón J. M., 2000, A&A, 357, 451

Fabricant D., Cheimets P., Caldwell N., Geary J., 1998, PASP, 110, 79

Fall S. M., Efstathiou G., 1980, MNRAS, 193, 189

Ferguson A. M. N., Wyse R. F. G., Gallagher J. S., Hunter D. A., 1998, ApJ, 506, L19

Finkenzeller U., Mundt R., 1984, A&AS, 55, 109

Fitzpatrick E. L., 1999, PASP, 111, 63

Fitzpatrick E. L., Massa D., 2007, ApJ, 663, 320

Foyle K., Rix H.-W., Dobbs C. L., Leroy A. K., Walter F., 2011, ApJ, 735, 101

Frémat Y., Zorec J., Hubert A.-M., Floquet M., 2005, A&A, 440, 305

Freudenreich H. T. et al., 1994, ApJ, 429, L69

Friedman S. D. et al., 2011, ApJ, 727, 33

Garcia-Hernandez D. A., Diaz-Luis J. J., 2013, ArXiv e-prints

Garmany C. D., Stencel R. E., 1992, A&AS, 94, 211

Gehrz R. D., Hackwell J. A., Jones T. W., 1974, ApJ, 191, 675

Georgelin Y. M., Georgelin Y. P., 1976, A&A, 49, 57

Ghez A. M., Klein B. L., Morris M., Becklin E. E., 1998, ApJ, 509, 678

Ghez A. M. et al., 2008, ApJ, 689, 1044

Giammanco C. et al., 2011, A&A, 525, A58+

Gilmore G., Reid N., 1983, MNRAS, 202, 1025

González-Solares E. A. et al., 2008, MNRAS, 388, 89

Goodwin S. P., Bastian N., 2006, MNRAS, 373, 752

Gray R. O., Corbally, J. C., 2009, Stellar Spectral Classification, Gray, R. O. & Corbally, C., J., ed.

Groot P. J. et al., 2009, MNRAS, 399, 323

Guarinos J., 1988, Bulletin d'Information du Centre de Donnees Stellaires, 34, 141

Gullbring E., Hartmann L., Briceno C., Calvet N., 1998, ApJ, 492, 323

Gummersbach C. A., Kaufer A., Schaefer D. R., Szeifert T., Wolf B., 1998, A&A, 338, 881

Hachisuka K., Brunthaler A., Menten K. M., Reid M. J., Hagiwara Y., Mochizuki N., 2009, ApJ, 696, 1981

Hachisuka K. et al., 2006, ApJ, 645, 337

Hamann F., Persson S. E., 1992, ApJS, 82, 285

Hartigan P., Edwards S., Ghandour L., 1995, ApJ, 452, 736

Hartmann L., Calvet N., Gullbring E., D'Alessio P., 1998, ApJ, 495, 385

Herbig G. H., 1975, ApJ, 196, 129

Herbig G. H., 1995, ARA&A, 33, 19

Hernández J., Calvet N., Briceño C., Hartmann L., Berlind P., 2004, AJ, 127, 1682

Heyer M. H., Brunt C., Snell R. L., Howe J. E., Schloerb F. P., Carpenter J. M., 1998, ApJS, 115, 241

Heyer M. H., Terebey S., 1998, ApJ, 502, 265

Hillenbrand L. A., Strom S. E., Vrba F. J., Keene J., 1992, ApJ, 397, 613

Hodge P. W., 1979, AJ, 84, 744

Honma M., Hirota T., Kan-Ya Y., Kawaguchi N., Kobayashi H., Kurayama T., Sato K., 2011, PASJ, 63, 17

Hou J. L., Prantzos N., Boissier S., 2000, A&A, 362, 921

Houk N., Swift C. M., Murray C. A., Penston M. J., Binney J. J., 1997, in ESA Special Publication, Vol. 402, Hipparcos - Venice '97, R. M. Bonnet, E. Høg, P. L. Bernacca, L. Emiliani, A. Blaauw, C. Turon, J. Kovalevsky, L. Lindegren, H. Hassan, M. Bouffard, B. Strim, D. Heger, M. A. C. Perryman, & L. Woltjer, ed., p. 279

Howells L., Steele I. A., Porter J. M., Etherton J., 2001, A&A, 369, 99

Humphreys R. M., 1976, PASP, 88, 647

Iben, Jr. I., Livio M., 1993, PASP, 105, 1373

Jaschek C., Jaschek M., 1987, The classification of stars, Jaschek, C. & Jaschek, M., ed.

Johnstone D., Hollenbach D., Bally J., 1998, ApJ, 499, 758

Jones C. E., Sigut T. A. A., Marlborough J. M., 2004, MNRAS, 352, 841

Jones C. E., Tycner C., Smith A. D., 2011, AJ, 141, 150

Jurić M. et al., 2008, ApJ, 673, 864

Kaiser D., 1989, A&A, 222, 187

Kalberla P. M. W., Kerp J., 2009, ARA&A, 47, 27

Karr J. L., Martin P. G., 2003, ApJ, 595, 900

Kenyon S. J., Hartmann L., 1987, ApJ, 323, 714

Kenyon S. J., Hartmann L., 1995, ApJS, 101, 117

Kerr F. J., Lynden-Bell D., 1986, MNRAS, 221, 1023

Kharchenko N. V., Piskunov A. E., Röser S., Schilbach E., Scholz R.-D., 2005, A&A, 438, 1163

Kimeswenger S., Weinberger R., 1989, A&A, 209, 51

Klypin A., Zhao H., Somerville R. S., 2002, ApJ, 573, 597

Koenig X. P., Allen L. E., Gutermuth R. A., Hora J. L., Brunt C. M., Muzerolle J., 2008, ApJ, 688, 1142

Kohoutek L., Wehmeyer R., 1999, A&AS, 134, 255

Kouwenhoven M. B. N., Brown A. G. A., Zinnecker H., Kaper L., Portegies Zwart S. F., 2005, A&A, 430, 137

Kregel M., van der Kruit P. C., de Grijs R., 2002, MNRAS, 334, 646

Krełowski J., Sneden C., 1995, in Astrophysics and Space Science Library, Vol. 202, The Diffuse Interstellar Bands, Tielens A. G. G. M., Snow T. P., eds., p. 13

Kurosawa R., Harries T. J., Symington N. H., 2006, MNRAS, 370, 580

Lacy J. H., Townes C. H., Geballe T. R., Hollenbach D. J., 1980, ApJ, 241, 132

Lada C. J., 1987, in IAU Symposium, Vol. 115, Star Forming Regions, Peimbert M., Jugaku J., eds., pp. 1–17

Lada C. J., Adams F. C., 1992, ApJ, 393, 278

Lada C. J., Elmegreen B. G., Cong H.-I., Thaddeus P., 1978, ApJ, 226, L39

Lamers H. J. G. L. M., Zickgraf F.-J., de Winter D., Houziaux L., Zorec J., 1998, A&A, 340, 117

Lee H.-T., Chen W. P., 2007, ApJ, 657, 884

Lee U., Osaki Y., Saio H., 1991, MNRAS, 250, 432

Lee Y. S. et al., 2011, ApJ, 738, 187

Lépine J. R. D., Roman-Lopes A., Abraham Z., Junqueira T. C., Mishurov Y. N., 2011, MNRAS, 414, 1607

Levine E. S., Blitz L., Heiles C., 2006, Science, 312, 1773

Lin C. C., Shu F. H., 1964, ApJ, 140, 646

Lindblad B., 1927, MNRAS, 87, 553

Lubow S. H., Cowie L. L., Balbus S. A., 1986, ApJ, 309, 496

Lucas P. W. et al., 2008, MNRAS, 391, 136

Maciejewski G., Niedzielski A., 2007, A&A, 467, 1065

Martayan C., Frémat Y., Hubert A.-M., Floquet M., Zorec J., Neiner C., 2007, A&A, 462, 683

Martin E. L., Claret A., 1996, A&A, 306, 408

Martins L. P., González Delgado R. M., Leitherer C., Cerviño M., Hauschildt P., 2005, MNRAS, 358, 49

Massey P., Johnson K. E., Degioia-Eastwood K., 1995, ApJ, 454, 151

Mathew B., Subramaniam A., 2011, Bulletin of the Astronomical Society of India, 39, 517

Mathew B., Subramaniam A., Bhatt B. C., 2008, MNRAS, 388, 1879

May J., Alvarez H., Bronfman L., 1997, A&A, 327, 325

McKee C. F., Ostriker E. C., 2007, ARA&A, 45, 565

McSwain M. V., Gies D. R., 2005, ApJS, 161, 118

Megeath S. T., Townsley L. K., Oey M. S., Tieftrunk A. R., 2008, Low and High Mass Star Formation in the W3, W4, and W5 Regions, Reipurth B., ed., p. 264

Meilland A. et al., 2007, A&A, 464, 59

Mel'Nik A. M., Dambis A. K., Rastorguev A. S., 1999, Astronomy Letters, 25, 518

Mermilliod J. C., 1982, A&A, 109, 48

Merrill P. W., 1934, PASP, 46, 206

Merrill P. W., Wilson O. C., 1938, ApJ, 87, 9

Meyer M. R., Calvet N., Hillenbrand L. A., 1997, AJ, 114, 288

Minniti D. et al., 2010, New Astronomy, 15, 433

Minniti D., Saito R. K., Alonso-García J., Lucas P. W., Hempel M., 2011, ApJ, 733, L43

Moitinho A., Vázquez R. A., Carraro G., Baume G., Giorgi E. E., Lyra W., 2006, MNRAS, 368, L77

Momany Y., Zaggia S., Gilmore G., Piotto G., Carraro G., Bedin L. R., de Angeli F., 2006, A&A, 451, 515

Monet D. G. et al., 2003, AJ, 125, 984

Moore T. J. T., Bretherton D. E., Fujiyoshi T., Ridge N. A., Allsopp J., Hoare M. G., Lumsden S. L., Richer J. S., 2007, MNRAS, 379, 663

Morgan W. W., Keenan P. C., Kellman E., 1943, An atlas of stellar spectra, with an outline of spectral classification

Morgan W. W., Whitford A. E., Code A. D., 1953, ApJ, 118, 318

Munari U., Sordo R., Castelli F., Zwitter T., 2005, A&A, 442, 1127

Muzzio J. C., Rydgren A. E., 1974, AJ, 79, 864

Negueruela I., Marco A., 2003, A&A, 406, 119

Neiner C., de Batz B., Cochard F., Floquet M., Mekkas A., Desnoux V., 2011, AJ, 142, 149

Normandeau M., Taylor A. R., Dewdney P. E., 1996, Nature, 380, 687

Oey M. S., Watson A. M., Kern K., Walth G. L., 2005, AJ, 129, 393

Oort J. H., 1927, Bulletin of the Astronomical Institutes of the Netherlands, 3, 275

Oort J. H., Kerr F. J., Westerhout G., 1958, MNRAS, 118, 379

Oudmaijer R. D., Parr A. M., 2010, MNRAS, 405, 2439

Oudmaijer R. D., Wheelwright H. E., Carciofi A. C., Bjorkman J. E., Bjorkman K. S., 2011, in IAU Symposium, Vol. 272, IAU Symposium, Neiner C., Wade G., Meynet G., Peters G., eds., pp. 418–419

Pandey A. K., Sharma S., Ogura K., 2006, MNRAS, 373, 255

Pandey A. K., Upadhyay K., Nakada Y., Ogura K., 2003, A&A, 397, 191

Pandey A. K., Upadhyay K., Ogura K., Sagar R., Mohan V., Mito H., Bhatt H. C., Bhatt B. C., 2005, MNRAS, 358, 1290

Pickles A. J., 1998, PASP, 110, 863

Plaskett J. S., Pearce J. A., 1930, MNRAS, 90, 243

Poeckert R., Marlborough J. M., 1978, ApJS, 38, 229

Porter J. M., Rivinius T., 2003, PASP, 115, 1153

Pottasch S. R., 1996, A&A, 307, 561

Pretorius M. L., Knigge C., O'Donoghue D., Henry J. P., Gioia I. M., Mullis C. R., 2007, MNRAS, 382, 1279

Quirrenbach A. et al., 1997, ApJ, 479, 477

Rand R. J., Kulkarni S. R., 1990, ApJ, 349, L43

Reid M. J., 1993, ARA&A, 31, 345

Reid M. J. et al., 2009a, ApJ, 700, 137

Reid M. J., Menten K. M., Zheng X. W., Brunthaler A., Xu Y., 2009b, ApJ, 705, 1548

Rieke G. H., Lebofsky M. J., 1985, ApJ, 288, 618

Rix H.-W., Zaritsky D., 1995, ApJ, 447, 82

Roberts W. W., 1969, ApJ, 158, 123

Roberts, Jr. W. W., 1972, ApJ, 173, 259

Robin A. C., Creze M., Mohan V., 1992, A&A, 265, 32

Rolleston W. R. J., Smartt S. J., Dufton P. L., Ryans R. S. I., 2000, A&A, 363, 537

Rowles J., Froebrich D., 2009, MNRAS, 395, 1640

Ruphy S., Robin A. C., Epchtein N., Copet E., Bertin E., Fouque P., Guglielmo F., 1996, A&A, 313, L21

Russeil D., 2003, A&A, 397, 133

Russeil D., Adami C., Georgelin Y. M., 2007, A&A, 470, 161

Sale S. E., 2012, MNRAS, 427, 2119

Sale S. E. et al., 2010, MNRAS, 402, 713

Sale S. E. et al., 2009, MNRAS, 392, 497

Sanna A., Reid M. J., Dame T. M., Menten K. M., Brunthaler A., Moscadelli L., Zheng X. W., Xu Y., 2012, ApJ, 745, 82

Schaller G., Schaerer D., Meynet G., Maeder A., 1992, A&AS, 96, 269

Schlegel D. J., Finkbeiner D. P., Davis M., 1998, ApJ, 500, 525

Sellwood J. A., Binney J. J., 2002, MNRAS, 336, 785

Shapley H., 1921, Bull. Nat. Res. Coun., 2, 171

Shu F. H., Adams F. C., Lizano S., 1987, ARA&A, 25, 23

Siess L., Forestini M., Dougados C., 1997, A&A, 324, 556

Skrutskie M. F. et al., 2006, AJ, 131, 1163

Slettebak A., 1985, ApJS, 59, 769

Snell R. L., Carpenter J. M., Heyer M. H., 2002, ApJ, 578, 229

Snow T. P., Zukowski D., Massey P., 2002, ApJ, 578, 877

Snow, Jr. T. P., York D. G., Welty D. E., 1977, AJ, 82, 113

Spitzer L., 1978, Physical processes in the interstellar medium

Steiman-Cameron T. Y., Wolfire M., Hollenbach D., 2010, ApJ, 722, 1460

Straizys V., Kuriliene G., 1981, APSS, 80, 353

Struve O., 1931, ApJ, 73, 94

Szczerba R., Siódmiak N., Stasińska G., Borkowski J., 2007, A&A, 469, 799

Taylor A. R., Irwin J. A., Matthews H. E., Heyer M. H., 1999, ApJ, 513, 339

The P. S., de Winter D., Perez M. R., 1994, A&AS, 104, 315

Thompson M. A., White G. J., Morgan L. K., Miao J., Fridlund C. V. M., Huldtgren-White M., 2004, A&A, 414, 1017

Townsend R. H. D., Owocki S. P., Howarth I. D., 2004, MNRAS, 350, 189

Trippe S. et al., 2008, A&A, 492, 419

Trumpler R. J., 1930, Lick Observatory Bulletin, 14, 154

Tycner C. et al., 2005, ApJ, 624, 359

Valdes F., Gupta R., Rose J. A., Singh H. P., Bell D. J., 2004, ApJS, 152, 251

Vallée J. P., 2002, ApJ, 566, 261

Vallée J. P., 2005, AJ, 130, 569

Vallée J. P., 2008, AJ, 135, 1301

van der Kruit P. C., 1979, A&AS, 38, 15

van der Kruit P. C., 1987, A&A, 173, 59

van der Kruit P. C., 2007, A&A, 466, 883

van der Kruit P. C., Searle L., 1981, A&A, 95, 116

Vázquez R. A., May J., Carraro G., Bronfman L., Moitinho A., Baume G., 2008, ApJ, 672, 930

Viironen K. et al., 2009, A&A, 504, 291

Viironen K. et al., 2011, A&A, 530, A107

Vink J. S., Drew J. E., Harries T. J., Oudmaijer R. D., 2002, MNRAS, 337, 356

Vink J. S., Drew J. E., Harries T. J., Oudmaijer R. D., Unruh Y., 2005, MNRAS, 359, 1049

von Zeipel H., 1924, MNRAS, 84, 684

Wampler E. J., 1963, ApJ, 137, 1071

Warner B., 2003, Cataclysmic Variable Stars

Waters L. B. F., Marlborough J. M., van der Veen W. E. C., Taylor A. R., Dougherty S. M., 1991, A&A, 244, 120

Waters L. B. F. M., Waelkens C., 1998, ARA&A, 36, 233

Wegner W., 2000, MNRAS, 319, 771

Weinberger R., 1989, A&AS, 78, 301

Westerhout G., 1958, Bulletin of the Astronomical Institutes of the Netherlands, 14, 215

Witham A. R., Knigge C., Drew J. E., Greimel R., Steeghs D., Gänsicke B. T., Groot P. J., Mampaso A., 2008, MNRAS, 384, 1277

Xu Y., Reid M. J., Zheng X. W., Menten K. M., 2006, Science, 311, 54

Yadav R. K. S., Kumar B., Subramaniam A., Sagar R., Mathew B., 2008, MNRAS, 390, 985

Zorec J., Briot D., 1991, A&A, 245, 150

Zorec J., Briot D., 1997, A&A, 318, 443

Zorec J., Cidale L., Arias M. L., Fremat Y., Muratore M. F., Torres A. F., Martayan C., 2009, ArXiv e-prints